An Experimental and Modelling Study of Oxygen Reduction in Porous LSM/YSZ Solid Oxide Fuel Cell Cathodes

by

Benjamin Anthony Kenney

A thesis submitted to the
Department of Chemical Engineering
in conformity with the requirements for
the degree of Doctor of Philosophy

Queen's University
Kingston, Ontario, Canada
December 2009

Abstract

Solid oxide fuel cells (SOFCs) are electrochemical devices that can convert a variety of fuels directly into electricity. Their commercialization requires efficient operation of its components. The sluggish kinetics for the oxygen reduction reaction (ORR) at the SOFC cathode contributes to the loss in the fuel cell efficiency. In this work, the ORR was investigated for the strontium-doped lanthanum manganite cathode (LSM) and yttria-stabilized zirconia electrolyte (YSZ) system. A combined mathematical modelling and experimental framework was developed to estimate, for the first time, the kinetics of the elementary processes of the ORR for porous LSM cathodes. The kinetics of each process was then analyzed to identify the contribution to the cathode resistance.

The steady state and impedance response for polarized and unpolarized LSM cathodes was collected over a temperature range between $750°C$ and $850°C$ and two different oxygen partial pressure (pO_2) ranges: (i) between 10^{-4}atm and 10^{-3}atm, where LSM is considered to be stoichiometric with respect to oxygen and (ii) between 0.01atm and 0.21atm, where LSM is considered to be superstoichiometric with respect to oxygen.

A mathematical model was developed to analyze both the steady state and impedance data. Two pathways for the ORR were considered: one where oxygen is transported in the gas phase and one where oxygen is transported along the surface of the LSM cathode. Rate constants, transport coefficients and their respective activation energies were obtained for the adsorption/desorption, surface diffusion and charge transfer processes.

The experimental results indicated different polarization behavior between low and high pO_2. It is hypothesized that the concentration of cation vacancies on the LSM surface changes with both pO_2 and extent of polarization and that cation vacancies on the LSM surface can promote the ORR.

Modelling results at low pO_2 suggested that the adsorption reaction was slow and that thermodynamic limitations resulting in low equilibrium oxygen surface coverage can play an important role at both low and high polarizations. Modelling in high pO_2 was complicated by the nature of the LSM surface in these conditions and suggests an electrochemical reaction at the gas/LSM interface and the transport of charged adsorbed oxygen atoms.

Co-Authorship Statement

I hereby declare that I am the sole author of this thesis. My supervisor, Dr. Kunal Karan, provided valuable input and editorial feedback and is a co-author of three publications that have so far resulted from this work. In addition, this thesis makes use of a method developed in collaboration with committee member Dr. Jon Pharoah and is published in [1] but is not described in detail in this thesis.

[1] B. Kenney, M. Valdmanis, C. Baker, J.G. Pharoah and K. Karan. Computation of TPB length, surface area and pore size from numerical reconstruction of composite solid oxide fuel cell electrodes. Journal of Power Sources, 189 (2), 2009.

Acknowledgements

I wish to express my deep gratitude to my advisor, Dr. Kunal Karan. His encouragement, leadership, patience and support throughout this project helped to make it a success. This work could not have been accomplished without the additional support and leadership from Dr. Brant Peppley and Dr. Jon Pharoah who have helped to make the Queen's-RMC Fuel Cell Research Centre an enjoyable and productive place to work and do research.

I wish to thank the past and present students and researchers at the Queen's-RMC Fuel Cell Research Centre, especially those who have been involved with the SOFC group. In particular, I would like to thank Dr. Rajender Kondakindi for discussions and for his company throughout this project. I am further indebted to many colleagues at FCRC: Dr. Ruhul Amin and Dr. Misha Monder for numerous technical discussions and problem solving sessions as well as Jason Wood for his technical assistance. The best of these discussions occurred at the Grad Club, a location that will always have a place in my heart. I would also like to thank members of the SOFC group at the Institute for Chemical Process and Environmental Technology at the National Research Council for their interest in my work and their help with various technical aspects of my research.

Last but not least, I thank my future wife, Erin, who has given me constant encouragement and unconditional emotional support. I would also like to thank Erin's family as well as my friends from Queen's University. Finally, I wish to thank my parents, Jean and Julian and my brother Patrick who have proudly supported me throughout all of my education.

Studying at the Queen's-RMC Fuel Cell Research Centre was an amazing experience that has enormously shaped my perspective on life. These years have provided me with a direction and will forever influence my future decisions.

Table of Contents

List of Tables

List of Figures

Chapter 1

Introduction and Background

1.1 Motivation

The quality of life in our society is linked to the consumption of energy. As measured by the United Nations human development index, those countries that have the highest per capita energy consumption also have the highest quality of life (see Figure 1.1). High energy consumption has caused environmental challenges and is exhausting much of the world's natural resources. According to the U.S. Energy Information Agency, the world's energy consumption is expected to increase by an average of 2% per year between 2003 and 2030 [1], a doubling period of 35 years. Over the same time frame, coal consumption is expected to increase by 2.5% per year, faster than all other fuel types while it has also been predicted [2,3] that oil production, currently the world's largest source of primary energy, will plateau before 2040.

It is now necessary to break the link between civilization's quality of life and energy consumption. In the interest of extending the life our natural resources and our environment, it is important to find acceptable ways of slowing growth in energy consumption. Energy efficiency is one important route that must be taken and solid oxide fuel cells are a technology that could help to make energy consumption more sustainable.

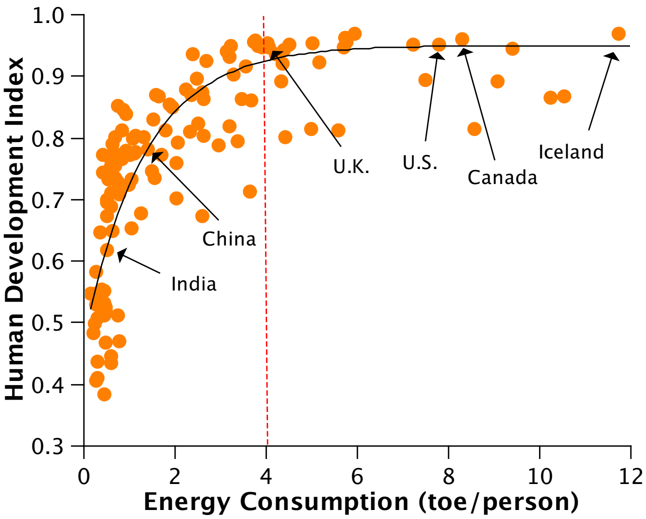

Figure 1.1: The influence of energy consumption (toe=tonne of oil equivalent) on the human development index, a measure of quality of life. Data adapted from United Nations Development Programme and the BP Statistical Review (2005).

1.2 Solid Oxide Fuel Cells

Solid oxide fuel cells (SOFCs) are solid state electrochemical devices that convert chemical energy into electricity and heat by oxidizing a fuel such as hydrogen or methane and concurrently reducing oxygen from a supply of air. Of the various types of fuel cells, solid oxide fuel cells operate at the highest temperature but they also have the highest tolerance for hydrocarbon fuels. The fuel flexibility of SOFCs make them attractive since they can theoretically bypass the step of externally converting the primary fuel into hydrogen. Also, under typical operating conditions, SOFCs have high electrical efficiencies (defined as electrical energy produced divided by the higher heating value of the fuel). For instance, SOFC units assembled by Fuel Cell Technologies (Kingston) achieved electrical efficiencies of 40% running on natural gas (AC out/LHV in) and Topsoe/Riso expect their 20kW natural gas fuelled SOFC to reach electrical efficiencies of 50-56% (AC out/LHV in) [4]. In addition to these high electrical efficiencies, valuable heat can be recovered from the SOFC system. Despite these advantages, the cost of the SOFC system remains high and the lifetime performance of the SOFC relatively low due to the challenges of operating at such high temperatures.

To address the issue of high cost, the U.S. Department of Energy has set a cost target of \$400/kW for an SOFC system by 2010 which will primarily be accomplished by lowering the system temperature. Achieving efficient, low temperature SOFC operation in the 500-700°C range is generally the focus of research groups around the world. It is thought that this will allow the system cost to be reduced since a wider selection of balance of plant materials can be used and the lifetime of the system can be increased by reducing degradation in the electrodes as well as the seals. Efficient low temperature operation is challenging though because the electrical processes such as the electrochemical reactions are thermally activated and any decrease in temperature results in a decrease in kinetics and ultimately in efficiency. Implicit in the goal for reduced temperature operation are improvements in the cell performance which are required to maintain acceptable efficiencies.

1.2.1 SOFC Operation

The functional components of SOFCs are made out of electrically conductive ceramic and metal materials whose electrical properties only become desirable at high temperatures. Figure 1.2 shows the main components of a solid oxide fuel cell and Table 1.1 shows the basic electrochemical reactions occurring at the electrodes.

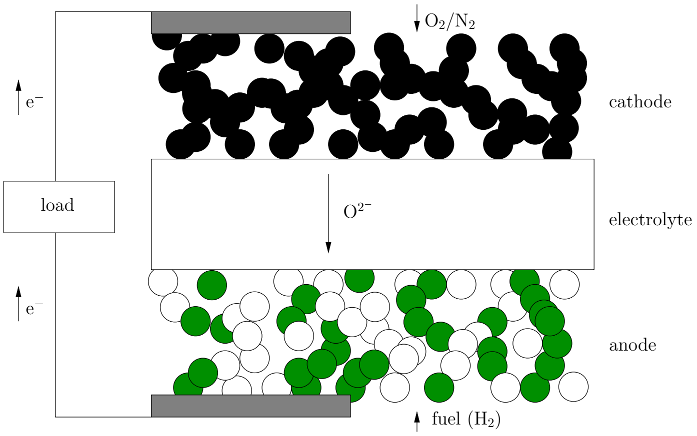

Figure 1.2: Main components of the solid oxide fuel cell

An SOFC unit cell is made of three key components: 1) a porous ceramic cathode, which reduces oxygen into oxygen ions, 2) a dense ceramic electrolyte, which conducts oxygen ions away from the

Table 1.1: Reactions occurring at the SOFC electrodes for H_2 and CH_4 fuel

Cathode:	$O_2 + 4e^- \rightleftharpoons 2O^{2^-}$
Anode:	$2H_2 + 2O^{2^-} \rightleftharpoons 2H_2O + 4e^-$
	$\frac{1}{2}CH_4 + 2O^{2^-} \rightleftharpoons H_2O + \frac{1}{2}CO_2 + 4e^-$
Overall:	$2H_2 + O_2 \rightleftharpoons 2H_2O$
	$\frac{1}{2}CH_4 + O_2 \rightleftharpoons H_2O + \frac{1}{2}CO_2$

cathode towards the anode and which is impermeable to gas, and 3) a porous ceramic-metal anode, which oxidizes a fuel such as hydrogen or methane. The cathode and the anode are electronically conducting and, depending on the material, can also conduct oxygen ions (in the form of oxygen vacancies) to some degree while the electrolyte can be considered a pure ionic conductor. The electrode reactions are heterogeneous and all species involved in the electrode reaction: (i) electrons (ii) ions and (iii) chemical species, must be transported to/from the reaction site. For common SOFC electrode materials, the reaction site is known as the triple phase boundary (TPB), that is, the location where the three phases co-exist: an electronically conducting phase, an ionically conducting phase and a gas transport pore phase.

1.2.2 SOFC Materials

Most solid oxide fuel cells are developed based on the yttria stabilized zirconia, $(\mathrm{Y_2O_3})_{0.08}(\mathrm{ZrO_2})_{0.92}$, electrolyte (YSZ) [5]. The state-of-the-art cathode material is $\mathrm{La_{1-x}Sr_xMnO_{3\pm\delta}}$ (LSM) and the anode is a ceramic-metal composite (mixture) of Ni and YSZ. Table 1.2 lists the electronic conductivities and thermal expansion coefficients of these materials. In addition to the electrical and thermal expansion requirements, the electrode material must be compatible with the electrolyte material in terms of chemical stability so as to not form insulating by-products at the electrode/electrolyte interface [6].

Since fuel cells must transport electrons and ions, the electrical conductivities of fuel cell materials are important so that they do not have prohibitively high electrical resistances. The oxygen ion conductivity of YSZ arises from the addition of Yttria to the Zirconium Oxide lattice which gives rise to oxygen vacancies. The ionic conductivity of YSZ depends on the Yttria content and has a maximum of around 9 mol % yttria. LSM is a semiconductor with its electrical conductivity and

Table 1.2: Properties of commonly used SOFC materials [7]

Material	Component	Electrical conductivity 1000°C (S/cm)	Thermal expansion coefficient ($\times 10^{-6}$ K^{-1})
8 mol% YSZ	Electrolyte	0.17	10.2
$La_{0.8}Sr_{0.2}MnO_3$	Cathode	100-200	12.4
40vol% Ni-60vol% YSZ	Anode	500-1000	12.7

thermal expansion coefficient influenced by the Sr content [8] and the conductivity and thermal expansion coefficient of the anode depend a large degree on the volume fraction of YSZ. While finding materials that have high electrical conductivities is important to the fuel cell performance, it is much more difficult to find materials that also have high electro-catalytic properties and which are stable over the operating conditions of typical solid oxide fuel cells.

In general, further research and development must be done to improve the efficiency of solid oxide fuel cells at low temperatures in order to make them cost effective. Most SOFC research is focused on the electrodes, for instance, by improving the tolerance of SOFC anodes towards sulfur poisoning or by searching for new cathode materials that have better oxygen reduction kinetics. Development of SOFC electrodes can take two general directions: 1) improving the electrode design such as tailoring the compositions and particle sizes for improved electro-catalytic performance and long term stability or 2) searching for new materials at the atomic level that have intrinsically better electro-catalytic performance.

For solid oxide fuel cells fuelled with hydrogen, it is thought that the cathode contributes to the majority of the efficiency losses [8] and so this dissertation is focused on the reactions occurring within the SOFC cathode.

1.3 SOFC Cathodes

Although noble-metals such as Pt have good activity towards oxygen reduction [9], the cost associated with fabricating electrodes made of such materials can be prohibitive. As an alternative, ceramic perovskite-type oxide materials with a structure containing three different ions of the form

ABO_3, shown in Figure 1.3a [10] are commonly used as SOFC cathode materials. For SOFC cathodes, the A site is typically a large ion such as La^{3+} and/or Sr^{2+} and the B site, located at the centre of the lattice, is typically a small transition metal ion such as Mn^{2+}, Mn^{3+} or Mn^{4+}. It has been determined that for the cathode structure $La_{1-x}Sr_xMO_{3\pm\delta}$, the catalytic activity varies with the B-site dopant and has been found to decrease in the order of M=Co, Mn, Fe, Cr [11]. The high electrochemical activity of Co containing cathodes is thought to be caused by its mixed electronic-ionic conducting behavior due to large equilibrium oxygen vacancy concentrations in the material compared to that of Mn based cathodes which exhibit primarily electronic conducting behavior. Another important feature of perovskite materials is their oxygen nonstoichiometry which is a function of the oxygen gas environment. As Figure 1.3b shows [12], the $La_{1-x}Sr_xMnO_{3\pm\delta}$ perovskite can have an oxygen excess at high oxygen partial pressures, an oxygen deficiency at low oxygen partial pressures or it can be stoichiometric at intermediate oxygen partial pressures.

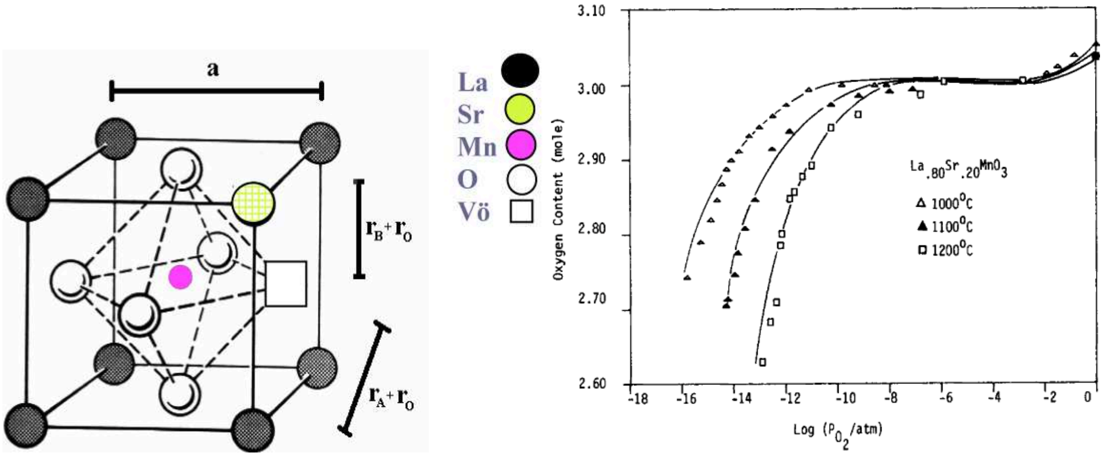

(a) (b)

Figure 1.3: (a) Example of a perovskite structure showing the A and B sites as well as oxygen species [10] (b) Example of the oxygen nonstoichiometry for the LSM perovskite [12]. Oxygen contents above or below 3 mole represent oxygen excess and oxygen deficient LSM.

1.3.1 Oxygen Reduction Pathways

The electrochemical activity of a cathode (typically quantified by the electrode polarization resistance, R_p) depends on the relative ease at which oxygen can be transported through the electrode and electrochemically incorporated into the YSZ electrolyte. In Kröger-Vink notation, the overall oxygen reduction reaction is:

$$O_2(g) + 2V_{\ddot{O}} + 4e^- \rightleftharpoons 2O_O^x \tag{1.1}$$

where $V_{\ddot{O}}$ is an oxygen vacancy in the electrolyte with 2 positive charges and O_O^x is an oxygen in the electrolyte with a neutral charge. The field of SOFC cathode kinetics is dominated by studies focused on the determination of the mechanism and rate determining step(s) of the oxygen reduction reaction. Adler [8] has provided a comprehensive review of the factors governing oxygen reduction in SOFC cathodes. In general, it is thought that there are two main competing pathways for oxygen transport through a perovskite electrode: 1) the surface pathway where oxygen is transported along the perovskite surface of the gas-solid interface 2) the bulk pathway where oxygen is transported through the bulk perovskite. In addition, the location of the charge transfer step may vary from the perovskite/electrolyte interface to the gas/perovskite interface [13, 14]. Figure 1.4 summarizes the basic processes for a surface pathway, the bulk pathway and a pathway involving the transport of charged adsorbates. In general, the processes that occur for each of these pathways are:

- The surface pathway shown in Figure 1.4 (left) can include (i) oxygen gas transport, (ii) molecular or dissociative oxygen adsorption onto the perovskite surface, followed by (iii) diffusion of the adsorbate along the surface towards the triple phase boundary and (iv) a subsequent charge transfer reaction incorporating the adsorbate into the electrolyte phase. This pathway is commonly assumed for electrodes with low bulk phase oxygen diffusion coefficients such as metals.

- The bulk pathway shown in Figure 1.4 (centre) is typical of a mixed electronic ionic conducting (MEIC) material and can include (i) oxygen gas transport, (ii) molecular or dissociative oxygen adsorption followed by (iii) a surface exchange reaction between surface oxygen species and oxygen vacancies in the perovskite (iv) diffusion of the incorporated oxygen towards the electrolyte phase (v) an oxygen exchange reaction between oxygen species in the perovskite phase and the oxygen vacancies in the electrolyte phase. This pathway is commonly assumed for perovskites that have high oxygen vacancy diffusion coefficients such as Cobalt containing perovskites.

- The charged adsorbate pathway indicates that the electrochemical reaction may occur at the gas/perovskite interface instead of or as well as at the perovskite/electrolyte interface. The electrochemical reaction at the gas/perovskite interface may involve adsorbate reactants such as $O_{ads} + e^- \rightleftharpoons O^-_{ads}$ on the perovskite surface or it could involve oxygen gas species directly in the form of an electrochemical adsorption reaction. There is some evidence of charged oxygen species on pervoskite materials based on temperature programmed techniques [15, 16] for the oxidation of methane.

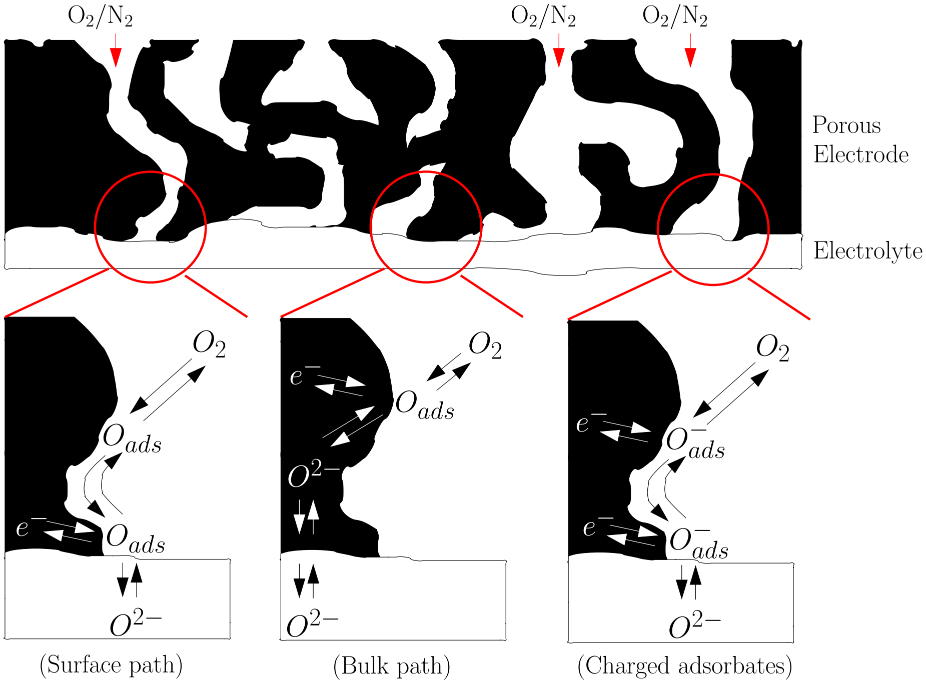

Figure 1.4: Various oxygen reduction pathways of perovskite cathodes: **Left)** The surface pathway for neutral adsorbates involving gas transport, adsorption, surface diffusion and charge transfer processes **Centre)** The bulk pathway involving gas transport, adsorption followed by surface exchange of adsorbed oxygen and oxygen in the perovskite lattice, bulk diffusion and charge transfer **Right)** The surface pathway for charged adsorbates involving gas transport, adsorption/charge transfer at the gas/perovskite interface followed by surface diffusion and charge transfer at the perovskite/YSZ interface.

The surface pathway for oxygen reduction is commonly proposed for the Pt/YSZ system [17–24] and has been carried over to a number of perovskite based cathode studies, especially for the LSM cathode. Some variations of these mechanisms exist, such as where and how many times the charge transfer reaction occurs [25, 26] and the exact form of the adsorption reaction such as Langmuir or Freundlich type adsorption [27]. In addition to the pathways presented above, recently it has been postulated that oxygen vacancy transport along the surface of the perovskite may be more favorable than oxygen vacancy transport through the bulk of the perovskite [28].

In principle, each of the pathways shown in Figure 1.4 can exist simultaneously in parallel. The dominant pathway will be the one with the fastest oxygen transport kinetics. For example, although all perovskite materials have a finite oxygen vacancy diffusion coefficient, $D_{V_{\ddot{O}}}$, implying that they can transport oxygen through the bulk, the $D_{V_{\ddot{O}}}$ for some materials is so low that it is typically thought that the bulk pathway is effectively blocked. These materials are distinguished here as predominantly electron conducting cathodes and those materials that have high $D_{V_{\ddot{O}}}$ are mixed conducting cathodes.

1.3.2 Cathode Materials

In general, the important perovskite cathode materials are either Manganites such as $LaMnO_{3\pm\delta}$ or Cobaltites such as $LaCoO_{3\pm\delta}$. Usually these materials are doped with Sr making $La_{1-x}Sr_xMnO_{3\pm\delta}$ (LSM) or $La_{1-x}Sr_xCoO_{3\pm\delta}$ (LSC). The electrical conductivity of LSM ranges from 175-300 S/cm at 950°C and is enhanced by doping with Sr^{2+} [7]. Although LSM based cathodes have a high electronic conductivity, a major limitation is their low oxygen ion conductivity [29–31]. For example, LSM has an oxygen self-diffusion coefficient (which is directly proportional to the material's ionic conductivity) in the range of 3.2×10^{-16} to 9.4×10^{-14} cm^2/s over the $700°C$-$900°C$ temperature range [31] compared to 1×10^{-8} to 4×10^{-8} cm^2/s for $La_{0.8}Sr_{0.2}CoO_{3\pm\delta}$ [32]. The relatively high oxygen vacancy diffusion coefficient of LSC-based cathodes results in much better oxygen reduction kinetics compared to LSM at low temperatures. It is also notable that unlike LSC which is usually oxygen deficient (quantified by $\delta < 0$ in $O_{3\pm\delta}$), creating oxygen vacancies, LSM has an oxygen excess (ie. $\delta > 0$) for $pO_2 > 0.001$ atm [33]. If $\delta > 0$, then the excess oxygen is balanced by cation vacancies and oxygen vacancies do not exist. For $10^{-8}atm \leq pO_2 \leq 10^{-3}atm$, LSM is stoichiometric (ie. $\delta = 0$) [12] and does not fall much below $\delta = 0$ until $pO_2 < 10^{-12}$ [34]. The oxygen vacancy concentration of LSM has also been shown to increase with Sr content [33].

Despite the fast kinetics of Cobaltites towards oxygen reduction, LSM based cathodes are currently considered to be "state-of-the-art", primarily due to practical aspects such as stability and compatibility with the YSZ electrolyte. For example, depending on the Sr concentration, LSM has a thermal expansion coefficient between 12.0 and 12.8ppm/°C (from low to high Sr content), comparable to the thermal expansion coefficient of the YSZ electrolyte (10.5ppm/°C) however, the thermal expansion coefficient of Co rich cathodes tends to be twice as high. In addition, LSC is highly reactive with YSZ electrolytes [6] forming insulating by-products at the LSC/YSZ interface which reduces electrochemical activity. LSM in contact with YSZ for prolonged periods of time above $1200°C$ also forms insulating by-products; $La_2Zr_2O_7$ can form at the interface or if Sr doping levels are greater than 30 mol %, $SrZrO_3$ [35] can form, however, these can be avoided by keeping the sintering temperature of the LSM cathode lower than 1200°C, by using A-site to B-site ratios in the perovskite lattice less than 1 or by using an alternative electrolyte, such as GDC (Gd doped $\mathrm{CeO_2}$) [6]. Moreover, Cobaltites are less stable than Manganites in low oxygen concentration environments; at 1000°C, $LaCoO_3$ decomposes at an oxygen partial pressure of 10^{-2}Pa [36]. These features make Cobalt rich materials unattractive for long term SOFC operation, although they do present interesting opportunities for further development. As an alternative to Cobalt rich perovskites, $La_{1-x}Sr_xCo_yFe_{1-y}O_{3-\delta}$ (LSCF) cathodes have lower oxygen ion conductivities but better mechanical stability compared to LSC. Recently there has been some interest in $Ba_{0.5}Sr_{0.5}Co_{0.8}Fe_{0.2}O_{3-\delta}$ (BSCF) cathodes which have very high activity towards oxygen reduction, attributed to its high oxygen ion conductivity [37]. Long term operation and stability has not yet been assessed for the BSCF cathode though.

To benchmark the performance of various cathode materials, their area specific resistances (ASR) can be compared. Steele [38] has suggested that the area specific resistance of an SOFC cathode should be no larger than 0.2 $\Omega\mathrm{cm}^2$ for efficient fuel cell operation. At 500°C, the best performing *single phase* cathode material known today, $\mathrm{Ba_{0.5}Sr_{0.5}Co_{0.8}Fe_{0.2}O_{3-\delta}}$, has a reported ASR of 0.51-0.60 $\Omega\mathrm{cm}^2$ [37] compared to a reported 77 $\Omega\mathrm{cm}^2$ for $\mathrm{La_{0.6}Sr_{0.4}Co_{0.2}Fe_{0.8}O_{3-\delta}}$ [39] and composite LSCF/GDC cathodes with ASR values of roughly 5 $\Omega\mathrm{cm}^2$ have been demonstrated [40] at 500°C. Although Steele has predicted that a cathode ASR of 0.20 $\Omega\mathrm{cm}^2$ at 500°C is technically feasible if the cathode has a high oxygen ion conductivity [41], LSM has virtually no ionic conductivity (at low overpotentials) and so a composite of LSM and YSZ can be used to enhance oxygen transport through the cathode.

Despite having lower activity towards oxygen reduction than Co containing electrodes, LSM is the most pursued cathode material [8] due to the trade-offs required between high electrochemical activity and high stability/chemical compatibility with YSZ electrolytes. This dissertation is concerned with the study of the kinetics of the oxygen reduction reaction of LSM cathodes with a goal of quantifying the contribution of various processes to the total electrode resistance.

1.4 Oxygen Reduction in LSM Cathodes

Despite the fact that the LSM cathode has been studied extensively, discrepancies in the cathode kinetics regarding the mechanism and rate determining step(s) still exist. Minh [5] has provided a review of general SOFC cathode kinetics work prior to 1995, while Adler's review [8] is more recent. Both of these reviews indicate that confusion exists as to which mechanism and processes dominate the LSM resistance. Compared to perovskite materials such as LSC, it is thought that under certain conditions, the low oxygen vacancy diffusivity of LSM ($D_{V_{\ddot{O}}}$) and excess of oxygen within the lattice effectively blocks the bulk pathway for oxygen reduction. However, it has also been proposed [42–44] that at high current loads, oxygen vacancies within the LSM lattice could be generated, opening the bulk oxygen transport pathway for oxygen reduction in LSM based cathodes. Studies on dense LSM microelectrodes [45, 46] have confirmed the possibility of the bulk pathway in LSM based materials despite a low $D_{V_{\ddot{O}}}$.

The study of oxygen reduction in solid state electrodes is a large field and although there can be considerable overlap, only oxygen reduction related to the LSM/YSZ system will be discussed here. In the discussion that follows, studies on the LSM/YSZ system are grouped into two main categories: (i) experimental studies investigating features of the oxygen reduction reaction in LSM based electrodes from a comparative or mechanistic point of view and (ii) modelling studies of the oxygen reduction reaction and the microstructure/performance relationship of LSM electrodes.

1.4.1 Experimental Studies

Qualitative aspects

A common technique used to compare the performance of LSM/YSZ systems is to report the polarization resistance (R_p), or area specific resistance. It has been established that the addition of the electrolyte material, YSZ, to the cathode, forming a composite cathode, can greatly enhance the electrode performance compared to a porous LSM electrode [29,30,47]. When discussing LSM electrodes, it is important to distinguish between studies on pure LSM cathodes and studies on LSM/YSZ composite cathodes. Although these both represent the same LSM/YSZ system, there can be considerable differences in the behavior of these two electrode types. To date, one of the lowest R_p values for the LSM/YSZ system using a composite cathode was reported by Song *et al.* [48] to be $0.46\Omega cm^2$ at $600°C$. This low resistance was thought to be the result of an optimized microstructure as well as fabrication process. In composite cathodes, structural factors play an especially important role since the presence of two solid phases poses the additional constraint of percolation between each phase [49]. In addition to the particle size and porosity, factors such as the electrode thickness [29,50,51] and the volume fraction of LSM and YSZ [52] are known to have an impact on the polarization resistance. A number of studies [53–55] have focused on more efficient techniques to optimize the cathode design through novel synthesis routes of LSM and YSZ ceramics to achieve more homogeneous mixing (compared to mechanical mixing of LSM and YSZ powders) and more intimate contact between the two phases. In addition to better initial performance, these novel synthesis techniques are reported to have better long term performance compared to fabrication techniques involving mechanical mixing [54]. Although the ultimate goal is to design a cathode with a low resistance, to pinpoint the mechanisms and processes responsible for the cathode resistance, it is often easier and more accurate to study electrodes that have a high resistance where certain processes can be isolated from the others.

One technique that can be used to provide some insight into the kinetics of oxygen reduction in LSM cathodes is to use electrochemical impedance spectroscopy (EIS). This technique is described in more detail in Section 2.4.2 of this dissertation. The shape of the impedance response can indicate the number and type of processes involved in the ORR. Jørgensen and Mogensen [56] have reported that in general, the impedance response of LSM/YSZ composite electrodes includes a high frequency induction tail ascribed to the measurement leads, an ohmic resistance (the high frequency intercept adjusted for induction) mainly originating from the electrolyte, and usually two to four processes which contribute to the electrode impedance spectrum. Although rare, an induction at low frequencies has also been reported [42, 51, 56, 57] and can occur after polarization of the electrode. The impedance of pure LSM includes the same features but may possess only a single arc contributing to the electrode impedance spectrum. Another important feature of the impedance of LSM based electrodes is that they show depressed arcs which is consistent with distributed charging of the double layer, requiring constant phase elements as opposed to pure capacitors to describe the shape. As reported in [56], even for nominally identical electrodes fabricated in parallel, the shape of the impedance can vary significantly due to different chemical and electrochemical prehistory. The number of arcs and magnitude of the impedance also depends on the temperature, oxygen partial pressure and current treatment. For pure LSM electrodes, Chen *et al.* [27] found three arcs in the impedance response in low oxygen partial pressures and two arcs in high oxygen partial pressures while Murray *et al.* [50] found Warburg type arcs at temperatures below $800°C$ and Siebert *et al.* [42] found a single arc at OCV. In addition, after polarizing the LSM electrode and measuring the impedance response at OCV, a reduction in the low frequency arc is often found [26, 58].

It is also possible to measure steady state polarization curves (or current-voltage curves) for LSM electrodes using a 3-electrode cell. Various polarization curves for LSM based cathodes are reported in [26,51,57,59–63]. One interesting aspect is that limiting currents are rarely reported in studies of LSM electrodes (except in [64]) and the impedance behavior under limiting current DC-bias has not been measured. This could be a result of a number of factors such as the magnitudes of the currents being drawn from the cell and the oxygen partial pressure but also the lack of limiting currents may be an indication of the mechanism involved in oxygen reduction [26].

Apart from microstructural differences, one factor that complicates comparative studies is the fact that the LSM powder can be made in a variety of different A-site deficiencies and mole fractions of La and Sr. In addition, various synthesis routes of LSM powder can result in different particle morphologies [55]. Although ultimately the desire is to reduce the polarization resistance of the electrode, the process of improving the electrode performance is trial-and-error unless a more mechanistic approach is undertaken. Aspects such as the polarization resistance or the shape of the impedance and polarization curves can provide a good baseline for a qualitative comparison but they must be combined with other tools to provide a more mechanistic approach.

Mechanistic aspects

Rate limiting step(s) To assess the reaction kinetics of LSM cathodes, a common approach has been to report the reaction order with respect to oxygen and the activation energy of the oxygen reduction reaction by measuring the electrode resistance using electrochemical impedance spectroscopy or steady state polarization curves in various oxygen concentrations and temperatures. The reaction order, γ, typically follows the relationship $R \propto pO_2^{-\gamma}$ (where R is the electrode resistance), and is often assumed to relate to a single rate determining step of the reaction mechanism. The activation energy, E_a, comes from the Arrhenius like dependency of the electrode resistance with temperature. A wide range of reaction orders and activation energies have been reported for the LSM/YSZ system, some of which are summarized in Table 1.3 and Table 1.4. In terms of the reaction order, $\gamma \approx 0.5$ has been reported in references [42, 64, 65], while $\gamma > 0.5$ has been reported in references [60, 65, 66] and $\gamma < 0.5$ reported in [27, 50, 52, 57, 61, 65]. From these studies, the rate determining step of the ORR for the LSM/YSZ system has been proposed to be dissociative adsorption [42, 50, 64] with E_a ranging from 1.8eV to 2.11eV, electrochemical adsorption [60], a mixture of adsorption/surface diffusion [27, 50, 65] with E_a ranging from 1.49eV to 2.0eV, a mixture of surface diffusion and charge transfer [26] and a mixture of gas diffusion, surface diffusion and ion incorporation into YSZ [27] with $E_a = 1.62eV$. In another study, La O' *et al.* [46] used dense LSM microelectrodes with various TPB lengths to study the contribution of the bulk and surface pathways for oxygen reduction. In this study, it was found that below $600°C$, the TPB provided the majority of the current but at higher temperatures, the bulk pathway dominated. Microelectrode studies are typically performed on electrodes with thicknesses less than $0.25\mu m$ though and at this length scale, the bulk pathway is favored. The study by La O' *et al.* also found that the rate determining process was the electrochemical reaction (or oxygen ion incorporation into YSZ electrolyte) below $700°C$ but this shifts to a surface chemical process on LSM above $700°C$.

In terms of the reaction order in composite LSM/YSZ cathodes, the interpretation can be more complex since it relies heavily on the cathode microstructure [67]. For composite LSM/YSZ cathodes, Co *et al.* [68] found $\gamma = 0.5$ and $E_a = 1.24eV$ for a temperature range of $600°C$ to $900°C$ but based on the charge-transfer coefficients, found that the electrode microstructure effects made it difficult to interpret the rate determining step. In another study, Murray *et al.* [50] found $\gamma = 0.29$ and $E_a = 1.49eV$ for the process corresponding to a medium frequency arc of the impedance spectra and assigned this to an oxygen dissociation and adsorption process whereas Kim *et al.* [52] found $\gamma = 0.25$ for a high frequency process and $\gamma = 1.0$ for a low frequency process which were ascribed to surface diffusion and gas phase diffusion limitations respectively.

Table 1.3: Summary of reaction orders found experimentally for the LSM/YSZ system

Group	Frequency‡	γ^*	Temp ($°C$) pO_2 range	Comment	Ref
Siebert *et al.*	all	0.5	960 $30ppm - 1.0atm$	Pin type LSM	[42]
Takeda *et al.*	all	0.6-0.7	800 $0.01atm - 0.5atm$	Porous LSM	[66]
Co *et al.*	all	0.5	700-900 $0.03atm - 1.0atm$	LSM/YSZ composite	[60]
Co *et al.*	all	1.0	700-900 $0.03atm - 1.0atm$	Dense LSM	[60]
Murray *et al.*	all low ($T > 800°C$)	0.14 0.8	650-850 $0.001atm - 1.0atm$	Porous LSM	[50]
Murray *et al.*	med low ($T > 800°C$)	0.29 0.57	650-850 $0.001atm - 1.0atm$	LSM/YSZ composite	[50]
Østergård *et al.*	high and low	0.3	1000 $0.002atm - 1.0atm$	Porous LSM	[57]
van Herle *et al.*	all	0.53	700-900 $100ppm - 1.0atm$	Porous LSM	[64]
Chen *et al.*	med low	0.25 1.0	750-900 $0.001atm - 1.0atm$	Porous LSM	[27]
Kim *et al.*	high low	0.25 1.0	800-950 $0.005atm - 1.0atm$	Porous LSM	[52]
Kim *et al.*	high low	0.25 1.0	800-950 $0.005atm - 1.0atm$	LSM/YSZ composite	[52]
Jiang *et al.*	high low	0.06-0.14 0.45-0.76	850-1000 $0.01atm - 0.21atm$	Porous LSM	[65]
Jiang *et al.*	all	0.08-0.25	500-950 $0.01atm - 1.0atm$	Porous LSM	[61]

‡ Indicates either a high, medium or low frequency EIS arc, or all arcs combined

* γ in $R \propto pO_2^{-\gamma}$

Table 1.4: Summary of activation energies found experimentally for LSM/YSZ system

Group	Frequency[‡]	E_a^* (eV)	pO_2	Comment	Ref
Siebert *et al.*	all	1.8	0.21atm	Pin type LSM	[42]
Takeda *et al.*	all	1.14-1.86	0.21atm	Porous LSM	[66]
Co *et al.*	all	1.24	0.21atm	LSM/YSZ composite	[68]
Murray *et al.*	all	1.61	0.21atm	Porous LSM	[50]
Murray *et al.*	med	1.49	0.21atm	LSM/YSZ composite	[50]
van Herle *et al.*	all	2.11	0.21atm	Porous LSM	[64]
Chen *et al.*	med	1.62	0.001atm	Porous LSM	[27]
Juhl *et al.*	all	2.0	0.21atm	LSM/YSZ composite	[51]
Jiang *et al.*	low	2.0	0.01-0.21atm	Porous LSM	[65]
Jiang *et al.*	all	1.24-1.65	0.21atm	Porous LSM	[61]

[‡] Indicates either a high, med or low frequency EIS arc, or all arcs combined

In general, most studies attribute a rate determining process based on the oxygen reaction order because it is relatively easy to theoretically derive the pO_2 dependency of specific rate limiting processes, as in [26, 27, 52]. Activation energies for specific processes such as adsorption and surface diffusion are more difficult to obtain because it is not easy to study these processes individually, however, recent quantum mechanics simulations have estimated activation energies for the adsorption reaction [28,69] but these are for single crystal structures and require assumptions such as the relative position and concentration of surface vacancies.

Activation of LSM with polarization In addition to studies focused on identifying the rate determining step(s) of the oxygen reduction reaction, a growing interest is to identify the mechanism responsible for the enhancement in electrode performance under polarization. It is often observed that the resistance of LSM decreases after polarizing the electrode with a cathodic current [26, 44, 70–73]. In the case of [26, 44, 71], it was observed that the low frequency arc of the impedance response recorded at OCV immediately after polarizing the electrode decreased substantially. Jiang *et al.* [70] hypothesized that high initial resistances were caused by a passive layer on the surface of LSM grains which were enriched with La and Sr. A later study [71] concluded that the activation effect after cathodic polarization was most likely due to the incorporation into the LSM lattice of passive surface species such as SrO. The process was found to be reversible over long periods of time which was attributed to the slow diffusion of cation vacancies towards the surface of the LSM grain. Another study by La O' *et al.* [44] used Auger electron spectroscopy and X-ray photoelectron spectroscopy on dense LSM microelectrodes and determined that cathodic polarization leads to significant reduction of surface La fraction and an increase in the surface Sr and Mn fractions. La O' *et al.* also found long relaxation times of over 10hrs which gave a linear relationship when plotted against $t^{1/2}$ indicating a diffusion process which they attributed to cation diffusion upon polarization and subsequent relaxation. In this case it was hypothesized that the enhancement was caused by the formation of oxygen vacancies on the surface of the LSM grains resulting in a bulk diffusion mechanism contributing towards the ORR. In these cases, polarization was also thought to influence primarily the surface exchange or adsorption kinetics. In another recent study, Backhaus-Ricoult *et al.* [72] used in-situ photoelectron microscopy on well defined LSM strip electrodes at $650°C$ and found that during cathodic treatment, Mn on the LSM surface changed oxidation state from $Mn^{3+,4+}$ to Mn^{2+} at high cathodic polarization and that Mn^{2+} spread from the TPB over the electrolyte surface. It was hypothesized that this could result in the YSZ surface being electrically conductive with the possibility of opening an additional oxygen reduction pathway involving the YSZ surface, responsible for the enhanced performance.

Tables 1.3 and 1.4 and the above discussion indicates that numerous rate-limiting reactions and pathways have been identified on porous LSM electrodes and that a discrepancy exists in the rate-limiting reactions and their associated activation energies. Some explanations for the variation observed in the literature for kinetic studies of the LSM electrode have been offered by Adler [8] and others and include:

- Sensitivity to operating history - For the LSM cathode, it is known that the polarization history of the electrode has a large impact on its overall resistance [44, 71, 74] where the resistance has been observed to fall as much as 50 times after cathodic polarization. Although this indicates the need to carefully control the polarization and electrical history during kinetic measurements, it is not obvious that this has been considered in many of the studies presented above. In addition, McIntosh *et al.* [75] bring up the concern that symmetrical cell studies, which are often used for mechanistic analysis, cannot be polarized and so they cannot account for sensitivities in the operating history.

- Sensitivity to processing - It is known that the microstructure can have a significant impact on the electrode resistance [8,47,51] indicating the need to develop reproducible techniques for manufacturing electrodes. As well, the formation of insulating by-products such as $La_2Zr_2O_7$ has been shown to influence the electrode kinetics [76] which is especially important for cathodes sintered above $1200°C$. Often critical details of the electrode microstructure, such as the porosity, triple phase boundary length, particle size and electrode thickness are omitted from mechanistic studies. One method that is increasingly used to ensure microstructural control is to use dense microelectrodes. These microelectrodes typically have thicknesses ranging from 0.1 to $0.25\mu m$, compared to a typical thickness of $\sim 20\mu m$ for a porous electrode, and as a consequence, can open up additional pathways for oxygen reduction that may not be present in porous electrodes [77].

- Experimental artifacts in electrochemical measurements - The use of a 3-electrode cell geometry to separate the contribution of the working electrode (or electrode of interest) from the counter electrode can introduce significant errors. There are many variations to the 3-electrode cell geometry reported in the literature. It has been shown [78–84] that certain 3-electrode cell configurations, such as the popular "planar" 3-electrode cell can generate experimental artifacts such as additional arcs that can be mistaken for electrode processes.

These items all highlight the need to develop careful experimental protocols to ensure that reliable and reproducible data can be obtained from porous LSM electrodes. Additionally, a study by Svensson *et al.* [85] shows that reaction orders such as those presented in Table 1.3 may not necessarily represent a single rate determining step but instead, a mixture of processes. In such a case, the reaction order could deviate substantially from what is typically considered for single rate determining steps.

1.4.2 Modelling Studies

Kinetic modelling

Models capable of capturing the multiple physico-chemical processes have been developed in the past. These types of models are generally 1-dimension and typically require parameters involving various reaction rate constants and transport coefficients of the elementary processes. For example, the ALS model (Adler-Lane-Steele) [86] modelled the impedance of mixed conducting electrodes, but it broke down for electrodes with low oxygen vacancy diffusion coefficients, such as LSM. van Hassel *et al.* [87,88] developed a steady state and impedance model to describe oxygen reduction at a dense Au/YSZ interface while Mitterdorfer and Gauckler [23,24] developed a steady state and impedance model for the dense Pt/YSZ system. In the case of van Hassel *et al.*, although their model considered charged adsorbates, it did not consider the transport of surface species along the electrode and in the case of Mitterdorfer and Gauckler [23, 24], the surface diffusion length was presupposed. More recently, steady state and impedance models of the full SOFC have been presented by Zhu *et al.* [89] however, the focus was on predicting the anode response and a relatively simple cathode model was employed. In addition, detailed models to analyze the steady state anode behavior have emerged from Vogler *et al.* [90] and Goodwin *et al.* [91] which considered the dense Ni/YSZ system. Reaction rate constants for adsorption of various species and surface transport coefficients were estimated by fitting against experimental data. In all cases mentioned above except in [89], because each study was concerned with dense electrodes, the intricacies of porous transport were ignored as well as gas phase diffusion. While Svensson *et al.* [85, 92] developed a model for perovskite cathodes which accounted for transport through a porous cathode, they did not account for gas phase diffusion nor did they present a method to calculate the electrode impedance. In addition, the steady state model presented by Svensson *et al.* did not try to fit against experimental conditions and therefore, the parameter set was varied over a very large range. One beneficial feature of some of these kinetic models is that they do not need to assume a rate determining step since the rate constants and transport parameters inherently account for the kinetics of each process. In addition, these models enhance the analysis of experimental data since assumptions based on the distribution of species involved in the electrochemical reactions are not required.

Microstructure/performance predictive modelling

Although models used for kinetic analysis can be useful, their complexity typically relegates them to modelling single phase systems (e.g. non-composite electrodes) and it is often difficult to determine the missing parameters. An alternative is to treat the elementary reactions as a lumped system by assuming a rate determining process. This simplification reduces the number of model parameters and the complexity of the model but often allows for a conceptual understanding of how various microstructures and electrode designs can influence the electrode resistance. Costamagna *et al.* [93] were one of the first to model composite electrodes and predict the microstructure/design/performance relationship of these electrodes. One of the most important parameters was the triple phase boundary length which was estimated based on particle coordination theory [94] and was calculated as a function of volume fraction and particle sizes of the two ceramic phases and the electrode porosity. In later work, Sunde [95] modelled the composite anode while Chen *et al.* [96, 97] and Kenney and Karan [67, 98] modelled the composite cathode, all using particle coordination theory to calculate the triple phase boundary length and effective electronic and ionic conductivities. These models are typically steady state models, however, impedance models have also been developed by Gazzarri *et al.* [99] and Shi *et al.* [100]. One concern of all the models mentioned above is that they use volume average techniques which assume that the electrode microstructure is perfectly homogeneous. Schneider *et al.* [101] as well as Golbert *et al.* [102] reconstructed the approximate electrode geometry to avoid volume average modelling techniques altogether, therefore, eliminating the need for this assumption. Although these models can be helpful in understanding the complexity of the microstructure/performance relationship of SOFC electrodes, they treat the electrode kinetics as a lumped system and so cannot delineate the various electrode contributions.

Modelling of microstructural parameters

In addition to models describing the electrochemical behavior of SOFC electrodes, there are also a number of models that have been developed with the sole purpose of estimating the porous electrode microstructure. As mentioned above, particle coordination theory has been used to estimate critical microstructural parameters such as the triple phase boundary length of composite electrodes, however, this theory does not represent the true microstructure of porous electrodes. As an alternative, Martinez and Brouwer [103] as well as Ali *et al.* [104] have developed geometrical models which numerically construct the porous composite electrode geometry and are used to evaluate the active triple phase boundary length in composite electrodes while Kenney *et al.* [105] developed a model to calculate not just the triple phase boundary length but also other relevant parameters such as the internal surface area, contact area and pore size of the porous electrode microstructure. These models can be thought of as tools to help in the determination of microstructural parameters which are known to influence the cathode performance [51] and are input parameters to many of the electrochemical models discussed above. In addition, these numerical construction models can be validated against focused ion beam-SEM (FIB-SEM) electrode reconstruction [106].

1.5 Research Opportunities

It is evident that multiple processes can contribute to the oxygen reduction reaction of porous LSM electrodes. One of the difficulties in analyzing experimental data from common methods such as impedance spectroscopy and steady state polarization curves is that individual processes, such as adsorption or surface diffusion, cannot be studied exclusively and that each process in the oxygen reduction reaction is coupled to one-another. In addition, microstructural features are known to have a large impact on the resistance of the LSM cathode but are not always reported in experimental investigations since they can be difficult to measure. This highlights the need to develop methods that can be used to deconvolute overlapping processes in SOFC cathodes from both steady state and impedance data while accounting for the electrode microstructure.

For these reasons, it is useful to analyze the experimental data from a physical perspective, that is, incorporating the coupled physico-chemical processes directly into the analysis of the polarization and impedance response. In essence, this involves modelling the details of the individual chemical and transport processes occurring within the electrode. In this type of physical based electrochemical analysis, microstructure independent kinetic rate constants and transport coefficients for each process can be estimated and so the contributions of individual processes to the overall electrode resistance can be easily determined and compared. While a number of modelling and experimental studies have considered the LSM/YSZ system, a rigorous combination of experimental data and physico-chemical modelling of porous LSM electrodes to determine microstructural kinetic and transport parameters has not yet been completed and may help in the analysis of experimental data where a single rate determining step is not guaranteed to exist. The advantage that this technique holds over the other analysis techniques mentioned above is: 1) it is not required to make an assumption of a rate determining step which may or may not exist 2) the technique inherently accounts for parallel reaction pathways 3) thermodynamic consistency for each chemical reaction can be enforced 4) unlike typical analysis methods, the full range of experimental data can be used simultaneously, rather than simply high or low overpotentials.

1.5.1 Thesis Scope

This dissertation aims to develop a framework for characterizing the transport, chemical and electrochemical processes of porous LSM electrodes by combining a rigorous experimental analysis with a physical based kinetic/transport model. A graphical representation of this approach is shown in Figure 1.5. The ultimate goal of this work is to estimate microstructure independent kinetic rate constants and transport coefficients associated with the various processes of the oxygen reduction reaction. This will be done by fitting these unknown parameters to experimental data.

The framework developed here requires two different research streams: 1) a modelling stream

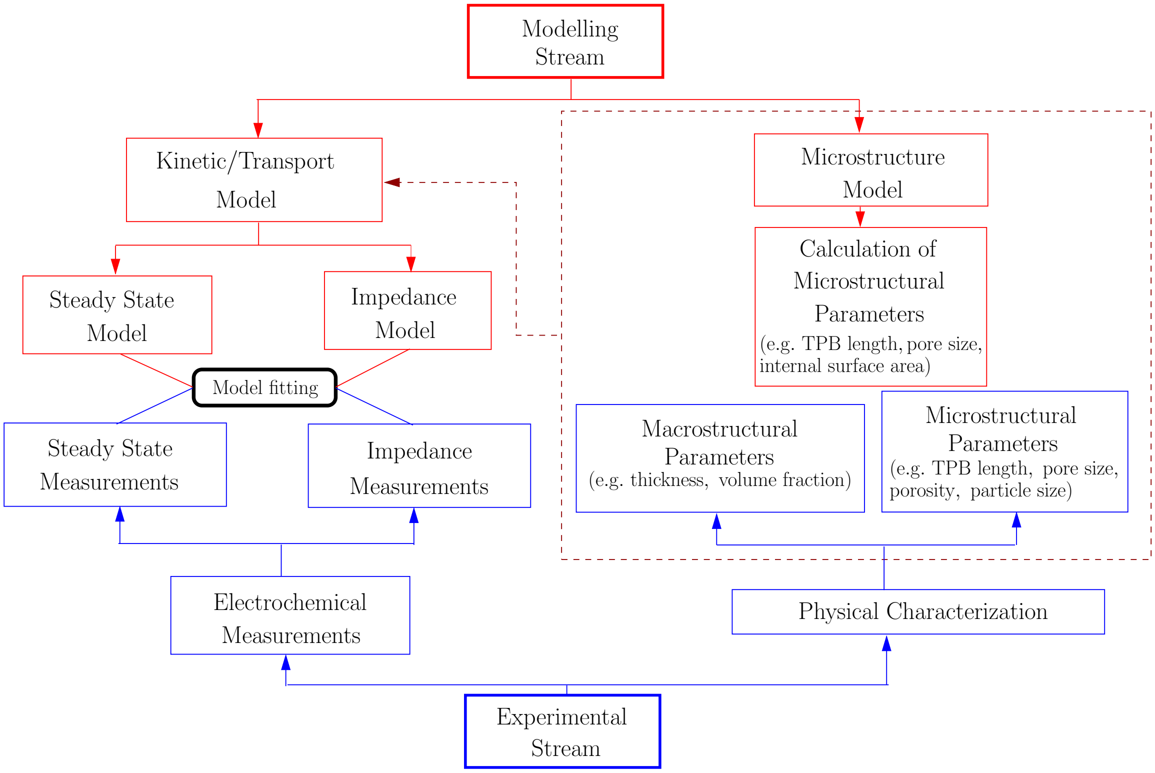

Figure 1.5: Framework for the characterization of porous LSM electrodes used in this dissertation.

that incorporates the physico-chemical processes of the oxygen reduction reaction in porous LSM electrodes 2) an experimental stream to obtain electrochemical data suitable for model fitting. In addition, a numerical tool that has been developed [105] will be used to quantify aspects of the electrode microstructure that cannot be obtained using easily accessible experimental techniques. Once the microstructural independent rate constants and transport coefficients have been determined, the contribution to the total electrode resistance of the individual processes that make up the oxygen reduction reaction can be quantified.

1.6 Thesis Structure

This dissertation is organized into two main streams: 1) the collection of experimental data for the porous LSM/YSZ system and 2) modelling of LSM cathodes. The experimental stream is presented in Chapter 2 and Chapter 3 and the modelling stream is presented in Chapter 4 and Chapter 5. Chapter 2 describes the fundamentals required to collect reliable experimental data and Chapter 3 describes the collection and basic analysis of the experimental data. Chapter 4 describes the development of a mathematical model of a porous LSM electrode incorporating various kinetic and transport processes of the oxygen reduction reaction. In Chapter 4, the comparison of the model to experimental data is also presented while Chapter 5 describes a model for a composite LSM/YSZ cathode. Concluding remarks and recommendations for further research are given in Chapter 6.

References

[1] U.S. Energy Information Administration. International Energy Outlook 2006, June 2006.

[2] U.S. Energy Information Administration. Long-Term World Oil Supply Scenarios, August 2004.

[3] D. Yergin. Peak Oil Theory - “World Running Out of Oil Soon” - Is Faulty; Could Distort Policy and Energy Debate. Technical report, Cambridge Energy Research Associates, November 2006.

[4] N. Christiansen, J. Hansen, H. Holm-Larsen, S. Linderoth, P. Larsen, P. Hendriksen, and M. Mogensen. Solid oxide fuel cell development at Topsoe Fuel Cell and Riso. *Fuel Cells Bulletin*, 8:12–15, 2006.

[5] Nguyen Quang Minh and Takehiko Takahashi. *Science and technology of ceramic fuel cells*. Elsevier Science, 1995.

[6] J. Ralph, C. Rossignol, and R. Kumar. Cathode Materials for Reduced-Temperature SOFCs. *Journal of the Electrochemical Society*, 150:A1518–A1522, 2003.

[7] S.P.S. Badwal and K. Foger. Materials for Solid Oxide Fuel Cells. *Materials Forum*, 21:187–224, 1997.

[8] S.B. Adler. Factors Governing Oxygen Reduction in Solid Oxide Fuel Cell Cathodes. *Chemical Reviews*, 104:4791–4843, 2004.

[9] J.W. Erning, T. Hauber, U. Stimming, and K. Wippermann. Catalysis of the electrochemical processes in solid oxide fuel cell cathodes. *Journal of Power Sources*, 61:205–211, 1996.

[10] D. F. Shriver, P. W. Atkins, and C. H. Langford. *Inorganic Chemistry.* W H Freeman & Co, 1990.

[11] Mette Juhl Jorgensen. *Lanthanum Manganate Based Cathodes for Solid Oxide Fuel Cells.* PhD thesis, Kelle University/Riso National Labs, July 2001.

[12] J.H. Kuo, H.U. Anderson, and D.M. Sparlin. Oxidation-Reduction Behavior of Undoped and Sr-Doped $LaMnO_3$ Nonstoichiometry and Defect Structure. *Journal of Solid State Chemistry*, 83:52–60, 1989.

[13] J. Fleig. On the current-voltage characteristics of charge transfer reactions at mixed conducting electrodes on solid electrolytes. *Physical Chemistry Chemical Physics*, 7:2027–2037, 2005.

[14] YongMan Choi, David S Mebane, Jeng-Han Wang, and Leilin Liu. Continuum and Quantum-Chemical Modeling of Oxygen Reduction on the Cathode in a Solid Oxide Fuel Cell. *Topics in Catalysis*, 46:386–401, 2007.

[15] R.T. Baker and I.S. Metcalfe. Activity and deactivation of $La_{0.8}Ca_{0.2}CrO_3$ in dry methane using temperature-programmed techniques. *Applied Catalysis A*, 126:297–317, 1995.

[16] N. Gunasekaran, S. Rajadurai, J.J. Carberry, N. Bakshi, and C.B. Alcock. Surface characterization and catalytic properties of $La_{1-x}A_xMO_3$ perovskite oxides. Part II: Studies on $La_{1-x}Ba_xMnO_3$ oxides. *Solid State Ionics*, 81:243–249, 1995.

[17] A. Winnubst, A. Scharenborg, and A. Burggraaf. The electrode resistance of $ZrO_2 - Y_2O_3(-Bi_2O_3)$ solid electrolytes with Pt electrodes. *Solid State Ionics*, 14:319–327, 1984.

[18] H. Okamoto, G. Kawamura, and T. Kudo. Study of oxygen adsorption on platinum through observation of exchange current in a solid electrolyte concentration cell. *Electrochimica Acta*, 28:379–382, 1983.

[19] M. Verkerk, M. Hammink, and A. Burggraaf. Oxygen Transfer on Substituted ZrO_2, Bi_2O_3, and CeO_2 Electrolytes with Platinum Electrodes. *Journal of the Electrochemical Society*, 130:70–78, 1983.

[20] D. Wang and A. Nowick. Cathodic and Anodic Polarization Phenomena at Platinum Electrodes with Doped CeO_2 as Electrolyte. *Journal of the Electrochemical Society*, 7:1155–1165, 1979.

[21] J. Mizusaki, K. Amano, S. Yamauchi, and K. Fueki. Electrode reaction at $Pt, O_2(g)$/stabilized zirconia interfaces. Part 1: Theoretical consideration of reaction model. *Soilid State Ionics*, 22:313–322, 1987.

[22] J. Mizusaki, K. Amano, S. Yamauchi, and K. Fueki. Electrode reaction at $Pt, O_2(g)$/stabilized zirconia interfaces. Part II: Electrochemical measurements and analysis. *Solid State Ionics*, 22:323–330, 1987.

[23] A. Mitterdorfer and L.J. Gauckler. Identification of the reaction mechanism of Pt, O2(g)/YSZ system Part 1: General framework, modeling and structural investigation. *Solid State Ionics*, 117:187–202, 1999.

[24] A. Mitterdorfer and L.J. Gauckler. Identification of the reaction mechanism of the $Pt, O_{2(g)}/YSZ$ system Part 2: Model implementation, parameter estimation, and validation. *Solid State Ionics*, 117:203–217, 1999.

[25] F.H. van Heuveln, H.J.M. Bouwmeester, and F.P.F. van Berkel. Electrode Properties of Sr-Doped $LaMnO_3$ on Yttria-Stabilized Zirconia: I. Three-Phase Boundary Area. *Journal of the Electrochemical Society*, 144(1):126–133, 1997.

[26] F.H. van Heuveln and H.J.M. Bouwmeester. Electrode Properties of Sr-Doped $LaMnO_3$ on Yttria-Stabilized Zirconia: II. Electrode Kinetics. *Journal of the Electrochemical Society*, 144(1):134–140, 1997.

[27] X.J. Chen, K.A. Khor, and S.H. Chan. Identification of O_2 reduction processes at yttria stabilized zirconia—doped lanthanum manganite interface. *Journal of Power Sources*, 123:17–25, 2003.

[28] Eugene A. Kotomin, Yuri A. Mastrikov, Eugene Heifets, and Joachim Maier. Adsorption of atomic and molecular oxygen on the $LaMnO_3$ (001) surface: ab initio supercell calculations and thermodynamics. *Physical Chemistry Chemical Physics*, 10:4644–4649, 2008.

[29] T. Kenjo, S. Osawa, and K. Fujikawa. High Temperature Air Cathodes Containing Ion Conductive Oxides. *Journal of the Electrochemical Society*, 138(2):349–355, 1991.

[30] T. Kenjo and M. Nishiya. $LaMnO_3$ air cathodes containing ZrO_2 electrolyte for high temperature solid oxide fuel cells. *Solid State Ionics*, 57:295–302, 1992.

[31] B.C.H. Steele, K.M. Hori, and S. Uchino. Kinetic parameters influencing the performance of IT-SOFC composite electrodes. *Solid State Ionics*, 135:445–450, 2000.

[32] S. Carter, A. Selcuk, R.J. Chater, J. Kajda, J.A. Kilner, and B.C.H. Steele. Oxygen transport in selected nonstoichiometric perovskite-structure oxides. *Solid State Ionics*, 53-56:597–605, 1992.

[33] A. Hammouche, E. Siebert, A. Hammou, M. Kleitz, and A. Caneiro. Electrocatalytic Properties and Nonstoichiometry of the High Temperature Air Electrode $La_{1-x}Sr_xMnO_3$. *Journal of the Electrochemical Society*, 138(5):1212–1216, 1991.

[34] Finn Willy Poulsen. Defect chemistry modelling of oxygen-stoichiometry, vacancy concentrations, and conductivity of $(La_{1-x}Sr_x)_yMnO_{3\pm\delta}$. *Solid State Ionics*, 129:145–162, 2000.

[35] M. Mogensen, S. Primdahl, M. Jorgensen, and C. Bagger. Composite Electrodes in Solid Oxide Fuel Cells and Similar Solid State Devices. *Journal of Electroceramics*, 5(2):141–152, 2000.

[36] P. Shuk, L. Tichonova, and U. Guth. Materials for electrodes based on rare earth manganites. *Soild State Ionics*, 68:177–184, 1994.

[37] Z. Shao and S.M. Haile. A high-performance cathode for the next generation of solid-oxide fuel cells. *Nature*, 431:170–173, 2004.

[38] B.C.H. Steele and A. Heinzel. Materials for fuel-cell technologies. *Nature*, 414:345–352, 2001.

[39] A. Esquirol, N. Brandon, J. Kilner, and M. Mogensen. Electrochemical Characterization of $La_{0.6}Sr_{0.4}Co_{0.2}Fe_{0.8}O_3$ Cathodes for Intermediate-Temperature SOFCs. *Journal of the Electrochemical Society*, 151(11):A1847–A1855, 2004.

[40] V. Dusastre and J.A. Kilner. Optimisation of composite cathodes for intermedita temperature SOFC applications LSCF. *Solid State Ionics*, 126:163–174, 1999.

[41] B.C.H. Steele. Materials for IT-SOFC stacks: 35 years R&D: the inevitability of gradualness? *Solid State Ionics*, 134:3–20, 2000.

[42] E. Siebert, A. Hammouche, and M. Kleitz. Impedance Spectroscopy Analysis of $La_{1-x}Sr_xMnO_3$-Yttria-Stabilized Zirconia Electrode Kinetics. *Electrochimica Acta*, 40(11):1741–1753, 1995.

[43] Y. Jiang, S. Wang, Y. Zhang, J. Yan, and W. Li. Kinetic Study of the Formation of Oxygen Vacancy on Lanthanum Manganite Electrodes. *Journal of the Electrochemical Society*, 145(2):373–378, 1998.

[44] G.J. La O', R.F. Savinell, and Y. Shao-Horn. Activity Enhancement of Dense Strontium-Doped Lanthanum Manganite Thin Films under Cathodic Polarization: A Combined AES and XPS Study. *Journal of the Electrochemical Society*, 156(6):B771–B781, 2009.

[45] V. Brichzin, J. Fleig, H.U. Habermeier, G. Cristiani, and J. Maier. The geometry dependence of the polarization resistance of Sr-doped LaMnO3 microelectrodes on yttria-stabilized zirconia. *Solid State Ionics*, 152-153:499–507, 2002.

[46] G.J. La O', B. Yildiz, S. McEuen, and Y. Shao-Horn. Probing Oxygen Reduction Reaction Kinetics of Sr-Doped $LaMnO_3$ Supported on Y_2O_3-Stabilized ZrO_3. *Journal of the Electrochemical Society*, 154(4):B427–B438, 2007.

[47] M. Ostergard, C. Clausen, C. Bagger, and M. Mogensen. Manganite-Zirconia Composite Cathodes for SOFC: Influence of Structure and Composition. *Electrochimica Acta*, 40(12):1971–1981, 1995.

[48] H.S. Song, W.H. Kim, S.H. Hyun, and J. Moon. Influences of starting particulate materials on microstructural evolution and electrochemical activity of LSM-YSZ composite cathode for SOFC. *Journal of Electroceramics*, 17:759–764, 2006.

[49] S. Kirkpatrick. Percolation and Conduction. *Review of Modern Physics*, 45(4):574–588, 1973.

[50] E.P. Murray, T. Tsai, and S.A. Barnett. Oxygen transfer processes in $(La, Sr)MnO_3/Y_2O_3$-stabilized ZrO_2 cathodes: an impedance spectroscopy study. *Solid State Ionics*, 110:235–243, 1998.

[51] M. Juhl, S. Primdahl, C. Manon, and M. Mogensen. Performance/structure correlation for composite SOFC cathodes. *Journal of Power Sources*, 61:173–181, 1996.

[52] J-D. Kim, G-D. Kim, J-W. Moon, Y. Park, W-H. Lee, K. Kobayashi, M. Nagai, and C-E. Kim. Characterization of LSM-YSZ composite electrode by ac impedance spectroscopy. *Solid State Ionics*, 143:379–389, 2001.

[53] Marc Mamak, Gabriella Metraux, Srebri Petrov, Neil Coombs, Geoffrey Ozin, and M.A. Green. Lanthanum Strontium Manganite/Yttria-Stabilized Zirconia Nanocomposites Derived from a Surfactant Assisted, Co-assembled Mesoporous Phase. *Journal of the American Chemical Society*, 125:5161–5175, 2003.

[54] Hwa Seob Song, Sang Hoon Hyun, Joosun Kim, Hae-Weon Lee, and Jooho Moon. A nanocomposite material for highly durable solid oxide fuel cell cathodes. *Journal of Materials Chemistry*, 18:1087–1092, 2008.

[55] Jian Xin Wang, You Kun Tao, Jing Shao, and Wei Guo Wang. Synthesis and preoperties of $(La_{0.75}Sr_{0.25})_{0.95}MnO_{3-\delta}$ nano-powder prepared via Pechini route. *Journal of Power Sources*, 186:344–348, 2009.

[56] M.J. Jorgensen and M. Mogensen. Impedance of Solid Oxide Fuel Cell LSM/YSZ Composite Cathodes. *Journal of the Electrochemical Society*, 148(5):A433–A442, 2001.

[57] M. Ostergard and M. Mogensen. ac Impedance Study of the Oxygen Reduction Mechanism on $La_{1-x}Sr_xMnO_3$ in Solid Oxide Fuel Cells. *Electrochimica Acta*, 38(14):2015–2020, 1993.

[58] X.J. Chen, K.A. Khor, and S.H. Chan. Electrochemical behaviour of La(Sr)MnO3 electrode under cathodic and anodic polarization. *Solid Stat Ionics*, 167:379–387, 2004.

[59] X.J. Chen, S. H. Chan, and K. A. Khor. Cyclic voltammetry of $(La, Sr)MnO_3$ electrode on YSZ substrate. *Solid State Ionics*, 164:17–25, 2003.

[60] A.C. Co and V. Birss. Mechanistic Analysis of the Oxygen Reduction Reaction at $(La, Sr)MnO_3$ Cathode in Solid Oxide Fuel Cells. *Journal of Physical Chemistry B*, 110:11299–11309, 2006.

[61] Y. Jiang, S. Wang, Y. Zhang, J. Yan, and W. Li. Electrochemical reduction of oxygen on a strontium doped lanthanum manganite electrode. *Solid State Ionics*, 110:111–119, 1998.

[62] A. Barbucci, M. Viviani, M. Panizza, M. Delucchi, and G. Cerisola. Analysis of the oxygen reduction process on SOFC composite electrodes. *Journal of Applied Electrochemistry*, 35:399–403, 2005.

[63] J. Choi, J. Jang, and S. Oh. Microstructure and cathodic performance of $La_{0.9}Sr_{0.1}MnO_3$/yttria-stabilized zirconia composite electrodes. *Electrochimica Acta*, 46:867–874, 2001.

[64] J. Van Herle, A.J. McEvoy, and K. Ravindranathan Thampi. A study on the $La_{1-x}Sr_xMnO_3$ oxygen cathode. *Electrochimica Acta*, 41(9):1447–1454, 1996.

[65] S.P. Jiang, J.G. Love, and Y. Ramprakash. Electrode behaviour at $(La, Sr)MnO_3/Y_2O_3 - ZrO_2$ interface by electrochemical impedance spectroscopy. *Journal of Power Sources*, 110:201–208, 2002.

[66] Y. Takeda, R. Kanno, M. Noda, Y.Tomida, and O. Yamamoto. Cathodic Polarization Phenomena of Perovskite Oxide Electrodes with Stabilized Zirconia. *Journal of the Electrochemical Society*, 134(11):2656–2661, 1987.

[67] B. Kenney and K. Karan. Impact of Nonuniform Potential in SOFC Composite Cathodes on the Determination of Electrochemical Kinetic Parameters: A Numerical Analysis. *Journal of the Electrochemical Society*, 153(6):A1172–A1180, 2006.

[68] A.C. Co, S.J. Xia, and V.I. Birss. A Kinetic Study of the Oxygen Reduction Reaction at $\mathrm{LaSrMnO_3 - YSZ}$ Composite Electrodes. *Journal of the Electrochemical Society*, 152(3):A570–A576, 2005.

[69] YongMan Choi, Matthew E. Lynch, M.C. Lin, and Meilin Liu. Prediction of O_2 Dissociation Kinetics on $LaMnO_3$-Based Cathode Materials for Solid Oxide Fuel Cells. *Journal of Physical Chemistry C*, 113:7290–7297, 2009.

[70] S.P. Jiang and J.G. Love. Observation of structural change induced by cathodic polarization on $(La, Sr)MnO_3$ electrodes of solid oxide fuel cells. *Solid State Ionics*, 158:45–53, 2003.

[71] Wei Wang and San Ping Jiang. A mechanistic study on the activation process of $(La, Sr)MnO_3$ electrodes of solid oxide fuel cells. *Solid State Ionics*, 177:1361–1369, 2006.

[72] M. Backhaus-Ricoult, K. Adib, T. St. Clair, B. Luerssen, L. Gregoratti, and A. Barinov. In-situ study of operating SOFC LSM/YSZ cathodes under polarization by photoelectron microscopy. *Solid State Ionics*, 179:891–895, 2008.

[73] Jimmi Nielsen and Torben Jacobsen. SOFC cathode/YSZ - Non stationary TPB effects. *Solid State Ionics*, 179:1314–1319, 2008.

[74] S.P. Jiang, J.G. Love, J.P. Zhang, M. Hoang, Y. Ramprakash, A.E. Hughes, and S.P.S. Badwal. The electrochemical performance of LSM/zirconia-yttria interface as a function of a-site non-stoichiometry and cathodic current treatment. *Soild State Ionics*, 121:1–10, 1999.

[75] S. McIntosh, S.B. Adler, J.M. Vohs, and R.J. Gorte. Effect of Polarization on and Implications for Characterization of LSM-YSZ Composite Cathodes. *Electrochemical and Solid State Letters*, 7(5):A111–A114, 2004.

[76] A. Mitterdorfer and L.J. Gauckler. $La_2Zr_2O_7$ formation and oxygen reduction kinetics of the $La_{0.85}Sr_{0.15}Mn_yO_3$, O_2(g)—YSZ system. *Solid State Ionics*, 111:185–218, 1998.

[77] J.R. Smith, A. Chen, D. Gostovic, D. Hickey, D. Kundinger, K.L. Duncan, R.T. DeHoff, K.S. Jones, and E.D. Wachsman. Evaluation of the relationship between cathode microstructure and electrochemical behavior for SOFCs. *Solid State Ionics*, 180:90–98, 2009.

[78] M. Nagata, Y. Itoh, and H. Iwahara. Dependence of observed overvoltages on the positioning of the reference electrode on the solid electrolyte. *Solid State Ionics*, 67:215–224, 1994.

[79] F.H. van Heuveln. *Characterization of porous cathodes for application in solid oxide fuel cells.* PhD thesis, University of Twente, 1997.

[80] J. Winkler, P. V. Hendriksen, N. Bonanos, and M. Mogensen. Geometric requirements of solid electrolyte cells with a reference electrode. *Journal of the Electrochemical Society*, 145:1184–1192, 1998.

[81] S.B. Adler, B.T. Henderson, M.A. Wilson, D.M. Taylor, and R.E. Richards. Reference electrode placement and seals in electrochemical oxygen generators. *Solid State Ionics*, 134:35–42, 2000.

[82] A. Hashibon, S. Raz, and I. Riess. Preferred position for the reference electrode in solid state electrochemistry. *Solid State Ionics*, 149:167–176, 2002.

[83] S.B. Adler. Reference Electrode Placement in Thin Solid Electrolytes. *Journal of the Electrochemical Society*, 149(5):E166–E172, 2002.

[84] W. He and T.V. Nguyen. Edge Effects on Reference Electrode Measurements in PEM Fuel Cells. *Journal of the Electrochemical Society*, 151(2):A185–A195, 2004.

[85] A. Svensson, S. Sunde, and K. Nisancioglu. Mathematical modeling of oxygen exchange and transport in air-perovskite-YSZ interface regions. 1. Reduction of intermediately adsorbed oxygen. *Journal of the Electrochemical Society*, 144(8):2719–2732, 1997.

[86] S.B. Adler, J.A. Lane, and B.C.H. Steele. Electrode kinetics of porous mixed-conducting oxygen electrodes. *Journal of the Electrochemical Society*, 143:3554–3564, 1996.

[87] B.A. van Hassel, B.A. Boukamp, and A.J. Burggraaf. Electrode polarization at the $Au, O_2(g)$/yttria stabilized zirconia interface. Part I: Theoretical considerations of reaction model. *Solid State Ionics*, 48:139–154, 1991.

[88] B.A. van Hassel, B.A. Boukamp, and A.J. Burggraaf. Electrode polarization at the $Au, O_2(g)$ / yttria stabilized zirconia interface. Part II: electrochemical measurements and analysis. *Solid State Ionics*, 48:155–171, 1991.

[89] H. Zhu, R. Kee, V. Janardhanan, O. Deutschmann, and D. Goodwin. Modeling Elementary Heterogeneous Chemistry and Electrochemistry in Solid-Oxide Fuel Cells. *Journal of the Electrochemical Society*, 152(12):A2427–A2440, 2005.

[90] Marcel Vogler, Anja Bieberle-Hutter, Ludwig Gauckler, Jurgen Warnatz, and Wolfgang Bessler. Modelling Study of Surface Reactions, Diffusion, and Spillover at a Ni/YSZ Patterned Anode. *Journal of the Electrochemical Society*, 156(5):xxx–xxx, 2009.

[91] David G. Goodwin, Huayang Zhu, Andrew M. Colclasure, and Robert J. Kee. Modeling Electrochemical Oxidation of Hydrogen on Ni-YSZ Pattern Anodes. *Journal of the Electrochemical Society*, 156(9):B1004–B1021, 2009.

[92] A. Svensson, S. Sunde, and K. Nisancioglu. Mathematical modeling of oxygen exchange and transport in air-perovskite-YSZ interface regions. 2. Direct exchange of oxygen vacancies. *Journal of the Electrochemical Society*, 145(4):1390–1400, 1998.

[93] P. Costamagna, P. Costa, and V. Antonucci. Micro-modelling of solid oxide fuel cell electrodes. *Electrochimica Acta*, 43(3-4):375–394, 1998.

[94] D. Bouvard and F. Lange. Relation between percolation and particle coordination in binary powder mixtures. *Acta metall. mater.*, 39(12):3083–3090, 1991.

[95] S. Sunde. Simulations of composite electrodes in fuel cells. *Journal of Electroceramics*, 5:2:153–182, 2000.

[96] X.J. Chen, S.H. Chan, and K.A. Khor. Simulation of a composite cathode in solid oxide fuel cells. *Electrochimica Acta*, 49:1851–1861, 2004.

[97] S.H. Chan, X.J. Chen, and K.A. Khor. Cathode micromodel of solid oxide fuel cell. *Journal of the Electrochemical Society*, 151(1):A164–A172, 2004.

[98] B. Kenney and K. Karan. Engineering of microstructure and design of a planar porous composite SOFC cathode: A numerical analysis. *Solid State Ionics*, 178:297–306, 2007.

[99] Javier I. Gazzarri and Olivera Kesler. Electrochemical AC impedance model of a solid oxide fuel cell and its application to diagnosis of multiple degradation modes. *Journal of Power Sources*, 167:100–110, 2007.

[100] Y. Shi, N. Cai, C. Li, C. Bao, E. Croiset, J. Qian, Q. Hu, and S. Wang. A General Approach for Electrochemical Impedance Spectroscopy Simulation Using Transient Mechanistic SOFC Model. In *ECS Transactions*, volume 7, pages 1889–1899. The Electrochemical Society, 2007.

[101] L. Schneider, C. Martin, Y. Bultel, L. Dessemond, and D. Bouvard. Percolation effects in functionally graded SOFC electrodes. *Electrochimica Acta*, 52(9):3190–3198, 2007.

[102] Joshua Golbert, Claire S. Adjiman, and Nigel P. Brandon. Microstructural Modeling of Solid Oxide Fuel Cell Anodes. *Industrial & Engineering Chemistry Research*, 47:7693–7699, 2008.

[103] Andrew S. Martinez and Jacob Brouwer. Percolation modeling investigation of TPB formation in a solid oxide fuel cell electrode-electrolyte interface. *Electrochimica Acta*, 53:3597–3609, 2008.

[104] Abbaspour Ali, X. Wen, K. Nandakumar, Jingli Luo, and Karl T. Chuang. Geometrical modeling of microstructure of solid oxide fuel cell composite electrodes. *Journal of Power Sources*, 185(2):961–966, 2008.

[105] Ben Kenney, Mikelis Valdmanis, Craig Baker, J.G. Pharoah, and Kunal Karan. Computation of TPB length, surface area and pore size from numerical reconstruction of composite solid oxide fuel cell electrodes. *Journal of Power Sources*, 128(2):1051–1059, 2009.

[106] James R. Wilson, Worawarit Kobsiriphat, Roberto Mendoza, Hsun-Yi Chen, Jon M. Hiller, Dean J. Miller, Katsuyo Thornton, Peter W. Voorhees, Stuart B. Adler, and Scott A. Barnett. Three-dimensional reconstruction of a solid-oxide fuel cell anode. *Nature*, 5:541–544, 2006.

[107] Max Cimenti, Anne Co, Viola Birss, and Josepine Hill. Distortions in Electrochemical Impedance Spectroscopy Measurements Using 3-Electrode Methods in SOFC. I - Effect of Cell Geometry. *Fuel Cells*, (5):364–376, 2007.

[108] Max Cimenti, Viola Birss, and Joesphine Hill. Distortions in Electrochemical Impedance Spectroscopy Measurements Using 3-Electrode Methods in SOFC. II - Effect of Eletrode Activity and Relaxation Times. *Fuel Cells*, (5):377–391, 2007.

[109] T. Armstrong and A. Virkar. Performance of Solid Oxide Fuel Cells with $LSGM - LSM$ Composite Cathodes. *Journal of the Electrochemical Society*, 149(12):A1565–A1571, 2002.

[110] J. Mizusaki, H. Tagawa, K. Tsuneyoshi, and A. Sawata. Reaction Kinetics and Microstructure of the Solid Oxide Fuel Cells Air Electrode $La_{0.6}Ca_{0.4}MnO_3/YSZ$. *Journal of the Electrochemical Society*, 138(7):1867–1873, 1991.

[111] Yusuke Sakamoto, Naoki Shikazono, and Nobuhide Kasagi. Effects of electrode microstructure on polarization characteristics of SOFC anodes. In *Sixth International Fuel Cell Science, Engineering and Technology Conference*, June 16-18 2008.

[112] R. Ganeshananthan and Anil Virkar. Measurement of transport properties of perovskite cathodes. In *Solid Oxide Fuel Cells IX (SOFC-IX)*, volume 2, pages 1487–1498. The Electrochemical Society, 2005.

[113] Mark E. Orazem and Bernard Tribollet. *Electrochemical Impedance Spectroscopy.* Wiley, 2008.

[114] J. Bockris and S. Srinivasan. *Fuel Cells: Their Electrochemistry.* McGraw-Hill Book Company, 1969.

[115] A.J. Bard and L.R. Faulkner. *Electrochemical Methods: Fundamentals and Applications.* John Wiley and Sons, 2 edition, 2001.

[116] J. Bockris and A.K.N. Reddy. *Modern Electrochemistry : An Introduction to an Interdisciplinary Area.* Plenum US, 1973.

[117] Evgenij Barsoukov and J. Ross Macdonald. *Impedance Spectroscopy: Theory, Experiment and Applications.* Wiley-Interscience, 2 edition, 2005.

[118] Andreas Mitterdorfer. *Identification of the Oxygen Reduction at Cathodes of Solid Oxide Fuel Cells.* PhD thesis, Swiss Federal Institute of Technology, February 1997.

[119] R.A. De Souza and J.A. Kilner. Oxygen transport in $La_{1-x}Sr_xMn_{1-y}Co_yO_{3-\delta}$ perovskites. Part 2. Oxygen surface exchange. *Solid State Ionics*, 126:153–161, 1999.

[120] Gabor A. Somorjai. *Introduction to surface chemistry and catalysis.* John Wiley & Sons, Inc, 1994.

[121] S.H. Jeong, I.S. Bae, Y.S. Shin, S.-B. Lee, H.-T. Kwak, and J.-H. Boo. Physical and electrical properties of ZrO_2 and YSZ high-k gate dielectric thin films grown by RF magnetron sputtering. *Thin Solid Films*, 475:354–358, 2005.

[122] A. Bondi. van der Waals Volumes and Radii. *Journal of Physical Chemistry*, 68(3):441–451, 1964.

[123] J. Ross Macdonald. *Impedance Spectroscopy: Emphasizing Solid Materials And Systems.* John Wiley & Sons, 1987.

[124] Ivar Waernhus, Natsuko Sakai, Harumi Yokokawa, Tor Grande, Mari-Ann Einarsrud, and Kjell Wiik. Cation diffusion in $La_{1-x}Sr_xFeO_{3-\delta}$, x=0 and 0.1 measured by SIMS. *Solid State Ionics*, 178:907–914, 2007.

[125] Marian Palcut, Jens S. Christensen, Kjell Wiik, and Tor Grande. Impurity diffusion of ^{141}Pr in $LaMnO_3$, $LaCoO_3$ and $LaFeO_3$ materials. *Physical Chemistry Chemical Physics*, 10:6544–6552, 2008.

[126] Shogo Miyoshi and Manfred Martin. B-Site cation diffusivity of Mn and Cr in perovskite-type $LaMnO_3$ with cation-deficit nonstoichiometry. *Physical Chemistry Chemical Physics*, 11:3063–3070, 2009.

[127] R.A. De Souza and J.A. Kilner. Oxygen transport in $La_{1-x}Sr_xMn_{1-y}Co_yO_{3-\delta}$ perovskites. Part 1. Oxygen tracer diffusion. *Solid State Ionics*, 106:175–187, 1998.

[128] Peter Atkins and Julio De Paula. *Atkins' Physical Chemistry.* W.H. Freeman and Company, 8 edition, 2006.

[129] J. Divisek, L.G.J. de Haart, P. Holtappels, T. Lennartz, W. Mallener, U. Stimming, and K. Wippermann. The kinetics of electrochemical reactions on high temperature fuel cell electrodes. *Journal of Power Sources*, 49:257–270, 1994.

[130] M. Mogensen, S. Primdahl, and M. Juhl. Revealing the mechanisms of SOFC electrodes using a combination of AC and DC methods. *Electrochemical Proceedings*, 97-18:385–393, 1997.

[131] R. Byron Bird, Warren E. Stewart, and Edwin N. Lightfoot. *Transport Phenomena.* John Wiley & Sons, 2 edition, 2002.

[132] Hae-Won Choi, Arganthael Berson, Ben Kenney, Jon G. Pharoah, Steven Beale, and Kunal Karan. Effective transport coefficients for porous microstructures in solid oxide fuel cells. In *Electrochemical Society?s 216th meeting (SOFC-XI)*, 2009.

[133] R. Suwanwarangkul, E. Croiset, M.W. Fowler, P.L. Douglas, E. Entchev, and M.A. Douglas. Performance comparison of Fick's, dusty-gas and Stefan-Maxwell models to predict the concentration overpotential of a SOFC anode. *Journal of Power Sources*, 122:9–18, 2003.

[134] Marco Cannarozzo, Adriana Del Borghi, and Paola Costamagna. Simulation of mass transport in SOFC composite electrodes. *Journal of Applied Electrochemistry*, 38:1011–1018, 2008.

[135] F. Zhao, T. Armstrong, and A. Virkar. Measurement of $O_2 - N_2$ Effective Diffusivity in Porous Media at High Temperatures Using an Electrochemical Cell. *Journal of the Electrochemical Society*, 150(3):A249–A256, 2003.

[136] Andrzej Wieckowski, Takeshi Kobayashi, Panakkattu K Babu, Jong Ho Chung, and Eric Oldfield. Coverage Dependence of CO Surface Diffusion on Pt Nanoparticles - an EC-NMR Study. In *Meterials Research Society Proceedings*, volume 984, 2007.

[137] Robert Gomer. Diffusion of adsorbates on metal surfaces. *Reports on Progress in Physics*, 53:917–1002, 1990.

[138] J.M. Zalc, S.C. Reyes, and E. Iglesia. Monte-Carlo simulations of surface and gas phase diffusion in complex porous structures. *Chemical Engineering Science*, 58:4605–4617, 2003.

[139] D.A. Nield and A. Bejan. *Convection in Porous Media*. Springer-Verlag, 1992.

[140] Emmanuel Resch. Numerical and Experimental Characterisation of Convective Transport in Solid Oxide Fuel Cells. Master's thesis, Queen's University, October 2008.

[141] Robert J. Kee, Michael E. Coltrin, and Peter Glarborg. *Chemically Reactive Flow: Theory and Practice*. Wiley Interscience, 2003.

[142] R.D. Cortright and J.A. Dumesic. Kinetics of Heterogenous Catalytic Reactions: Analysis of Reaction Schemes. *Advances in Catalysis*, 46:161–264, 2001.

[143] Richard I. Masel. *Principles of Adsorption and Reaction on Solid Surfaces*. John Wiley and Sons, 1996.

[144] P. Kisliuk. The Sticking Probabilities of Gases Chemisorbed on the Surfaces of Solids. *Journal of Physical Chemistry of Solids*, 3:95–101, 1957.

[145] David G. Goodwin. A Patterned Anode Model With Detailed Chemistry. In *Solid Oxide Fuel Cells IX (SOFC-IX)*, volume 1, 2005.

[146] Bonnie J. McBride, Michael J. Zehe, and Sanford Gordon. Nasa glenn coefficients for calculating thermodynamic properties of individual species.

[147] *FEMLAB Modeling Guide*. COMSOL AB, 2004.

[148] J. A. Nelder and R. Mead. A Simplex Method for Function Minimization. *The Computer Journal*, 7(4):308–313, 1965.

[149] Kenneth J. Beers. *Numerical Methods for Chemical Engineering: Applications in MatLab*. Cambridge University Press, 2007.

[150] W.G. Bessler. A new computation approach for SOFC impedance from detailed electrochemical reaction-diffusion models. *Solid State Ionics*, 176:997–1011, 2005.

[151] B.E. Conway and E. Gileadi. Kinetic Theory of Pseudo-Capacitance and Electrode Reactions at Appreciable Surface Coverage. *Transactions of the Farraday Society*, 58:2493–2509, 1962.

[152] Richard Tilley. *Understanding Solids: The Science of Materials*. Wiley, 2004.

[153] V.A.C. Haanappel, J. Mertens, D. Rutenbeck, C. Tropartz, W. Herzhof, D. Sebold, and F. Tietz. Optimisation of processing and microstructural parameters of LSM cathodes to improve the electrochemical performance of anode-supported SOFCs. *Journal of Power Sources*, 141:216–226, 2005.

[154] M. Kleitz and F. Petitbon. Optimized SOFC electrode microstructure. *Solid State Ionics*, 92:65–74, 1996.

[155] M.J. Jorgensen, S. Primdahl, and M. Mogensen. Characterisation of composite SOFC cathodes using electrochemical impedance spectroscopy. *Electrochimica Acta*, 44:4195–4201, 1999.

[156] C.W. Tanner, K-Z. Fung, and A.V. Virkar. The effect of porous composite electrode structures on solid oxide fuel cell performance. *Journal of the Electrochemical Society*, 144:21–30, 1997.

[157] James R. Wilson, J. Scott Cronin, Anh T. Duong, Sherri Rukes, Hsun-Yi Chen, Katsuyo Thornton, Daniel R. Mumm, and Scott Barnett. Effect of composition of $(La_{0.8}Sr_{0.2}MnO_3 - Y_2O_3$-stabilized $ZrO_2)$ cathodes: Correlating three-dimensional microstructure and polarization resistance. *Journal of Power Sources*, 195(7):1829–1840, 2009.

[158] J. Deseure, Y. Bultel, L. Dessemond, and E. Siebert. Theoretical optimisation of a SOFC composite cathode. *Electrochimica Acta*, 50:2037–2046, 2005.

[159] S.H. Chan and Z.T. Xia. Polarization effects in electrolyte/electrode-supported solid oxide fuel cells model. *Journal of Applied Electrochemistry*, 32:339–347, 2002.

[160] P. Costamagna, P. Costa, and E. Arato. Some more considerations on the optimization of cermet solid oxide fuel cell electrodes. *Electrochimica Acta*, 43(8):967–972, 1998.

[161] L.J. van der Pauw. A method of measuring specific resistivity and hall effect of discs of arbitrary shape. *Philips Research Reports*, 13(1):1–9, 1958.

[162] Keiji Yamahara, Tal Z. Sholklapper, Craig P. Jacobson, Steven J. Visco, and Lutgard C. De Jonghe. Ionic conductivity of stabilized zirconia networks in composite SOFC electrodes. *Solid State Ionics*, 176:1359–1364, 2005.

[163] J.C.Y. Koh and A. Fortini. Prediction of Thermal Conductivity and Electrical Resistivity of Porous Metallic Materials. *International Journal of Heat and Mass Transfer*, 16:2013–1022, 1973.

[164] M. Kaviany. *Principles of Heat Transfer in Porous Media*. Springer, second edition, 1999.

Chapter 2

Sample Preparation and Electrode Characterization Theory

2.1 Introduction

For generation of reliable data and subsequent meaningful analysis of the data, it is essential that reproducible samples are fabricated. In addition, the experimental data generated on similar electrode samples must be reproducible. Several experimental factors can influence the quality of electrochemical data. These include the test cell configuration, the design of the electrochemical test system/reactor and the electrochemical test protocol.

The test cell configuration, either a 2-electrode or a 3-electrode cell, determines the nature of the electrochemical data. A 3-electrode cell requires a reference electrode in addition to the working and counter electrodes. Unlike a 2-electrode cell configuration, the 3-electrode setup, in principle, allows for the evaluation of the working electrode (WE) independently from the counter electrode (CE). However, the suitable placement of the reference electrode (RE) can offer significant challenges during the fabrication process [1]. Further, the nature or the microstructure of a porous electrode is influenced by the fabrication method. It is well known that the electrode microstructure (features such as the triple phase boundary length, the internal surface area, the pore size and the porosity) can have a significant impact on the electrochemical response of the electrode [2]. Thus, the choice of cell configuration and the fabrication method can affect both the electrode performance and the variability of the electrochemical data, which arises due to both macroscopic cell geometry variations and to microstructural differences.

In addition to the test cell, the electrochemical reactor must be suitably designed so that it has a minimal impact on the electrode response. The main factors to consider in the design of the electrochemical test system, or the reactor, include the ability to monitor and control the thermal and chemical environment in the immediate vicinity of the electrode and the ability to measure the cell current and voltage. Improper reactor design can result in measurement artifacts that may be misinterpreted to arise from physical electrode processes.

Finally, the nature of the experimental data also depends on the type of electrochemical measurement employed. A steady-state polarization measurement can yield kinetics related information under the proper polarization conditions; however, this is only possible when using a 3-electrode test cell. Time-varying techniques such as electrochemical impedance spectroscopy (EIS) can in principle allow for deconvolution of kinetic and transport effects but the data analysis may not be straightforward. Further, for SOFC electrodes, it is known that the electrical history can have significant influence on the electrode performance [3, 4].

In this chapter, a detailed discussion of the aforementioned issues is presented and is organized as follows:

- Section 2.2 discusses the different cell configuration options; the cell/electrode fabrication method and the physical characterization of the electrode is also presented.
- Section 2.3 presents the design of the electrochemical reactor employed for electrochemical testing.
- Section 2.4 discusses the different electrochemical test methods employed in this thesis. The section also presents a brief overview of the underlying theory for analysis of electrochemical data.

2.2 Sample Fabrication

The key matters pertaining to sample fabrication for cell testing are the choice of the cell design (such as the placement of the reference electrode) and the method for the electrode fabrication. Since a number of test samples are required to examine the wide range of operating conditions of interest, such as temperature, reactant (oxygen) concentration and electrode potentials, it is important to adopt a fabrication method that yields samples of reproducible macroscopic and microscopic features. In the following sub-section, the different cell configuration options are discussed followed by the presentation of a detailed description of the electrode/cell fabrication method and physical characterization method.

2.2.1 Cell Configuration

An electrochemical cell comprises a working electrode (a cathode in present study), a counter electrode and an electrolyte. In addition, a reference electrode can be employed to isolate the polarization potential of the working electrode from that of the counter electrode. Further, the chemical environment on the counter and working electrode can be the same, as in a symmetrical cell, or different from one another, as in a full cell. The classification of various cell configurations is then based on the type of electrode setup and chemical environment for the electrodes. Four different cell configurations are depicted in Figure 2.1. The key characteristics of these configurations are discussed below.

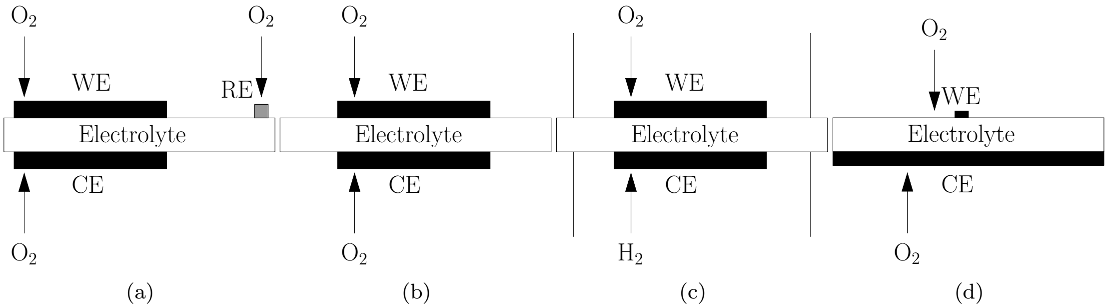

Figure 2.1: Examples of: (a) 3-electrode configuration (b) 2-electrode symmetrical cell configuration (c) 2-electrode full cell configuration (d) 2-electrode microelectrode configuration. WE=working electrode, CE=counter electrode, RE=reference electrode.

1. 3-electrode cell configuration: This configuration can be operated either as a symmetrical cell or full cell. If the reference electrode is suitably placed, then the working electrode potential with respect to a constant reference potential can be obtained, eliminating the contribution of the counter electrode.

2. 2-electrode symmetrical cell configuration: In this configuration, the chemical environment (gas composition) on both electrodes is the same. Further, both the WE and the CE should be composed of the same material and should be identical in terms of the macroscopic (e.g. thickness and size) and microscopic (porosity, internal surface area and triple phase boundary) characteristics. The electrochemical data is obtained near the equilibrium conditions such that reversible behavior on the two electrodes is assumed. Accordingly, the polarization data analysis is based on the assumption that both electrode behave symmetrically in terms of both the fundamental electrochemical processes and the electrode area over which activity takes place.

3. 2-electrode full cell configuration: In this configuration the chemical environment on the WE and CE is different. Further, the WE and CE can be made of different materials. The electrochemical measurement over a wide range of polarization conditions can be made, but, the contribution of the WE polarization to the total polarization cannot be isolated without knowing the resistance of the counter electrode.

4. 2-electrode microelectrode configuration: In this configuration, the WE is a dense microelectrode, usually 10-250 microns in diameter. The WE active area is orders of magnitude smaller than that of the CE and thereby, it is assumed that the CE polarization is negligible with respect to WE polarization. Due to low current densities generated, the ohmic or electrolyte resistance may also be neglected. Thus, the total cell polarization can be approximated to be equal to that of the WE polarization. The geometry of a microelectrode is vastly different from the geometry of a real SOFC electrode which may influence kinetic measurements. For example, microelectrodes are typically fabricated to be extremely thin, usually less than $1 \mu m$ in thickness, and owing to this length scale, additional pathways for oxygen transport such as transport of oxygen through the bulk electrode may become important since this is the

shortest length scale [5].

In this dissertation, both the 3-electrode configuration and 2-electrode symmetrical cell configurations were used to characterize the current/voltage behavior of porous LSM electrodes.

Cell dimensions Specific geometric details of the 3-electrode and symmetrical cell geometries used in this work are presented in Figure 2.2 and Table 2.1. Figures 2.2c and 2.2e are 3-electrode cells in "planar" and "pellet" form, respectively. In the case of the planar 3-electrode geometry, a Pt wire reference electrode was placed on the same side as a WE but at a distance of Δ. For the pellet 3-electrode geometry, the Pt wire reference electrode was placed within a groove machined along the perimeter of the YSZ pellet equidistant from the WE and the CE.

Table 2.1: Dimensions of cell configurations shown in Figure 2.2 (after sintering)

Cell Type	Dimension	Value
Symmetrical cell	D_1	1-3mm
	D_2, L_2	12.2mm
	L_1	5-50μm
Planar 3-electrode cell	D_1	1-2mm
	D_2	22mm
	L_1	5-50μm
	L_2	10mm
	Δ	5mm
	δ	NA
Pellet 3-electrode cell	D_1	6mm
	D_2, L_2	12.2mm
	L_1	5-50 μm
	Δ	3mm
	Groove	0.3mm wide 0.2mm deep

Special attention must be paid to the physical dimensions of the 3-electrode cell design since they can influence the potential being measured by the reference electrode. The challenges associated with the placement of the reference electrode has been the subject of a number of studies [1, 6–11] that discuss these geometry requirements. For the case of the "planar" 3-electrode design, the placement of the reference electrode and the alignment of the working and counter electrodes must be carefully considered. The difficulty arises especially for the planar configuration because ideally

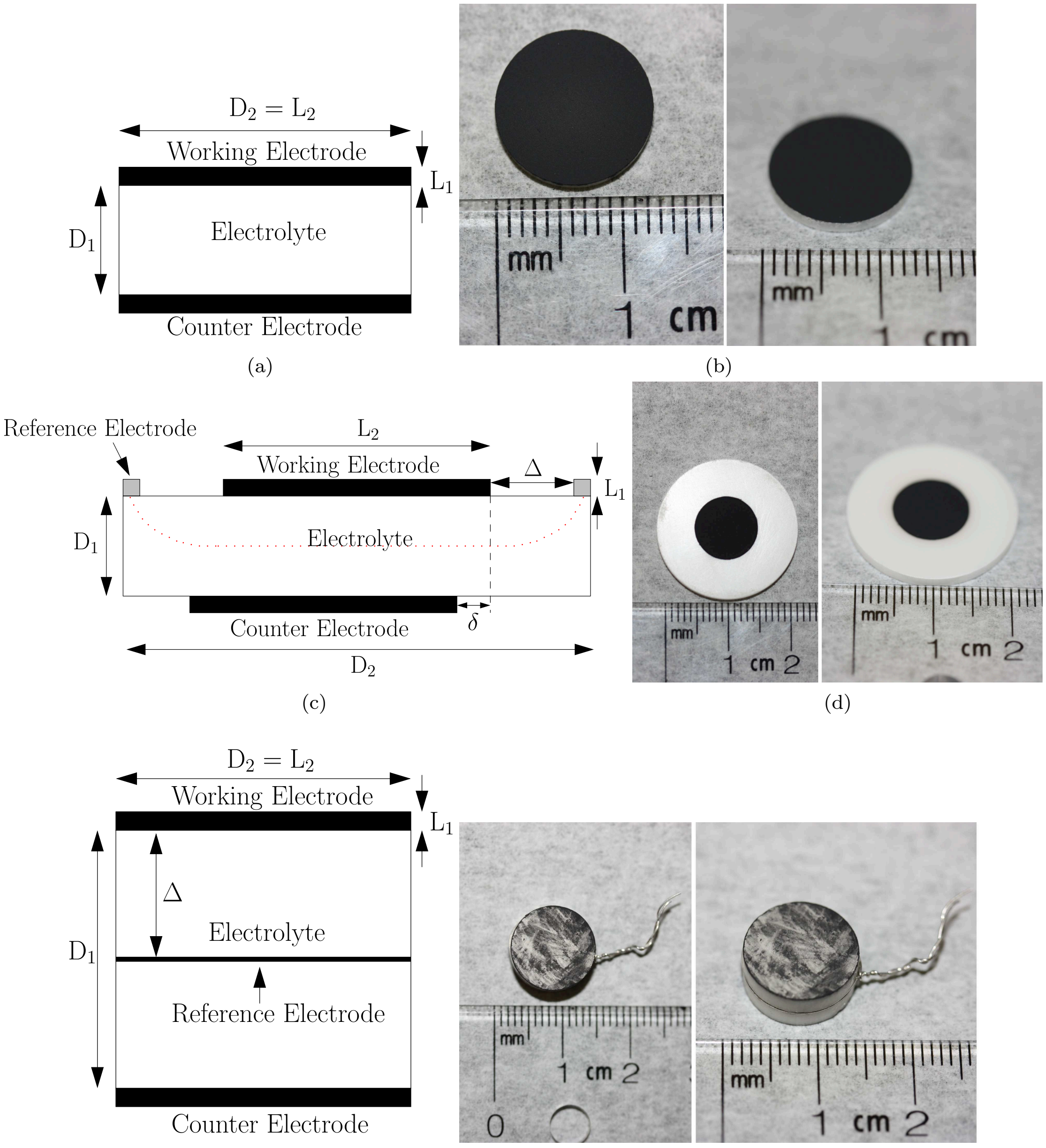

Figure 2.2: Various cell configurations used in this work: (a)-(b) 2-electrode symmetrical cell configuration with identical working and counter electrodes (c)-(d) Planar 3-electrode configuration with a Pt ring reference electrode on the electrolyte surface (dotted line through electrolyte shows the theoretical potential streamline monitored by the reference electrode) (e)-(f) Pellet 3-electrode configuration with a Pt ring reference electrode wrapped in a groove around the circumference of the YSZ pellet (location of potential monitored by the reference electrode is at the physical location of the reference electrode)

the potential to be monitored by the reference electrode should correspond to that at the centre of the electrolyte (indicated by the dotted line in Figure 2.2c), and not at the physical location of the reference electrode. For the planar case, mathematical models have shown that the potential distribution through the electrolyte depends on the design parameters D_1, Δ and δ, shown in Figure 2.2c. If $\delta > 0$, then the potential measured by the reference electrode may be distributed unevenly between the WE and CE and it may change during the experiment. In general, for the planar 3-electrode design, it is desirable to maximize D_1 and Δ and minimize δ. Simulations performed by van Heuveln [7] suggests that Δ should be greater than $5D_1$, while Adler *et al.* [8] suggests that Δ should be greater than $3D_1$ to minimize errors associated with δ and Winkler *et al.* [1] showed that the relative placement depends on the size of the reference electrode and the resistance of the WE and CE. Simulation results in [1] suggest that the best geometries for 3-electrode measurements are pellet type geometries such as the "Risø geometry" or that in Figure 2.2e because: 1) the WE and CE are inherently symmetrically placed resulting in uniform potential distribution through the electrolyte and 2) the RE monitors the potential at its physical location and so does not depend on other geometrical factors. The dimensions of the electrodes summarized in Table 2.1 have been carefully chosen so that they reflect, as best possible, all suggested dimensions to reduce any errors related to cell geometry. The most difficult parameter to control and measure is the working and counter electrode offset, δ, in Figure 2.2c.

Assessment of 3-electrode set-up Measuring the serial resistance (or electrolyte resistance) as well as the polarization resistance (or electrode resistance) using impedance spectroscopy (which is further discussed in Section 2.4.2) can be useful in detecting experimental artifacts. One method that can be used to verify the ability of the RE to separate the contributions of the WE from the CE is to fabricate a 3-electrode cell with identical WE and CE. In such a cell, the polarization resistance of the WE should be equal to the polarization resistance of the CE (both measured using the RE) and they should both sum to the polarization resistance of the entire cell (measured without the RE) [12, 13]. Since a symmetrical cell does not have a RE, experimental artifacts due to the cell geometry do not exist when using a symmetrical cell (assuming that the electrodes are in fact symmetrical). If the polarization resistance of the WE and CE in this situation are not equal, then this is an indication that the placement of the reference electrode is inadequate. In addition, for the case of a planar 3-electrode configuration, if the cell geometry is valid, then the potential measured by the RE would be measured at a location equal to half the thickness of the electrolyte (as shown by the dotted line in Figure 2.2c) and so the serial resistance of the impedance of the WE and CE should be the same and equal to half of the serial resistance of the impedance of the symmetrical cell. It should be recognized though that for a pellet 3-electrode cell, the serial resistance of the impedance of the WE only depends on the relative distance of the RE between the WE and CE and so does not necessarily have to equal half of the serial resistance of the impedance of the symmetrical cell.

In order to assess the 3-electrode design, 3-electrode cells were fabricated using the planar and pellet type configurations shown in Figures 2.2c and 2.2e with the working and counter electrodes being porous LSM. By changing the lead wire connection on the impedance analyzer, the impedance of the WE and CE (measured using a RE) could be measured and the impedance of the symmetrical cell (without the RE) could also be measured. Figure 2.3 shows the impedance of the WE, CE, symmetrical cell and the sum of the WE and CE impedances using porous LSM cathodes at 850°C in air in both the planar 3-electrode cell configuration (Figure 2.3a) and the pellet 3-electrode cell configuration (Figure 2.3b).

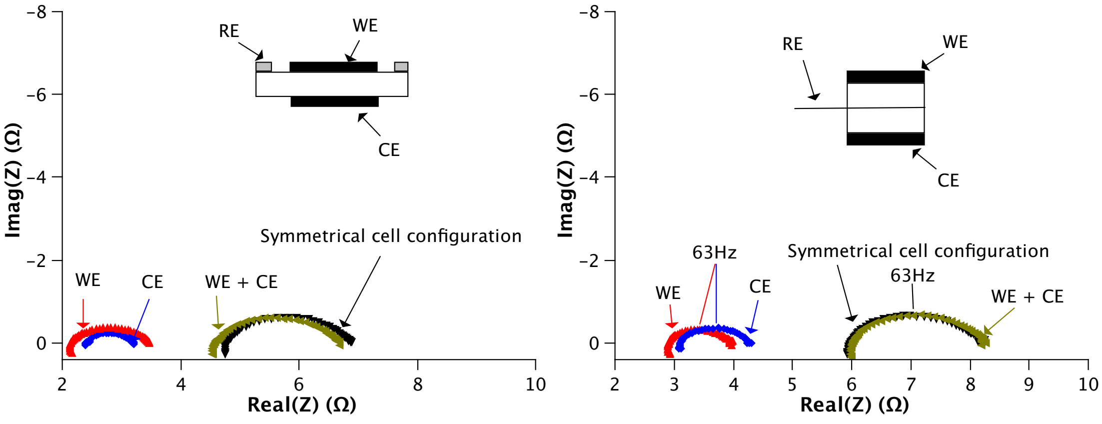

(a) (b)

Figure 2.3: Comparison of the impedance response of the WE and CE (both porous LSM) in 3-electrode cell configuration against the impedance response of the symmetrical cell configuration: (a) Planar 3-electrode cell configuration (b) Pellet 3-electrode cell configuration at 850°C in air.

In the case of the planar 3-electrode cell shown in Figure 2.3a, there were two indications that the reference electrode did not measure the correct potential: 1) the polarization resistance of the WE and CE were not equal and their sum did not equal the impedance of the symmetrical cell and 2) the serial resistance of the WE and CE were different from each other. For the planar cell, the WE contributed 63% towards the total symmetrical cell impedance whereas the serial resistance of the WE and CE impedance differed by 11%. For the pellet type 3-electrode cell, the electrode impedances of the WE and CE were essentially equivalent with the WE contributing 48% towards the total symmetrical cell impedance. The reasons for the discrepancies in the planar 3-electrode cell were likely caused by variability in the manufacturing process, especially in the parameter δ described in Figure 2.2c which is particularly difficult to control. While it was possible to create planar 3-electrode cells that did show equivalent impedances between the WE and CE that summed up to the symmetrical cell impedance, this was less consistent and more difficult than for pellet 3-electrode cells.

For the reasons given above, the pellet 3-electrode cell was the preferred configuration and all 3-electrode measurements presented in subsequent chapters of this thesis use the pellet type geometry.

2.2.2 Sample Fabrication

A key goal of the cell and electrode fabrication method development was to ensure that cell to cell and electrode to electrode variability was minimized. To this end, an automated electrode fabrication set-up was developed and protocols for the fabrication of electrodes were developed and strictly adhered to. The following subsections describe the methods for the fabrication of the electrolyte as well as the fabrication of the electrode.

Electrolyte fabrication

Electrolyte processing techniques vary depending on the desired electrolyte thickness. Common processing techniques to manufacture electrolytes thinner than $50\mu m$ include screen-printing and electrophoretic deposition and require a thick support layer. Thin electrolytes are desirable if the purpose is to decrease the resistance of the entire cell, however, when evaluating individual electrodes, thicker electrolytes (typically thicker than $0.5mm$) are often required. For thick electrolytes, or electrolyte supported cells, methods such as tape-casting or dry-pressing can be used. Tape-casting requires a thick paste of ceramic powder and various organic compounds which can be difficult to perfect, but can produce a large quantity of samples in each batch with various dimensions. In contrast, dry-pressing involves pressing the ceramic powder in a die set and is generally more time consuming and limited to relatively smaller dimensions compared to the tape-casting method, however, it is simple to perfect.

The method for fabrication of YSZ electrolytes used in this thesis is outlined in Figure 2.4. For the fabrication of YSZ electrolytes for symmetrical and 3-electrode cells, YSZ powder, $(Y_2O_3)_{0.08}(ZrO_2)_{0.92}$ (Tosoh, USA), was pressed in a steel die set using a Carver 10 ton press at a pressure of 15000psi. In all cases, the electrolytes were sintered at 1400°C for 5hrs, polished with silicon carbide paper (240 grit, 400 grit and 800 grit) and re-fired to 1400°C for 5hrs at $4°C/min$. For the thick 3-electrode samples, immediately after dry-pressing the YSZ powder, the pellets were pressed at 200MPa in a cold isostatic press, pre-sintered to 1000°C for 2hrs and machined using a CNC lathe to create a groove 0.5mm wide and 0.2mm deep around the centre of the pellet before full sintering to 1400°C for 5hrs.

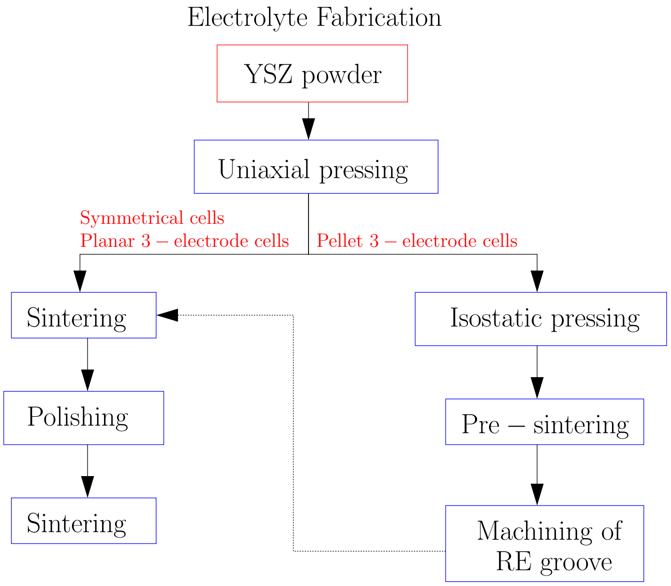

Figure 2.4: Electrolyte fabrication routine for thin electrolytes destined for planar type 3-electrode cells or symmetrical cells and for thick electrolytes destined for pellet type 3-electrode cells.

Table 2.2 outlines the various electrolyte dimensions which were fabricated depending on the type of sample being tested. This method produced fully dense electrolytes which were then used as the substrate while depositing thin porous electrodes.

Table 2.2: Electrolyte dimensions after sintering (before sintering)

Purpose	Diameter (mm)	Thickness (mm)
2-electrode cell	12.2 (13)	1-3 (2-4)
Pellet 3-electrode cell	12.2 (13)	6 (8)
Planar 3-electrode cell	22 (25)	1-3 (2-4)

Electrode fabrication

Most electrode fabrication techniques employ a ceramic paste or ink with mixtures of the cathode ceramic powder and organic compounds. The quantity and type of organic compounds along with sintering conditions influence micro/macrostructural features such as the porosity and the thickness of the electrode. Common fabrication techniques include slurry coating (using a paint brush), dip coating, spin coating, screen-printing and spray coating. Of the automated processes, screen-printing is the most common electrode fabrication method, used by the Virkar group at the University of Utah [14], Chan group at Nanyang Technological University (Singapore) [15] and Birss group at University of Calgary [16], where a ceramic paste is deposited onto a sintered electrolyte through a mesh. Typically the screen-printing technique results in porous electrodes ranging from 15-30 μm in thickness. The spray coating method has been used by groups such as the Mogensen group at Risø [17] and the Brandon group at Imperial College, London [18], where a low viscosity ceramic ink is deposited onto the electrolyte using an airbrush. The wet-spraying technique can make thin electrode layers in the range of 5-50 μm, however, depositing thick layers can be time consuming.

Reproducibility of electrode samples can be significantly improved by automation of the process. An important consideration, especially when depositing composite electrodes or when using powders with large particle size distributions, is to ensure that the ceramic powders form a stable suspension, otherwise the electrolyte material may not be interdispersed amongst the cathode material. This can be challenging for the spray technique [17] since the viscosity of the ink is typically very low and organic dispersants can be detrimental to the quality of the spray.

In this thesis, an automated pulsed-spray coating system was developed. The system is depicted in Figure 2.5. This system was designed to make electrodes of uniform and controlled thickness. The main component of the system was a gravity fed double action airbrush (Unico, AB722) whose trigger was connected to a timer controlled solenoid. The timer activated the solenoid for a set amount of time which sprayed a small quantity of the ink contained in the ink cup. The solenoid was deactivated for a set amount of time during which time the solvent in the deposited ink was allowed to evaporate from the substrate, leaving behind the ceramic particles. A bubbler was used to ensure that the ceramic particles remained well mixed in the ink cup. To improve uniformity of the deposited layer, the substrate was attached to a low speed motor which rotated the substrate at a speed of about 30 revolutions per minute. A typical deposition time was about 30 minutes to deposit a layer 20 microns thick.

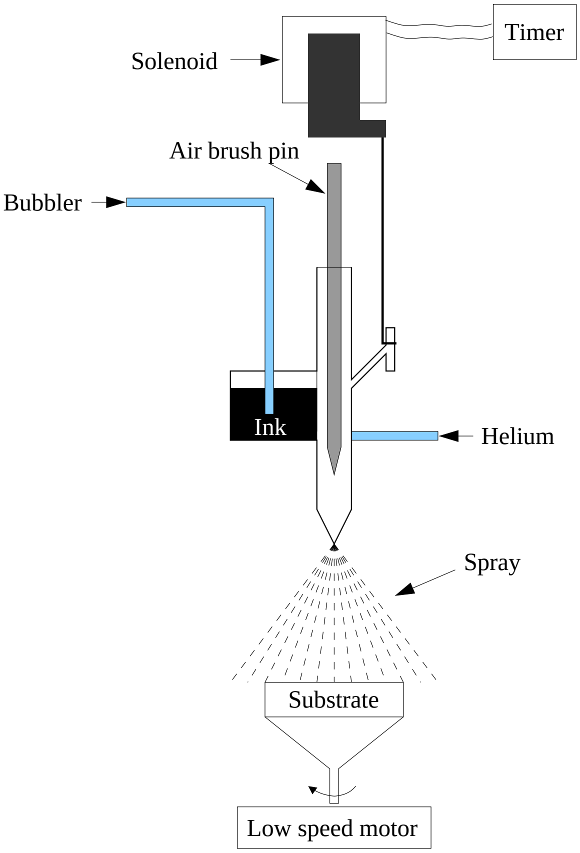

Figure 2.5: Automatic ceramic spray system designed to deposit reproducible electrode layers.

To ensure reproducible electrodes, it was important to control as many of the spray parameters as possible. These parameters included: 1) the ink formulation 2) the solenoid activation/deactivation time 3) the working distance between spray nozzle and substrate and 4) the inlet gas pressure. The reproducibility of the spray system was assessed based on the electrode thickness for various ceramic loadings on the electrolyte.

Ceramic ink The spray system was designed so that the ink formulation was simple and easily reproducible. The suspension medium for the ink formulation was ethanol and contained a ceramic powder loading of 1.11 wt % and 0.022 wt % Polyvinylpyrrolidone (PVP) which helped film formation. The ethanol, PVP, ceramic powder and 5mm diameter Zirconia milling media were mixed in a ball mill for 20hrs before the ink was sprayed.

Spray parameters The solenoid activation time, which set the volume of ink ejected from the gun at each pulse, was set between 0.05s and 0.10s and the idle time was set to 1.0s. The working distance between the gun nozzle and the electrolyte substrate was 38mm and the inlet gas pressure was set to 10psi.

After the working and counter electrodes had been sprayed, the electrodes were sintered at $1150°C$ for 2hrs using a heating and cooling rate of $2°C/min$. The electrode fabrication process is outlined in Figure 2.6.

2.2.3 Physical Characterization

The electrode physical characteristics such as thickness and estimates of the pore size as well as the triple phase boundary length of pure LSM electrodes were determined from scanning electron microscopy (SEM). Figures 2.8, 2.9 and 2.11 show cross-section, plan view and etched LSM on YSZ surface images obtained from SEM (JEOL JSM-840) for various LSM and LSM-YSZ composite electrodes fabricated by the wet-spraying technique. The software package ImageJ was used to measure the electrode thickness, pore size, as well as the triple phase boundary length of pure LSM electrodes from SEM images. Lines were traced on the SEM image using the ImageJ software and the length of the lines were calibrated against a known distance in the SEM image.

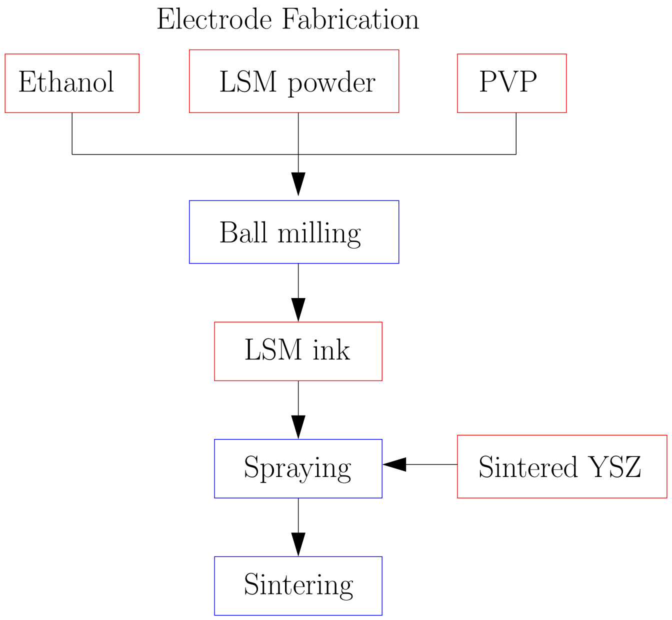

Figure 2.6: Process for fabrication of porous LSM electrodes.

Electrode Thickness and Porosity

The thickness of the electrodes was a function of the spray parameters. Figure 2.7 shows the influence of adjusting the solenoid activation time between 0.05s and 0.1s in terms of the deposited layer thickness for various ceramic loadings. The deposition time was approximately $0.5\mu m$/min. The electrode porosities were estimated with the knowledge of the electrode mass (M), which were weighed after spraying and after sintering using a micro-balance, the electrode thickness (L), which was measured using SEM, the geometric area (A) and the density of the ceramic particle (ρ^{bulk}), which was known from the literature and from fabrication of fully dense LSM and YSZ pellets. An effective electrode density, or the density of the porous structure, can be calculated from

$$\rho^{eff} = \frac{M}{AL} \tag{2.1}$$

and the electrode porosity can be calculated with the knowledge of the electrode density at zero porosity (the density of the ceramic particle, ρ^{bulk}):

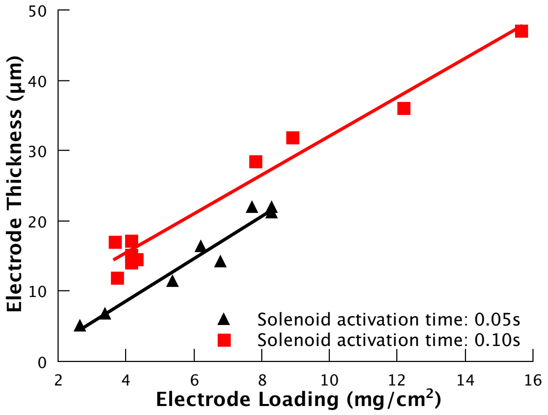

Figure 2.7: Electrode thickness as a function of LSM loading on the YSZ substrate. All thickness measured from SEM images.

$$\epsilon = 1 - \frac{\rho^{eff}}{\rho^{bulk}} \tag{2.2}$$

The effective electrode density was lower for a solenoid activation time of 0.10s which resulted in electrodes about $8\mu m$ thicker and double the porosity compared to a solenoid activation time of 0.05s for the same electrode loadings. This might be explained by particle rearrangement through capillary action as ethanol evaporated from the surface of the sprayed layer. For each pulse, low ink volumes may form a film only a couple of particles thick and as the ethanol evaporates, each particle shifts into a more stable position, densifying the structure. For larger ink volumes, each pulse may form a film many particles thick and during ethanol evaporation, particle-particle interaction can prevent individual particles from filling void spaces creating a less dense structure.

In general the reproducibility of the electrode layers, assessed on the basis of the electrode thickness and estimated porosity, was better for a solenoid activation time of 0.05s. The electrode porosities were 0.41 ± 0.03 to 0.29 ± 0.01 for large and small solenoid activation times, respectively. For each sample that was tested, the electrode thickness and porosity were measured to ensure the macroscopic reproducibility.

Figure 2.8 shows examples of the cross-section SEM images that were used to measure the thickness and the thickness variation of the electrodes. The thickness of each electrode was obtained by averaging the measurements at 10 or more locations from the SEM image. The difference between the maximum and minimum electrode thickness measured by image analysis was always less than $1.5\mu m$ and typically around $1.0\mu m$ while the standard deviations were less than $0.5\mu m$. The thinnest electrode imaged by SEM was $2.2\mu m \pm 0.1\mu m$ while the thickest was $46\mu m \pm 0.5\mu m$. Composite electrodes were fabricated by spraying the functional layer (such as 50vol% LSM-50vol% YSZ) and then a current collector layer of pure LSM, as shown in Figure 2.8c. For each sample that had undergone electrochemical testing, an additional sample was made on a thinner electrolyte consisting of only the functional layer with the same loading. This sample was subjected to SEM analysis and allowed for easy sectioning of the sample for cross-section analysis to overcome the difficulty in image analysis of combined functional and current collector layers for composite electrodes. Figure 2.8b shows a 60vol% LSM-40vol% YSZ functional layer with an identical loading to the sample shown in Figure 2.8c ($3.15mg/cm^2$).

Pore Size Estimation

In principle, there are a number of methods that can be used to determine the pore size and pore size distribution of porous materials, such as BET adsorption and mercury intrusion porosimetry techniques. These techniques require extremely sensitive instruments in order to measure the low surface areas and pore volumes of the electrodes. In addition, there are varying definitions of pore size, especially for non-spherical pores and the pore structure can greatly influence the measurement of pore sizes which can give widely varying results. SEM image analysis can also be used as a method to obtain a first-order estimate of pore sizes.

Figure 2.9 shows plan view images at various magnifications of an LSM electrode. These images were used to estimate the pore size distribution of the electrodes using image analysis. The distribution of pore sizes is shown in Figure 2.10. The pore sizes were estimated in two ways: 1) the "circular diameter" is the effective diameter of the pore calculated by determining the area of the pore and assuming a circular shape 2) Feret's diameter is the longest distance within the pore. For both the circular diameter method and the Feret diameter method, the largest fraction of pore diameters were between 0.2-$0.4\mu m$ and the largest pore size was $2.2\mu m$. The average pore diameter was $0.42\mu m$ and $0.64\mu m$ for the circular diameter and Feret diameter methods, respectively. It should be emphasized that this technique is only a first-order estimate of the pore size distribution

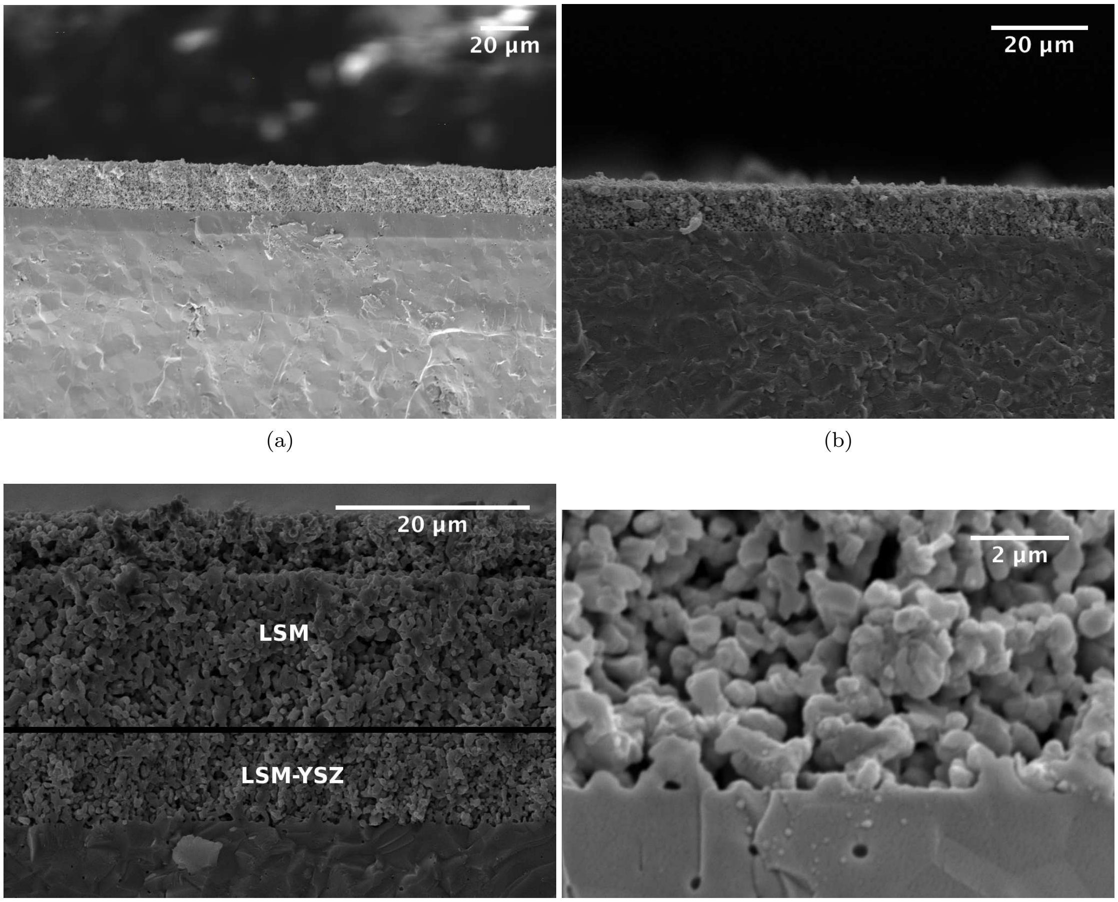

(a) (b)

(c) (d)

Figure 2.8: Cross section of electrodes fabricated by spray system: (a) Pure LSM - $18.9\mu m \pm 0.54\mu m$ (b) 60vol% LSM - 40vol% YSZ - $9.1\mu m \pm 0.22\mu m$ (c) 60vol% LSM - 40vol% YSZ ($10.1\mu m \pm 0.28\mu m$) with LSM current collector ($20.2\mu m \pm 0.51\mu m$) (d) Pure LSM

due to the fact that SEM images are 2-dimensional but not all pores in the image lie on the same plane.

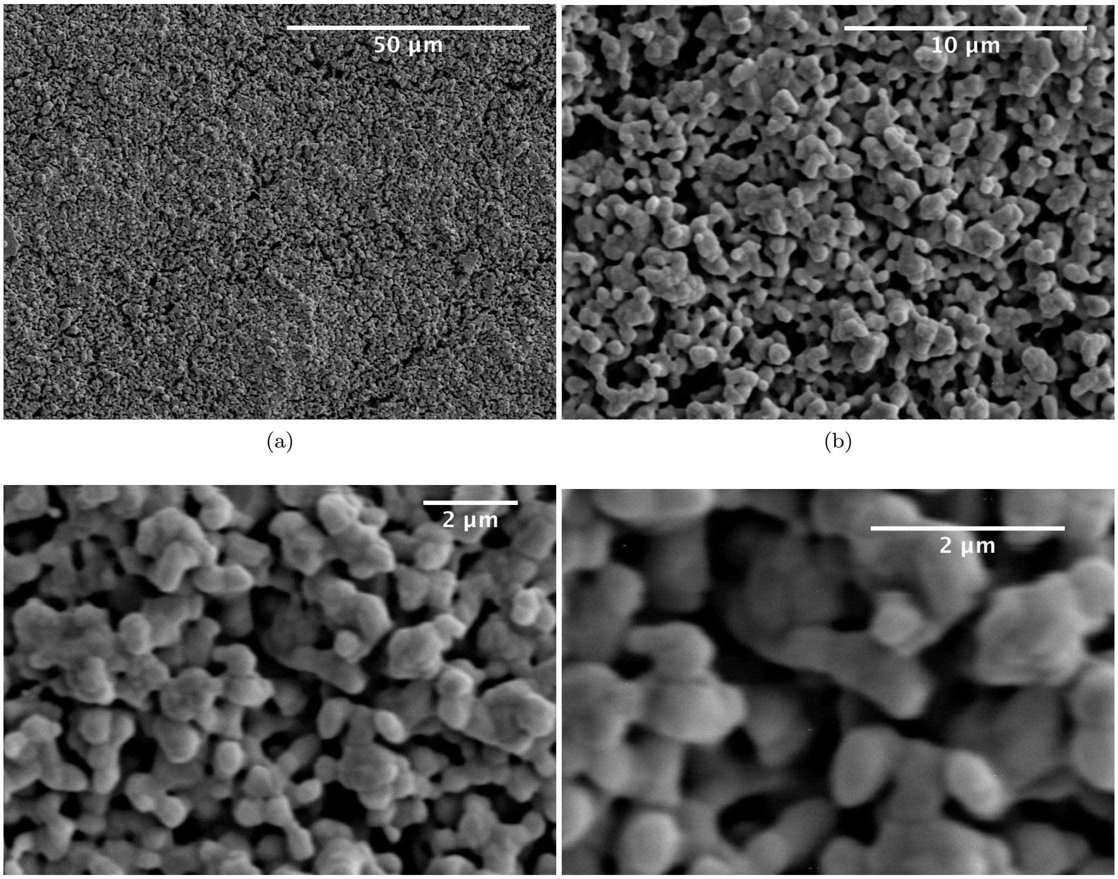

(a) (b)

(c) (d)

Figure 2.9: Plan view of electrodes fabricated by spray system: (a) LSM plan view 1000X magnification (b) LSM plan view 5000X magnification (c) LSM plan view 10000X magnification (d) LSM plan view 20000X magnification

An alternative technique for the estimation of the pore sizes is by numerically constructing a porous LSM geometry and analytically calculating pore sizes [19]. This technique reveals that the pore size distribution is a function of the particle sizes. For particle sizes equivalent to the LSM ceramic powder used in this study, the average pore size was calculated to be $p_{avg} = 0.25\mu m$ compared to SEM analysis which estimated a range between 0.42 and $0.64\mu m$. The discrepancy may be caused by the fact that the resolution of SEM images is not high enough to measure very small

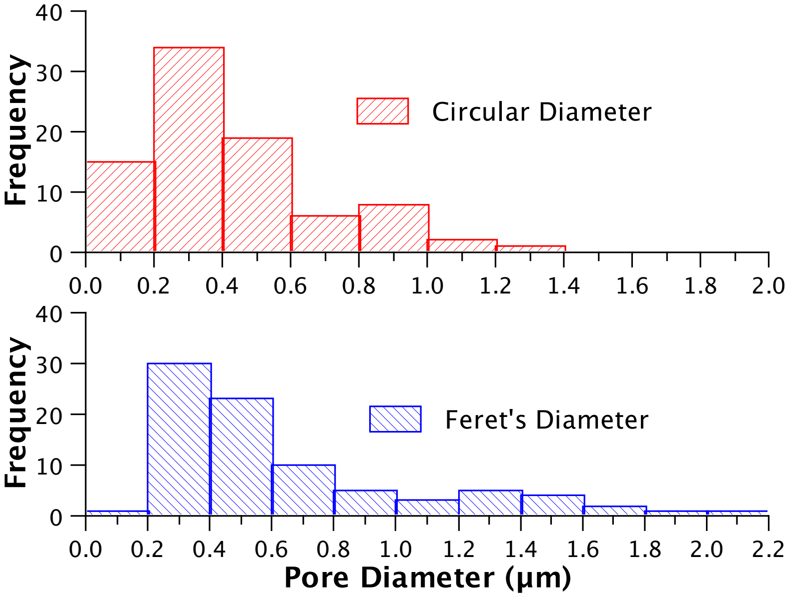

Figure 2.10: Distribution of electrode pore sizes estimated by image analysis from plan view SEM images.

features which can be captured from the calculation of the pore size from the numerical construction technique.

Triple Phase Boundary Length Estimation

The triple phase boundary (TPB) is of special interest for electrochemical kinetics because it is thought to be the site for electrochemical charge transfer reactions. The TPB is the location where three electrode phases intersect: 1) the solid, electron conducting phase 2) the solid ion conducting phase 3) the gas phase. Various attempts have been made to estimate the TPB length (λ_{tpb}) for porous electrodes. For example, for single phase $La_{0.6}Ca_{0.4}MnO_3$ electrodes, Mizusaki et al. [20] estimated λ_{tpb} from SEM cross sections and found values to range from 0.16-1.0 $\mu m \mu m^{-2}$. A number of researchers have examined λ_{tpb} of single phase LSM cathodes by etching the ceramic electrode from the electrolyte surface to examine the imprint from the contacting electrode particles under SEM. Reported values for this method range from 1 to 3 $\mu m \mu m^{-2}$ [21, 22]. Experimental methods for the determination of λ_{tpb} for composite electrodes rely primarily on stereological methods [23].

Recent attempts to reconstruct porous electrodes from FIB-SEM images [24] offer promise with good resolution of SEM images (on the order of 10-50 nm [24]) but phase identification can pose some challenge. The theoretical approach for estimation of λ_{tpb} has been based on coordination particle theory that allows calculation of the percolation and coordination number of binary random packed spheres [25–29]. This approach is limited to mono-sized particles and by the fact that the particle-particle contact angle is not coupled to the electrode porosity. More recently, Schneider *et al.* [30] as well as Golbert *et al.* [31] reconstructed the approximate electrode geometry for modelling purposes where the value of λ_{tpb} was calculated by the random geometry. Martinez and Brouwer [32] as well as Ali *et al.* [33] and Kenney *et al.* [19] have also developed geometrical models to evaluate λ_{tpb} in composite electrodes. In the case of Ali *et al.*, their analysis concluded that the spatial distribution of active reaction sites could be important and that the region near the current collector/electrode and the electrode/electrolyte interfaces can have a different λ_{TPB} than that in the bulk. The works by Schneider *et al.*, Golbert *et al.*, Martinez and Brouwer and Ali *et al.* have so far used mono-sized particles, however, ceramic powders can have broad particle size distributions which can have a large impact on the microstructure. Another limitation of these techniques are the difficulties in modelling the sintering behavior of the ceramic particles and the fact that they assume perfectly spherical particles.

In this work, the technique used to evaluate λ_{tpb} for porous LSM electrodes on YSZ electrolytes was the chemical etching technique. The LSM electrode was fabricated as usual using the wet-spray technique, sintered and then the LSM phase was dissolved in HCl for 20 minutes leaving the YSZ surface unchanged. The imprint of the LSM particles on the YSZ surface as a result of the sintering process was then imaged by a high resolution scanning electron microscope and the outline of the perimeter of the imprint was calculated using the software package ImageJ (NIH, USA) and taken to be λ_{tpb}. For each chemically etched sample, 10 high resolution SEM images were taken at random locations on the YSZ surface and analyzed. Figure 2.11 shows an example of the etched YSZ surface with LSM imprints and Table 2.3 shows the results for a number of different samples.

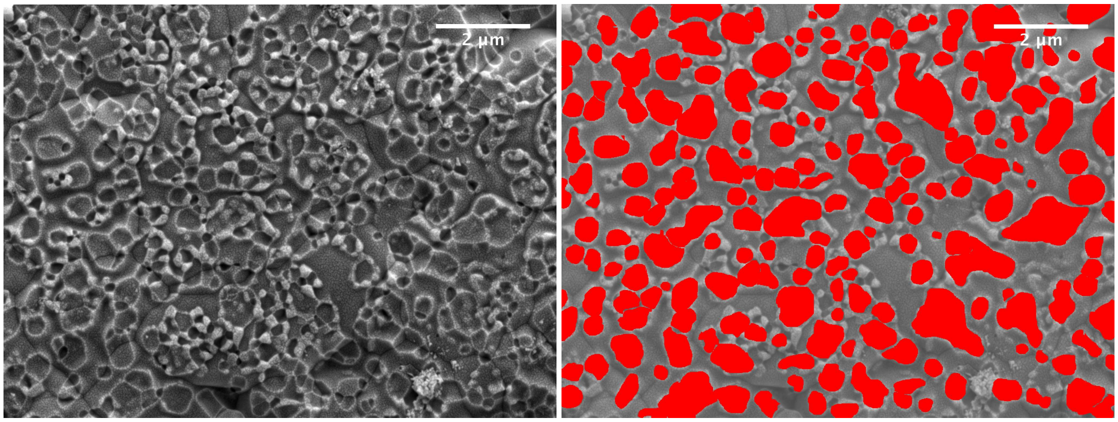

(a) (b)

Figure 2.11: (a) SEM image of the YSZ surface after dissolving the porous LSM electrode in HCl (b) The same image as (a) but showing the triple phase boundary (λ_{tpb}) after image analysis.

Table 2.3: Pure phase LSM triple phase boundary lengths (λ_{tpb}) and the LSM/YSZ contact area (A_{dl}) measured by the chemical etching technique at 10 random SEM images for each sample.

Sample	λ_{tpb} ($\mu m \mu m^{-2}$)	A^*_{dl}
Sample 1	3.16 ± 0.21	48.7%
Sample 2	3.40 ± 0.29	51.0%
Sample 3	3.46 ± 0.22	43.3%
Sample 4	3.27 ± 0.20	49.4%
Overall	3.32 ± 0.23	48.1%

* As a percentage of total area

Internal Surface Area Estimate

The internal surface area (or gas-solid surface area) is the area of the solid phase that is accessible to the gas for adsorption or desorption. In principle, the total internal surface area can be measured via the liquid nitrogen (or krypton) BET adsorption measurements or mercury intrusion porosimetry. However, in practice, these instruments must be extremely sensitive in order to measure the low surface areas and pore volumes of real electrodes. Moreover, the measured internal surface area does not distinguish between the surface area of the two different solid materials (LSM and YSZ in case of SOFC composite cathode).

To estimate the internal surface area, imaging techniques are generally required. For example, Ganeshananthan and Virkar [34] used quantitative stereology to estimate the internal surface area for $La_{0.5}Sr_{0.5}CoO_{3-\delta}$ cathodes and found a value of 2.9×10^6 m^2m^{-3} while Wilson *et al.* [24] used FIB-SEM to reconstruct an SOFC anode and found a value of 4.6×10^6 m^2m^{-3}. Alternatively, a crude technique used by Svensson [35] is to assume that the pores are cylindrical which results in an internal surface area of $a = 2\epsilon/r_p$ where ϵ is the electrode porosity and r_p is the pore radius. For a pore radius of $0.5\mu m$ and a porosity of $\epsilon = 0.3$, $a = 1.2 \times 10^6$ m^2m^{-3}. In this work, we used the numerical construction technique described in [19] which can account for particle size distributions to calculate the internal surface area. For the LSM particle sizes used to make our electrodes, the internal surface area was 3.49×10^6 m^2m^{-3}.

2.2.4 Section Summary

In the above section, the selection of the cell design used to evaluate porous electrodes as well as the fabrication of the sample cells and physical characterization of the fabricated electrodes was discussed. Both 3-electrode cells as well as symmetrical cells are considered in this work. To minimize any experimental artifacts as a result of the 3-electrode cell geometry, a pellet type design was chosen where the reference electrode is wrapped around the circumference of the pellet. This design is inherently symmetric and ensures that the potential measured by the reference electrode is consistent throughout the electrochemical measurement.

The fabrication process required two steps: 1) fabrication of dense YSZ electrolytes 2) fabrication of porous electrodes. YSZ electrolytes were fabricated by uniaxial pressing and for the case of pellet type 3-electrode cells, subsequent isostatic pressing as well as CNC machining. A wet spraying technique was developed to deposit electrodes with uniform, controlled and reproducible layers.

A combination of techniques were used to characterize the microstructure of the porous electrodes: 1) using SEM imaging techniques to measure the electrode thickness, the triple phase boundary length of pure LSM electrodes, to estimate the pore size and indirectly, to estimate the electrode porosity 2) a numerical construction technique to calculate the triple phase boundary length of composite electrodes and to calculate the internal surface area.

2.3 Reactor Set-up

While the design of the working electrode | electrolyte | counter electrode system is important as well as ensuring a reproducible electrode fabrication technique, it is also important to consider the design of the electrochemical reactor. In general, the electrochemical reactor should fulfil the following tasks: 1) the ability to operate at temperatures between $500°C$ and $1000°C$ 2) the ability to maintain a closed atmosphere allowing for various gas mixtures to be supplied directly to the working and counter electrodes 3) the ability to measure the temperature close to the electrode 4) the ability to minimize the influence of the electrical lead wires.

2.3.1 Description of Reactor

For all electrochemical experimental measurements carried out in this thesis, the electrochemical reactor ProboStat (NorECs, Norway) was used along with mass flow controllers to control the supply of gas mixtures and a high temperature electrical furnace to control the temperature. The ProboStat electrochemical reactor is convenient since it provides a ceramic spring load assembly allowing for high temperature operation and ensuring good contact between the current collectors at the working and counter electrodes and at the same time, it provides a gas tight environment. In addition, 4 Pt lead wires can be (and were) used to eliminate any resistance associated with the lead wires and a thermocouple was placed directly next to the sample cell so that the local temperature could be read. Figure 2.12 shows a schematic drawing of the electrochemical reactor test chamber.

The electrochemical reactor was connected to a Solartron 1260 and a Solartron 1287 impedance

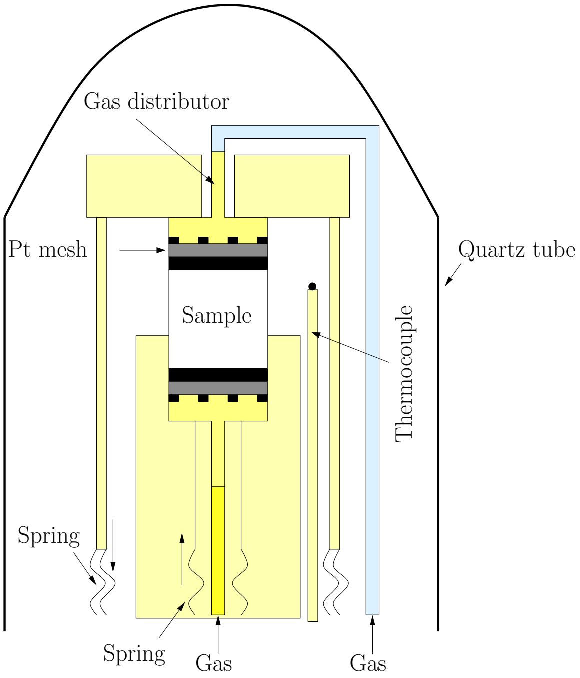

Figure 2.12: Chamber of electrochemical reactor used for electrochemical testing

analyzer/electrochemical interface. The wiring of the sample inside the electrochemical reactor was dependent on whether a symmetrical cell configuration was used or whether a 3-electrode cell configuration was used. The exact wiring for these two cells is shown in Figure 2.13. To ensure that the electrochemical reactor had a negligible contribution to the cell resistance, a sample cell of known impedance was measured at room temperature with and without the electrochemical reactor. The impedance results were identical for these two cases indicating that the lead wires of the electrochemical reactor had no influence over the cell resistance. This is expected when using the 4 wire configuration. In addition, during the measurement of the SOFC samples, the flow rates of the gases were varied to ensure that the gas flow rate had no contribution to the electrode resistance.

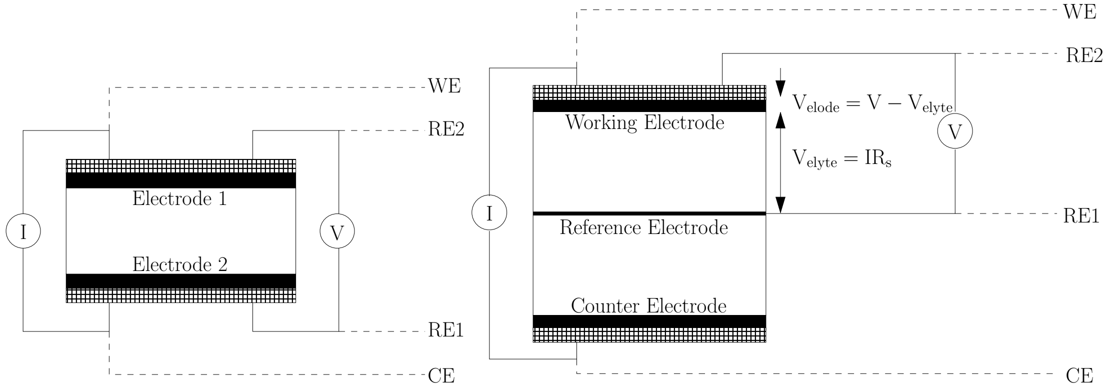

(a) (b)

Figure 2.13: Configuration of lead wires between the electrochemical reactor and the potentiostat/impedance analyzer for: (a) Symmetrical cells (b) 3-electrode cells. The symbols WE, RE1, CE, RE2 refer to the BNC ports on the Solartron 1287.

2.3.2 Reactor Artifacts

One method that can be used to help identify experimental artifacts caused by the experimental system is to ensure that the impedance data is Kramers-Kronig consistent [36]. The Kramers-Kronig relations provide a theoretical framework that, if the experimental data is Kramers-Kronig consistent, ensures that the system (i) is stable in the sense that perturbations to the system do not grow (ii) gives a linear response to a perturbation and (iii) is causal, in the sense that a response to a perturbation does not precede the perturbation.

Some experimental artifacts introduced by the system may be mistaken as physical processes.

They can, however, sometimes be detected by inconsistencies with the Kramers-Kronig relations. In the impedance of fuel cell systems, the most common type of instrumentation-based experimental artifact is an inductance behavior at high frequencies. All impedance spectra collected in this thesis had this inductance behavior, examples of which are shown in Figure 2.14.

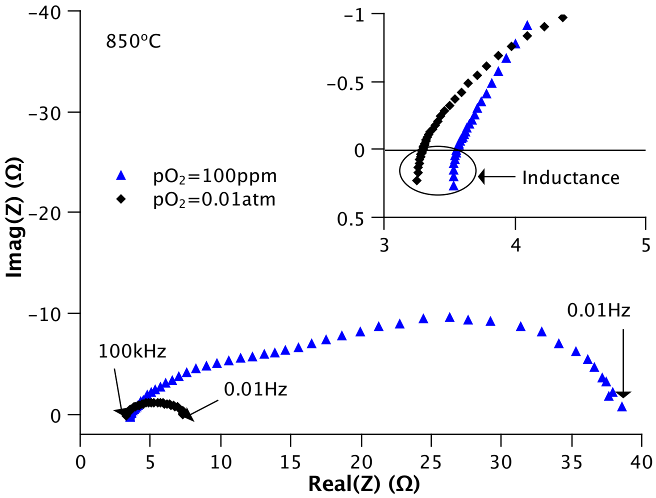

Figure 2.14: Example of inductance observed in the impedance response of LSM electrodes for two different samples in 100ppm and 0.01atm O_2 at 850°C.

The inductance shown in Figure 2.14 is not consistent with the Kramers-Kronig relations and is likely introduced by the furnace of the electrochemical system. There are a number of methods that can be used to account for this inductance behavior, such as: 1) disregard all high frequency data points showing inductance behavior 2) fit the inductance behavior to an equivalent circuit and then remove its contribution at each frequency in the experimental data. The danger of ignoring the inductance behavior is that the inductance can influence the perceived value of the serial resistance which becomes important when correcting for the iR drop in a polarization curve and so the method used within this thesis was to fit the inductance using an equivalent circuit. After accounting for the inductance behavior by fitting an equivalent circuit to the experimental data using the ZPlot software package, all impedance spectra collected were consistent with the Kramers-Kronig relations. Figure 2.15 shows examples of the impedance data for LSM electrodes measured in 100ppm and 0.01atm O_2 at 850°C along with the Kramers-Kronig relations. The good match between the experimental data and the Kramers-Kronig relations indicate that the experimental data is Kramers-Kronig consistent after removing the high frequency inductance.

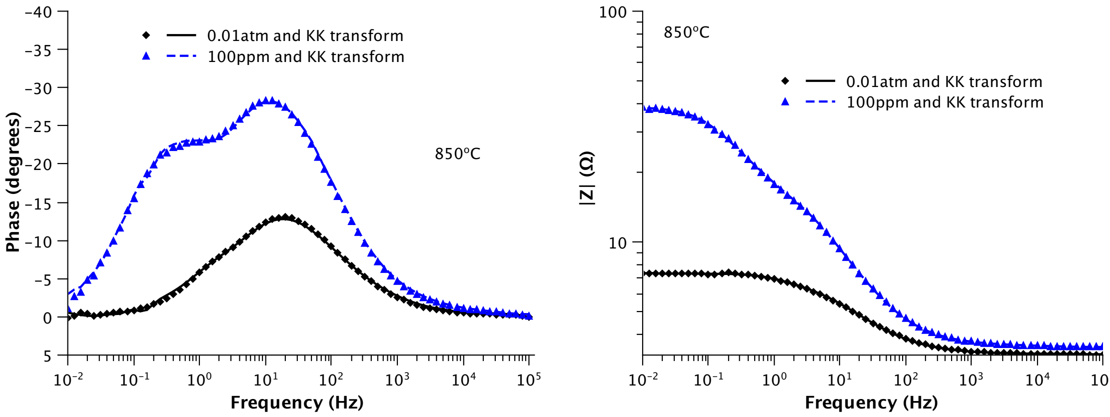

(a) (b)

Figure 2.15: (a) Phase shift and (b) Magnitude of the impedance of LSM electrodes in 100ppm and 0.01atm O_2 at $850°C$ showing the Kramers-Kronig relations. The good match between the Kramers-Kronig relations and the experimental data indicate that the data is Kramers-Kronig consistent.

2.4 Electrochemical Methods

Electrochemical methods involve applying a potential (or a current) between two electrodes and measuring the resulting current (or potential) in the cell. This can be done for a range of potentials/currents which are used to make a polarization curve. The current/potential behavior of an electrode depends on the rates of the various physico-chemical steps involved in the overall electrochemical reaction, such as the transport of oxygen (in the gas phase or solid LSM phase), the adsorption/desorption of oxygen and the charge transfer reaction. A theoretical framework which links the current/potential behavior of an electrode can then be used to evaluate the electrode kinetics. The following sections discuss electrochemical kinetic theory as well as various experimental methods that can be used to measure the current/potential relationship of an electrode.

The following topics are discussed in this section:

- Section 2.4.1 discusses basic electrochemical kinetic theory and various methods are presented which can be used to obtain electrochemical kinetic parameters.

- Section 2.4.2 discusses the various electrochemical techniques that are used to obtain and analyze the current/voltage behavior of an electrode.

2.4.1 Electrochemical Kinetic Theory

The Butler-Volmer Equation

Electrochemical reactions involve the transfer of charge from one species or phase to another species or phase and are critical to the operation of fuel cells. In theory, the difference between an elementary chemical reaction and an elementary electrochemical reaction is that for the latter, the rate constants depend exponentially on the electrode potential [37]. Also, the rate of the electrochemical reaction relates the electrode potential to the cell current. The Butler-Volmer equation, originally proposed as an empirical relation and later explained by theory, links the kinetics of the electrochemical reaction to the electrode potential/current density allowing kinetic studies to be undertaken with the knowledge of the current/voltage behavior of an electrode.

Elementary electrochemical reaction For a simple *elementary* electrochemical reaction involving reactants (R) and products (P), their associated rates of consumption/formation are given by Equation 2.3:

$$R + e^- \underset{k_b}{\overset{k_f}{\rightleftharpoons}} P$$

$$\frac{dC_R}{dt} = -k_f C_R + k_b C_P \tag{2.3}$$

The forward reaction is a reduction reaction where species R is reduced to P and the reverse reaction is an oxidation reaction. The kinetic rate constants, k_f and k_b are related to the energy barrier of the transition state by the following equations [38]:

$$k_f = A_f \exp\left(\frac{-(\Delta G^{\ominus}_{0c} + \beta nF\Delta\phi)}{RT}\right) = k^0_f \exp\left(\frac{-\beta nF\Delta\phi}{RT}\right) \tag{2.4a}$$

$$k_b = A_b \exp\left(\frac{-(\Delta G^{\ominus}_{0a} - (1-\beta) nF\Delta\phi)}{RT}\right) = k^0_b \exp\left(\frac{(1-\beta) nF\Delta\phi}{RT}\right) \tag{2.4b}$$

where the terms $\Delta G^{\ominus}_{0c}$ and $\Delta G^{\ominus}_{0a}$ are the height of the energy barrier of the transition state at equilibrium and the terms $\beta nF\Delta\phi$ and $(1-\beta)nF\Delta\phi$ represent the influence of electric potential between electrode and electrolyte on the size of the energy barrier between reactants/products and the transition state. The term β is the symmetry coefficient which represents the position of the transition state relative to the reactants and products along the reaction coordinate. β falls between 0 and 1 and is usually assumed to be equal to 0.5. k^0_f and k^0_b are the chemical components of the electrochemical rate constants.

The potential difference $\Delta\phi$ can further be split into an equilibrium potential and an overpotential (η), which represents the deviation of $\Delta\phi$ away from its equilibrium value: $\Delta\phi = \Delta\phi^{eq} + \eta$. Also, the rate of an electrochemical reaction can be converted into a current by multiplying by the factor nF so that the current associated with the forward reaction (or cathodic current) and the current associated with the reverse reaction (or anodic current) becomes:

$$i_{cathodic} = nFk^0_f C_R \exp\left(-\frac{\beta nF}{RT}\Delta\phi^{eq}\right)\exp\left(-\frac{\beta nF}{RT}\eta\right) \tag{2.5a}$$

$$i_{anodic} = nFk^0_b C_P \exp\left(\frac{(1-\beta)nF}{RT}\Delta\phi^{eq}\right)\exp\left(\frac{(1-\beta)nF}{RT}\eta\right) \tag{2.5b}$$

The net current is defined as $i = i_{anodic} - i_{cathodic}$. When the electrochemical reaction is at equilibrium, by definition $\eta = 0$ and the rate of the forward reaction equals the rate of the reverse reaction. In such circumstances, the equilibrium potential, $\Delta\phi^{eq}$, can be evaluated:

$$\Delta\phi^{eq} = \frac{RT}{nF}\ln\left(\frac{k^0_f}{k^0_b}\right) + \frac{RT}{nF}\ln\left(\frac{C^{eq}_R}{C^{eq}_P}\right) \tag{2.6}$$

Equation 2.6 is the Nernst equation. Although not necessary, for convenience we can simplify the equations by plugging Equation 2.6 into Equations 2.5a and 2.5b, which, after some algebra, results in the following expressions for the cathodic and anodic currents:

$$i_{cathodic} = \underbrace{nF(k_f^0 C_R^{eq})^{1-\beta}(k_b^0 C_P^{eq})^{\beta}}_{i_0} \frac{C_R}{C_R^{eq}} \exp\left(-\frac{\beta nF}{RT}\eta\right) \tag{2.7a}$$

$$i_{anodic} = \underbrace{nF(k_f^0 C_R^{eq})^{1-\beta}(k_b^0 C_P^{eq})^{\beta}}_{i_0} \frac{C_P}{C_P^{eq}} \exp\left(\frac{(1-\beta)nF}{RT}\eta\right) \tag{2.7b}$$

This formulation allows for a simple expression for the net current:

$$i = i_0 \left[\frac{C_P}{C_P^{eq}} \exp\left(\frac{(1-\beta)nF}{RT}\eta\right) - \frac{C_R}{C_R^{eq}} \exp\left(-\frac{\beta nF}{RT}\eta\right)\right] \tag{2.8}$$

where

$$i_0 = nF(k_f^0 C_R^{eq})^{1-\beta}(k_b^0 C_P^{eq})^{\beta} \tag{2.9}$$

In many cases, the form of the Butler-Volmer reaction is taken to be

$$i = i_0 \left[\exp\left(\frac{(1-\beta)nF}{RT}\eta\right) - \exp\left(-\frac{\beta nF}{RT}\eta\right)\right] \tag{2.10}$$

which assumes that local reactant and product concentrations do not differ much from that of the bulk [38] or that the definition of η has changed to include local concentrations of reactants and products.

Multi-step electrochemical reaction In most cases, the measured current/voltage behavior of an electrode is a combination of many processes and so the overall electrochemical reaction cannot be considered as an elementary reaction. For example, this is the case for the overall oxygen reduction reaction in SOFC cathodes, $O_2 + 4e^- \rightleftharpoons 2O^{2-}$. In such a case, it is possible to define the Butler-Volmer equation for a multi-step electrochemical reaction as:

$$i = i_0 \left[\exp\left(\frac{\alpha_a F}{RT}\eta\right) - \exp\left(-\frac{\alpha_c F}{RT}\eta\right)\right] \tag{2.11}$$

where α_a and α_c are the anodic and cathodic charge transfer coefficients and represent a lumped parameter associated with various steps of the overall reduction or oxidation reaction. It has been shown [39] that for a multi-step electrochemical reaction with a charge transfer rate determining step:

$$\alpha_a = \frac{\iota_a}{\nu} + r - r\beta \tag{2.12a}$$

$$\alpha_c = \frac{\iota_b}{\nu} + r\beta \tag{2.12b}$$

$$\alpha_a + \alpha_c = r + \frac{\iota_b + \iota_a}{\nu} = \frac{n}{\nu} \tag{2.12c}$$

where ι_a and ι_b are the number of electrons transferred before and after the rate determining step, β is the symmetry coefficient, r is the number of electrons in the rate determining step, n is the total number of electrons involved in the reaction and ν is the number of times the rate determining step occurs for one act of the overall reaction.

The Electrode Resistance

In electrochemistry, it is sometimes convenient to quantify an electrode's current/voltage behavior in terms of an electrode resistance. The total resistance of the electrode is known as the polarization resistance, R_p, and is defined by:

$$R_p = \frac{\partial \eta}{\partial i} \tag{2.13}$$

R_p can be evaluated at any point along the polarization curve. Since R_p is the total differential resistance of the overall electrochemical reaction, it is composed of the differential resistances associated with the individual processes that make up the overall reaction. It is also common to split R_p into a charge transfer resistance, R_{ct}, and a chemical resistance, R_{chem}, where:

$$R_p = R_{ct} + R_{chem} \tag{2.14}$$

The charge transfer resistance, R_{ct}, is the resistance of the elementary electrochemical reaction assuming no mass transport limitations which are accounted for by the chemical resistance, R_{chem}. The chemical resistance includes the resistance of the chemical/transport processes such as adsorption and/or gas transport.

By applying Equation 2.13 to the Butler-Volmer equation for a multi-step process, Equation 2.11, the polarization resistance can be calculated as:

$$R_p = \frac{\partial \eta}{\partial i} = \left[\frac{i_0}{RT} \left[\alpha_a F \exp\left(\frac{\alpha_a F}{RT} \eta \right) + \alpha_c F \exp\left(\frac{-\alpha_c F}{RT} \eta \right) \right] \right]^{-1} \tag{2.15}$$

and so the electrode resistance then depends on the exchange current density, i_0, as well as the charge transfer coefficients, α_a and α_c. In turn, the exchange current density can be assumed to depend on temperature through Arrhenius type kinetics in addition to the concentration of reactants and products by:

$$i_0 = i_0(C_R, T)^{ref} \lambda_{tpb} \cdot C_R^{\gamma} \exp\left(\frac{-E_a}{RT} \right) \tag{2.16}$$

where λ_{tpb} is the number of active reaction sites, known as the triple phase boundary length, γ is the reaction order which describes the dependence of i_0 or the electrode resistance on the oxygen concentration, and E_a is the activation energy, which describes the dependence of i_0 or the electrode resistance on temperature.

The electrochemical kinetic parameters, α_a, α_c, γ, E_a are related to the mechanism and the rate determining step(s) of the overall electrochemical reaction and therefore, they can be useful when evaluating the kinetics of the electrode reactions.

Determination of Electrochemical Kinetic Parameters

The electrochemical kinetic parameters, α_a, α_c, γ, E_a, along with the electrode microstructure and the material properties, determine the current/voltage behavior of the electrode (and hence the electrode resistance). They can be evaluated from the current/voltage behavior of an electrode by using the Butler-Volmer equation, Equations 2.11 and 2.16.

The Butler-Volmer equation is often linearized to simplify the analysis. In general there are two techniques that can be used: 1) low field approximation where the current/voltage behavior is analyzed at low potentials 2) high field approximation where the current/voltage behavior is analyzed at high potentials.

Low field approximation: For small values of x, the exponential e^x can be approximated as $1 + x$. Likewise, when the overpotential is sufficiently low (ie $|\eta| \ll RT/F$) then the Butler-Volmer equation can be linearized to the low field approximation:

$$i = i_0 \frac{F}{RT}(\alpha_a + \alpha_c)\eta \tag{2.17}$$

The reaction order, γ, can be obtained by combining Equations 2.16 and 2.17 at constant temperature:

$$\log i_0 = \log K - \log R_p = \gamma \log pO_2 \tag{2.18}$$

By fitting the above linear equation to experimental data of the exchange current density vs oxygen partial pressure at constant temperature conditions, the dependence of the exchange current density (or polarization resistance) on oxygen concentration, γ, can be obtained from the slope of either log i_0 vs log pO_2 or log R_p vs log pO_2. The parameter K in Equation 2.18 contains R, T, F, i_0^{ref} and the value $\alpha_a + \alpha_c$. Similarly, the activation energy of the electrode resistance can be found from the slope of a plot of $\ln i_0$ vs $1/T$ or $\ln(1/R_p)$ vs $1/T$ at constant oxygen concentrations, as shown in Equation 2.19:

$$\ln i_0 = \ln\left(\frac{1}{R_p}\right) - \ln K = \frac{-E_a}{RT} \tag{2.19}$$

High field approximation: For high values of η, one of the bracketed terms in Equation 2.11 becomes negligible and the Butler-Volmer equation can easily be linearized into the high field approximation:

$$\eta = \frac{RT}{\alpha_c F}\ln i_0 - \frac{RT}{\alpha_c F}\ln|i| \tag{2.20}$$

In this case, the charge transfer coefficient, α, can be obtained by plotting η vs $\ln|i|$. This approximation can be considered to hold whenever the contribution of the back reaction (ie, the anodic process when considering large negative overpotentials) is small compared to that of the forward reaction. The contribution of the anodic process to the total cathodic current is (assuming $\alpha_c = \alpha_a = 0.5$) [38]:

$$\exp\left(\frac{F}{RT}\eta\right) = \frac{i_{anodic}}{i_{tot}} \tag{2.21}$$

At $750°C$, if the target ratio of i_{anodic}/i_{tot} (for a cathodically polarized electrode) is to be 1% or less, then the required overpotential is $\eta \geq -400mV$ whereas if the target contribution is 5%, the required cathodic overpotential is $\eta \geq -264mV$.

While these methods can all be useful, the low field approximation is most commonly used since 1) it allows for the use of symmetrical cells which are much easier to fabricate and test compared to 3-electrode cells, but are limited to near open circuit voltage (OCV) operation 2) high overpotentials can be difficult to achieve in practice, especially in solid state electrochemistry which requires the use of thick electrolytes resulting in large iR corrections of the applied voltage 3) under high overpotentials, large gradients in species such as gas concentration may exist and so the exact local conditions are unknown. In addition, the low field approximation can be combined with impedance spectroscopy at open circuit conditions, ideally allowing for the analysis of the individual processes that make up the total electrode resistance.

2.4.2 Electrochemical Measurements

Section 2.4.1 presented a theory for the relationship between the current/potential of an electrode. Various experimental techniques are available to measure the current/potential relationship, which is the focus of the discussion below.

Figure 2.13 shows the two cell designs that have been used in this work. When using the 3-electrode configuration shown in Figure 2.13b, a voltage difference, $V_{applied}$, is applied between the working electrode and the reference electrode and the cell current, i, is measured. If the electrolyte resistance ($R_{electrolyte}$) is known, the electrode potential and resistance of the working electrode at a given current density can be calculated from:

$$V_{WE} = V_{applied} - iR_{electrolyte} \tag{2.22a}$$

$$R_p = \frac{V_{applied}}{i} - R_{electrolyte} \tag{2.22b}$$

In this way, a set of working electrode potentials and currents can be obtained, resulting in a polarization curve. In the case of symmetrical cells shown in Figure 2.13a, only the total cell potential and cell current is known. In this case, the polarization resistance of the working electrode is:

$$R_p = \frac{1}{2}\frac{V_{applied}}{i} - R_{electrolyte} \tag{2.23}$$

where the factor 1/2 comes from the fact that the cell resistance contains both the working and counter electrodes. Symmetrical cells can only be used for conditions close to equilibrium because when a cathodic cell voltage is applied, a cathodic current flows through the working electrode, forcing the reduction reaction to occur in the case of an SOFC cathode while an anodic current flows through the counter electrode forcing the oxidation reaction. At high potentials, the cathodic polarization behaves differently compared to the anodic polarization and therefore, the working electrode and counter electrodes can have different resistances. However, at low potentials, linear behavior is often observed in the cathodic and anodic polarization curves and so the working and counter electrodes have the same resistances.

There are two general classes of electrochemical measurements that can be used: 1) steady-state polarization measurements 2) transient measurements. Both of these methods can be used to collect useful current/voltage information.

Steady State Measurements

In steady state measurements, a potential (or a current) is applied and the steady state current (or potential) is measured. This technique generates a polarization curve expressing the current/potential behavior of the electrode over a wide range of potentials. Steady state measurements are typically performed on 3-electrode cells so that the potential being applied can be related to the potential of the working electrode. For these measurements, it is important to ensure that a steady state has been achieved. For the LSM electrodes measured in this thesis, it often required between 3-10hrs to achieve a steady state current after applying a potential. Figure 2.16 shows some examples of the currents that were measured after applying a steady state potential of $V_{applied} = -200mV$ for various oxygen concentrations at temperatures of $750°C$ and $800°C$. Experimental data such as that shown in Figure 2.16 was collected for a number of applied potentials at various oxygen concentrations and temperatures.

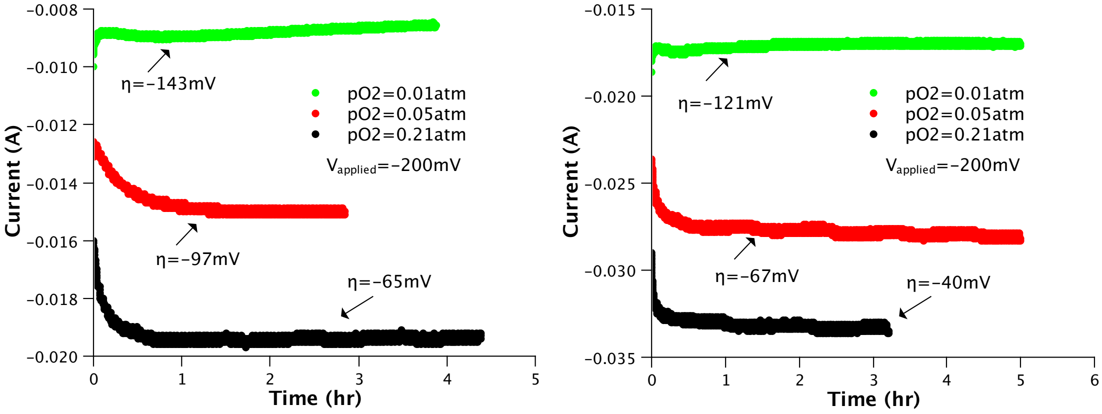

(a) (b)

Figure 2.16: Example of steady state currents measured at various oxygen concentrations from an applied cell voltage of -200mV: (a) $750°C$ (b) $800°C$

The potential of the working electrode was calculated from Equation 2.22a with the resistance of the working electrode obtained from impedance spectroscopy. From the polarization curve, the polarization resistance can be measured by using Equation 2.13, however, unless using sophisticated modelling techniques, it is not possible to obtain the resistances R_{ct} and R_{chem} (defined in Equation 2.14) from steady state measurements.

Transient Measurements

Another technique that can be used to obtain the current/potential behavior is by applying a time-dependent potential and measuring the resulting time-dependent current. Apart from the time dependence of the applied potential/measured current, transient measurements have the added complexity of a current arising from the charging/discharging of the double layer between the electrode and electrolyte. Since the double layer behaves like a capacitor, an ideal double layer current can be expressed by:

$$i_{dl} = C_{dl}\frac{d\eta}{dt} \tag{2.24}$$

where C_{dl} is the double layer capacitance. Under steady state conditions, $d\eta/dt = 0$ and so the double layer current vanishes. The total current observed during a transient electrochemical measurement is then $i_{tot} = i_{far} + i_{dl}$ where i_{far} is the Faradaic current, the name typically given to the steady state current. The two most common transient electrochemical techniques are cyclic voltammetry and electrochemical impedance spectroscopy.

Cyclic voltammetry The basic concept of cyclic voltammetry is similar to that of a steady state measurement except the potential is cycled from low to high values and back again at a specified scan rate (typically between 1 and 100mV/s). The benefit of cyclic voltammetry is that it offers some insight into the dynamics of the transport processes of species involved in the electrochemical reaction. Sometimes, as a cathodic potential is scanned from low to high values, the current density is higher than the reverse scan direction due to mass transport limitations at the reaction interface. This information can be used to help assess the kinetics of the electrochemical reaction.

Electrochemical impedance spectroscopy Electrochemical impedance spectroscopy (EIS) is the most common transient based measurement technique. In EIS, the potential applied to the cell is a frequency dependent sinusoidal potential and the current response is a sinusoidal current shifted in phase. The applied potential and resulting current density is:

$$V_{applied} = V_{applied}^{s.s.} + V_{applied}^{var}\sin(\omega t) \tag{2.25a}$$

$$i = i^{s.s.} + i^{var}\sin(\omega t + \theta) \tag{2.25b}$$

where $V_{applied}^{s.s.}$ and $i^{s.s.}$ are steady state components of the applied potential and measured current,

$V^{var}_{applied}$ and i^{var} are the amplitudes of the potential and current densities, $\omega = 2\pi f$ where f is the frequency, typically between 100kHz and 0.01Hz and θ is the phase shift between the current and applied potential. Each process of the overall electrochemical reaction responds to different frequencies so that $\theta = \theta(f)$. In addition, for slow processes, θ is large and so for ideal cases, EIS can provide information about specific processes in the overall electrochemical reaction.

Since the various processes occurring in an electrode can be represented by a resistor, an equivalent circuit can be used to equate physical processes to circuit elements such as a resistor and capacitor. The impedance of the equivalent circuit can then be calculated and the individual circuit elements can be compared directly against experimental impedance data. While many equivalent circuits can be devised, the two most prevalent circuits are shown in Figure 2.17.

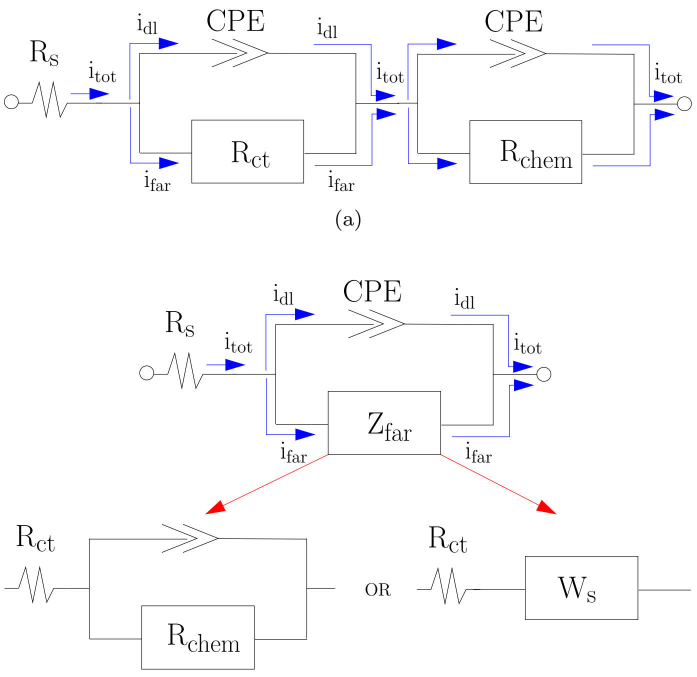

(a)

(b)

Figure 2.17: Common equivalent circuits used to model impedance response: (a) Voigt circuit (b) Randles circuit

Using the equivalent circuit, it is possible to identify the R_{ct} and R_{chem} components of R_p. In Figure 2.17, R_s is the serial resistance, which is equal to the resistance of the electrolyte, CPE is a constant phase element which is a non-ideal capacitor and Z_{far} is the Faradaic impedance. The Faradaic impedance is essentially the impedance resulting from only Faradaic processes, or, the impedance when the double layer capacitance is equal to 0. Figure 2.17 also shows how the total current is split into i_{far} and i_{dl}. While the occurrence of the Voigt circuit (Figure 2.17a) and Randles circuit (Figure 2.17b) are both common in the literature, the Randles circuit has a strong theoretical basis [40] and has been shown to be more consistent [5]. The Randles circuit was used for all equivalent circuit fitting in this thesis.

Figure 2.18 shows an example of an impedance response simulated using the Randles circuit shown in Figure 2.17a with Z_{far} equalling the R|CPE elements in parallel, for various values of the double layer capacitance. The main advantage of EIS over other electrochemical methods is that it can separate R_p into its two main components, R_{ct} and R_{chem}. By setting the value of $C_{dl} = 0$ using the equivalent circuits, it is also possible to simulate the Faradaic impedance, shown in Figure 2.18. The Faradaic impedance is the most important component of the total impedance because it contains information about the physico-chemical processes. Figure 2.18a is known as a Nyquist plot which shows the real and imaginary components of the impedance at each frequency and Figure 2.18b is a Bode plot showing the phase shift between the potential and current. For large values of C_{dl}, i_{dl} is also large and so the Faradaic impedance, resulting from, i_{far}, is much smaller than i_{dl}. The resulting effect is evident from the Bode plot in Figure 2.18b which shows that the double layer current masks the Faradaic impedance.

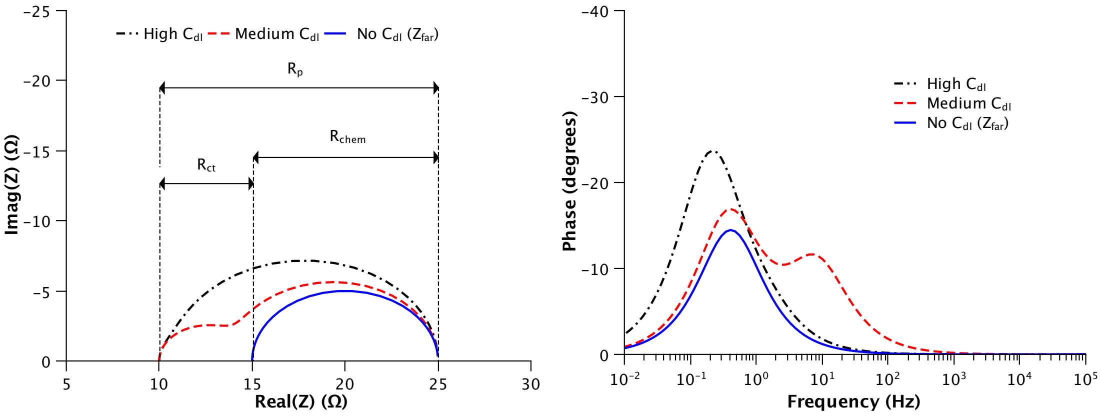

(a) (b)

Figure 2.18: Example impedance response calculated from Randles circuit for $R_s = 10\Omega$, $R_{ct} = 5\Omega$, $R_{chem} = 10\Omega$, $C_{chem} = 0.05F$ and variable C_{dl} : (a) Nyquist plot (b) Bode plot

While electrochemical impedance spectroscopy can be a powerful technique, a number of issues may arise: 1) the choice of the equivalent circuit influences the breakdown of R_p into its individual components 2) many equivalent circuits can fit the same experimental data 3) modelling the complex phyisico-chemical processes occurring within an electrode with an equivalent circuit is a simplification of reality 4) high values of the double layer capacitance can hide the true Faradaic impedance.

2.4.3 Section Summary

In the above section, electrochemical kinetic theory and experimental electrochemical methods that are used throughout this thesis were discussed. A theoretical framework linking the current/potential of an electrode was presented and resulted in the Butler-Volmer equation. Techniques to calculate electrochemical kinetic parameters such as the reaction order, γ, the activation energy, E_a and the charge transfer coefficients, α_a, α_c were presented.

The electrochemical methods used throughout this thesis were also introduced as well as techniques that can be used to obtain the total electrode resistance, R_p and the components that make up the total resistance, the charge transfer resistance, R_{ct}, and the chemical resistance, R_{chem}. R_{ct} represents the resistance of the elementary electrochemical reaction without mass transfer contributions while R_{chem} represents the resistance of the chemical and transport processes. The concept of the Faradaic impedance, Z_{far} was also introduced and will be encountered later in this thesis.

2.5 Summary/Conclusion

The successful evaluation of SOFC electrodes requires a combination of a number of fields including: 1) the ability to fabricate reproducible electrodes that have geometries suitable for electrochemical testing 2) the fabrication of a suitable electrochemical reactor that can operate at high temperatures and does not affect the measurements 3) knowledge of electrochemical methods used to characterize the electrodes. Each of these can affect the collection of reliable experimental data and may result in experimental artifacts that could be confused with real electrode processes.

To minimize the experimental artifacts and variation within electrode testing, a ceramics processing technique has been developed to make 3-electrode and symmetrical cells and it was found that a pellet type 3-electrode geometry was a better 3-electrode design than a planar type 3-electrode geometry. In addition, a method was developed to deposit electrodes of various controlled thicknesses onto both 3-electrode and symmetrical cells. Imaging and numerical techniques to characterize the electrode microstructure were also developed.

The electrochemical reactor used throughout this thesis was the commercially available ProboStat reactor which minimizes the influence of the reactor on the experimental measurement. In addition, a theory was presented which allowed for the kinetic analysis of electrodes based on their current/voltage behavior.

References

[1] J. Winkler, P. V. Hendriksen, N. Bonanos, and M. Mogensen. Geometric requirements of solid electrolyte cells with a reference electrode. *Journal of the Electrochemical Society*, 145:1184–1192, 1998.

[2] M. Ostergard, C. Clausen, C. Bagger, and M. Mogensen. Manganite-Zirconia Composite Cathodes for SOFC: Influence of Structure and Composition. *Electrochimica Acta*, 40(12):1971–1981, 1995.

[3] S. McIntosh, S.B. Adler, J.M. Vohs, and R.J. Gorte. Effect of Polarization on and Implications for Characterization of LSM-YSZ Composite Cathodes. *Electrochemical and Solid State Letters*, 7(5):A111–A114, 2004.

[4] G.J. La O', R.F. Savinell, and Y. Shao-Horn. Activity Enhancement of Dense Strontium-Doped Lanthanum Manganite Thin Films under Cathodic Polarization: A Combined AES and XPS Study. *Journal of the Electrochemical Society*, 156(6):B771–B781, 2009.

[5] J.R. Smith, A. Chen, D. Gostovic, D. Hickey, D. Kundinger, K.L. Duncan, R.T. DeHoff, K.S. Jones, and E.D. Wachsman. Evaluation of the relationship between cathode microstructure and electrochemical behavior for SOFCs. *Solid State Ionics*, 180:90–98, 2009.

[6] M. Nagata, Y. Itoh, and H. Iwahara. Dependence of observed overvoltages on the positioning of the reference electrode on the solid electrolyte. *Solid State Ionics*, 67:215–224, 1994.

[7] F.H. van Heuveln. *Characterization of porous cathodes for application in solid oxide fuel cells.* PhD thesis, University of Twente, 1997.

[8] S.B. Adler, B.T. Henderson, M.A. Wilson, D.M. Taylor, and R.E. Richards. Reference electrode placement and seals in electrochemical oxygen generators. *Solid State Ionics*, 134:35–42, 2000.

[9] A. Hashibon, S. Raz, and I. Riess. Preferred position for the reference electrode in solid state electrochemistry. *Solid State Ionics*, 149:167–176, 2002.

[10] S.B. Adler. Reference Electrode Placement in Thin Solid Electrolytes. *Journal of the Electrochemical Society*, 149(5):E166–E172, 2002.

[11] W. He and T.V. Nguyen. Edge Effects on Reference Electrode Measurements in PEM Fuel Cells. *Journal of the Electrochemical Society*, 151(2):A185–A195, 2004.

[12] Max Cimenti, Anne Co, Viola Birss, and Josepine Hill. Distortions in Electrochemical Impedance Spectroscopy Measurements Using 3-Electrode Methods in SOFC. I - Effect of Cell Geometry. *Fuel Cells*, (5):364–376, 2007.

[13] Max Cimenti, Viola Birss, and Joesphine Hill. Distortions in Electrochemical Impedance Spectroscopy Measurements Using 3-Electrode Methods in SOFC. II - Effect of Eletrode Activity and Relaxation Times. *Fuel Cells*, (5):377–391, 2007.

[14] T. Armstrong and A. Virkar. Performance of Solid Oxide Fuel Cells with $LSGM - LSM$ Composite Cathodes. *Journal of the Electrochemical Society*, 149(12):A1565–A1571, 2002.

[15] X.J. Chen, K.A. Khor, and S.H. Chan. Electrochemical behaviour of La(Sr)MnO3 electrode under cathodic and anodic polarization. *Solid Stat Ionics*, 167:379–387, 2004.

[16] A.C. Co and V. Birss. Mechanistic Analysis of the Oxygen Reduction Reaction at $(La, Sr)MnO_3$ Cathode in Solid Oxide Fuel Cells. *Journal of Physical Chemistry B*, 110:11299–11309, 2006.

[17] N. Christiansen, J. Hansen, H. Holm-Larsen, S. Linderoth, P. Larsen, P. Hendriksen, and M. Mogensen. Solid oxide fuel cell development at Topsoe Fuel Cell and Riso. *Fuel Cells Bulletin*, 8:12–15, 2006.

[18] A. Esquirol, N. Brandon, J. Kilner, and M. Mogensen. Electrochemical Characterization of $La_{0.6}Sr_{0.4}Co_{0.2}Fe_{0.8}O_3$ Cathodes for Intermediate-Temperature SOFCs. *Journal of the Electrochemical Society*, 151(11):A1847–A1855, 2004.

[19] Ben Kenney, Mikelis Valdmanis, Craig Baker, J.G. Pharoah, and Kunal Karan. Computation of TPB length, surface area and pore size from numerical reconstruction of composite solid oxide fuel cell electrodes. *Journal of Power Sources*, 128(2):1051–1059, 2009.

[20] J. Mizusaki, H. Tagawa, K. Tsuneyoshi, and A. Sawata. Reaction Kinetics and Microstructure of the Solid Oxide Fuel Cells Air Electrode $La_{0.6}Ca_{0.4}MnO_3/YSZ$. *Journal of the Electrochemical Society*, 138(7):1867–1873, 1991.

[21] F.H. van Heuveln, H.J.M. Bouwmeester, and F.P.F. van Berkel. Electrode Properties of Sr-Doped $LaMnO_3$ on Yttria-Stabilized Zirconia: I. Three-Phase Boundary Area. *Journal of the Electrochemical Society*, 144(1):126–133, 1997.

[22] X.J. Chen, S.H. Chan, and K.A. Khor. Simulation of a composite cathode in solid oxide fuel cells. *Electrochimica Acta*, 49:1851–1861, 2004.

[23] Yusuke Sakamoto, Naoki Shikazono, and Nobuhide Kasagi. Effects of electrode microstructure on polarization characteristics of SOFC anodes. In *Sixth International Fuel Cell Science, Engineering and Technology Conference*, June 16-18 2008.

[24] James R. Wilson, Worawarit Kobsiriphat, Roberto Mendoza, Hsun-Yi Chen, Jon M. Hiller, Dean J. Miller, Katsuyo Thornton, Peter W. Voorhees, Stuart B. Adler, and Scott A. Barnett. Three-dimensional reconstruction of a solid-oxide fuel cell anode. *Nature*, 5:541–544, 2006.

[25] P. Costamagna, P. Costa, and V. Antonucci. Micro-modelling of solid oxide fuel cell electrodes. *Electrochimica Acta*, 43(3-4):375–394, 1998.

[26] S. Sunde. Simulations of composite electrodes in fuel cells. *Journal of Electroceramics*, 5:2:153–182, 2000.

[27] S.H. Chan, X.J. Chen, and K.A. Khor. Cathode micromodel of solid oxide fuel cell. *Journal of the Electrochemical Society*, 151(1):A164–A172, 2004.

[28] B. Kenney and K. Karan. Impact of Nonuniform Potential in SOFC Composite Cathodes on the Determination of Electrochemical Kinetic Parameters: A Numerical Analysis. *Journal of the Electrochemical Society*, 153(6):A1172–A1180, 2006.

[29] B. Kenney and K. Karan. Engineering of microstructure and design of a planar porous composite SOFC cathode: A numerical analysis. *Solid State Ionics*, 178:297–306, 2007.

[30] L. Schneider, C. Martin, Y. Bultel, L. Dessemond, and D. Bouvard. Percolation effects in functionally graded SOFC electrodes. *Electrochimica Acta*, 52(9):3190–3198, 2007.

[31] Joshua Golbert, Claire S. Adjiman, and Nigel P. Brandon. Microstructural Modeling of Solid Oxide Fuel Cell Anodes. *Industrial & Engineering Chemistry Research*, 47:7693–7699, 2008.

[32] Andrew S. Martinez and Jacob Brouwer. Percolation modeling investigation of TPB formation in a solid oxide fuel cell electrode-electrolyte interface. *Electrochimica Acta*, 53:3597–3609, 2008.

[33] Abbaspour Ali, X. Wen, K. Nandakumar, Jingli Luo, and Karl T. Chuang. Geometrical modeling of microstructure of solid oxide fuel cell composite electrodes. *Journal of Power Sources*, 185(2):961–966, 2008.

[34] R. Ganeshananthan and Anil Virkar. Measurement of transport properties of perovskite cathodes. In *Solid Oxide Fuel Cells IX (SOFC-IX)*, volume 2, pages 1487–1498. The Electrochemical Society, 2005.

[35] A. Svensson, S. Sunde, and K. Nisancioglu. Mathematical modeling of oxygen exchange and transport in air-perovskite-YSZ interface regions. 1. Reduction of intermediately adsorbed oxygen. *Journal of the Electrochemical Society*, 144(8):2719–2732, 1997.

[36] Mark E. Orazem and Bernard Tribollet. *Electrochemical Impedance Spectroscopy.* Wiley, 2008.

[37] J. Bockris and S. Srinivasan. *Fuel Cells: Their Electrochemistry.* McGraw-Hill Book Company, 1969.

[38] A.J. Bard and L.R. Faulkner. *Electrochemical Methods: Fundamentals and Applications.* John Wiley and Sons, 2 edition, 2001.

[39] J. Bockris and A.K.N. Reddy. *Modern Electrochemistry : An Introduction to an Interdisciplinary Area.* Plenum US, 1973.

[40] Evgenij Barsoukov and J. Ross Macdonald. *Impedance Spectroscopy: Theory, Experiment and Applications.* Wiley-Interscience, 2 edition, 2005.

Chapter 3

Experimental Evaluation of Porous LSM Cathodes

3.1 Introduction

Owing to their mechanical stability and compatibility with YSZ electrolytes $(Y_2O_3)_{0.08}(ZrO_2)_{0.92}$, LSM cathodes $(La_{1-x}Sr_xMnO_{3\pm\delta})$ are currently the state-of-the-art cathode in SOFC systems [1]. However, LSM-based cathodes are known to contribute significantly towards the overall efficiency loss of hydrogen-fuelled solid oxide fuel cells [1]. For this reason, the underlying processes leading to the polarization of LSM cathodes have been extensively studied [2–15]. It is commonly assumed that the oxygen reduction process occurs by the following sequence of steps - oxygen is transported through the porous electrode in the form of gas species, adsorbed surface species or as oxygen species incorporated into the LSM lattice, before the oxygen atom is incorporated as O^{2-} species into the electrolyte. In addition to these transport processes, a number of chemical processes are thought to occur such as oxygen adsorption onto the LSM surface and various electrochemical reactions. Despite these studies, the mechanism and rate determining step(s) of the oxygen reduction reaction for the LSM/YSZ system is still not clear and many studies have reported conflicting results.

Some possible explanations for the disagreement were given in Section 1.4.1 of Chapter 1 and include aspects such as the extreme sensitivity of LSM electrodes to operating history, processing conditions and the presence of experimental artifacts in solid state electrochemistry. In addition, the nature of the oxygen nonstoichiometry, which changes with pO_2, likely plays an important role in determining the LSM behavior [16].

In this work, the kinetics of the oxygen reduction reaction for the LSM/YSZ system is assessed using electrochemical techniques over a pO_2 region where LSM is considered to be stoichiometric in terms of its oxygen deficiency as well as superstoichiometric, that is, where there is an oxygen excess in the LSM lattice. The oxygen excess is thought to be balanced by cation vacancies [17] which may become mobile with the passage of net current [4], however, little electrochemical data is available for LSM cathodes in conditions where oxygen in the lattice is stoichiometric. In this Chapter:

- Section 3.2 discusses the development of an experimental protocol used to control the electrical history of LSM electrodes when measuring the polarization behavior.
- Section 3.3 discusses the electrochemical analysis of experimental data measured under open circuit conditions and under polarized conditions. In this section a comparison is made between the behavior of LSM electrodes before and after polarization for conditions where oxygen is stoichiometric and superstoichiometric, or in low oxygen partial pressures ($10^{-4}atm \leq pO_2 \leq 10^{-3}atm$) and high oxygen partial pressures ($0.01atm \leq pO_2 \leq 0.21atm$), respectively.

3.2 Experimental

Since SOFC electrodes are known to be sensitive to the operating history [1], it is important to develop a careful protocol for testing the current/voltage behavior. This section describes the preparation and fabrication of LSM electrodes as well as the experimental protocol used to measure the current/voltage relationship of porous LSM electrodes. In addition, examples of the collected experimental data are presented.

3.2.1 Sample Fabrication

A more detailed description of the fabrication process is available in Section 2.2 of Chapter 2 and only a brief description will be given here. 3-electrode and symmetrical cell geometries were constructed using $(La_{0.8}Sr_{0.2})_{0.95}MnO_{3\pm\delta}$ (Praxair, USA) cathode (LSM) and $(Y_2O_3)_{0.08}(ZrO_2)_{0.92}$

(Tosoh, USA) electrolyte (YSZ). Pellet type 3-electrode cells were fabricated by isostatically pressing YSZ powder at 200MPa, machining a groove around the center of the pellet for the Pt reference electrode and sintering at 1400°C for 5hrs. After sintering, the electrolyte was about 6mm thick and 12.2mm in diameter. The electrolyte was then polished and refired to 1400°C. For the 3-electrode geometries, the working electrode was porous LSM deposited by a wet spray technique and sintered at 1150°C for 2hrs while the counter electrode was either LSM or LSM/YSZ composite. Symmetrical cells were constructed similarly except the working and counter electrodes were the same and the electrolyte disks were uniaxially pressed and about 1mm thick after sintering. The working and counter electrodes of the 3-electrode cells and symmetrical cells were lightly painted with Pt paste (Fuel Cell Materials, Pt-l-10) to aid in current collection and to provide adhesion between the Pt mesh connected to Pt lead wires and the electrode. This Pt paste did not have an effect on the cathode resistance however, the serial resistance decreased slightly when it was applied. For each sample, the electrode thickness and microstructural information such as the porosity, pore size and triple phase boundary length estimates were obtained from scanning electron microscope cross-section images.

3.2.2 Experimental Protocol

For electrochemical characterization, the 2 or 3-electrode samples were placed in a gas tight electrochemical reactor where Pt mesh was pressed onto the working and counter electrodes using a spring-load assembly (see Figure 2.12 page 64). The working, counter and reference electrodes were exposed to the same oxygen gas composition which consisted of two sets: 1) high pO_2 conditions wherein the pO_2 was varied over a range of 0.01atm to 0.21atm and 2) low pO_2 conditions wherein the pO_2 was varied over a range of 10^{-4}atm to 10^{-3}atm. The oxygen concentrations were set either by blending air and nitrogen using mass flow controllers to control the flow rates of each gas or by supplying ultra high purity gas stored in cylinders. For each gas mixture, the pO_2 was verified using an oxygen gas sensor (Cambridge Sensotec, Rapidox 3100, UK).

A Solartron 1260/1287 potentiostat/frequency response analyzer was used for the electrochemical measurements. For both symmetrical cells and 3-electrode cells, the OCV polarization resistance was measured by electrochemical impedance spectroscopy using excitation voltages of 5mV, 10mV and 14mV rms, between frequency ranges of 100kHz and 0.01Hz and over various oxygen partial pressures.

A careful experimental routine was developed for testing the polarization behavior. For each oxygen concentration, the experimental routine for collecting polarization curves on 3-electrode samples consisted of the following:

1. To investigate any non-linear impedance behavior, the impedance at OCV was measured at a number of AC amplitudes from 5mV to 60mV rms.
2. Cyclic voltammograms were recorded between potentials of -0.6V and 0.1V using a scan rate of 10mV/s, 5mV/s and 1mV/s .
3. A set of 10 potential values between 0V and -0.6V were chosen and for each applied potential, the current was measured until a steady state was reached, which took anywhere from 1 to 10hrs to achieve for each potential.
4. Once a steady state current had been achieved, the cell impedance under applied DC bias was recorded and then the cell impedance under OCV conditions was recorded.
5. Once the final polarization measurement was complete, a second set of cyclic voltammograms were recorded using the same scan rates and potential ranges as before.
6. Before moving to the next oxygen concentration, the cell was relaxed until the impedance at OCV closely matched the impedance before starting the polarization curve. This took between 10 to 48hrs but could be accelerated by applying a small anodic bias ($\sim +50mV$).

The above procedure generally took about 72hrs to complete and was performed at temperatures of $750°C$, $800°C$ and $850°C$. A graphical representation of this experimental protocol is shown in Figure 3.1.

The experimental routine for testing symmetrical cells was somewhat less complex since they were not polarized and so were not influenced by their electrical history. The following routine was used to test symmetrical cells:

1. Samples were exposed to a certain oxygen partial pressure for 30 mins before the impedance at OCV was measured. Before moving on to the next oxygen concentration, the impedance

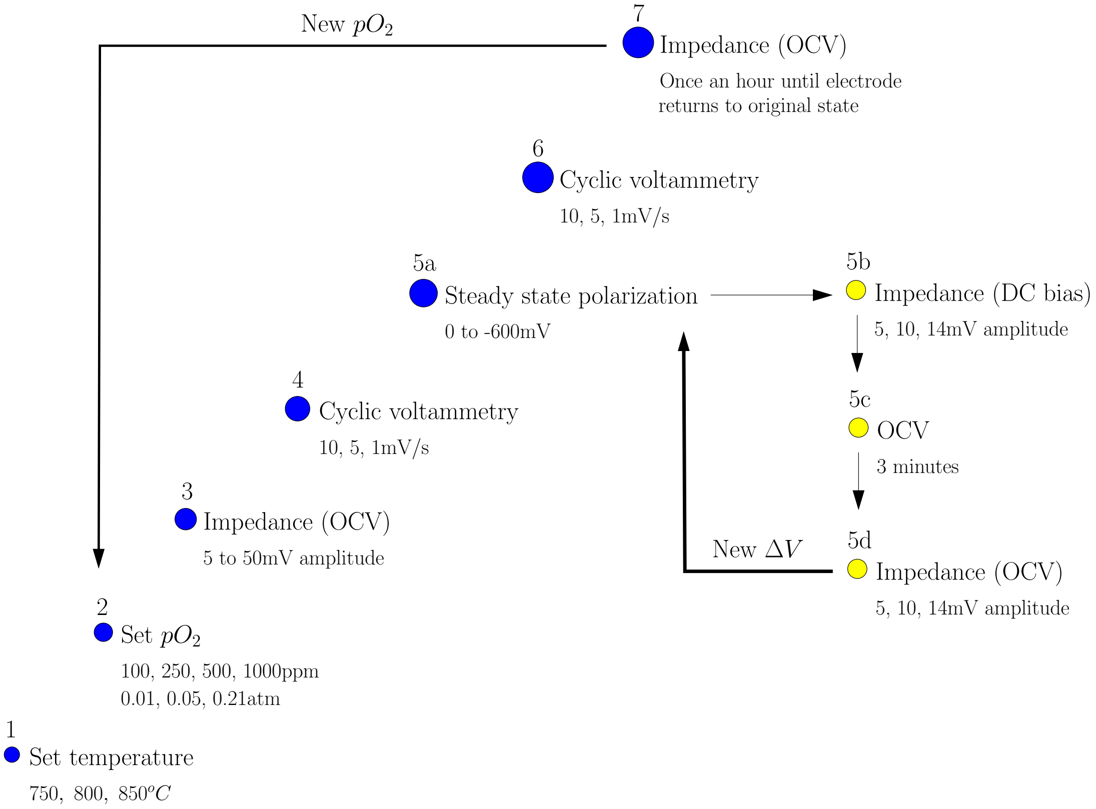

Figure 3.1: Graphical representation of experimental protocol for 3-electrode testing.

was measured again after another 30 minutes to ensure that no change in the impedance was observed.

2. Step 1 was repeated from low to high oxygen partial pressures and then the impedance at the lowest oxygen partial pressure was measured again to ensure that conditions had not changed.
3. After each oxygen concentration had been measured, the temperature was increased and Steps 1 and 2 were repeated.

3.2.3 Sample Data

The following presents examples of the data collected using the experimental routine described in Section 3.2.2.

Steady-State Polarization Behavior

Steady-state polarization behavior of electrodes are most commonly presented as a polarization curve showing the current vs voltage response of the electrode. Figure 3.2 shows some example steady state polarization curves in Tafel form ($\log|\, i \,|$ vs η) and in current-voltage format for temperatures of $750°C$ and $800°C$ and oxygen partial pressures between 10^{-4}atm and 0.21atm. Lines through the data points in Figure 3.2 are to guide the eye. These curves were obtained by applying a potential from 0 to -600mV between the working and reference electrodes, and then correcting for the ohmic contribution of the electrolyte from the following equation:

$$\eta = V_{applied} - iR_{electrolyte} \tag{3.1}$$

The resistance of the electrolyte ($R_{electrolyte}$) was obtained immediately after the steady state measurement using impedance spectroscopy. The polarization curves presented in Figure 3.2 show cathodic potentials/currents (negative potentials/currents) which drives the cathode reaction towards the formation of oxygen ions and it shows anodic potentials/currents which drives the cathode reaction towards the formation of oxygen gas. The focus of this work was on the cathodic reaction since this is the reaction important to fuel cells whereas the anodic reaction is important for electrolyzers. In addition, it is known that anodic currents tend to degrade LSM cathodes by forming micro cracks and delamination from the electrolyte [4]. This degradation was also observed in this work for high anodic currents which is why the anodic portion of the polarization curve was kept to low potentials. Within the range of applied potentials, the polarization curves exhibited limiting current behavior at pO_2s between 10^{-4}atm and 10^{-3}atm but no limiting current behavior in pO_2s of 0.01, 0.05 and 0.21atm.

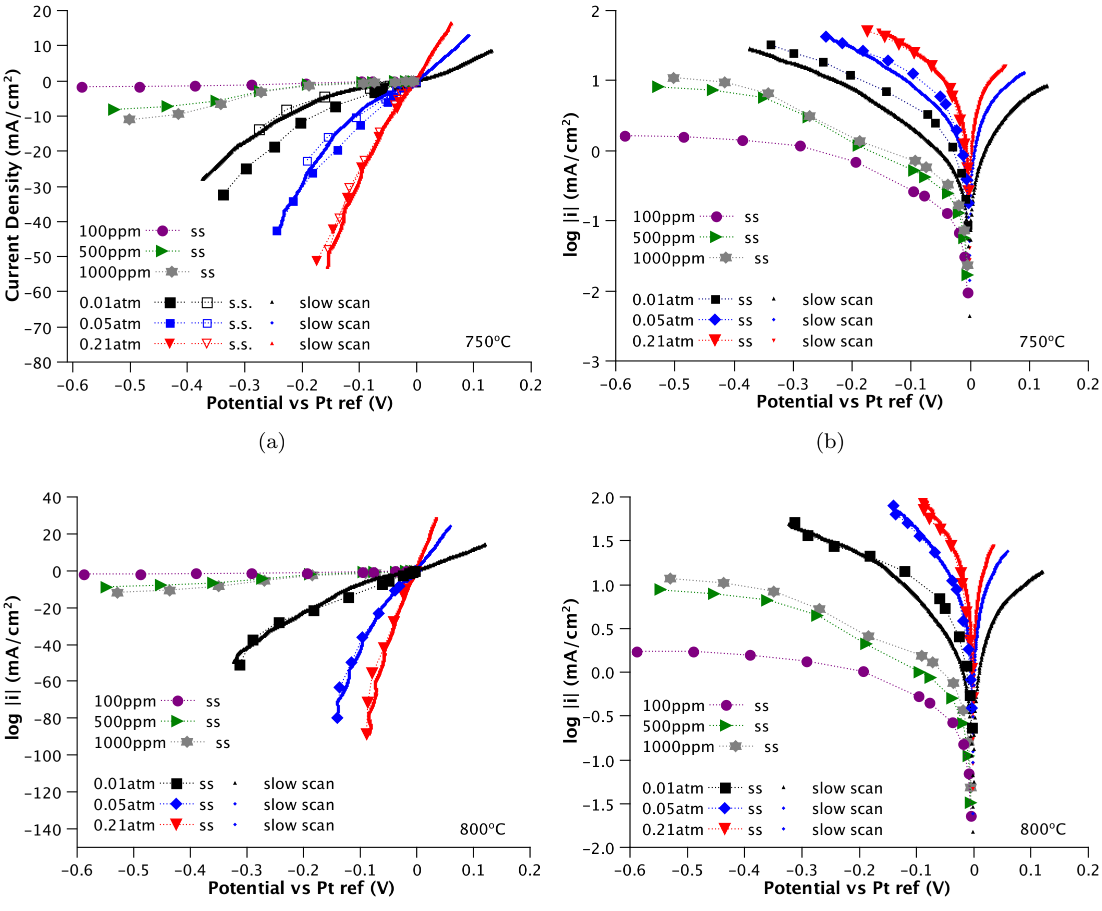

(a)

(b)

(c)

(d)

Figure 3.2: Sample polarization curves at 750 and 800°C and pO_2s between 10^{-4}atm and 0.21atm: (a)-(c) Current-voltage curve (b)-(d) Tafel plots. Dotted lines connecting the steady state data points are to guide the eye. Slow scan refers to a 1mV/s cathodic scan rate.

Cyclic Voltammetry

In cyclic voltammetry (CV), the potential is cycled between two limits at a given scan rate (mV/s), from low potentials to high potentials and then back again. Differences in the CV response with respect to scan rate, ie. hysteresis, can indicate certain features of the electrode processes such as reactant concentration limitations. Figure 3.3 shows examples of cyclic voltammograms at $750°C$ in oxygen concentrations of 10^{-4} and 10^{-2}atm with scan rates of 10, 5, and 1mV/s recorded either before polarizing the electrode or after polarizing the electrode to -600mV. Since these CV measurements are not at steady state, they differ from steady state measurements in two aspects. During the CV measurement: 1) there is a contribution from the double layer current 2) the gradients in oxygen species may not have reached a steady state before the potential is changed.

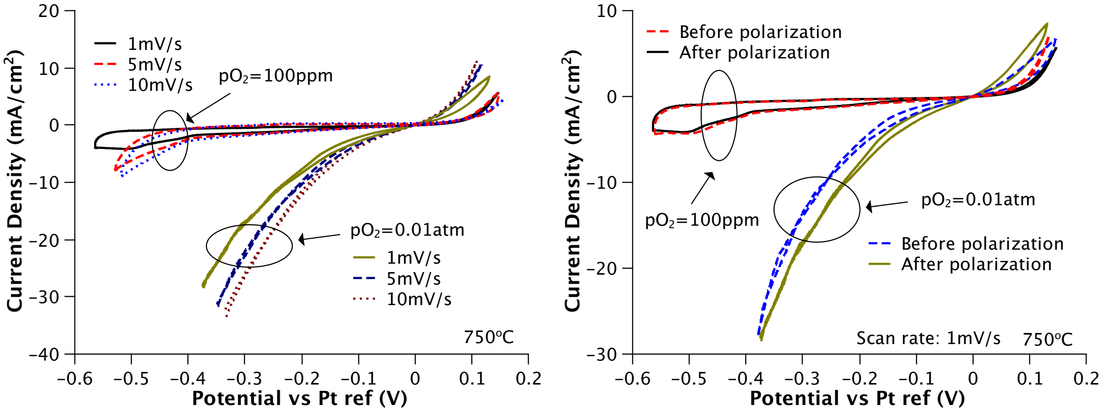

(a) (b)

Figure 3.3: Example cyclic voltammagrams at $750°C$ and pO_2s of 10^{-4}atm and 0.01atm: (a) CVs in scan rates of 10, 5 and 1mV/s after polarizing the electrode to -600mV (b) CVs in scan rates of 1mV/s before and after polarizing the electrode.

The contribution from the double layer current is apparent in Figure 3.3a where cyclic voltammograms (CVs) at different scan rates are compared. The higher currents associated with high scan rates are related to the double layer current. Mathematically, the double layer current is $i_{dl} = C_{dl}\partial\eta/\partial t$ where η is the overpotential at the electrode/electrolyte interface and C_{dl} is the double layer capacitance. As the scan rate decreases, the steady state condition is approached and the change in overpotential with respect to time is minimized resulting in $i_{dl} \rightarrow 0$. Figure 3.3b shows the difference between CVs recorded before and after polarizing the electrode. In 10^{-4}atm O_2, the CV scans are similar for the two cases however, in 0.01atm O_2, they differ at low potential. For an electrode potential of -250mV, the current is 28% larger for the CV recorded in 0.01atm O_2 after polarizing the electrode compared to the CV recorded before polarizing the electrode. This increase in current is likely caused by changes in the LSM cathode during the polarization process. In these figures there is also a significant hysteresis effect observed between forward and reverse scans in the CV measurements collected in 10^{-4}atm O_2 which is not seen in the measurements collected in 0.01atm O_2. This hysteresis effect may be caused by a depletion of reactants at the site of the electrochemical reaction which may also be the cause of the limiting currents observed in some of the steady state polarization curves.

Impedance Response

Figure 3.4 shows example impedance curves at a numbers of pO_2s, temperatures and electrode polarizations. The difference between the high and low frequency intercepts of the real impedance in the Nyquist plots in the left hand side of Figure 3.4 indicate the electrode resistance whereas the right hand side of Figure 3.4 shows the phase shift in the Bode plot which indicates the characteristic frequency of the electrode processes. As expected, the impedances are larger in low pO_2 and at low temperatures. In low oxygen concentrations (below 0.01atm), Figure 3.4b shows two clear peaks in phase shift around 0.3Hz and 6Hz. The low frequency peak that dominates at low pO_2 vanishes as the oxygen pO_2 increases, whereas the higher frequency peak decreases and shifts to slightly higher frequencies but is still visible in 0.21atm O_2. As Figure 3.4d shows, the only visible peak in 0.21atm O_2 shifts from a frequency of 6Hz to a frequency of 60Hz between temperatures of $750°C$ and $850°C$. This shift to higher frequencies also occurs when the electrode is biased with DC potential, as shown in Figure 3.4f for and LSM electrode in 0.01atm O_2 at $850°C$.

Reproducibility and Sensitivity to Gas Flow Rate

Figure 3.5 shows the reproducibility of the impedance response of 3-electrode cells at $850°C$ and OCV conditions for four different samples fabricated in identical ways. The variability in the impedance for these four samples, defined by taking the ratio of the standard deviation of the polarization

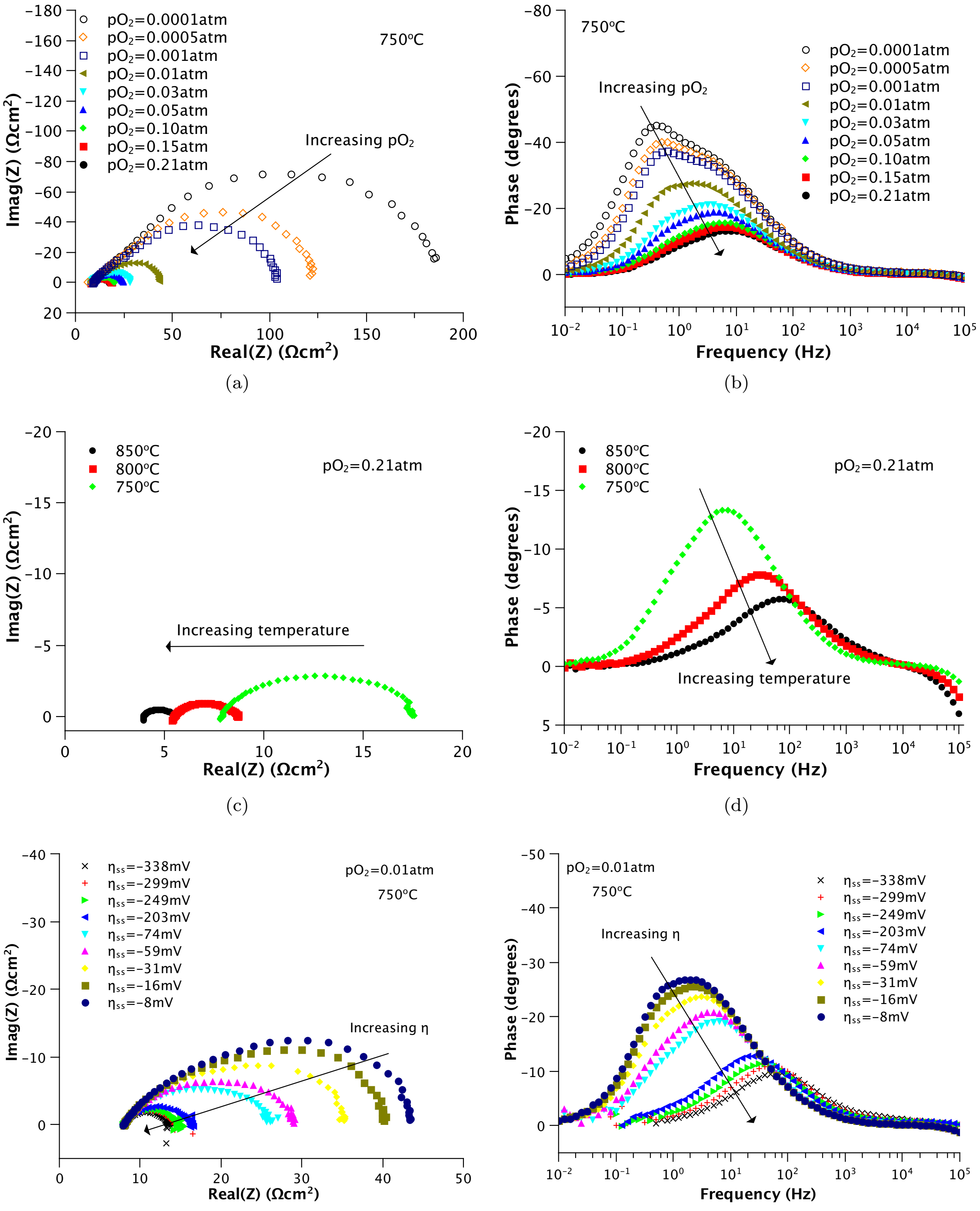

(a) (b)

(c) (d)

(e) (f)

Figure 3.4: Example impedance plots of 3-electrode cells showing: (a)-(b) Effect of increasing oxygen concentration (c)-(d) Effect of increasing temperature (e)-(f) Effect of increasing the DC bias (η_{ss}). All impedance plots given here were recorded with an AC amplitude of $\eta_{var} = 5mV$ rms.

resistance (R_p) and the average of the polarization resistances of the four samples was 11.5%. This variability can be attributed to: 1) microstructural differences during fabrication 2) differences in the reactor setup such as variations in the contact between Pt mesh and LSM electrode or thermocouple placement resulting in slight changes in the temperature of the sample 3) the electrical and/or thermal history. Due to the speed at which a symmetrical cell can be fabricated and tested, the reproducibility was mostly assessed based on impedance measurements on symmetrical cells near OCV operating conditions (ie. zero net current). For symmetrical cells, the sample to sample variability in R_p at OCV at $850°C$ was 8.8% and this increased to 9.8% at $800°C$, 14.1% at $750°C$ and 18.9% at $700°C$.

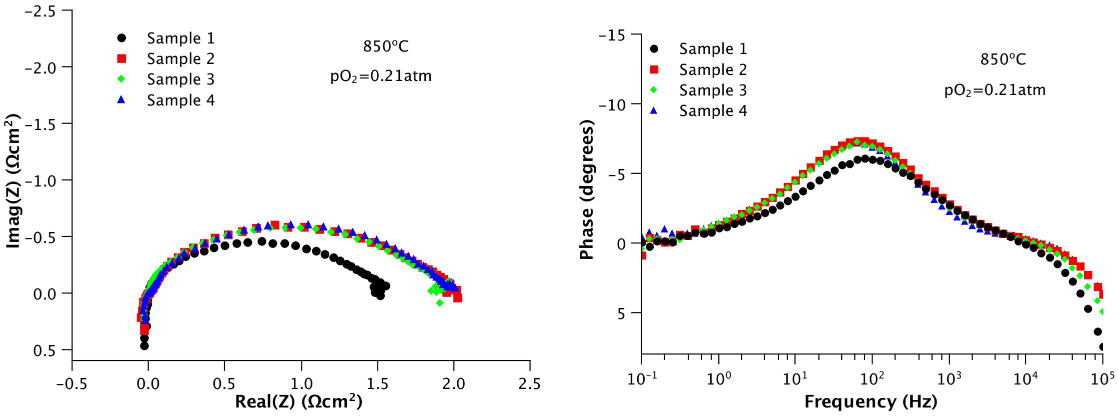

(a)

(b)

Figure 3.5: Reproducibility of impedance measured using 3-electrode cells at OCV - 11.5% variability between four samples.

Figure 3.2a also shows the reproducibility of the polarization curves between two different samples at pO_2s of 0.01atm, 0.05atm and 0.21atm. In 0.01atm O_2 at an overpotential of $\eta = -16mV$, the difference in the currents between the two samples was 41%. This difference decreased to 4% in 0.21atm O_2. In general, it was more difficult to obtain reproducible polarization curve measurements than reproducible impedance results (at OCV). This may be attributed to the influence of the electrical history of the electrode.

One factor that might influence the electrode resistance is any sensitivity to the gas flow rate. Figure 3.6 shows the impedance response at various inlet gas flow rates at $850°C$ in 0.21 atm O_2

and in 10^{-4} atm O_2. Under these conditions, the impedance measured at OCV was insensitive to the flow rate. It should be noted though that for the low pO_2 measurements, the limiting current was sensitive to gas flow rates. The minimum flow rate at which the limiting current did not change was chosen. This flow rate was 30 ml/min. For oxygen concentrations above 10^{-3}atm, the current density and impedance was insensitive to all gas flow rates tested.

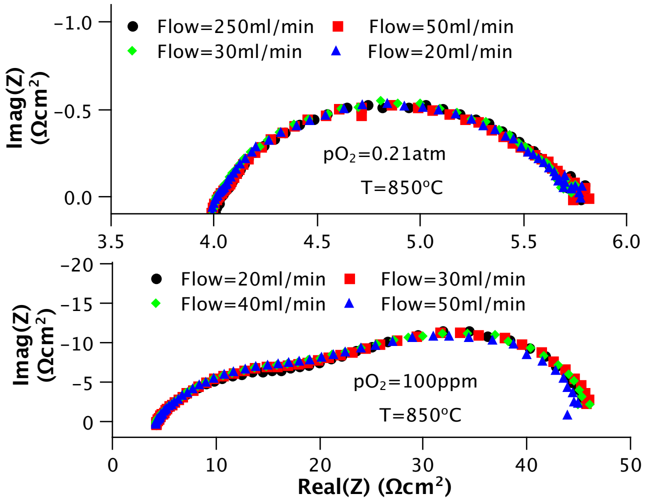

(a)

Figure 3.6: Sensitivity of impedance response at OCV to the gas flow rate at 850°C and in oxygen concentrations of 0.21atm and 10^{-4}atm.

3.3 Electrochemical Analysis

The aim of electrochemical analyses of SOFC cathodes is to determine the mechanism of oxygen reduction and also identify the specific processes that contribute to the electrode resistance. Once the mechanism and important processes are identified, then various electrode improvements may be proposed to reduce the overall electrode resistance. The primary means for elucidation of the intermediate or elementary steps of the overall oxygen reduction reaction is through the thermal activation energy (E_a) of electrode processes and the oxygen reaction order (ie. γ in $R_p \propto pO_2^{-\gamma}$). For a general reaction $A \rightarrow B$, the rate of the reaction depends on these two parameters as follows:

$$r_f = k_f^0 \exp\left(\frac{-E_a}{RT}\right)[A]^\gamma \tag{3.2}$$

The parameters E_a and γ can be related to specific steps of a mechanism. Since the rate of an electrochemical reaction can be related to the electrode potential and the current density, it can also be related to the resistance of the electrode.

In the sections that follow, reaction orders are theoretically derived by assuming individual steps in a specific reaction mechanism to be the rate determining step and activation energies of various steps in the reaction mechanism are obtained from the literature. Then, reaction orders and activation energies are determined from the experimental data and compared against those that were derived theoretically or found through other means using techniques such as isotope exchange measurements. This method can provide useful insight into the reaction processes occurring in the electrode and into the overall mechanism for oxygen reduction.

In the following sections, the theory of electrochemical analysis is presented and applied to the experimental data. The analysis is split into three categories:

- Section 3.3.1 provides an overview of the electrochemical analysis theory which was given in more detail in Section 2.4 (page 67) of Chapter 2. A theoretical framework is also presented allowing for the identification of certain processes based on the reaction order and charge transfer coefficients.
- Section 3.3.2 presents the analysis of experimental data before polarizing the electrode, near open circuit conditions, where species gradients are expected to be low.
- Section 3.3.3 presents the analysis of experimental data of polarized electrodes where gradients may be large.

3.3.1 Theory

Determination of Kinetic Parameters

The determination of electrochemical kinetic parameters was discussed in detail in Section 2.4.1 (page 68) of Chapter 2 and will only briefly be discussed here.

The rate of an overall electrochemical reaction is related to the current/potential of the electrode by the Butler-Volmer equation:

$$i = i_0 \left[\exp\left(\frac{\alpha_a F}{RT} \eta \right) - \exp\left(-\frac{\alpha_c F}{RT} \eta \right) \right] \tag{3.3}$$

where α_a and α_c are the charge transfer coefficients and i_0 is the exchange current density, described by:

$$i_0 = i_0(pO_2, T)^{ref} \lambda_{tpb} \cdot pO_2^{\gamma} \exp\left(\frac{-E_a}{RT} \right) \tag{3.4}$$

The parameters γ and E_a are the same parameters appearing in Equation 3.2 except in the case of an electrochemical reaction, they can be determined from the resistance of the overall reaction. The electrochemical kinetic parameters: α_a and α_c, γ and E_a can be related to specific processes of the overall oxygen reduction reaction. Experimentally, they can be determined by linearizing the Butler-Volmer equation into two regimes: 1) low overpotentials 2) high overpotentials.

For low potentials ($\mid \eta \mid \ll RT/F$), a plot of $\log R_p$ vs $\log pO_2$ at constant temperature should result in a straight line with the slope equal to $-\gamma$. In addition, a plot of $\ln(1/R_p)$ vs $1/T$ should result in a straight line with the slope equal to $-E_a/R$ (where R in this case is the gas constant). At high cathodic potentials ($\mid \eta \mid \gg RT/F$), a plot of η vs $\ln \mid i \mid$ should result in a straight line with slope equal to $RT/\alpha_c/F$.

The electrode polarization resistance, R_p, can be determined from steady state measurements using the relationship $R_p = \partial\eta/\partial i$ or from impedance spectroscopy. Using impedance spectroscopy, R_p can be further broken into the charge transfer resistance, R_{ct}, and the chemical resistance, R_{chem}, where R_{ct} is the resistance to the elementary electrochemical reaction and R_{chem} is the resistance of the various chemical and transport processes such as adsorption and gas transport. The parameters γ and E_a can then be determined for R_p, R_{ct} and R_{chem}.

Interpretation of Impedance Data

The interpretation of impedance data was explained in detail in Section 2.4.2 (page 77) of Chapter 2 and so will only briefly be discussed here.

Electrochemical impedance spectroscopy (EIS) is a common technique used to find the electrochemical kinetic parameters such as γ and E_a because it can be used to determine these parameters for each of the resistances R_p, R_{ct} and R_{chem}. EIS data is commonly interpreted using an equivalent circuit that represents the electrode processes in terms of pure resistors and capacitors which can then be fit to experimental data. Physical processes such as the charge transport through the electrolyte or resistance to a chemical or electro-chemical reaction are represented by these various circuit elements configured in series and/or parallel.

The Randles circuit, shown in Figure 2.17b (page 78) is considered to be the most theoretically sound equivalent circuit for electrode processes that involve charge transfer and chemical/diffusion processes [18]. An alternative circuit is the Voigt circuit, which is not necessarily physically meaningful [18] but is used because it tends to provide good fits to the experimental data. The Randles circuit was used for all equivalent circuit fitting in this work.

In the Randles circuit, R_s is a serial resistance which is mostly composed of the bulk electrolyte resistance, available at high frequencies where electrode processes are "short-circuited" by the double layer capacitance, R_{ct} is the resistance to the charge transfer reaction at the triple phase boundary and is related to the exchange current density, i_0, and R_{chem} is a lumped resistance that arises from distributed processes such as adsorption and surface or gas diffusion. As explained in [19], the chemical impedance can be represented by a Warburg element when diffusion processes are dominant or by a resistor in parallel with a capacitor when adsorption processes dominate, both shown in Figure 2.17b (page 78).

Identification of Reaction Steps

The electrochemical kinetic parameters γ, α_c and α_a in Equation 3.3 can be related to specific processes in the mechanism of the overall oxygen reduction reaction. In this section, their values are theoretically derived for processes within a variety of assumed mechanisms.

Although many variations to the oxygen reduction mechanism may exist, the oxygen reduction reaction must involve the transport of oxygen species to the electrode/electrolyte interface followed by subsequent incorporation into the electrolyte. The pathway may involve neutral adsorbed oxygen,

O_{ads}, or charged oxygen species such as O_{ads}^{-} or O_{ads}^{2-}. For the derivation of theoretical electrochemical kinetic parameters, we will start with a simple reaction mechanism involving dissociative oxygen adsorption, surface diffusion of adsorbed oxygen to the LSM/YSZ interface and an electrochemical reaction at the LSM/YSZ interface. This mechanism is outlined in Table 3.1.

Table 3.1: Simple oxygen reduction mechanism (Mechanism 1)

$O_2 + 2s_{ads} \rightleftharpoons 2O_{ads}$	R1.1
$O_{ads} + s_{tpb} \rightleftharpoons O_{tpb} + s_{ads}$	R1.2
$O_{tpb} + 2e^{-} \rightleftharpoons O^{2-} + s_{tpb}$	R1.3

Reaction R1.1 in Table 3.1 is a dissociative adsorption reaction where s_{ads} is a free surface site for adsorption, R1.2 is a surface diffusion represented as a quasi-reaction form where s_{tpb} is a free surface site at the *tpb* and reaction R1.3 is an electrochemical reaction at the LSM/YSZ interface. Considering these three reactions and using the laws of mass action, we can write their rates (forward rate - backwards rate) as:

$$r_1 = k_1 pO_2 N_{ads}^2 (1-\theta_{ads})^2 - k_{-1} N_{ads}^2 \theta_{ads}^2 \tag{3.5a}$$

$$r_2 = k_2 N_{ads} \theta_{ads} N_{tpb} (1-\theta_{tpb}) - k_{-2} N_{tpb} \theta_{tpb} N_{ads} (1-\theta_{ads}) \tag{3.5b}$$

$$r_3 = k_3 N_{tpb} \theta_{tpb} \exp\left(\frac{-(1-\beta)nF}{RT}\Delta E\right) - k_{-3} N_{tpb} (1-\theta_{tpb}) \exp\left(\frac{\beta nF}{RT}\Delta E\right) \tag{3.5c}$$

where k_i and k_{-i} are the forward and reverse reaction rate constants of reaction i, the adsorbate concentration is represented by the quantity $N_j\theta_j$ where j is either *ads* or *tpb* referring to the location of the adsorbate, N_j is the maximum number of adsorption sites, θ_j is the fractional coverage of adsorbates and the free surface sites are represented by $N_j(1-\theta_j)$. To simplify this analysis, we will only consider the case for low surface coverage where $\theta_j \ll 1$ such that the free surface sites can be mathematically neglected, $(1-\theta_j) \approx 1$.

Case 1 - R1.3 is rate determining: If we assume the electrochemical reaction (R1.3 in Table 3.1) to be the rate determining step of this reaction sequence, then all other steps can be assumed to be in pseudo-equilibrium, meaning $r_1 \approx 0$ and $r_2 \approx 0$ in Equations 3.5a and 3.5b. θ_{ads} and θ_{tpb} can therefore be derived:

$$\theta_{ads} = \frac{\sqrt{K_1 pO_2}}{1 + \sqrt{K_1 pO_2}} \tag{3.6}$$

$$\theta_{tpb} = \frac{K_2 \theta_{ads}}{(1 - \theta_{ads}) + K_2 \theta_{ads}} \tag{3.7}$$

where K_i is the ratio k_i/k_{-i}. By assuming low coverage (ie. $(1 - \theta) \rightarrow 1$), Equations 3.6 and 3.7 can be approximated as follows:

$$\theta_{ads} = \sqrt{K_1}\sqrt{pO_2} \tag{3.8}$$

$$\theta_{tpb} = K_2 \theta_{ads} \tag{3.9}$$

With the electrochemical reaction considered to be the slow process, the cathodic and anodic currents (after multiplying the reaction rate by $-nF$) can be written as follows:

$$i_{3c} = -nFk_3 N_{tpb} K_2 \sqrt{K_1} (pO_2)^{0.5} \exp\left(\frac{-(1-\beta)nF}{RT}\Delta E\right) \tag{3.10a}$$

$$i_{3a} = nFk_{-3} N_{tpb} \exp\left(\frac{\beta nF}{RT}\Delta E\right) \tag{3.10b}$$

By definition, the electrode potential is $\Delta E = E^{eq} + \eta$ where E^{eq} is the equilibrium potential and η is the deviation away from equilibrium potential, known as the overpotential. The equilibrium potential is defined as:

$$E^{eq}(T) = E^0(T) + \frac{RT}{nF} \ln(pO_2)^{0.5} \tag{3.11}$$

where $E^0(T)$ is a thermodynamic quantity related to $\Delta G^{\ominus}$ of the electrochemical reaction. When incorporating the definition of the electrode potential into Equation 3.10, the cathodic and anodic currents become

$$i_{3c} = -nFk_3N_{tpb}K_2\sqrt{K_1}\Upsilon(pO_2)^{0.5}(pO_2)^{(-0.5+0.5\beta)}\exp\left(\frac{-(1-\beta)nF}{RT}\eta\right) \tag{3.12a}$$

$$i_{3a} = nFk_{-3}N_{tpb}\Upsilon(pO_2)^{0.5\beta}\exp\left(\frac{\beta nF}{RT}\eta\right) \tag{3.12b}$$

where $\Upsilon = K_3^{(-1+\beta)}$ is a constant arising from the quantity $E^0(T)$.

In the development of the cathodic current (Equation 3.12a), it is evident that there are two contributions to the total pO_2 dependency: 1) a chemical contribution resulting from the oxygen adsorption reaction, $(pO_2)^{0.5}$ 2) an electrochemical contribution resulting from the equilibrium potential, $(pO_2)^{-0.5+0.5\beta}$. In addition, the charge transfer coefficients can be identified as $\alpha_c = (1-\beta)n$ and $\alpha_a = \beta n$. Assuming that the symmetry coefficient is $\beta = 0.5$, then it is clear that if Reaction 3 from Mechanism 1 is the rate determining step, the pO_2 dependency on the current is such that $i_0 \propto (pO_2)^{0.25}$ and $\alpha_c = 0.5$ and $\alpha_a = 0.5$.

Case 2 - R2.3 is rate determining: A similar approach can be used when considering other reactions to be the rate determining step as well as other mechanisms. For example, when considering Reaction 2 in Mechanism 1 to be the rate determining step, the cathodic and anodic currents are

$$i_{2c} = -nFk_2\sqrt{K_1}N_{ads}(pO_2)^{0.5} \tag{3.13a}$$

$$i_{2a} = nFk_{-2}K_3^{-1}N_{tpb}\exp\left(\frac{nF}{RT}\Delta E\right) = nFk_{-2}K_3^{-1}N_{tpb}\Upsilon(pO_2)^{0.5}\exp\left(\frac{2F}{RT}\eta\right) \tag{3.13b}$$

In this case, the cathodic current has a chemical reaction order of 0.5 and an electrochemical reaction order of 0 while the anodic current has a chemical reaction order of 0 and an electrochemical reaction order of 0.5. This analysis has been completed for a range of possible mechanisms and rate determining steps and the chemical and electrochemical reaction orders as well as charge transfer coefficients are summarized in Table 3.2.

In Table 3.2, Mechanisms 1, 2 and 4 involve dissociative oxygen adsorption and differ in the location and sequence of the charge transfer process. Mechanism 1 involves a single charge transfer

Table 3.2: Possible oxygen reduction mechanisms and associated electrochemical kinetic parameters for each step assuming that it is rate determining

Mechanism	Step	Reaction	pO_2^{chem}	pO_2^{e-chem}	α_c, α_a	$pO_2^{tot^*}$	α_c^*, α_a^*
1	1	$O_2 + 2s_{ads} \rightleftharpoons 2O_{ads}$	1	0	0, 2	1	0, 2
	2	$O_{ads} + s_{tpb} \rightleftharpoons O_{tpb} + s_{ads}$	$\frac{1}{2}$	0	0, 2	$\frac{1}{2}$	0, 2
	3	$O_{tpb} + 2e^- \rightleftharpoons O^{2-} + s_{tpb}$	$\frac{1}{2}$	$-\frac{1}{2} + \frac{1}{2}\beta_3$	$2 - 2\beta_3$, $2\beta_3$	$\frac{1}{4}$	1, 1
2	1	$O_2 + 2s_{ads} \rightleftharpoons 2O_{ads}$	1	0	0, 4	1	0, 4
	2	$O_{ads} + e^- \rightleftharpoons O^-_{ads}$	$\frac{1}{2}$	$-\frac{1}{4} + \frac{1}{4}\beta_2$	1-β_2, 1+β_2	$\frac{3}{8}$	$\frac{1}{2}$, $\frac{3}{2}$
	3	$O^-_{ads} + s_{tpb} \rightleftharpoons O^-_{tpb} + s_{ads}$	$\frac{1}{2}$	$-\frac{1}{4}$	1, 1	$\frac{1}{4}$	1, 1
	4	$O^-_{tpb} + e^- \rightleftharpoons O^{2-} + s_{tpb}$	$\frac{1}{2}$	$-\frac{1}{2} + \frac{1}{4}\beta_4$	$2 - \beta_4$, β_4	$\frac{1}{8}$	$\frac{3}{2}$, $\frac{1}{2}$
3	1	$O_2 + s_{ads,m} \rightleftharpoons O_{2ads}$	1	0	0, 4	1	0, 4
	2	$O_{2ads} + 2s_{ads} \rightleftharpoons 2O_{ads} + s_{ads,m}$	1	0	0, 4	1	0, 4
	3	$O_{ads} + s_{tpb} \rightleftharpoons O_{tpb} + s_{ads}$	$\frac{1}{2}$	0	0, 2	$\frac{1}{2}$	0, 2
	4	$O_{tpb} + 2e^- \rightleftharpoons O^{2-} + s_{tpb}$	$\frac{1}{2}$	$-\frac{1}{2} + \frac{1}{2}\beta_4$	$2 - 2\beta_4$, $2\beta_4$	$\frac{1}{4}$	1, 1
4	1	$O_2 + 2s_{ads} + 2e^- \rightleftharpoons 2O^-_{ads}$	1	$-\frac{1}{4} + \frac{1}{4}\beta_1$	$1 - \beta_1$, $2 + \beta_1$	$\frac{7}{8}$	$\frac{1}{2}$, $\frac{5}{2}$
	2	$O^-_{ads} + s_{tpb} \rightleftharpoons O^-_{tpb} + s_{ads}$	$\frac{1}{2}$	-$\frac{1}{8}$	-, 1	$\frac{3}{8}$	-, 1
	3	$O^-_{tpb} + e^- \rightleftharpoons O^{2-} + s_{tpb}$	$\frac{1}{2}$	$-\frac{3}{8} + \frac{1}{4}\beta_3$	-, 1	$\frac{1}{4}$	-, 1
5	1	$O_2 + s_{ads,m} + e^- \rightleftharpoons O^-_{2ads}$	1	$-\frac{1}{4} + \frac{1}{4}\beta_1$	$1 - \beta_1$, $3 + \beta_1$	$\frac{7}{8}$	$\frac{1}{2}$, $\frac{7}{2}$
	2	$O^-_{2ads} + 2s_{ads} + 2e^- \rightleftharpoons 2O^-_{ads} + s_{ads,m}$	1	$-\frac{1}{2} + \frac{1}{4}\beta_2$	$3 - \beta_2$, $2 + \beta_2$	$\frac{5}{8}$	$\frac{5}{2}$, $\frac{5}{2}$
	3	$O^-_{ads} + s_{tpb} \rightleftharpoons O^-_{tpb} + s_{ads}$	$\frac{1}{2}$	$-\frac{1}{4}$	1, 1	$\frac{1}{4}$	1, 1
	4	$O^-_{tpb} + e^- \rightleftharpoons O^{2-} + s_{tpb}$	$\frac{1}{2}$	$-\frac{1}{2} + \frac{1}{4}\beta_4$	$2 - \beta_4$, β_4	$\frac{1}{8}$	$\frac{3}{2}$, $\frac{1}{2}$

Notes: Derivations are for cathodic current and assuming low surface coverage so that $(1 - \theta_j) \approx 1$
Total reaction order is found by adding chemical and electro-chemical reaction orders
* Assuming $\beta = 0.5$

reaction at the LSM/YSZ interface whereas Mechanisms 2 and 4 involve a charge transfer reaction at the gas/LSM interface as well as at the LSM/YSZ interface. Mechanisms 3 and 5 involve associative adsorption followed by a dissociation step. The pO_2 dependencies are high for processes occurring earlier in the reaction sequence and range between $\gamma = 1$ for a pure adsorption process involving molecular oxygen to $\gamma = 1/8$ for an electrochemical reaction at the LSM/YSZ interface involving a single electron.

3.3.2 Analysis of Data Collected Near Open Circuit Conditions

In the following analysis, both symmetrical cells and 3-electrode cells were used to measure the electrode impedance near open circuit conditions. Symmetrical cells were tested under a pO_2 range of 0.01atm to 0.21atm O_2 in order to determine the variability between electrodes and to compare against 3-electrode measurements and 3-electrode cells were tested between 10^{-4}atm and 0.21atm O_2 which was used for kinetic analysis. Open circuit voltage (OCV) conditions refer to the operating point of the electrode where the electrode is subjected to zero DC-bias and there is no net steady state or DC current being drawn from the cell. Although fuel cells operate far from open circuit conditions, useful kinetic information can be obtained at OCV. This information includes the polarization resistance and exchange current density (at OCV) and the reaction order of the oxygen reduction reaction (γ).

Choice of Adsorption or Diffusion Controlled Equivalent Circuits

A Randles circuit, shown in Figure 2.17b (page 78) was used to fit the experimental impedance data using a least-squares minimization approach. The assumption was that the Faradaic impedance, Z_{far}, could be represented with either an adsorption process or a diffusion process. The adsorption process was modelled using the resistor and capacitor elements in parallel and the diffusion process was modelled with a Warburg element, shown in Figure 2.17b (left) and (right) respectively.

Figure 3.7 shows the differences in the fit as well as the shape of the Faradaic impedance resulting from these two assumptions when compared against an LSM electrode at $750°C$ in 0.01atm O_2. For clarity, the inductance as well as the serial resistance was subtracted from the Nyquist plots of Figure 3.7. Using the Randles circuit, the charge transfer resistance is manifested as a single point on the

Nyquist plot (highlighted in Figures 3.7a and 3.7c), while the chemical processes of the Faradaic impedance show a capacitative behavior. Assuming that a diffusion process dominates the chemical component of the Faradaic impedance, it can be represented by a Warburg element resulting in the impedance shown in Figure 3.7c. On the other hand, Figure 3.7a shows the impedance of an adsorption controlled Faradaic impedance which is a perfect semi-circle.

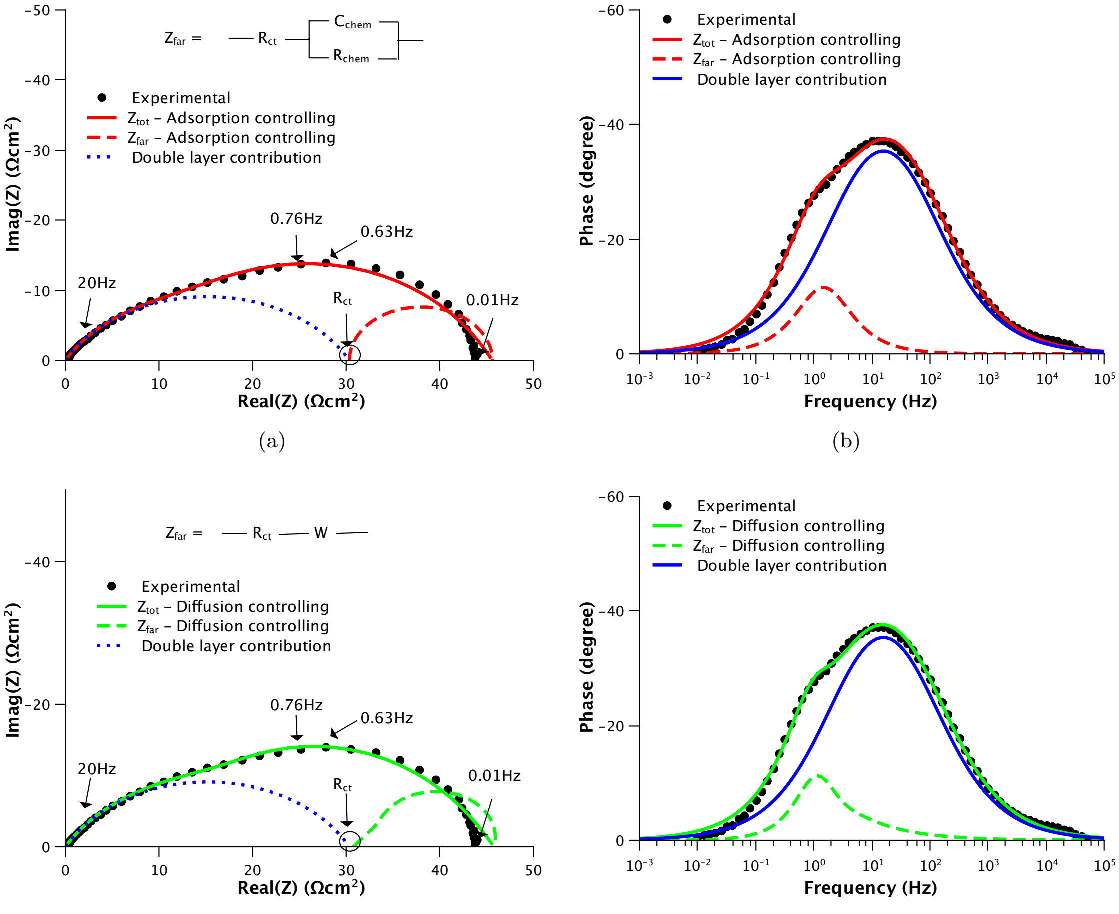

(a) (b)

(c) (d)

Figure 3.7: Symmetrical cell impedance showing differences between fitting of: (a)-(b) Adsorption behavior in the Faradaic impedance (c)-(d) Diffusion behavior in Faradaic impedance for an LSM electrode at $750°C$ in 0.01atm O_2.

Figures 3.7b and 3.7d show the phase shift vs frequency for these two different scenarios. Two peaks are observed at frequencies of 12.5Hz and 0.65Hz. By breaking down the Randles circuit into its individual components, it is evident that the large peak at 12.5Hz is the influence from the double layer capacitance whereas the low frequency peak at 0.65Hz can be attributed to the Faradaic impedance. The assumption of diffusion or adsorption controlling processes generates the same phase shift and also the same magnitude of R_{chem} under these conditions. However, at higher temperatures the adsorption controlled model proved to be a better fit than the diffusion controlled model and kinetic parameters such as the reaction order (γ) as well as the activation energies (E_a) followed clearer trends with the Faradaic impedance described by the resistor and capacitor in parallel as opposed to the Warburg element. For this reason, all further analysis was done using the Randles circuit with a resistor and constant phase element in parallel, representing an adsorption-like Faradaic impedance.

Using the Randles circuit, the charge transfer resistance R_{ct}, chemical resistance R_{chem} and polarization resistance R_p were obtained from the experimental impedance data. Figure 3.8 shows the relative contribution of the chemical resistance to the total electrode resistance (R_{chem}/R_p) for porous LSM electrodes in oxygen partial pressures between 10^{-4}atm and 0.21atm at OCV and temperatures of 750°C, 800°C and 850°C. In 10^{-4}atm O_2 at 750°C, the oxygen concentration was low enough so that 75% of the total electrode resistance came from R_{chem}. In air at 750°C, the total contribution of the chemical processes dropped to 15%. This ratio decreased to only 0.1% in air at 850°C.

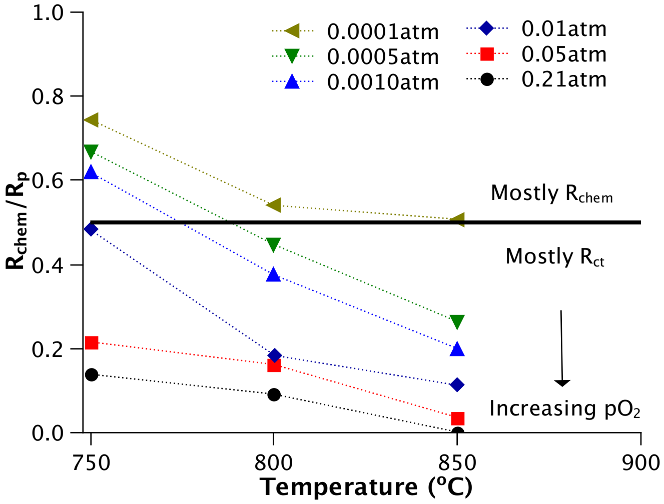

Figure 3.8: Contribution of the chemical resistance, R_{chem}, to the total polarization resistance R_p. Lines through data points are to guide the eye.

To determine which specific processes controlled the electrode resistance, a more detailed analysis of the reaction orders and activation energies of the electrode resistances as well as the electrode capacitances was performed.

Analysis of the Oxygen Reaction Order

In this section, the reaction order was determined for the electrode resistances R_{ct}, R_{chem} and R_p obtained from impedance spectroscopy near OCV conditions. The reaction order (γ) can be described by the following proportionality: $R \propto pO_2^{-\gamma}$. These reaction orders determined from experimental data were then compared to theoretically derived reaction orders for specific processes shown in Table 3.2.

As discussed in Section 2.4.1, the reaction order, γ, is determined from the slope of a plot of $\log R$ vs $\log pO_2$. This data is shown in Figure 3.9 for the components that contribute to the overall electrode resistance: 1) the charge transfer resistance, R_{ct} 2) the chemical resistance, R_{chem} and for the total electrode resistance, R_p. A least-squares fit was used to calculate the slope of the $\log R$ vs $\log pO_2$ experimental data.

The reaction orders are summarized in Table 3.3 which shows values measured using the 3-electrode configuration in oxygen concentrations between 10^{-4}atm and 10^{-3}atm and using both symmetrical cells and a 3-electrode configuration in oxygen concentrations between 0.01 and 0.21atm. The similarity of the reaction orders between symmetrical cells and 3-electrode cells indicates that the 3-electrode configuration chosen in this work was suitable to assess the cathode kinetics. For all measurements, the reaction order of the polarization resistance, R_p, fell between the reaction order of R_{ct} and that of R_{chem} and, therefore, represented a mixture of these two processes. At low pO_2s ($10^{-4}atm \leq pO_2 \leq 10^{-3}atm$), as the temperature increased from $750°C$ to $850°C$, the reaction order of the charge transfer resistance varied from 0.12 to 0.22 while at high pO_2s ($0.01atm \leq pO_2 \leq 0.21atm$), it remained relatively constant at around 0.33. On the other hand, the reaction order of R_{chem} was much more variable over the $750°C$ to $850°C$ temperature range, increasing from 0.36 to 0.81 for low pO_2s and decreasing from 0.83 to 0.58 at high pO_2s. The fact that the reaction order changes between low and high pO_2s indicates that there may be a shift in the mechanism from the low pO_2 regime and high pO_2 regime, perhaps caused by the shift in the oxygen nonstoichiometry

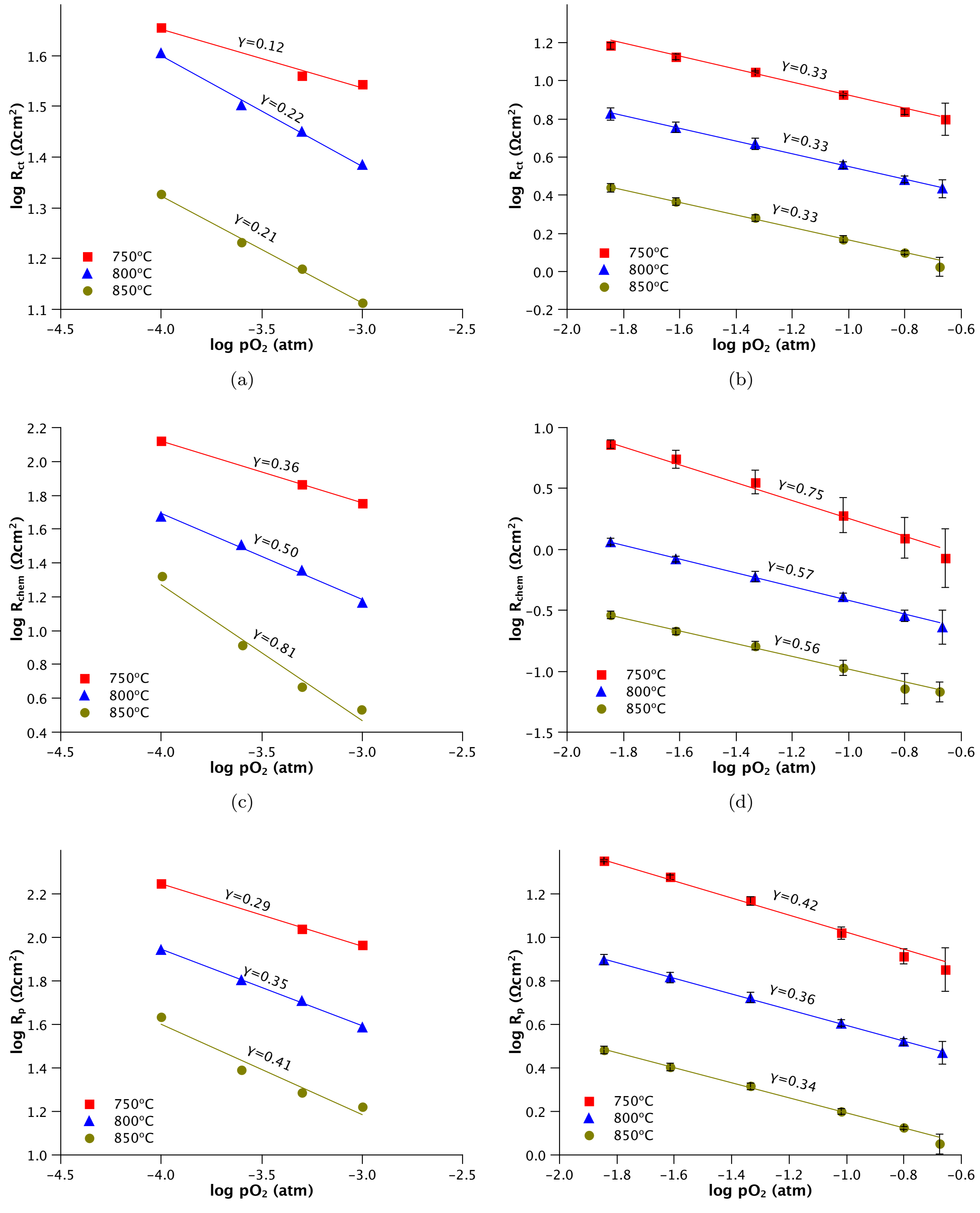

(a) (b)

(c) (d)

(e) (f)

Figure 3.9: Reaction orders (γ) of (a)-(b) R_{ct} (c)-(d) R_{chem} and (e)-(f) R_p. Figures on the left were collected in low pO_2 ($10^{-4}atm \leq pO_2 \leq 10^{-3}atm$) and figures on the right were collected in high pO_2 ($0.01atm \leq pO_2 \leq 0.21atm$). Resistances were measured from impedance spectroscopy on porous LSM electrodes at temperatures of $750°C$ to $850°C$ and pO_2s. Error bars represent the standard deviation in the measured resistance for three different samples and lines through data points represent least squares fit of linearized $R \propto pO_2^{-\gamma}$ relationship.

in the LSM lattice. A similar shift in the pO_2 dependency between low and high pO_2s has also been observed by Mitterdorfer and Gauckler [20] and was ascribed to a change in the rate determining step between surface diffusion controlled at low pO_2 and a combination of charge transfer and surface diffusion controlled at high pO_2. It should be noted though that for pO_2s above 10^{-3}atm, the LSM lattice contains an excess of oxygen which is balanced by cation vacancies whereas for pO_2s between 10^{-4}atm and 10^{-3}atm, the LSM is stoichiometric whith fewer cation vacancies. A shift in the LSM structure as pO_2 changes could cause a shift in the rate determining step or in the mechanism. Using theoretical pO_2 dependencies from Table 3.2, we can attempt to identify these controlling processes as well as the mechanism for oxygen reduction.

Table 3.3: Apparent reaction order, γ, at OCV for the charge transfer, chemical and total polarization resistance of symmetrical cells and 3-electrode cells measured by impedance spectroscopy.

pO_2 Range	Temperature	Symmetrical Cells			3-Electrode*		
	($^\circ C$)	γ (R_{ct})	γ (R_{chem})	γ (R_p)	γ (R_{ct})	γ (R_{chem})	γ (R_p)
$10^{-4} - 10^{-3}$atm	750	0.10	0.65	0.50	0.12	0.36	0.29
	800	-	-	-	0.22	0.50	0.35
	850	-	-	-	0.21	0.81	0.41
0.01-0.21atm	750	0.33	0.75	0.42	0.30	0.83	0.44
	800	0.33	0.57	0.36	0.30	0.54	0.32
	850	0.33	0.56	0.34	0.35	0.58	0.37

* Before polarization

Reaction order of R_{ct}: Assuming that the symmetry coefficient of the charge transfer reaction is $\beta = 0.5$, the reaction order for the charge transfer resistance at low pO_2s corresponds most closely with a theoretical value of 1/4, equivalent to a charge transfer process involving neutral adsorbates at the triple phase boundary, as in Step 3 of Mechanism 1 in Table 3.2. Although an exact match for the pO_2 dependency of the charge transfer resistance at high pO_2s does not exist, values in Table 3.3 correspond most closely with a theoretical value of 0.375 which is an electrochemical reaction at the gas/LSM interface involving adsorbed oxygen, for example, Step 2 of Mechanism 2 in Table 3.2. If we allow the symmetry coefficient, β, to vary between 0.4 and 0.6, the process that minimizes the absolute difference between the experimental and theoretical reaction orders is again found to be Step 2 of Mechanism 2, with $\beta = 0.4$ giving a theoretical $\gamma = 0.35$. It is then hypothesized that the mechanism of oxygen reduction shifts from one where the charge transfer reaction takes place at the LSM/YSZ interface (for low pO_2s) to a mechanism where the charge transfer reaction takes place at the gas-LSM interface (for high pO_2s).

Reaction order of R_{chem}: Compared with the charge transfer reaction, the reaction order of the chemical resistance is much more dependent on temperature. In the low pO_2 regime, the reaction order of R_{chem} increased from 0.36 to 0.81 as the temperature increased whereas in the high pO_2 regime, it fell from 0.83 to 0.58 as the temperature increased from $750°C$ to $850°C$. Table 3.2 indicates that there can be a wide variation in theoretical reaction orders, depending on the process. For example, a pure adsorption reaction, such as that of Step 1 in Mechanism 1 in Table 3.2 has $\gamma = 1$, while for an electrochemical adsorption reaction such as that of Step 1 Mechanism 4, has $\gamma = 0.875$. In addition, the surface diffusion processes can range from $\gamma = 0.5$ for neutral oxygen adsorbates to $\gamma = 0.25$ for charged oxygen adsorbates.

Low pO_2: In the low pO_2 regime, at $850°C$, the reaction order of R_{chem} was 0.81 which falls somewhere between adsorption and surface diffusion rate limiting steps whereas at $800°C$, the reaction order of R_{chem} for low pO_2s was 0.5 which matches well with a surface diffusion reaction in Mechanism 1 of Table 3.2. These processes are both related to Mechanism 1 of Table 3.2 which is also consistent with the interpretation of the reaction order for R_{ct} in low pO_2s.

High pO_2: At high pO_2s, from the analysis of the reaction order of R_{ct}, there is evidence that the oxygen species is charged and so we might expect the pO_2 dependency of a mixed-controlled process involving adsorption and diffusion of charged species to range anywhere from 0.25 to 0.875 with the two limits being pure transport of charged adsorbates and pure electrochemical adsorption. Indeed, the reaction order of R_{chem} does fall within this broad range. The drop in reaction order of the chemical process from 0.75 to 0.56 with increasing temperature might be explained by a larger relative contribution from the adsorption process at $750°C$ compared to the contribution of the diffusion process, with these dynamics shifting as the temperature is increased. This could be reflective of a higher activation energy for the diffusion process compared to the adsorption process. By taking the symmetry coefficient to range between 0.4 and 0.6, the process that matches most closely with a $\gamma = 0.75$ is an electrochemical adsorption reaction shown in Step 1 of Mechanisms 4 and 5, which for $\beta = 0.4$, results in $\gamma = 0.85$. When $\beta = 0.4$, Step 2 of Mechanism 5, an electrochemical oxygen dissociation step, gives the closest match for the reaction order of R_{chem} at $850°C$.

When comparing the reaction orders obtained experimentally to those derived in Table 3.2, there are a number of points that should be kept in mind: 1) the reaction orders derived in Table 3.2 assumed low coverage which likely holds best at low pO_2s 2) the reaction orders derived in Table 3.2 assumed a single rate determining step, however, many processes may contribute to the electrode resistance and a single rate determining step may not exist 3) alternative processes that are more difficult to account for using this type of analysis and may be viable options include the bulk diffusion of vacancies through the cathode or the possibility of a convective transport mechanism for charged oxygen adsorbates owing to the surrounding electric field.

In summary, it is likely that a shift in the mechanism occurs between low pO_2s (10^{-4}atm-10^{-3}atm) and high pO_2s (0.01atm-0.21atm). The mechanism that most closely matches the reaction order in low oxygen concentrations involves oxygen adsorption, surface diffusion of neutral adsorbates and a charge transfer step at the LSM/YSZ interface whereas the mechanism that most closely matches the pO_2 dependency in high oxygen concentrations involves surface diffusion of charged oxygen species followed by an electrochemical reaction at the LSM/YSZ interface. The nature of the adsorption reaction for high pO_2s could be either an electrochemical adsorption reaction or pure adsorption followed by an electrochemical reaction at the gas-LSM interface.

Due to the relative consistency of the reaction orders of R_{ct} with temperature, it is likely that the mechanism does not shift considerably with temperature. The variations in the reaction order of R_{chem} with temperature and with pO_2 may reflect a number of important aspects related to this analysis: 1) the various resistances can be composed of a number of different physical processes such as gas diffusion, adsorption and surface diffusion (or other types of diffusion processes such as bulk diffusion) and therefore the reaction order of R_{chem} is a combination of these processes 2) each of these processes can have different activation energies which may make some processes relatively important at a certain temperature but not important at another temperature 3) without more in-depth modelling techniques, it is difficult to account for the subtle variations that these processes can have such as various adsorption isotherms or the influence of the electric field on the transport of charged oxygen species.

Analysis of Activation Energies

As well as the reaction order, each process can have its own activation energy. An activation energy, E_a, for a reaction represents the energy barrier that must be overcome so that the reaction can transition from one state (or site) to another. The activation energy can be determined from the slopes of a plot of $\ln(1/R)$ vs $1/T$. This data is shown in Figure 3.10 for the charge transfer resistance, R_{ct}, the chemical resistance, R_{chem} and the total polarization resistance, R_p. Although the derivation of theoretical activation energies is outside the scope of this thesis, a number of activation energies can be found in the literature. Table 3.4 provides a list of activation energies available from the literature obtained for both theoretical thermodynamic calculations such as density functional theory studies as well as experimental studies using isotope exchange measurements or simple conductivity measurements. The activation energies of processes such as oxygen adsorption and surface diffusion are difficult to measure experimentally, especially on oxide materials, and so activation energies for these values must be obtained from DFT studies.

Table 3.4: Summary of activation energies and their associated processes found in the literature

Activation energy	Process	Method	Ref
0.23eV (873-1273K)	Dissociative adsorption on LSM5 oxygen vacancy	DFT	[21]
0.50eV (873-1273K)	Dissociative adsorption on $LaMnO_3$	DFT	[21]
2.0eV	Surface diffusion of O_{ads}	DFT	[22]
0.69eV	Surface diffusion of $V_{\ddot{O}}$ on $LaMnO_3$	DFT	[22]
0.88eV (773-1273K)	Bulk $V_{\ddot{O}}$ diffusion in YSZ	Experimental	This work
1.33 ± 0.2eV (873-1273K)	Surface exchange on LSM2	Experimental	[23]
2.80 ± 0.13eV (873-1273K)	Bulk $V_{\ddot{O}}$ diffusion in LSM2	Experimental	[23]

Note: LSM2 = $La_{0.8}Sr_{0.2}MnO_{3\pm\delta}$, LSM5 = $La_{0.5}Sr_{0.5}MnO_{3\pm\delta}$

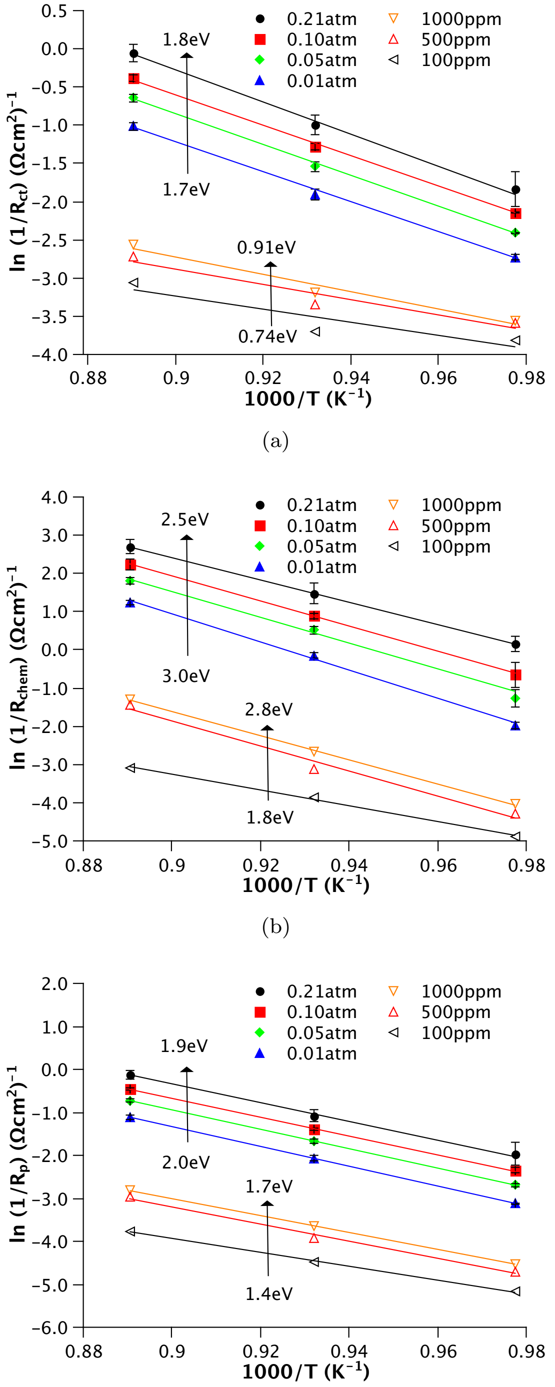

(a)

(b)

(c)

Figure 3.10: Activation energies (E_a) measured from impedance spectroscopy with porous LSM electrodes between temperatures of $750°C$ and $850°C$ and pO_2s from 10^{-4}atm to 0.21atm for (a) R_{ct} (b) R_{chem} (c) R_p. Error bars represent the standard deviation in the measured resistance for three different samples.

Figures 3.10a, 3.10b, 3.10c show the activation energies for the R_{ct} and R_{chem} components as well as for the total R_p, as a function of oxygen partial pressure. For low pO_2s, the activation energy of R_{ct} ranged from 0.74eV to 0.86eV and for high pO_2s it ranged from 1.7eV to 1.8eV. For the R_{chem} component in low pO_2s, the activation energy increased with oxygen concentration from 1.8eV to 2.8eV and decreased with oxygen concentration from 3.0eV to 2.5eV in high pO_2s. At low pO_2, the activation energy of R_{ct} was close to the activation energy of oxygen vacancy transport through the YSZ electrolyte. Since the electrochemical reaction also depends on the equilibrium surface coverage, E_a for R_{ct} may also be influenced by the activation energy for the adsorption reaction which has been calculated using DFT techniques [21] to be $\sim 0.23 - 0.5eV$. Therefore, it may be possible that the activation energy of R_{ct} represents a mixture of the activation energy for electrochemical incorporation of oxygen into the YSZ electrolyte and that of the adsorption reaction.

In comparing the activation energies of R_{chem} against those values in Table 3.4, at low pO_2s it might be thought that the chemical component is either a surface diffusion process ($E_a \approx 2eV$) or the diffusion of oxygen vacancies ($V_{\ddot{O}}$) through the bulk LSM ($E_a \approx 2.8eV$) whereas at high pO_2s it may just be bulk oxygen vacancy diffusion. In order for bulk vacancy transport to be a viable pathway, a source of oxygen vacancies is required. Under open circuit conditions, generally oxygen vacancies are thought to form at low pO_2s from the surface exchange reaction:

$$\frac{1}{2}O_2 + (2e^-)^{ed} + (V_{\ddot{O}})^{ed} \underset{k_{sxb}}{\overset{k_{sxf}}{\rightleftharpoons}} (O_{O}^{x})^{ed} \tag{3.14}$$

where $V_{\ddot{O}}$ is an oxygen vacancy in LSM and O_{O}^{x} is an oxygen atom incorporated into the LSM lattice. However, it should be pointed out that if the oxygen reduction reaction did follow a bulk diffusion process, then we would expect the polarization resistance in low oxygen concentrations to be higher than the polarization resistance in high oxygen concentrations [24] because based on Equation 3.14, the equilibrium oxygen vacancy concentration is inversely proportional to pO_2:

$$[V_{\ddot{O}}]^{eq} = \frac{k_{sxb}}{k_{sxf}} \frac{[O_{O}^{x}]}{pO_2^{0.5}} \tag{3.15}$$

In addition, LSM is superstoichiometric with cation vacancies at oxygen partial pressures above 10^{-3}atm [4]. In this “high pO_2” regime, LSM has an excess of oxygen which is balanced with metal cation vacancies on the A and B sites of the perovskite lattice and therefore it is expected to have very few oxygen vacancies even at oxygen concentrations as low as 10^{-10}atm [17]. Based on a defect model proposed by Kuo *et al.* [17], for oxygen concentrations above 10^{-3}atm (within the high pO_2 data range of this thesis), LSM is stoichiometrically:

$$[(La^x_{La})_{1-y}(Sr^{'}_{La})_y(V^{'''}_{La})_{\delta/3}][(Mn^x_{Mn})_{1-y}(Mn^{\cdot}_{Mn})_y(V^{'''}_{Mn})_{\delta/3}](O^x_O)_{3+\delta}$$

where the excess of oxygen (represented by $\delta \geq 0$) is balanced by cation vacancies on the A and B-sites of the perovskite. Below 10^{-10}atm, LSM is oxygen deficient:

$$[(La^x_{La})_{1-y}(Sr^{'}_{La})_y][(Mn^x_{Mn})_{1-y+2\delta}(Mn^{\cdot}_{Mn})_{y-2\delta}](O^x_O)_{3-\delta}(V_{\ddot{O}})_\delta$$

where δ represents the mole fraction of oxygen vacancies in the LSM lattice and between these pO_2 ranges (the low pO_2 range of this thesis), LSM is stoichiometric, with $\delta = 0$:

$$[(La^x_{La})_{1-y}(Sr^{'}_{La})_y][(Mn^x_{Mn})_{1-y}(Mn^{\cdot}_{Mn})_y](O^x_O)_3$$

Since the oxygen vacancy concentration of LSM at relevant oxygen partial pressures is extremely low, it is not expected that LSM would transport oxygen through the bulk unless oxygen vacancies were formed by polarizing the electrode [4]. The process with an activation energy between 1.8eV and 3.0eV could be a surface diffusion process with an activation energy that is a function of surface coverage, as is common for a surface diffusion process [25].

Analysis of the Double Layer and Chemical Capacitance

The capacitances associated with the electrode processes may be important since they can be an indication of the nature of the double layer or of the adsorbed species. There are generally two types of capacitances that arise from electrochemistry: 1) a double layer capacitance (C_{dl}) resulting from the charging of an interface such as the electrode/electrolyte interface and 2) a chemical capacitance (C_{chem}) resulting from transport and adsorption processes “accumulating” reactants either in the bulk or on the LSM surface.

Typically for solution based electrolytes, it is thought that the double layer at the electrode/liquid-electrolyte interface can be described by two capacitors in series comprising an inner (Stern) layer and an outer (Gouy-Chapman) layer. The inner layer consists of a monolayer of charged ions adsorbed at the interface and beyond this monolayer a diffuse layer is extended into the solution. As a first order approximation, we can calculate the double layer capacitance assuming the majority of the capacitance arises from the inner layer, which is given by [26]:

$$C_i = \frac{A_{geom} A_{cov} \epsilon_0 \epsilon}{r} \tag{3.16}$$

where A_{geom} is the geometric area, A_{cov} is the electrolyte coverage by the electrode, ϵ_0 is permittivity of vacuum ($8.85 \times 10^{-12} Fm^{-1}$), ϵ is the static relative permittivity which is usually on the order of 1 but found to be $\sim$24 for YSZ [27] and r is the distance between charged plates. If the capacitance arises from the electrode/electrolyte interface, then r is usually assumed to be in the range of 1 to $10\mathring{A}$ [26]. With $A_{geom} = 1.2cm^2$ and with $A_{cov} = 0.5$, then $C_{dl} \approx 13 - 130\mu Fcm^{-2}$. However, if the capacitance arises from the gas/electrode interface, then r is the radius of an adsorbed oxygen atom. The radius of an oxygen molecule is $1.52\mathring{A}$ [28] and so the radius of an oxygen atom would be $r \approx 0.76\mathring{A}$. In addition, A_{geom} becomes the gas/solid internal surface area of the electrode which has been estimated to be $4 \times 10^4 cm^2/cm^3$ [29] and for an electrode thickness of $20\mu m$, assuming unit coverage area, $C_{dl} \approx 27mFcm^{-2}$, roughly 1000 times larger. Note that this assumes the entire electrode thickness contributes to the C_{dl} which may not be the case. Assuming only $1\mu m$ of the $20\mu m$ thick electrode contributed, then $C_{dl} \approx 2.7mFcm^{-2}$.

The double layer capacitance and the chemical capacitance were obtained by fitting the equivalent circuit to the EIS response. Figure 3.11 plots both the double layer capacitance and the chemical capacitance against oxygen concentration. Although a constant phase element was used to model the behavior of the double layer, it was converted into an effective capacitance using the relationship:

$$C_{dl} = \frac{(Q_{cpe} R)^{1/P_{cpe}}}{R} \tag{3.17}$$

where Q_{cpe} and P_{cpe} are the fitting parameters of the constant phase element and R is the total resistance of the electrode. The large error bars in Figure 3.11b reflect the fact that at high temperatures and high pO_2s, the R_{chem} contribution to R_p was small and therefore difficult to fit using equivalent circuits.

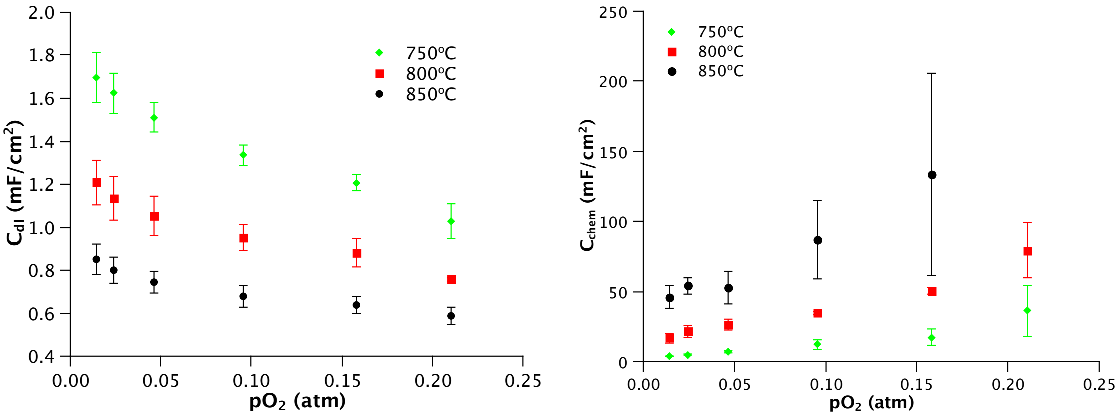

(a)

(b)

Figure 3.11: “Double layer” and chemical capacitances calculated from Randles circuit assuming adsorption controlled process: (a) Double layer capacitance (b) Chemical capacitance. Error bars represent the standard deviation of the measured quantity over three different samples.

As can be seen from Figure 3.11a, the double layer capacitances are functions of both temperature and pO_2 and they are high enough to support a capacitance arising from the gas/electrode interface rather than at the electrode/electrolyte interface. These high capacitance values may provide evidence that a charge transfer reaction occurs at the gas/LSM interface and may indicate that adsorbates are charged species.

In addition to the capacitance, it might also be useful to look at the parameter P_{cpe} which is reflective of the fact that a non-ideal capacitor must be used to describe the charging of the double layer. An ideal capacitor would have $P_{cpe} = 1$ whereas a non-ideal capacitor has $P_{cpe} < 1$. The constant phase element accounts for the distributed nature of the interface, such as a distribution in surface defects or a distribution in particle shape [30]. For $pO_2 \geq 0.01atm$, $P_{cpe} \approx 0.7$ was observed over the pO_2 range and temperature range tested however, for $pO_2 \leq 0.001atm$, P_{cpe} was relatively constant over the pO_2 range but decreased as the temperature increased, from $P_{cpe} = 0.77$ at $750°C$ to $P_{cpe} = 0.68$ at $850°C$. This indicates that as the temperature increased, the double layer shifted further away from ideal capacitative behavior and may indicate changes in the LSM surface composition such as an increase in the defect concentration or oxidation state of Mn as temperature increases.

Summary of Data Analysis Under Open Circuit Conditions

The above analysis of LSM cathode operation near OCV conditions used impedance spectroscopy to examine the pO_2 dependency and activation energy of the charge transfer resistance and the chemical resistance, the two main components that make up the total electrode resistance. From this analysis, Figure 3.12 shows a possible mechanism for oxygen reduction in low and high pO_2s supported by:

- An analysis of the reaction orders showed that a shift occurred between low ($10^{-4}atm \leq pO_2 \leq 10^{-3}atm$) and high ($0.01atm \leq pO_2 \leq 0.21atm$) which may be an indication of a shift in the rate of the dominant step in the mechanism or there may be a shift in the mechanism itself. Based on the reaction orders, the most likely mechanism for the low pO_2 regime was found to be a mechanism involving adsorption and surface diffusion of neutral adsorbates followed by a charge transfer reaction at the LSM/YSZ interface. In the high pO_2 regime, an electrochemical reaction at the gas-LSM surface was determined to be likely.
- High activation energies were found for these processes which theoretically correspond most closely with the diffusion of oxygen vacancies, however, it was argued that at open circuit conditions, the concentration of oxygen vacancies in LSM is likely low and so these high activation energies may be a result of surface species interactions with surface diffusion processes.
- Finally, from an analysis of the magnitude of the double layer capacitance it is argued that high values of C_{dl} might be a result of an electrochemical reaction at the gas-LSM interface.

3.3.3 Data Analysis Under Polarized Conditions

In this subsection, the experimental data of polarized electrodes is presented. The discussion is split into two main parts: 1) a comparison of the electrode resistance under open circuit conditions for “pre-polarized” electrodes (electrodes that have not yet been exposed to a net cathodic or anodic current) and polarized electrodes 2) the electrode kinetics away from open circuit conditions.

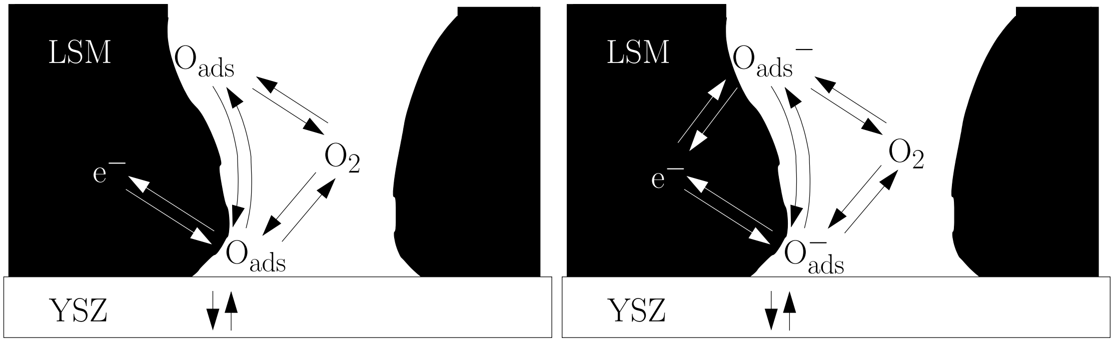

(a) (b)

Figure 3.12: Proposed mechanism for oxygen reduction in: (a) $10^{-4}atm \leq pO_2 \leq 10^{-3}atm$ (b) $0.01atm \leq pO_2 \leq 0.21atm$

The benefit of using a 3-electrode cell to investigate electrode behavior is that the kinetics of the working electrode can be investigated under real fuel cell operating conditions, that is, when a net current flows through the cell, otherwise known as being operated under load. The passage of a net cathodic current through an LSM electrode has been shown to reduce the open circuit polarization resistance by up to 50 times [31]. It has also been found that microstructural factors can impact the degree of electrode activation [11]. It should also be pointed out that the magnitude of the current and the length of time that the current is applied is also an important factor and many researchers have not explained the reasons for choosing their polarization routine. In most cases, this electrical history effect was found to be reversible after long periods of time or by applying a small anodic current. Since the electrical history of the electrode can have a significant impact on the resistance of the electrode, it is extremely important to develop a careful routine for the analysis of polarized electrodes. Due to the electrical history effect, precautions were taken so that the electrical history of the sample was as controlled as possible, helping to increase the reproducibility between samples. Section 3.2.2 outlined the experimental routine used to measure the current/voltage behavior of polarized electrodes.

One common way of characterizing the polarization behavior of an electrode is by measuring a polarization curve. Figure 3.13 shows iR corrected cathodic steady state (s.s.) polarization curves as well as a cathodic scan at 1mV/s (CV) of porous LSM cathodes measured in oxygen partial pressures between 0.01 and 0.21atm (left hand column) and in oxygen partial pressures between 10^{-4}atm and 10^{-3}atm (right hand column) at temperatures of $750°C$, $800°C$ and $850°C$. As expected, for the same electrode potential, the current density increased with temperature and with the oxygen concentration. A limiting current was observed for some of the polarization curves measured in low pO_2 but not at high pO_2. Although potentials were applied from 0 to -600mV, after correcting for the potential drop through the electrolyte, for some cases the electrode potential was much smaller than the applied potential. For example, applying a potential of -600mV at $850°C$ in air resulted in an electrode potential of just -50mV after correcting for the iR loss through the electrolyte. This was caused by a combination of high current densities achieved in high pO_2 atmospheres as well as high electrolyte resistances due to the 6mm thick (3mm effective thickness) electrolyte, which had a resistance of 3.4Ω, 4.7Ω and 6.8Ω at $850°C$, $800°C$ and $750°C$ respectively. On the other hand, polarization curves collected for $pO_2 \leq 0.001atm\ O_2$ resulted in very low iR corrections owing to the low current densities.

In addition to measuring the steady state current/voltage behavior shown in Figure 3.13, the impedance under load and then at OCV conditions was measured after each current/voltage had reached a steady state. Some examples of the impedance spectra collected were already shown in Figure 3.4 (page 95).

Open Circuit Behavior of Polarized Electrodes

Comparison of polarized and pre-polarized electrodes The behavior of polarized electrodes under open circuit conditions was investigated by calculating the polarization resistance from the steady state polarization curves using $R_p = \partial\eta/\partial i$ and by measuring the impedance response immediately after polarizing the electrode with various magnitudes of cathodic currents. Table 3.5 compares the R_p values and their reaction orders (γ) obtained from steady state polarization curves and those obtained from impedance spectroscopy for pre-polarized electrodes. For $pO_2 \geq 0.01atm$, R_p values from steady state polarization measurements were lower at almost all temperatures and pO_2s compared to those measured using impedance spectroscopy on pre-polarized electrodes. At $750°C$ in 0.01atm O_2, R_p calculated from EIS measurements were 1.5 times larger than those from polarized electrodes. As the temperature increased, the R_p values from these measurements more closely matched. When comparing R_p values between polarized and pre-polarized electrodes in

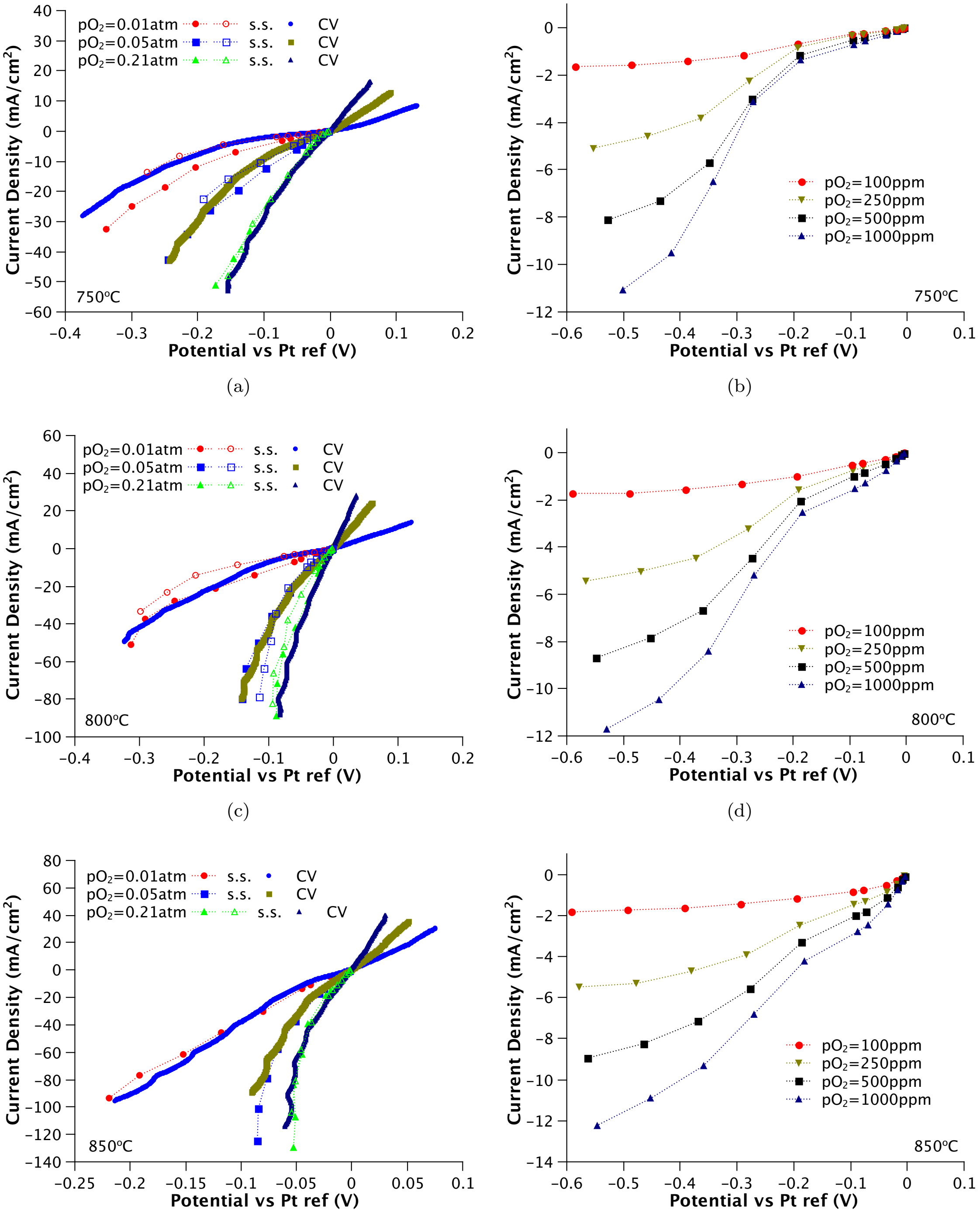

(a)

(b)

(c)

(d)

(e)

(f)

Figure 3.13: Polarization curves for porous LSM electrodes in oxygen concentrations of 0.01-0.21atm: (a) 750°C (c) 800°C (e) 850°C and in oxygen concentrations of 10^{-4}atm-10^{-3}atm: (b) 750°C (d) 800°C (f) 850°C. Lines through steady state data points are to guide the eye.

$pO_2 \leq 0.001atm$, R_p values from steady state measurements were consistently higher than for the pre-polarized electrodes, the opposite of the high pO_2 case.

Table 3.5: Summary of polarization resistances measured at OCV between 750°C and 850°C and pO_2 between 10^{-4}atm and 0.21atm and their respective reaction orders.

		Steady State		EIS[1]	
Temp (°C)	pO_2	Rp ($\Omega\ cm^2$)	γ	Rp ($\Omega\ cm^2$)	γ
750	10^{-4}atm	243	0.40	176	0.29
	5×10^{-4}atm	126		109	
	0.001atm	96.9		91.9	
	0.01atm	23.7	0.52	36.0	0.44
	0.05atm	8.83		16.9	
	0.21atm	4.77		9.66	
800	10^{-4}atm	113	0.43	87.8	0.35
	2.5×10^{-4}atm	79.4		64.0	
	5×10^{-4}atm	60.0		51.0	
	0.001atm	40.8		38.8	
	0.01atm	9.09	0.45	8.53	0.32
	0.05atm	3.66		4.92	
	0.21atm	2.21		3.28	
850	10^{-4}atm	54.2	0.44	43.1	0.41
	2.5×10^{-4}atm	31.6		24.6	
	5×10^{-4}atm	24.6		19.4	
	0.001atm	19.1		16.6	
	0.01atm	4.62	0.39	4.94	0.37
	0.05atm	1.99		2.72	
	0.21atm	1.42		1.62	

[1] Before polarization

In terms of the reaction order, over all oxygen concentrations, the reaction orders were higher for the polarized electrodes (using steady-state measurements) than for the pre-polarized electrodes (using EIS measurements). The reaction orders presented in Table 3.5 are for the total polarization resistance though since steady state techniques cannot distinguish between the individual R_{ct} and R_{chem} components of the resistance. However, in general, the reaction order of a chemical process such as adsorption or diffusion is higher than that of a charge transfer reaction, and so a shift in reaction order towards higher values, as observed here for the steady state measurements, may indicate a change in the R_{chem} process.

Influence of polarization history on electrode resistance in high pO_2 To determine how the individual components of R_p (at OCV) changed after various degrees of polarization, the impedance at OCV was measured immediately after polarizing the electrode with a certain current/voltage. This polarization/impedance sequence was described in Figure 3.1 (Section 3.2.2, page 88) as part of the experimental protocol and is also further illustrated in Figure 3.14. The horizontal lines in Figure 3.14 reflect the level and length of time that a steady state potential was applied to the electrode and the squares represent the point in time at which an impedance curve was measured under the same DC bias conditions as the applied potential and then under OCV conditions. Figure 3.14 indicates that a steady state potential was applied to the electrode and a current was measured until it reached a steady state, which generally took between 2 to 10hrs. After a steady state current had been reached, the impedance was measured under DC bias conditions and then at OCV. In addition, after polarizing the electrode to -600mV (the final potential applied during the polarization sequence), the electrode was relaxed at OCV and the impedance was measured once an hour until the impedance at OCV returned to its pre-polarized levels. Using this methodology, the change in R_{ct} and R_{chem} from the impedance response could be measured as a function of polarization for the impedance measured under DC bias conditions as well as at OCV.

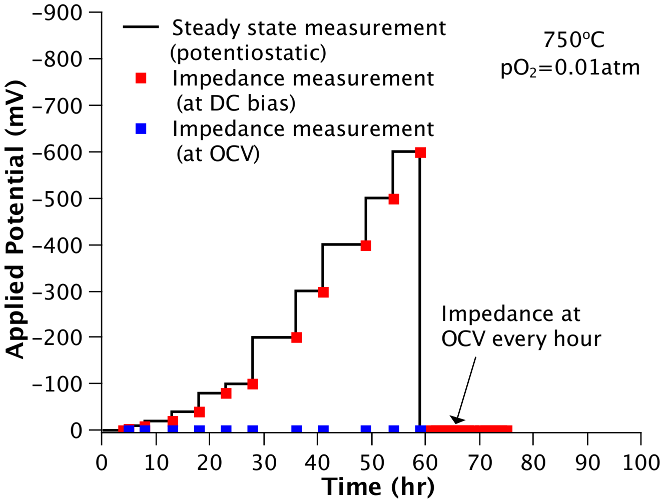

Figure 3.14: Example polarization sequence at 750°C in 0.01atm O_2. Lines represent the length of the steady state current/voltage measurements in potentiostatic mode while the squares represent the point in time at which the impedance was measured under DC bias conditions and then at OCV. Applied potentials in the figure are not iR corrected.

Figure 3.15a shows the change in R_p, R_{ct} and R_{chem} resistances at $750°C$ in 0.01atm O_2 measured from the electrode impedance for various extents, or levels of electrode polarization, between an applied potential of 0mV and -600mV and Figure 3.15b shows the relative contribution of R_{chem} to the total electrode resistance over the same polarization sequence. Results shown in Figure 3.15 represent the impedance measurements under OCV conditions in the sequence of experiments between times of 0 and 60hrs in Figure 3.14. Figures 3.15a and 3.15b show that before any electrode polarization (equivalent to a net current of 0 mA/cm^2), the resistances of R_{ct} and R_{chem} and their relative contributions to the total electrode resistance were equal. However, R_{ct} decreased with polarization but the decrease in R_{chem} was much more pronounced for the same level of polarization. As Figure 3.15b shows, the contribution of R_{chem} to the total electrode resistance fell to as low as 14% (indicating that the rest of the contribution came from R_{ct}) with an applied current of just $-7.3mA/cm^2$ before decreasing to 12%. It is useful to recall that R_{chem} arises from adsorption/desorption or gas/adsorbate diffusion effects.

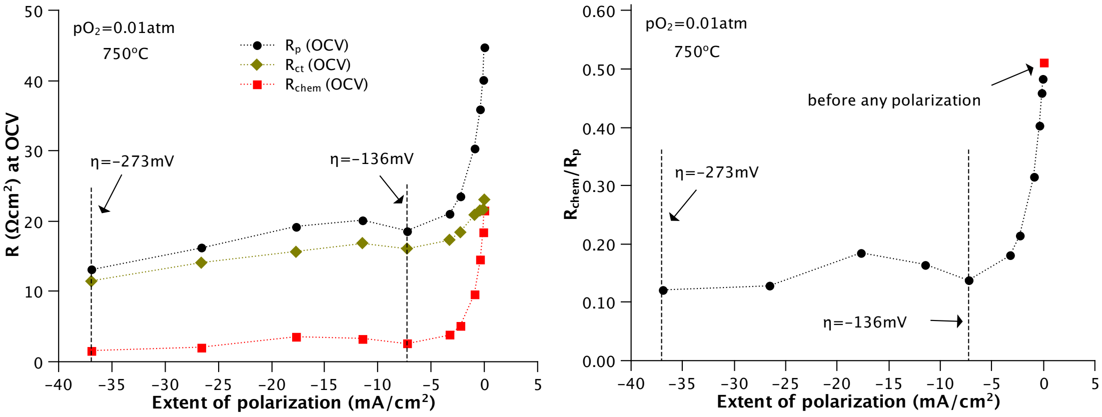

(a) (b)

Figure 3.15: Breakdown of R_{ct} and R_{chem} contributions to total polarization resistance at OCV (a) Contribution of R_{ct} and R_{chem} measured at various degrees of polarization and (b) the relative contribution of R_{chem} to R_p at OCV measured immediately after polarizing the electrode. All measurements were obtained from impedance spectroscopy at OCV in $pO_2 = 0.01atm$ at $750°C$. The extent of polarization is the steady state current density achieved by the cell. Lines through data points are to guide the eye.

Intuitively, it would be expected that polarizing the electrode could create gradients in the species concentrations or potentials involved in the reaction which would cause an increase in R_{chem} due to concentration polarization, and not a decrease. There are, however, some possible explanations for this decrease in R_{chem} with polarization: 1) potential dependent adsorption/desorption rate constants 2) enhancement in surface diffusion due to electric field interactions with charged adsorbates and 3) modification of the LSM surface composition with applied current.

A potential dependent adsorption/desorption reaction could take the form:

$$O_2 + 2e^- + 2s \rightleftharpoons 2O_{ads}^- \tag{3.18}$$

where the adsorption and desorption rate constants become electrochemical rate constants and depend exponentially on the potential difference across the gas/LSM interface [32], such as:

$$k_{ads} = k_{ads}^0 \exp(-\alpha_c f \Delta\chi) \tag{3.19a}$$

$$k_{des} = k_{des}^0 \exp(\alpha_a f \Delta\chi) \tag{3.19b}$$

where $f = F/R/T$ and $\Delta\chi$ is the potential difference across the gas/LSM interface. For cathodic currents, k_{ads} would increase and k_{des} would decrease, resulting in a shift in the adsorption reaction favoring the formation of adsorbates on the LSM surface, thereby reducing concentration losses at higher overpotentials. In addition (or alternatively), if negatively charged oxygen species such as O^- or O^{2-} were present on the LSM surface, then they might be influenced by the surrounding electric field which could enhance their transport towards the LSM/YSZ interface where they could be more easily incorporated into the electrolyte. This could reduce concentration losses due to the increased flux of adsorbates towards the LSM/YSZ interface.

For either potential dependent adsorption and/or enhanced transport of adsorbates towards the LSM/YSZ interface, we might expect the relaxation time of these processes to be nearly instantaneous as the applied potential is switched from a polarized level to open circuit conditions. This is not observed experimentally though. Figure 3.16a plots the electrode resistance measured at OCV conditions, once an hour, after polarizing the electrode to $-37mA/cm^2$ (equivalent to -600mV applied potential or $\eta = -273mV$ after iR correction) until the electrode impedance returned to its pre-polarized levels. This is equivalent to the experimental sequence shown in Figure 3.14 between times of 60hrs and 75hrs. As Figure 3.16a shows, the charge transfer resistance returned to its pre-polarization level of activity within 3hrs, however, the relaxation time for the R_{chem} enhancement was on the order of 10 to 15hrs.

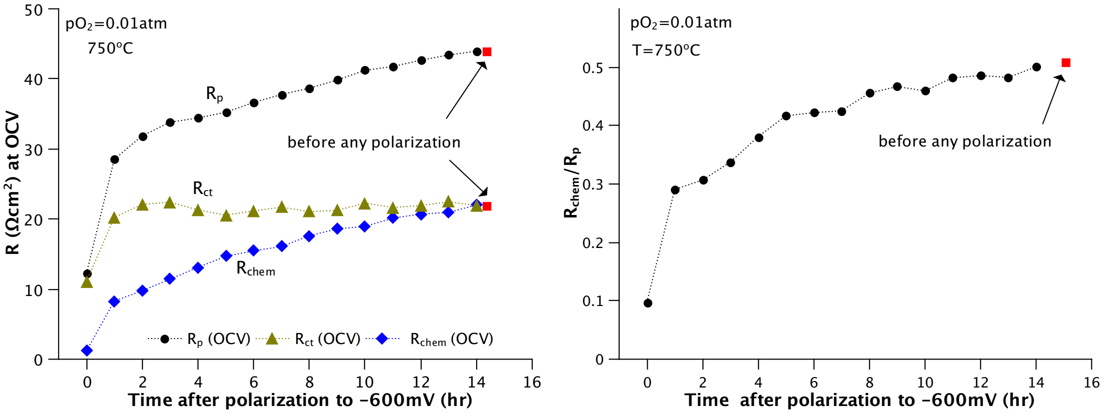

(a) (b)

Figure 3.16: Breakdown of R_{ct} and R_{chem} contributions to total polarization resistance at OCV (a) Change over time of R_{ct} and R_{chem} measured at open circuit conditions after being polarized to -0.6V ($-37mA/cm^2$) and (b) The relative contribution of R_{chem} to R_p measured at OCV after being polarized at -0.6V. All measurements were obtained from impedance spectroscopy at OCV in $pO_2 = 0.01atm$ at $750°C$. The extent of polarization is the steady state current density achieved by the cell. Lines through data points are to guide the eye.

The enhancement of the oxygen reduction reaction after polarization has been investigated by some researchers in the past [4,11,14] and a picture of the mechanism responsible for the enhancement is slowly developing. These studies all found a reduction in a low frequency arc (influencing R_{chem}) of the impedance spectra at OCV taken after polarization of the electrode. Jiang *et al.* [33] hypothesized that high initial resistances were caused by a passive layer on the surface of LSM grains which were enriched with La and Sr. A later study by the same group [14] concluded that the activation effect after cathodic polarization was most likely due to the incorporation into the LSM lattice of passive surface SrO species. The process was found to be reversible over long periods of time which was attributed to the slow diffusion of cation vacancies towards the surface of the LSM grain. A recent study by La O' *et al.* [4] used Auger electron spectroscopy and X-ray photoelectron spectroscopy on dense LSM microelectrodes and determined that cathodic polarization leads to significant reduction of surface La fraction and an increase in the surface Sr and Mn fractions. La O' *et al.* also found long relaxation times of over 10hrs which gave a linear relationship when plotted against $t^{1/2}$ indicating a diffusion process which was attributed to cation diffusion upon polarization and subsequent relaxation, however, they did not estimate the diffusion coefficient for this process. In all cases, polarization was thought to influence primarily the surface exchange or adsorption kinetics.

Theoretical evidence may support an enhancement in adsorption kinetics due to chemical modification of the LSM surface during polarization. From a recent DFT thermodynamics study on $LaMnO_3$ perovskites, it was concluded that the most favorable adsorption site for oxygen is on a Mn [22] site however, if the adsorption site involved a vacancy, the rate of adsorption is expected to increase [21]. If the surface Mn composition or oxidation state or surface vacancy composition was altered due to cation diffusion during the polarization process, then this might influence the kinetics of the oxygen adsorption reaction.

Influence of polarization history on electrode resistance in low pO_2 As noted by other researchers, in this study also it was observed that polarizing the LSM electrodes in high oxygen concentrations ($pO_2 \geq 0.01atm$) resulted in a decrease in resistances. However, a new finding of this work is that upon polarizing in low oxygen concentrations ($pO_2 \leq 0.001atm$), a reverse behavior was observed, i.e. an increase in the electrode resistance. As an example, Figure 3.17 shows the relaxation of R_{ct}, R_{chem} and R_p after being polarized to -600mV at $800°C$ in 10^{-4}atm O_2. Unlike in Figure 3.15a for high pO_2, the electrode resistance was high immediately after polarization and gradually fell back to pre-polarized levels. This trend, relaxing from a high resistance to a low resistance, was found for all $pO_2 \leq 0.001atm$ while the opposite trend (relaxing from a low resistance to a high resistance) was found for all $pO_2 \geq 0.01atm$. Part of the increase in the R_p after polarizing at high levels resulted from the fact that the electrode was operated in a current limiting regime where $R_{chem} \rightarrow \infty$ due to reactant concentrations approaching zero, however, this effect was short lived after relaxing the electrode at OCV.

Figure 3.18 shows a proposed mechanism for the diffusion of vacancy species between the surface and bulk of the LSM cathode under cathodic current. For $pO_2 \geq 0.01atm$, under cathodic current, it is proposed that vacancies from the bulk diffuse towards the surface. The reduction in R_{chem} under polarized conditions and subsequent increase in R_{chem} when the LSM electrode is relaxed, observed in Figure 3.16, could be a result of an enhanced adsorption rate constant k_{ads}^{vac} when oxygen adsorbs onto a surface vacancy, as predicted by DFT work in [21]. On the other hand, when the $pO_2 \leq 0.001atm$, it is proposed that vacancies diffuse from the surface to the bulk, resulting in a reduction in the average adsorption rate constant, k_{ads}, as oxygen adsorbs onto a metal species such as La, Sr, or Mn. Under these conditions, we can expect $k_{ads}^{vac} > k_{ads}$ which could explain why R_{chem} decreases under cathodic current for $pO_2 \geq 0.01atm$ and increases under cathodic current for $pO_2 \leq 0.001atm$.

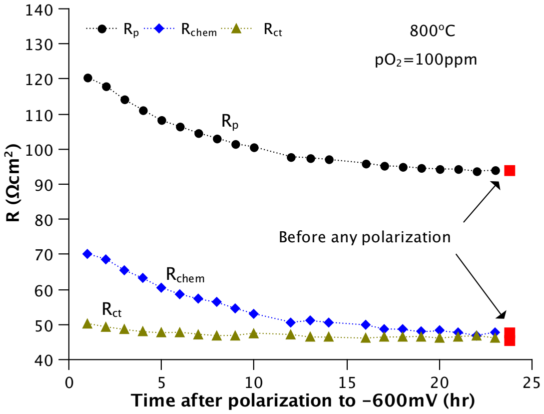

Figure 3.17: Relaxation of R_{ct}, R_{chem} and R_p at OCV with time after being polarized to -600mV. Resistances evaluated from impedance spectroscopy at $800°C$ in 10^{-4}atm O_2. Lines through data points are to guide the eye.

Estimation of relaxation time constant and cation diffusivity In the relaxation experiments described above, a steady state potential was applied to the cell until the cell current reached a steady state, then the impedance at open circuit conditions was measured until the electrode returned to pre-polarized levels. This is analogous to a step change in potential from -600mV to 0mV. From the relaxation data shown in Figures 3.16a and 3.17 and other data collected in this work, the time constant of the relaxation process was calculated. The time response of the resistance as it was relaxed from polarized levels to open circuit levels was modelled using a 1st-order ODE with a step input:

$$\frac{dV}{dt} + \frac{1}{\tau}V = Au(t) \tag{3.20}$$

where V is the time varying quantity which either increases or decreases with time, τ is the time

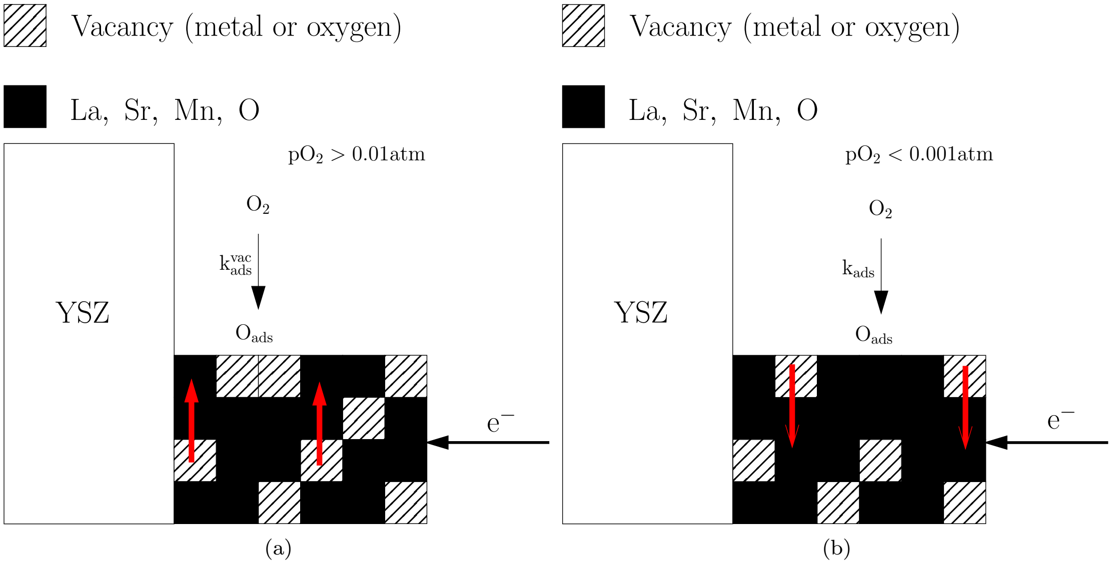

Figure 3.18: (a) Diffusion of vacancies (such as cation vacancies) from the bulk towards the surface in $pO_2 > 0.01atm$ (b) Diffusion of vacancies (such as cation vacancies) from the surface to the bulk in $pO_2 < 0.001atm$. It is proposed that $k_{ads}^{vac} > k_{ads}$.

constant which characterizes the time varying response of V and $Au(t)$ is a step input at time t (equivalent to the step change in going from -600mV to OCV). The general solution to Equation 3.20, with $V(t=0) = V_0$ is:

$$V(t) = V_0 \exp\left(\frac{-t}{\tau}\right) + V_\infty \left[1 - \exp\left(\frac{-t}{\tau}\right)\right] \tag{3.21}$$

By replacing V with the resistance R in Figure 3.17, where R_∞ is the resistance at $t = \infty$, R_0 is the initial resistance, the time constant, τ, for the process can be calculated. The time constant can be obtained from the slope of a plot of $\ln(R(t) - R(t=\infty))$ vs time. Figure 3.19 shows example plots of $\ln(R(t) - R(t=\infty))$ vs time for conditions of 0.01atm, 750°C as well as 10^{-4}atm, 800°C and 5×10^{-4}atm, 850°C. The time constant τ for these processes were all ~ 6 hrs and differences in the time constant for various pO_2s could not be distinguished.

If we assume that the long relaxation time is a result of a cation diffusion process as suggested by [4], the diffusion coefficient can then be estimated from [34]:

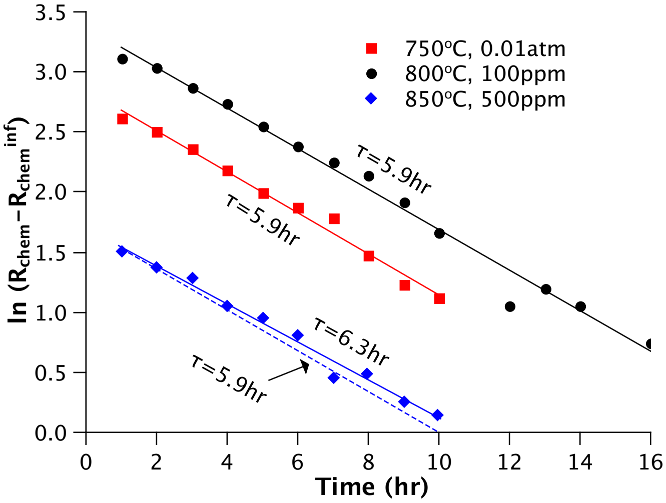

Figure 3.19: Determination of the time constant of the diffusion process resulting from the change in R_{chem} after polarizing the porous LSM electrode. Solid lines through data points show linear least-square fit to experimental data..

$$D = \frac{\delta^2}{2\tau} \tag{3.22}$$

where D is the diffusion coefficient and δ is the diffusion length. Although we can determine the time constant, δ must be approximated. As a first order approximation, the maximum diffusion length of a cation from the LSM surface into the LSM bulk (in the case of $pO_2 \geq 0.01atm$) can be taken to be the radius of an LSM particle. This assumption would result in the highest possible cation diffusivity, D_{cat}, since any lower diffusion lengths would decrease D_{cat}.

If the diffusion length was equal to 50% of the LSM particle size, or $\sim 0.25\mu m$, the maximum cation diffusivity calculated from Equation 3.22 would be $D_{cat} \approx 2 \times 10^{-18}\ m^2/s$ whereas if the diffusion length was equal to 10% of the LSM particle size, 50nm, the cation diffusivity would be $D_{cat} \approx 7 \times 10^{-20}\ m^2/s$. Cation diffusion coefficients have been measured for various perovskite materials. Waernhus *et al.* [35] used SIMS to measure the cation diffusion of A and B site dopants in $La_{1-x}Sr_xFeO_{3-\delta}$ and found values of $4 \times 10^{-21}\ m^2/s$ at $900°C$ for the A site cations with $x = 0.1$. In addition, these authors found that the diffusion of the B site cation was faster than diffusion of the A site cation. Similar measurements were performed for the $LaMnO_3$ system: Palcut *et al.* [36] measured A site cation diffusivities of $\sim 1.6 \times 10^{-18}\ m^2/s$ at $750°C$ whereas

Miyoshi *et al.* [37] measured B site cation diffusivities of $\sim 1.2 \times 10^{-16}\ m^2/s$. The higher cation diffusivities in $LaMnO_3$ materials reflects the relatively high concentrations of cation vacancies in these materials [36, 37]. The close agreement between the cation diffusivities obtained by Palcut *et al.* [36] and those estimated in this work may suggest that the time dependence of the impedance response after removing the cathodic polarization results from cation diffusion on the A site. It should be noted that bulk $V_{\ddot{O}}$ diffusion in LSM has been measured by oxygen isotope techniques to range from $10^{-20}\ m^2/s$ to $10^{-18}\ m^2/s$ between temperatures of $750°C$ and $850°C$ [38], however, since the concentration of cation vacancies in LSM is expected to be much higher than the concentration of oxygen vacancies [16], it is likely that the diffusivities being measured in this work are cation vacancies.

From the above analysis and in accordance with [4], the reduction in polarization resistance at OCV for $pO_2 \geq 0.01atm$ results from a diffusion of cations from the surface into the bulk of LSM whereas the increase in the polarization resistance for $pO_2 \leq 0.001atm$ results from the removal of cations vacancies from the LSM surface. Both of these processes have similar time constants and the maximum diffusion coefficient has been estimated to be $2 \times 10^{-18}\ m^2/s$.

At this point, the reason for the decrease in R_{chem} can only be hypothesized, however, it has been suggested that oxygen vacancies may form at the LSM surface as a result of the application of current which may open up the bulk diffusion pathway for oxygen transport. Another possible explanation might be the enhancement in adsorption kinetics resulting from changes (such as enrichment of Mn) at the LSM surface at high pO_2s whereas in low pO_2s the opposite might be true.

Behavior of LSM Electrodes Away From Open Circuit Conditions

So far, the analysis has only focused on a comparison between un-polarized and polarized electrodes under open circuit conditions. As noted in the above section, comparing the open circuit behavior of an LSM electrode before and after polarization can yield useful information about the processes occurring in the electrode. In this section, the behavior of LSM electrodes when they are operated under cathodic polarization, away from equilibrium, is discussed.

Polarization influences on R_p In traditional electrochemical systems, when the cell is polarized, two general phenomena can be said to occur: 1) unless transport limitations influence the reactant concentration, the electrode polarization resistance is expected to decrease due to the exponential dependence of the electrochemical rate constants with electrode potential 2) gradients in the species concentrations within the electrode increase due to the fact that these gradients are proportional to the current density. In the case of LSM electrodes, another complication arises due to the apparent chemical changes of the LSM surface caused by the passage of net current. For this reason, it is useful to compare the resistance of polarized electrodes at OCV with the resistance of polarized electrodes under DC bias so that the effects of chemical changes can be separated from the effects of the purely electrochemical influences (ie. those mentioned in points 1 and 2 above). In doing so, the differences between these two data sets should give the pure electrochemical contribution.

Figure 3.20 shows the impedance response of LSM electrodes under applied DC bias, between $\eta = -8mV$ and $\eta = -273mV$ (iR corrected), in 0.01atm O_2 at $750°C$. As the electrode potential increases, the electrode resistance decreases, which is consistent behavior when compared to the polarization curve in Figure 3.13a (page 122). As the bode plot in Figure 3.20b indicates, a low frequency ($\sim 0.8Hz$) peak at low potentials ($\eta = -8mV$) gradually disappears as the electrode potential increases. For reasons that will be discussed in the modelling section of this thesis, Chapter 4, this low frequency peak is likely associated with the oxygen adsorption/desorption reaction. As discussed previously, it was found that the value of R_{chem} decreased after polarizing the electrode. This decrease in the low frequency peak with electrode polarization might indicate that the adsorption process is being enhanced by electrode polarization, perhaps further evidence that the reduction in R_{chem} caused by chemical changes at the LSM surface primarily influences the adsorption process. However, this does not rule out the influence of typical electrochemical effects such as the enhancement of the electrochemical rate constants with increasing electrode potential, which may also play a role in reducing R_{chem} as the electrode is polarized.

Figures 3.21a compares the total electrode resistance measured at $750°C$ and in 0.01atm O_2 under applied DC bias and at OCV immediately after polarizing the electrode whereas Figure 3.21b shows the relative contribution of R_{chem} to the total electrode resistance for these two cases. As Figure 3.21a shows, the polarization resistance at OCV and under DC bias are identical up to an operating point of around $\eta = -136mV$, $i = -7.3mA/cm^2$ is reached, at which point the electrode resistance under DC bias becomes lower than the electrode resistance at OCV conditions. The difference in

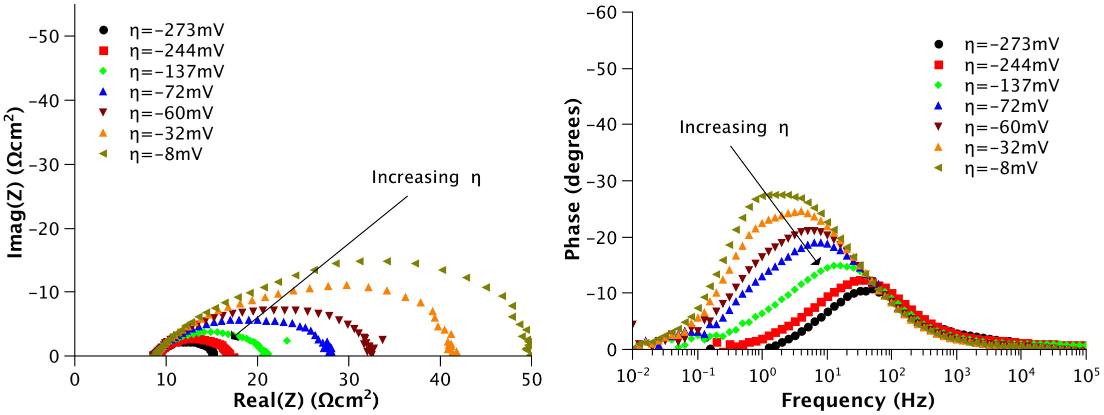

(a) (b)

Figure 3.20: Impedance spectra for overpotentials between $\eta = -8mV$ and $\eta = -273mV$ at 750°C in 0.01atm O_2 (a) Nyquist plot (b) Bode plot.

R_p between these two curves beyond $\eta = -136mV$ (signified by ΔR_p) is likely the influence of the typical electrochemical effects, independent of any chemical changes caused by factors such as cation diffusion in the LSM structure. Evidently, the electrode resistance is reduced as the electrode is polarized for two reasons: 1) because of chemical changes in the LSM structure caused by the passage of net current and 2) because of the electrochemical promotion which is common to classical electrochemical systems. Figure 3.21b shows that although the contribution of R_{chem} measured at OCV on polarized electrodes decreases, R_{chem} also decreases dramatically as a result of the DC bias. Since R_{chem} decreases with the application of a DC bias, then this might support an oxygen reduction mechanism where either: 1) the adsorption/desorption reaction is electrochemically activated or/and 2) the transport of adsorbed oxygen is enhanced by the applied potential.

In this analysis, the effects of the surface modification of LSM due to the passage of net current from the classical electrochemical aspects can be separated. Figure 3.22 shows a proposed mechanism for oxygen reduction in LSM cathodes under cathodic operation for $pO_2 \geq 0.01atm$. In addition to reduction in R_{chem} due to adsorption onto a vacancy on the LSM surface (described in Figure 3.18a), there could be an electrochemical reaction at the gas/LSM interface such as that proposed in Equation 3.18 and depicted earlier in Figure 3.12b. Thus, the reason for the drop in R_p at OCV in Figure 3.20a is caused by the larger adsorption rate constant when oxygen adsorbs onto a vacancy at the LSM surface and the reason for the difference between R_p (OCV) and R_p under polarized conditions is a result of an electrochemical reaction at the LSM surface which further increases the rate constant of adsorption.

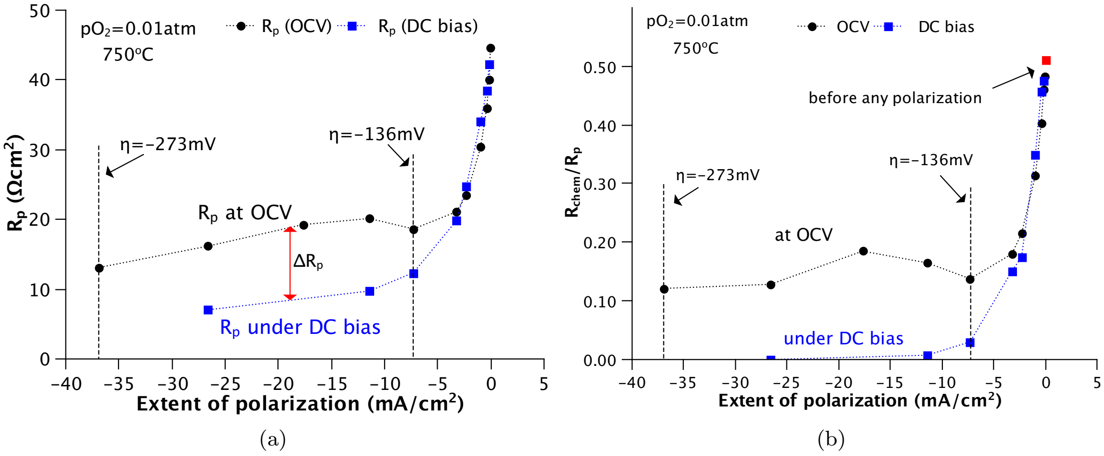

(a) (b)

Figure 3.21: Comparison of the electrode resistance of polarized electrodes measured under DC bias conditions against the resistance of polarized electrodes measured at OCV in $pO_2 = 0.01atm$ at $750°C$: (a) R_p at OCV immediately after polarization and under DC bias (b) R_{chem} contribution at OCV and under DC bias. Extent of polarization is the steady state current density achieved by the cell. Lines through data points are to guide the eye.

Concentration limited currents Some of the polarization curves presented in Figure 3.13 for $pO_2 \leq 0.001atm$ showed limiting current behavior. Limiting current behavior can be identified from a polarization curve when an increase in the electrode potential does not result in an increase in current density, and as a consequence $R_p = \partial\eta/\partial i \rightarrow \infty$. For the oxygen reduction reaction, limiting currents could occur because the flux of oxygen species is limited due to the depletion of reactants at the electrode/electrolyte interface. In addition to the identification of limiting currents from polarization curves, limiting currents can be identified in impedance spectroscopy measurements by very large values of R_{chem}.

Figure 3.23 shows sample impedance responses (Nyquist plots on the left hand column and Bode plots on the right hand column) under polarized conditions at $750°C$ in 10^{-4}atm O_2. The impedance as a function of electrode potential is presented in Figure 3.23a and shows that the total resistance increases with applied potential between $\eta = -10mV$ and $\eta = -80mV$ followed

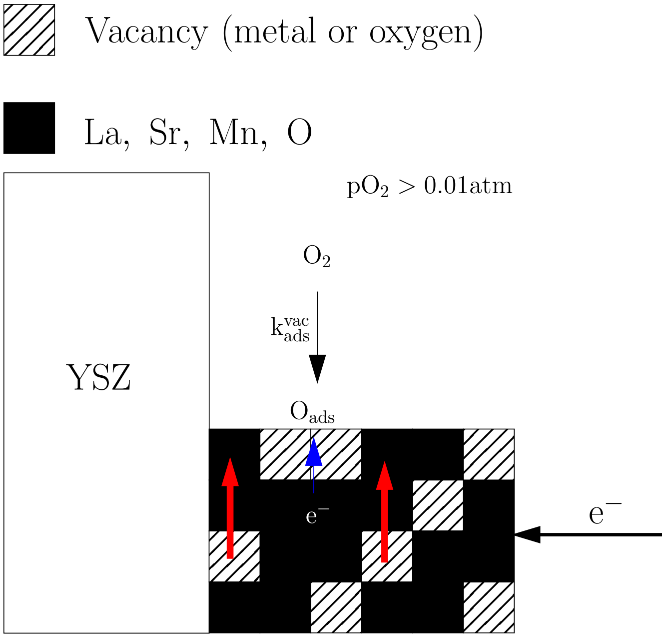

(a)

Figure 3.22: Proposed reaction mechanism for oxygen reduction on LSM electrodes in $pO_2 > 0.01atm$ under cathodic current operation. The flow of current results in a higher number of vacancies at the LSM surface which enhances the rate of adsorption. In addition, an electrochemical reaction at the gas/LSM interface provides an electrochemical activation of the adsorption reaction.

by a decrease between $\eta = -100mV$ and $\eta = -300mV$ and finally reaching a limiting current at $\eta > -300mV$. The decrease in R_p starting at around -100mV is also consistent with the slope of the polarization curve in Figure 3.13b and is caused by the reduction of the polarization resistance. Figures 3.23c and 3.23d show the impedance of the limiting current regime in more detail. As the potential is increased, the Nyquist plot of the impedance response exhibits a 45^o angle between the real and imaginary components and does not intersect the real axis at low frequencies. Fitting this impedance to an equivalent circuit results in $R_{chem} \rightarrow \infty$ and $R_{chem}/R_p = 1$, indicating limiting current behavior. The development of this limiting current at around -300mV is also mirrored in the polarization curve (Figure 3.13b).

Although the electrode was operated in a regime such that the reactant concentrations were close to zero (resulting in a limiting current), under open circuit conditions the species concentration gradients were able to return to their normal levels relatively quickly. Figures 3.23e and 3.23f show the impedance response under limiting current as well as under open circuit conditions immediately after polarizing the electrode compared against the impedance measured at OCV before any polarization. The larger impedance after being polarized to -600mV compared to the pre-polarized level is attributed to cation diffusion as previously discussed.

Ascribing the limiting current density to a single phenomenon is not straightforward for the present case. This is because there can be a number of parallel pathways for the supply of reactant species to the triple phase boundary where the current is generated. However, the processes limiting the current may include: 1) adsorption limitation 2) surface diffusion limitation 3) gas diffusion limitation. Adsorption induced concentration limitations may occur when the equilibrium surface coverage is low enough to cause concentration limitations at the LSM/YSZ interface. The equilibrium surface coverage (θ^{eq}) for dissociative adsorption is defined as:

$$\theta^{eq} = \frac{\sqrt{K_{ads}}\sqrt{pO_2}}{1 + \sqrt{K_{ads}}\sqrt{pO_2}} \tag{3.23}$$

where K_{ads} is the ratio of the adsorption and desorption rate constants which are material dependent. When the oxygen concentration is low, such as in the experiments shown in Figure 3.23, so is θ^{eq}. At the same time, if the transport of oxygen was limited due to small pore sizes, then it might be expected that the local oxygen concentration would be low which could also influence the adsorption

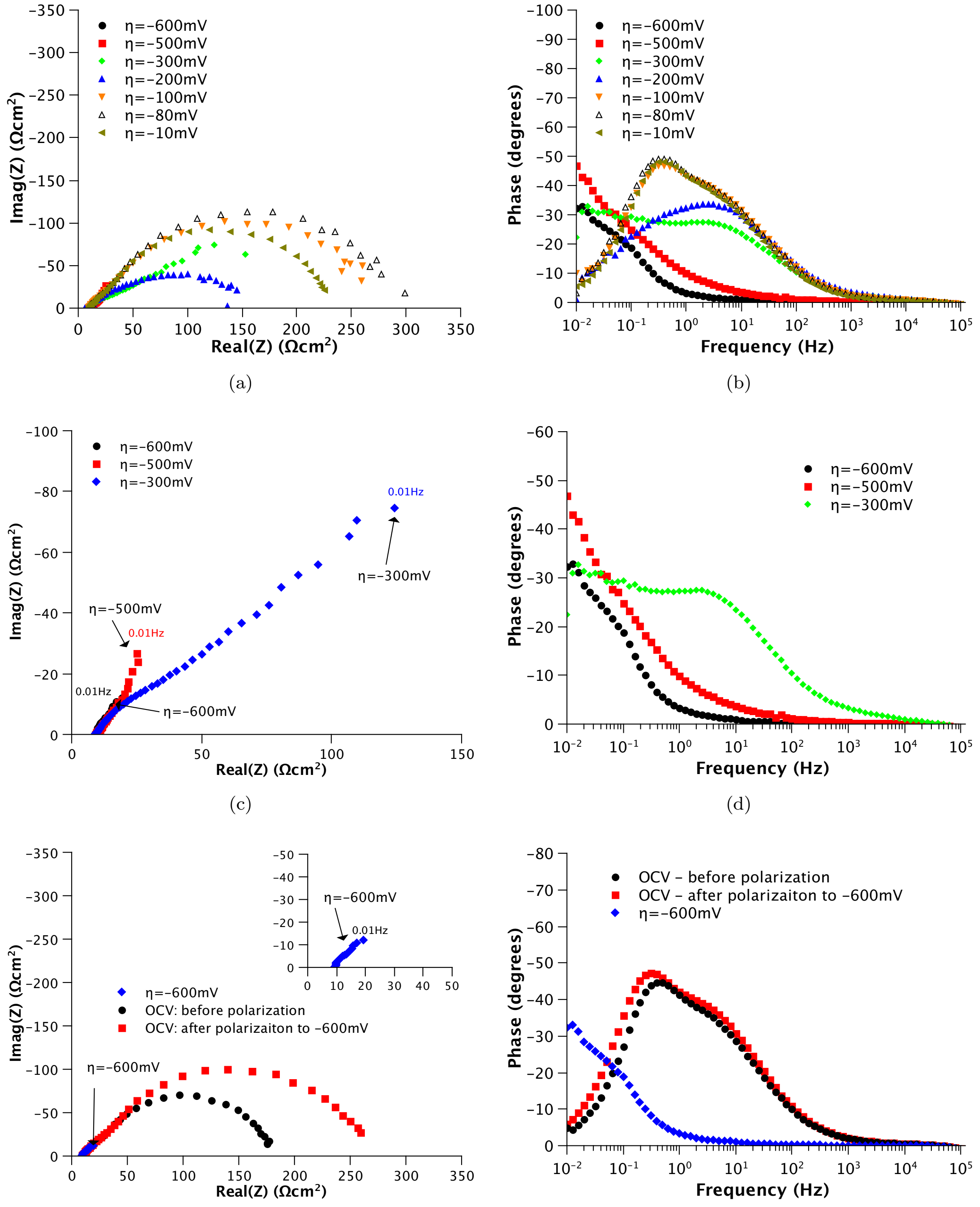

(a) (b)

(c) (d)

(e) (f)

Figure 3.23: Evolution of impedance with applied potential in 10^{-4}atm O_2 and $750°C$: (a)-(b) Nyquist and Bode plot (c)-(d) Nyquist and Bode plot at high overpotentials in concentration limited regime (e)-(f) Comparison of Nyquist and Bode plots for $\eta = -600mV$ (inset) and at OCV immediately after $\eta = -600mV$ and at OCV before any polarization.

reaction. Surface diffusion limitations however occur not necessarily because of low surface coverages but because of low surface diffusivities which may be a result of a tortuous pathway or as a result of limitations from surface species interactions.

Table 3.6 shows the overpotentials, for each pO_2, at which the electrode was completely concentration limited. The operating point at which the electrode was completely concentration limited was defined as the operating condition where $R_{chem}/R_p = 1$ (measured by impedance spectroscopy), indicating that $R_{chem} \gg R_{ct}$, and the limiting currents were taken from the polarization curve at those operating conditions. Interestingly, as the temperature increased, the overpotential at which $R_{chem}/R_p = 1$ decreased, indicating that limiting currents were reached earlier at higher temperatures. The limiting currents shown in Table 3.6 had a low activation energy of $E_a = 0.10eV$ for pO_2s between 10^{-4}atm and 5×10^{-4}atm and obeyed the relationship $i_{lim} \propto pO_2^{-n}$ with $n = 1$ over all temperature ranges.

Table 3.6: Overpotentials at which the electrode is completely concentration limited (measured by impedance spectroscopy) and their associated limiting currents (measured from polarization curves).

pO_2	Temperature	η^*	i^{**}
ppm	$^\circ C$	mV	mA/cm^2
100	750	-387	-1.64
	800	-390	-1.73
	850	-294	-1.83
250	750	-457	-5.10
	800	-372	-5.44
	850	-380	-5.50
500	750	-528	-8.13
	800	-453	-8.70
	850	-370	-8.95
1000	750	> -500	> -11.1
	800	> -530	> -11.7
	850	-547	-12.2

* From EIS when $R_{chem}/R_p = 1$
** From polarization curve

Theoretical activation energies and pO_2 dependencies of limiting currents assuming they are caused by gas diffusion limitations can be derived from the flux of oxygen gas through the porous electrode:

$$J_{O_2} = \frac{i}{4F} = -D^{eff}_{O_2-N_2}\frac{dC_{O_2}}{dx} = -D^{eff}_{O_2-N_2}\frac{C_{O_2}|_{L_1} - C_{O_2}|_{L_2}}{L_1 - L_2} \tag{3.24}$$

where $D^{eff}_{O_2-N_2}$ is the effective binary diffusion coefficient, $C_{O_2}|_{L_1}$ is the concentration of oxygen gas at the electrode/gas interface, $C_{O_2}|_{L_2}$ is the concentration of oxygen gas at the electrode/electrolyte interface, i is the current density and F is Faraday's constant. $D^{eff}_{O_2-N_2}$ depends on the electrode porosity and tortuosity and at SOFC operating temperatures, it also depends on the pore size (see Section 4.2.5 on page 164 for details).

Under gas concentration limitations, we can take $C_{O_2}|_{L_2} = 0$ and with the thickness of the electrode set at $20\mu m$, we can calculate the gas limiting current for various oxygen concentrations, temperatures and electrode microstructures. From this analysis, the theoretical pO_2 dependency of the limiting current is equal to 1 and the theoretical activation energy is equal to 0.04eV. Although the pO_2 dependency of the gas phase diffusion limitation matches well with experimental results, the activation energy differs by a factor of 2.3. This discrepancy could be a result of a mixed controlled process such as gas and adsorption limited behavior but it also does not account for the parallel pathway that exists when transporting oxygen to the triple phase boundary through either 1) the gas diffusion pathway 2) the surface diffusion pathway. Additionally, purely gas phase limitations cannot explain the observation that the concentration limitations start at lower overpotentials for higher temperatures. Additional analysis of these limiting currents is provided in Chapter 4.

Analysis of cyclic voltammagrams Some additional insight can be gained from the cyclic voltammagrams that were collected before and after electrode polarization in low pO_2. Figure 3.24a shows CVs collected at $750°C$ for oxygen partial pressures between 10^{-4}atm and 0.01atm and Figure 3.24b shows CVs collected in 10^{-4}atm at $750°C$ and $800°C$. The CVs show the current density vs overpotential when the overpotential is scanned at a rate of 1mV/s from 0mV→-600mV→0.2mV→-600mV. These CVs show a hysteresis effect whereby the forward scan rate (from 0→-600mV) has a higher current density than the reverse scan rate (-600→0mV). This hysteresis effect is caused by the fact that in the reverse scan, reactants at the triple phase boundary have been consumed (after reaching the limiting current in the forward scan) and mass transfer further limits the current density in the reverse scan direction. The larger these mass transfer limitations, the larger the hysteresis area between the forward and backwards scans.

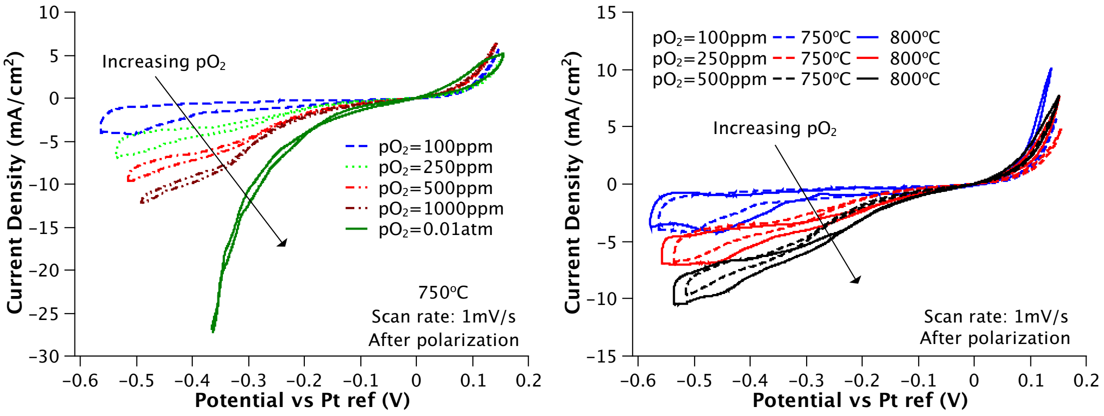

(a) (b)

Figure 3.24: Comparison of cyclic voltammagrams in low pO_2: (a) At $750°C$ and 1mV/s after electrode polarization as a function of pO_2 (b) At 1mV/s after electrode polarization as a function of temperature.

As the pO_2 is increased, as in Figure 3.24a, the hysteresis area decreases because mass transfer limitations are less restrictive. This same trend is observed in Table 3.6 which shows that the overpotentials at which $R_{chem}/R_p = 1$ increase with increasing pO_2. Figure 3.24b however shows that as the temperature increases, the hysteresis area increases, meaning that the supply of reactants to the reaction site is lower at higher temperatures. This cannot be explained by a diffusion process such as gas transport or surface diffusion, since diffusion processes are facilitated at higher temperatures. If a diffusion process was the sole cause of the concentration limitation, then we would expect the hysteresis area between the forward and reverse scans to decrease as the temperature is increased. This leads to the conclusion that the adsorption process could be important in dictating the limiting currents.

The equilibrium surface coverage was given in Equation 3.23 and depends on the adsorption/desorption equilibrium constant K_{ads}. The change in equilibrium surface coverage with temperature can be described by the van 't Hoff equation [39]:

$$\left(\frac{\partial \ln K_{ads}}{\partial T}\right)_{\theta} = \frac{\Delta_{ad} H^{\ominus}}{RT^2} \tag{3.25}$$

where K_{ads} is the ratio k_{ads}/k_{des} and $\Delta_{ad}H^{\ominus}$ is the enthalpy of adsorption. For almost all adsorption reactions on metal surfaces, $\Delta_{ad}H^{\ominus} < 0$ (and $\Delta_{ad}S < 0$) [39] which means that K_{ads}, and by extension, θ^{eq}, should decrease as the temperature increases. Reduced θ^{eq} caused by adsorption limitations could explain the larger hysteresis areas observed as temperature increases in Figure 3.24b and it could also explain the fact that limiting currents were observed to form at lower overpotentials as the temperature increased (shown in Table 3.6). This limiting current behavior for $pO_2 \leq 0.001atm$ could be further evidence for a mechanism where the adsorption reaction is not electrochemical in nature, such as that in Figure 3.12a.

Summary of Data Analysis Under Polarized Conditions

The above analysis of polarized electrodes showed that the electrical history of an LSM electrode can significantly influence its polarization resistance and pO_2 dependency. As the LSM cathode is polarized, in pO_2s $\geq$ 0.01atm, the electrode resistance decreases, primarily from a decrease in R_{chem}, caused by two mechanisms: 1) modification of the electrode surface attributed to cation diffusion into the bulk 2) an additional electrochemical process such as electrochemical adsorption or/and the migration of adsorbed oxygen species. In pO_2s $\leq$ 0.001atm, we observed a diffusion process which increases the electrode resistance. This process was attributed to cation vacancy diffusion, likely A-site vacancies, from the bulk towards the surface. The diffusion coefficients of the cation diffusion process were estimated at a maximum of 2×10^{-18} m^2/s.

At pO_2s $\geq$ 0.01atm, no limiting currents were observed however, they were observed at pO_2s $\leq$ 0.001atm. An analysis of the limiting currents from impedance measurements and CV measurements reveal that they must be influenced by adsorption limitations and although the theoretical pO_2 dependency of gas limiting currents matches well with experimental data, this cannot explain the increase in concentration limitations with temperature.

3.4 Summary/Conclusion

This chapter examined the kinetics of porous LSM electrodes in low pO_2s ($\leq$ 0.001atm) and in high pO_2s ($\geq$ 0.01atm) before and after electrode polarization. From the evaluation of the pre-polarized electrodes, the following conclusions were made:

1. The mechanism of oxygen reduction likely changes between low and high oxygen partial pressures, likely as a result of a shift in the oxygen nonstoichiometry.
2. The mechanism of oxygen reduction likely remains constant over a temperature range of $750°C$ and $850°C$.
3. For low oxygen partial pressures, there is evidence to support a mechanism where neutral adsorbed oxygen is reduced at the LSM/YSZ interface based on the reaction order of R_{ct} and the behavior of limiting currents.
4. For high oxygen partial pressures, there is evidence to support an electrochemical reaction at the gas-LSM interface, based on the reaction order of R_{ct} and on the comparison between R_{chem} of polarized electrodes under DC bias and under OCV conditions.

An important aspect of LSM electrodes is their behavior change after being polarized. From the evaluation of polarized electrodes, the following conclusions were found:

1. At high oxygen partial pressures, the resistance from the chemical components (R_{chem}) of the oxygen reduction reaction is dramatically reduced from electrode polarization which is caused by both: a) chemical modification of the LSM surface likely from cation vacancy diffusion from the bulk towards the surface which could enhance adsorption kinetics and b) electrochemical activation of a chemical process such as adsorption or migration of adsorbed oxygen species.
2. For $10^{-4}atm \leq pO_2 \leq 10^{-3}atm$, polarization increases the resistance from the chemical components of the oxygen reduction reaction which may be caused from chemical modification of the LSM surface, likely the removal of cation vacancies from the LSM surface, whereas the reverse is likely true for $0.01atm \leq pO_2 \leq 0.21atm$. This is also consistent with the oxygen nonstoichiometry of LSM within these oxygen partial pressures.
3. Cation diffusion, which may be the cause of the electrical history effect of LSM, has a maximum diffusion coefficient of $2 \times 10^{-18}\ m^2/s$ in both high and low pO_2s.
4. The effects of the electrical history are reversible over long periods of time.

5. Limiting currents were observed in low pO_2s and were related to a mixture of adsorption and gas diffusion limitations.

References

[1] S.B. Adler. Factors Governing Oxygen Reduction in Solid Oxide Fuel Cell Cathodes. *Chemical Reviews*, 104:4791–4843, 2004.

[2] E. Siebert, A. Hammouche, and M. Kleitz. Impedance Spectroscopy Analysis of $La_{1-x}Sr_xMnO_3$-Yttria-Stabilized Zirconia Electrode Kinetics. *Electrochimica Acta*, 40(11):1741–1753, 1995.

[3] Y. Jiang, S. Wang, Y. Zhang, J. Yan, and W. Li. Kinetic Study of the Formation of Oxygen Vacancy on Lanthanum Manganite Electrodes. *Journal of the Electrochemical Society*, 145(2):373–378, 1998.

[4] G.J. La O', R.F. Savinell, and Y. Shao-Horn. Activity Enhancement of Dense Strontium-Doped Lanthanum Manganite Thin Films under Cathodic Polarization: A Combined AES and XPS Study. *Journal of the Electrochemical Society*, 156(6):B771–B781, 2009.

[5] V. Brichzin, J. Fleig, H.U. Habermeier, G. Cristiani, and J. Maier. The geometry dependence of the polarization resistance of Sr-doped LaMnO3 microelectrodes on yttria-stabilized zirconia. *Solid State Ionics*, 152-153:499–507, 2002.

[6] J. Van Herle, A.J. McEvoy, and K. Ravindranathan Thampi. A study on the $La_{1-x}Sr_xMnO_3$ oxygen cathode. *Electrochimica Acta*, 41(9):1447–1454, 1996.

[7] Y. Takeda, R. Kanno, M. Noda, Y.Tomida, and O. Yamamoto. Cathodic Polarization Phenomena of Perovskite Oxide Electrodes with Stabilized Zirconia. *Journal of the Electrochemical Society*, 134(11):2656–2661, 1987.

[8] A.C. Co and V. Birss. Mechanistic Analysis of the Oxygen Reduction Reaction at $(La, Sr)MnO_3$ Cathode in Solid Oxide Fuel Cells. *Journal of Physical Chemistry B*, 110:11299–11309, 2006.

[9] E.P. Murray, T. Tsai, and S.A. Barnett. Oxygen transfer processes in $(La, Sr)MnO_3/Y_2O_3$-stabilized ZrO_2 cathodes: an impedance spectroscopy study. *Solid State Ionics*, 110:235–243, 1998.

[10] M. Ostergard and M. Mogensen. ac Impedance Study of the Oxygen Reduction Mechanism on $La_{1-x}Sr_xMnO_3$ in Solid Oxide Fuel Cells. *Electrochimica Acta*, 38(14):2015–2020, 1993.

[11] F.H. van Heuveln and H.J.M. Bouwmeester. Electrode Properties of Sr-Doped $LaMnO_3$ on Yttria-Stabilized Zirconia: II. Electrode Kinetics. *Journal of the Electrochemical Society*, 144(1):134–140, 1997.

[12] A.C. Co, S.J. Xia, and V.I. Birss. A Kinetic Study of the Oxygen Reduction Reaction at $\mathrm{LaSrMnO_3 - YSZ}$ Composite Electrodes. *Journal of the Electrochemical Society*, 152(3):A570–A576, 2005.

[13] X.J. Chen, K.A. Khor, and S.H. Chan. Identification of O_2 reduction processes at yttria stabilized zirconia—doped lanthanum manganite interface. *Journal of Power Sources*, 123:17–25, 2003.

[14] Wei Wang and San Ping Jiang. A mechanistic study on the activation process of $(La, Sr)MnO_3$ electrodes of solid oxide fuel cells. *Solid State Ionics*, 177:1361–1369, 2006.

[15] Y. Jiang, S. Wang, Y. Zhang, J. Yan, and W. Li. Electrochemical reduction of oxygen on a strontium doped lanthanum manganite electrode. *Solid State Ionics*, 110:111–119, 1998.

[16] Finn Willy Poulsen. Defect chemistry modelling of oxygen-stoichiometry, vacancy concentrations, and conductivity of $(La_{1-x}Sr_x)_yMnO_{3\pm\delta}$. *Solid State Ionics*, 129:145–162, 2000.

[17] J.H. Kuo, H.U. Anderson, and D.M. Sparlin. Oxidation-Reduction Behavior of Undoped and Sr-Doped $LaMnO_3$ Nonstoichiometry and Defect Structure. *Journal of Solid State Chemistry*, 83:52–60, 1989.

[18] Andreas Mitterdorfer. *Identification of the Oxygen Reduction at Cathodes of Solid Oxide Fuel Cells*. PhD thesis, Swiss Federal Institute of Technology, February 1997.

[19] Evgenij Barsoukov and J. Ross Macdonald. *Impedance Spectroscopy: Theory, Experiment and Applications*. Wiley-Interscience, 2 edition, 2005.

[20] A. Mitterdorfer and L.J. Gauckler. $La_2Zr_2O_7$ formation and oxygen reduction kinetics of the $La_{0.85}Sr_{0.15}Mn_yO_3$, O_2(g)—YSZ system. *Solid State Ionics*, 111:185–218, 1998.

[21] YongMan Choi, Matthew E. Lynch, M.C. Lin, and Meilin Liu. Prediction of O_2 Dissociation Kinetics on $LaMnO_3$-Based Cathode Materials for Solid Oxide Fuel Cells. *Journal of Physical Chemistry C*, 113:7290–7297, 2009.

[22] Eugene A. Kotomin, Yuri A. Mastrikov, Eugene Heifets, and Joachim Maier. Adsorption of atomic and molecular oxygen on the $LaMnO_3$ (001) surface: ab initio supercell calculations and thermodynamics. *Physical Chemistry Chemical Physics*, 10:4644–4649, 2008.

[23] R.A. De Souza and J.A. Kilner. Oxygen transport in $La_{1-x}Sr_xMn_{1-y}Co_yO_{3-\delta}$ perovskites. Part 2. Oxygen surface exchange. *Solid State Ionics*, 126:153–161, 1999.

[24] A. Svensson, S. Sunde, and K. Nisancioglu. Mathematical modeling of oxygen exchange and transport in air-perovskite-YSZ interface regions. 2. Direct exchange of oxygen vacancies. *Journal of the Electrochemical Society*, 145(4):1390–1400, 1998.

[25] Gabor A. Somorjai. *Introduction to surface chemistry and catalysis*. John Wiley & Sons, Inc, 1994.

[26] J. Bockris and S. Srinivasan. *Fuel Cells: Their Electrochemistry*. McGraw-Hill Book Company, 1969.

[27] S.H. Jeong, I.S. Bae, Y.S. Shin, S.-B. Lee, H.-T. Kwak, and J.-H. Boo. Physical and electrical properties of ZrO_2 and YSZ high-k gate dielectric thin films grown by RF magnetron sputtering. *Thin Solid Films*, 475:354–358, 2005.

[28] A. Bondi. van der Waals Volumes and Radii. *Journal of Physical Chemistry*, 68(3):441–451, 1964.

[29] Ben Kenney, Mikelis Valdmanis, Craig Baker, J.G. Pharoah, and Kunal Karan. Computation of TPB length, surface area and pore size from numerical reconstruction of composite solid oxide fuel cell electrodes. *Journal of Power Sources*, 128(2):1051–1059, 2009.

[30] J. Ross Macdonald. *Impedance Spectroscopy: Emphasizing Solid Materials And Systems.* John Wiley & Sons, 1987.

[31] S. McIntosh, S.B. Adler, J.M. Vohs, and R.J. Gorte. Effect of Polarization on and Implications for Characterization of LSM-YSZ Composite Cathodes. *Electrochemical and Solid State Letters*, 7(5):A111–A114, 2004.

[32] J. Fleig. On the current-voltage characteristics of charge transfer reactions at mixed conducting electrodes on solid electrolytes. *Physical Chemistry Chemical Physics*, 7:2027–2037, 2005.

[33] S.P. Jiang and J.G. Love. Observation of structural change induced by cathodic polarization on $(La, Sr)MnO_3$ electrodes of solid oxide fuel cells. *Solid State Ionics*, 158:45–53, 2003.

[34] A. Mitterdorfer and L.J. Gauckler. Identification of the reaction mechanism of Pt, O2(g)/YSZ system Part 1: General framework, modeling and structural investigation. *Solid State Ionics*, 117:187–202, 1999.

[35] Ivar Waernhus, Natsuko Sakai, Harumi Yokokawa, Tor Grande, Mari-Ann Einarsrud, and Kjell Wiik. Cation diffusion in $La_{1-x}Sr_xFeO_{3-\delta}$, x=0 and 0.1 measured by SIMS. *Solid State Ionics*, 178:907–914, 2007.

[36] Marian Palcut, Jens S. Christensen, Kjell Wiik, and Tor Grande. Impurity diffusion of ^{141}Pr in $LaMnO_3$, $LaCoO_3$ and $LaFeO_3$ materials. *Physical Chemistry Chemical Physics*, 10:6544–6552, 2008.

[37] Shogo Miyoshi and Manfred Martin. B-Site cation diffusivity of Mn and Cr in perovskite-type $LaMnO_3$ with cation-deficit nonstoichiometry. *Physical Chemistry Chemical Physics*, 11:3063–3070, 2009.

[38] R.A. De Souza and J.A. Kilner. Oxygen transport in $La_{1-x}Sr_xMn_{1-y}Co_yO_{3-\delta}$ perovskites. Part 1. Oxygen tracer diffusion. *Solid State Ionics*, 106:175–187, 1998.

[39] Peter Atkins and Julio De Paula. *Atkins' Physical Chemistry.* W.H. Freeman and Company, 8 edition, 2006.

Chapter 4

Modelling of Transport and Kinetic Processes of Porous LSM Cathodes

4.1 Introduction

Electrode processes typically involve a combination of coupled transport, chemical and electrochemical processes. The kinetics of these processes determine the overall current/voltage behavior of the electrode, which can be measured using either steady state or transient techniques such as electrochemical impedance spectroscopy. The analysis of electrochemical data usually considers simple models of a proposed oxygen reduction mechanism in an attempt to relate electrochemical kinetic parameters, such as the reaction order and the charge transfer coefficients, to a specific process, as was done in Chapter 3. This analysis technique is widely used for SOFC cathodes in studies such as [1–9]. Usually, an underlying assumption in these simple models is the existence of a single rate determining step. This implies that either measured or experimentally obtained electrochemical kinetic parameters are for a specific process and that there is no influence of processes that precede or follow the rate determining step and further, that parallel pathways do not exist. However, as was pointed out by Svensson *et al.* [10], when multiple processes contribute to the overall resistance of the electrode, theoretically the reaction order can fall within a wide range and will depend on the specific transport coefficients or kinetic rate constants of each process. Although tools such as electrochemical impedance spectroscopy allow delineation of the contribution of different processes from the cell impedance, if two processes have similar time constants or if there are two parallel reaction pathways, then the distinguishing features of the impedance response of separate arcs end up overlapping [11], complicating the interpretation. Further, a porous electrode represents a "distributed" system wherein spatial variations in relevant potentials – concentration, electronic potential, ionic potential – can exist. An example analysis of effects of the distributed system on "apparent" kinetic parameters was examined by Kenney and Karan [12].

For these reasons, it is useful to analyze the electrochemical data from a physical perspective, that is, considering the coupled physico-chemical processes in the analysis of the polarization and impedance response. In essence, this involves modelling of the rates of each of the chemical and transport processes involved in the electrode reactions. In this type of physics based electrochemical analysis, microstructure independent kinetic rate constants and transport coefficients for each process can be estimated and so the contributions of individual processes to the overall electrode resistance can be determined and compared. The advantage that this technique holds over a conventional simplified analysis mentioned above is: 1) it is not required to make an assumption of a rate determining step, which may or may not exist 2) the technique inherently accounts for parallel pathways since the kinetics of individual processes determine the relative contributions of each pathway 3) thermodynamic consistency can be enforced 4) the full range of experimental data can be used simultaneously, rather than just the limits of high or low overpotentials.

Multi-step electrochemical models have been used in the past to analyze the oxygen reduction reaction in electrochemical systems. For example, van Hassel *et al.* [13, 14] developed a steady state and impedance model to describe the oxygen reduction at a dense Au/YSZ interface while Mitterdorfer and Gauckler [15, 16] developed a steady state and impedance model for the dense Pt/YSZ system. Although van Hassel *et al.* considered charged adsorbates in their model, they did not consider the transport of surface species along the electrode, and in the model of Mitterdorfer and Gauckler [15,16], the surface diffusion length was presupposed. More recently, multi-step models to analyze the steady state anode behavior have emerged from Vogler *et al.* [17] and Goodwin *et al.* [18] which considered the dense Ni/YSZ system. In all cases mentioned above, because each study was concerned with dense electrodes, the intricacies of porous transport were ignored along with gas phase transport. While Svensson *et al.* [10, 19] considered transport through a porous cathode, they also did not account for gas phase transport nor did they present a method to calculate the electrode impedance. In addition, the steady state model presented by Svensson *et al.* was primarily a theoretical study and no attempt was made to fit the model to experimental data and therefore, the model parameter set was varied over a very large range.

In the present work, a physics based steady-state and impedance model is developed for a porous LSM electrode where two parallel pathways for the transport of oxygen are considered: 1) molecular oxygen transport through the gas phase 2) atomic oxygen transport along the surface of the porous LSM cathode. Estimates of the microstructural independent kinetic rate constants and transport coefficients are then obtained by fitting the model against experimental data presented in Chapter 3. From these kinetic rate constants and transport coefficients, the contributions of each process to the total electrode resistance can be obtained.

The focus of the model fitting is limited to experimental data collected in $10^{-4} atm \leq pO_2 \leq 10^{-3} atm$ where it is thought (see conclusions of Chapter 3) that the LSM surface behaves more metallic due to the fact that oxygen in the LSM lattice is stoichiometric within this oxygen partial pressure range. In addition, at these low oxygen partial pressures, gas phase transport is expected to be important owing to the low oxygen concentrations and additional experimental features such as limiting currents and the presence of low frequency peaks in the impedance response offer improved discrimination of processes and thereby better estimation of associated characteristic kinetic and transport parameters.

This Chapter is split into the following sections:

- Section 4.2 outlines the model development, including a derivation of the kinetic and transport equations describing oxygen reduction in the porous LSM cathode. In this section, the estimation of model parameters is also discussed.
- Section 4.3 discusses the general behavior of the model and how various parameters can influence the current/voltage response of the electrode.

- Section 4.4 discusses the fitting of kinetic rate constants and transport coefficients to experimental steady state polarization curves and experimental impedance curves.

4.2 Model Development

In this section, the development of the kinetic/transport model of oxygen reduction in porous LSM cathodes is described. The model is developed for both the steady state and the transient cases so that both steady state polarization curves and the impedance responses can be calculated. Figure 4.1 shows a representation of the processes at various length scales considered in the model of the porous LSM cathode, from the macro-scale (Figure 4.1a) to the micro-scale (Figure 4.1b). The physico-chemical processes that are considered in this model include: 1) gas phase convection and diffusion through the porous electrode 2) adsorption and desorption of oxygen species onto or from the LSM surface 3) transport of adsorbed oxygen along the LSM surface 4) transport of electronic charge through the electrode 5) charge transfer at the LSM/YSZ interface. It was assumed that the pathway involving bulk oxygen transport through LSM was blocked due to the low oxygen vacancy diffusion coefficient of LSM.

The model uses volume averaging techniques to calculate species fluxes while relevant microstructural parameters such as the triple phase boundary length, the internal surface area and the pore size were obtained either from SEM images of real electrodes or from a numerical electrode construction technique described in [20]. The transport of oxygen and charged species are described by general species balances in porous media and coupled to the adsorption/desorption reactions described by the laws of mass action as well as the electrochemical reaction described by classical Butler-Volmer kinetics.

The sections that follow discuss key aspects of the model derivation and solution methodology. Specifically:

- Section 4.2.1 discusses the model geometry
- Section 4.2.2 discusses the model assumptions
- Section 4.2.3 discusses the general species balance in porous media used to describe the transport of various species in this model

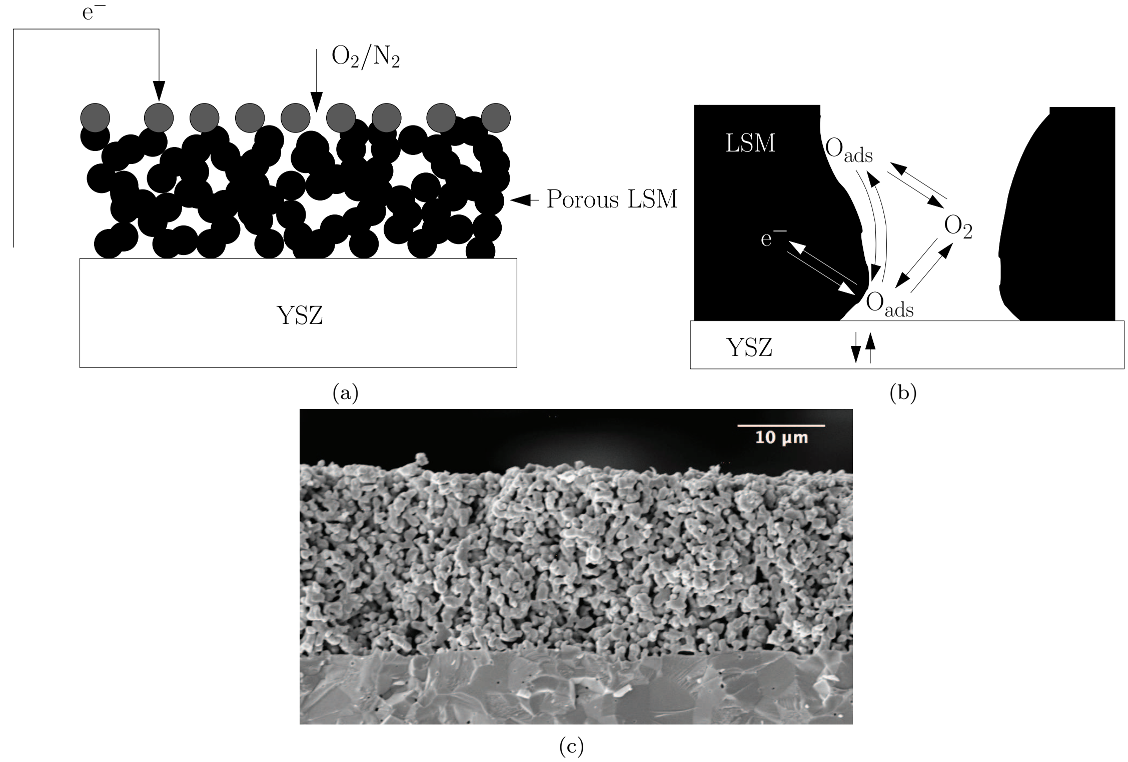

(a) (b)

(c)

Figure 4.1: (a) Representation of porous LSM electrode being modelled (b) Oxygen reduction mechanism considered in the detailed model involving transport of oxygen to LSM/YSZ interface by either (i) adsorption and surface diffusion pathway (ii) gas phase transport and adsorption pathway. Each of these pathways are then followed by an electrochemical reaction at the LSM/YSZ interface. (c) Example SEM cross-section image of actual LSM electrode being modelled.

- Section 4.2.4 discusses the derivation of the model equations
- Section 4.2.5 discusses the various model parameters
- Section 4.2.6 discusses the solution of the coupled partial differential equations

4.2.1 Model Geometry

The model geometry approximates the porous LSM samples evaluated in Chapter 3. The model domain is a one-dimensional line drawn from the current collector-gas/electrode interface to the electrode/electrolyte interface. This domain is applicable to the model assumptions stated below. Figure 4.2a shows the domain along with the locations of the boundary conditions, at $x = 0$ corresponding to the gas/electrode interface, $x = L$ corresponding to the electrode/electrolyte interface and $x = L_e$ corresponding to the location of the reference electrode in the electrolyte. The electrode thickness (L) was $20\mu m$, which reflects the thickness of the cathodes characterized experimentally. Figure 4.2b shows an example of the geometry and grid points representing the one-dimensional line drawn through the porous LSM cathode. The geometry was meshed using the commercial software package Comsol Multiphysics so that grid points were more densely packed close to the LSM/YSZ interface where gradients are expected to be large.

4.2.2 Model Assumptions

The model contains a number of assumptions:

1. Although possible to include in the model, it was assumed that oxygen adsorption and surface transport on the YSZ electrolyte was negligible owing to the much larger surface area of the porous LSM cathode. The total surface area of the LSM phase available for oxygen adsorption in a standard $20\mu m$ thick electrode with cross sectional area of $1.2cm^2$ is $96cm^2$ (with an internal surface area of $4 \times 10^6\ m^2/m^3$) whereas the exposed surface of the YSZ electrolyte is only $0.7cm^2$. It was also assumed that the dominant mechanism for oxygen reduction involved gas transport, adsorption, surface diffusion of neutral adsorbates followed by a charge transfer reaction. Based on the analysis of the experimental data, this mechanism is most applicable to LSM cathodes which have stoichiometric quantities of oxygen in the lattice (ie. $\delta = 0$) which

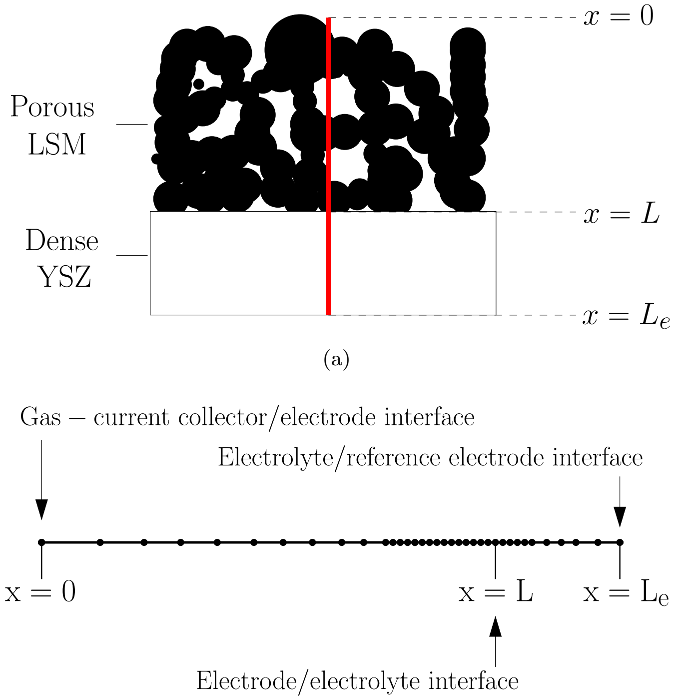

(a)

(b)

Figure 4.2: (a) Model domain - the line through the image represents the 1 dimensional domain with current collector-gas/LSM interface at $x = 0$, LSM/YSZ interface at $x = L$ and the electrolyte at $x = L_e$ (b) Example of grid placement in model (not to scale)

occurs for a pO_2 range between 10^{-8}atm and 10^{-3}atm. A mechanism involving a charge transfer reaction at the gas/LSM surface, which may occur for LSM with an excess of oxygen in the lattice, is outside of the scope of this thesis, but, model equations for this scenario were derived and are presented in Appendix A.

2. It was assumed that the electrode was completely homogeneous in particle shape and pore shape. In addition, it was assumed that the influence of grain boundaries as well as any local composition changes within the $La_xSr_{1-x}MnO_{3\pm\delta}$ lattice only influenced the double layer capacitance which was ignored for the steady state case and modelled using a constant phase element for the transient impedance simulations. The particle size and pore size and their distributions were not modelled explicitly, although these microstructural features were accounted for when calculating [20] or measuring the characteristic dimension used to describe the rate of the process (for example, the internal surface area used to model the adsorption/desorption reactions).

3. Owing to the small size of the electrode being modelled, it was assumed that temperature gradients did not exist in the electrode. If these gradients were present, then they would affect a number of processes and require additional information, most importantly, the activation energy of the adsorption/desorption process, surface diffusion process and charge transfer process. Similarly, it was assumed that the microstructural features such as internal surface area, pore size and triple phase boundary length did not change with temperature. Although it is difficult to verify this assumption, the temperature range being modelled was relatively small, between $750°C$ and $850°C$ and so within this $100°C$ temperature change, it was assumed that there would be no significant microstructural changes within the electrode.

4.2.3 General Species Balance in Porous Media

The differential equations describing various transport steps were derived from the generalized species balance through porous media. Figure 4.3 represents a thin slab of a porous LSM cathode volume through which the species involved in the oxygen reduction reaction (ORR) are transported. The general balance on any species through this control volume is represented by Equation 4.1.

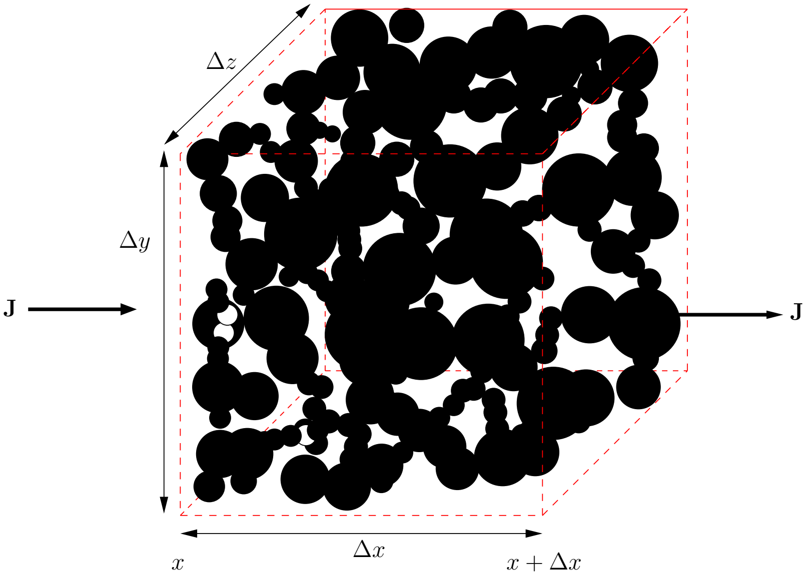

Figure 4.3: Control volume of a porous LSM cathode through which species are transported, consumed, and/or produced.

$$\begin{pmatrix}\text{species accumulation}\\ \text{in its respective phase}\end{pmatrix} = \begin{pmatrix}\text{species in}\\ \text{at } x \text{ over } \Delta t\end{pmatrix} - \begin{pmatrix}\text{species out}\\ \text{at } x+\Delta x \text{ over } \Delta t\end{pmatrix} + \begin{pmatrix}\text{Net rate of volumetric}\\ \text{generation over } \Delta t\end{pmatrix} \tag{4.1}$$

If J represents the flux of a species such as oxygen gas, oxygen adsorbates, electronic charge or ionic charge with units of $(quantity/m^2/s)$ and Ψ is the concentration of that species within its phase with units of $(quantity/m^3)$, then the balance described by Equation 4.1 becomes:

$$\xi \Delta\Psi \Delta V = J\big|_{x} \Delta A \Delta t - J\big|_{x+\Delta x} \Delta A \Delta t + a R_{net} \Delta V \Delta t \tag{4.2}$$

where $\Delta V = \Delta x \Delta y \Delta z$ and $\Delta A = \Delta y \Delta z$, R_{net} is the net rate of species generation, ξ accounts for the porous nature of the control volume and a is the characteristic dimension of the reaction (such as the gas-LSM internal surface area in the case of the adsorption/desorption reactions). ξ corrects for the volume that is not considered by the species concentration. Dividing both sides of Equation 4.2 by $\Delta x \Delta y \Delta z \Delta t$ and taking the limit as Δx and Δt go to 0 results in

$$\xi \frac{d\Psi}{dt} = -\frac{dJ}{dx} + aR_{net} \tag{4.3}$$

In general, the flux can be divided into two components: 1) a convective flux, J_{conv} 2) a diffusive flux, J_{diff}. Other types of fluxes such as a thermal flux are ignored here. The convective and diffusive fluxes can be defined by

$$J_{tot} = J_{conv} + J_{diff} = \xi u_x \Psi - \Gamma^{eff} \frac{d\Psi}{dx} \tag{4.4}$$

where u_x is the pore velocity of the fluid and Γ^{eff} is an effective transport coefficient for a species accounting for the porous nature of the electrode and the tortuous pathway that the species must travel. Combining Equations 4.3 and 4.4 and generalizing to 3-dimensions results in the general transport equation for species Ψ:

$$\xi \frac{d\Psi}{dt} + \nabla(\xi u \Psi) = \nabla \cdot (\Gamma^{eff} \nabla \Psi) + aR_{net} \tag{4.5}$$

Equation 4.5 can be used for any species transported through porous media, where Ψ is the species concentration. It is important however to ensure that proper units are used which typically means that the species balance should always be derived from basic flux balances to ensure consistency.

4.2.4 Mathematical Description of Reaction-Transport Processes in Porous LSM Electrodes

The overall oxygen reduction reaction (ORR) is:

$$O_2(g) + (4e^-)^{ed} \rightleftharpoons (2O^{2^-})^{el} \tag{4.6}$$

where superscripts *ed* refers to the cathode and *el* refers to the electrolyte phase. Figure 4.1b graphically depicts the key processes considered in this porous electrode model. The mathematical expressions describing the individual steps of the oxygen reduction reaction processes are shown below:

(i) Gas transport:

$$J_{O_2} = \epsilon u \rho_{O_2} - D_{O_2-N_2} \frac{\epsilon}{\tau} \frac{d\rho_{O_2}}{dx} \tag{4.7}$$

(ii) Dissociative adsorption/desorption of O_2:

$$O_2(g) + 2s \underset{k_{des}}{\overset{k_{ads}}{\rightleftharpoons}} 2O_{ads}$$

$$\frac{1}{2} N R_\theta = -\frac{1}{M_{O_2}} R_{O_2} = k_{ads} pO_2 N^2 (1-\theta)^2 - k_{des} N^2 \theta^2 \tag{4.8}$$

(iii) Surface diffusion:

$$J_{O_{ads}} = -D_{O_{ads}} \frac{a}{\tau} N \frac{d\theta}{dx} = -aND^{eff}_{O_{ads}} \frac{d\theta}{dx} \tag{4.9}$$

(iV) Charge transfer at the LSM/YSZ interface:

$$O_{ads} + (2e^-)^{ed} + (V_{\ddot{O}})^{el} \underset{k_b}{\overset{k_f}{\rightleftharpoons}} (O_O^x)^{el} + s$$

$$i_{far} = -nF\lambda_{tpb} k_f N \theta C_{V_{\ddot{O}}} + nF\lambda_{tpb} k_b C_{O_O^x} N(1-\theta) \tag{4.10}$$

In Equation 4.7, ρ_{O_2} is the density of oxygen gas, u is the pore velocity and τ is the gas phase tortuosity. The net rate of the adsorption and desorption reaction is given by Equation 4.8 where R_θ gives the net rate in terms of adsorbed oxygen and R_{O_2} gives the net rate in terms of molecular oxygen. In Equation 4.8, $\theta = C_{O_{ads}}/N$ where $C_{O_{ads}}$ is the surface concentration of oxygen adsorbates, N is the total surface site concentration, θ the dimensionless surface coverage and M_{O_2} is the molar mass of O_2. The rate constants of adsorption and desorption, k_{ads} and k_{des} have units of $m^2/mol/s/atm$ and $m^2/mol/s$ respectively. The rate of the electrochemical reaction describes the Faradaic current through the electrode, Equation 4.10, where k_f and k_b are electrochemical rate constants with units of $m^4/mol^2/s$, λ_{tpb} is the triple phase boundary length with units of m/m^2 and $C_{V_{\ddot{O}}}$ and $C_{O_O^x}$ are the concentrations of oxygen vacancies and oxygen in the YSZ lattice, each with units of mol/m^3, assumed to be constant and assumed to be set by the Yttria dopant concentration in Zirconia.

Species transport The model considers the transport of five species: 1) oxygen gas 2) adsorbed oxygen 3) electrons 4) ions and 5) momentum. Each of these species are coupled to each other through the cell current and/or the net rate of adsorption/desorption. The adsorption/desorption reaction represents the net consumption or generation of oxygen gas and surface species as these species are transported through the porous electrode, and the net rate is given by Equation 4.8. Making use of the general transport equation (Equation 4.5), the species transport coefficients are presented in Table 4.1.

Table 4.1: List of transport coefficients to describe mathematical model using generalized transport equation (Equation 4.5)

Species	Ψ	Γ^{eff}	R_{net}	u	ξ
Oxygen gas	ρ_{O_2}	$D^{eff}_{O_2-N_2}$	R_{O_2}	$-\kappa/\mu\ \nabla P_{tot}$	ϵ
Adsorbed oxygen	θ	aD^{eff}_{θ}	R_θ	0	a
Electronic charge	ϕ_{el}	σ^{eff}_{el}	0	0	0
Ionic charge	ϕ_{io}	σ_{io}	0	0	0
Momentum	P_{tot}	$-\rho_{tot}\kappa/\mu$	R_{O_2}	0	0

The five transport equations described in Table 4.1 require boundary conditions at the gas-current collector/electrode interface ($x = 0$) and at the LSM/YSZ interface ($x = L$) in addition to initial conditions. These boundary conditions are either species blocking conditions such as $J = 0$, flux conditions proportional to the current density such as $J \propto i$ or concentration boundary conditions. The boundary conditions for each species are presented in Table 4.2. A thorough derivation of these transport equations and their boundary conditions is given in Appendix A.

Table 4.2: List of boundary conditions for the transport equations shown in Table 4.1. The boundary locations are shown in Figure 4.2.

Species	Ψ	$x = 0^*$	$x = L^{**}$	$t = 0$
Oxygen gas	ρ_{O_2}	$\rho_{O_2} = \rho^{bulk}_{O_2}$	$d\rho_{O_2}/dx = 0$	$\rho_{O_2} = \rho^{bulk}_{O_2}$
Adsorbed oxygen	θ	$d\theta/dx = 0$	$-D^{eff}_{\theta}\ d\theta/dx = i_{far}/(2F)$	$\theta = \theta^{eq}$
Electronic charge	ϕ_{el}	$\phi_{el} = \Delta\phi^{applied}_{el}$	$\sigma^{eff}_{el}\ d\phi_{el}/dx = i_{tot}$	$\phi_{el} = \Delta\phi^{applied}_{el}$
Ionic charge	ϕ_{io}	$-\sigma_{io}\ d\phi_{io}/dx = i_{tot}$	$\phi_{io} = 0$	$\phi_{io} = 0$
Momentum	P_{tot}	$P_{tot} = P$	$dP_{tot}/dx = 0$	$P_{tot} = P$

* For ionic potential, this boundary is actually $x = L$

** For ionic potential, this boundary is actually $x = L_e$

Once the current is related to the potential and species concentrations, the equations described in Table 4.1 with boundary conditions shown in Table 4.2 represent a well defined system and can be solved.

Electrochemical kinetics The derivations above described the transport of species through the porous electrode, however, they are all coupled to the electrochemical reaction at the LSM/YSZ interface. A generalized approach to describe the kinetics of electrochemical reactions was given in Section 2.4.1 (page 68, Chapter 2) and is followed here. The Faradaic current can be calculated by multiplying the rate of the charge transfer reaction at the LSM/YSZ interface by the factor nF and is shown in Equation 4.10. For convenience, we can separate the electrochemical reaction rate constants into their chemical and electrochemical components and we can define the electrode potential as $\Delta\phi = \Delta\phi^{eq} + \eta$. The cathodic and anodic components of the Faradaic current become:

$$i_{cathodic} = nF\lambda_{tpb}k_f^0 N\theta C_{V_{\ddot{O}}} \exp\left(\frac{-\beta nF}{RT}\Delta\phi^{eq}\right)\exp\left(\frac{-\beta nF}{RT}\eta\right) \tag{4.11a}$$

$$i_{anodic} = nF\lambda_{tpb}k_b^0 C_{O_O^x} N(1-\theta)\exp\left(\frac{(1-\beta)nF}{RT}\Delta\phi^{eq}\right)\exp\left(\frac{(1-\beta)nF}{RT}\eta\right) \tag{4.11b}$$

where the equilibrium potential, $\Delta\phi^{eq}$, is

$$\Delta\phi^{eq} = \frac{RT}{nF}\ln\left(\frac{k_f^0}{k_b^0}\right) + \frac{RT}{nF}\ln\left(\frac{\theta^{eq}}{1-\theta^{eq}}\right) + \frac{RT}{nF}\ln\left(\frac{C_{V_{\ddot{O}}}}{C_{O_O^x}}\right) \tag{4.12}$$

Further following the mathematical treatment of Section 2.4.1, the exchange current density is

$$i_0 = nF[\lambda_{tpb}k_b^0 N(1-\theta^{eq})C_{O_O^x}]^{\beta}[\lambda_{tpb}k_f^0 N\theta^{eq}C_{V_{\ddot{O}}}]^{(1-\beta)} \tag{4.13}$$

and the net Faradaic current is

$$i_{far} = i_0\left[\frac{1-\theta}{1-\theta^{eq}}\exp\left(\frac{(1-\beta)nF}{RT}\eta\right) - \frac{\theta}{\theta^{eq}}\exp\left(-\frac{\beta nF}{RT}\eta\right)\right] \tag{4.14}$$

Since i_0 is a function of θ^{eq}, it is also related to pO_2^{eq} when the oxygen adsorption/desorption reaction, given in Equation 4.8, is at equilibrium. The current described by Equation 4.14 is known as the

Faradaic current, or a current resulting from steady state conditions without the influence of the charge double layer. In the transient case, the double layer at the electrode/electrolyte interface is either charged or discharged and this charging/discharging results in a capacitative current, which, for an ideal capacitor, can be described by

$$i_{dl} = A_{dl} C_{dl} \frac{d\eta}{dt} \tag{4.15}$$

where A_{dl} is the contact area between the electrode and the electrolyte with units of m^2 contact area/m^2 total area and C_{dl} is the capacitance of the double layer with units of F/m^2. Under transient conditions such as an impedance calculation, the total current at the LSM/YSZ interface is:

$$i_{tot} = i_{far} + i_{dl} = i_0 \left[\frac{1-\theta}{1-\theta^{eq}} \exp\left(\frac{(1-\beta)nF}{RT} \eta \right) - \frac{\theta}{\theta^{eq}} \exp\left(-\frac{\beta nF}{RT} \eta \right) \right] + A_{dl} C_{dl} \frac{d\eta}{dt} \tag{4.16}$$

The electrode overpotential, η, was defined as the difference in the electric potential of the electrode and the electric potential of the electrolyte at the point $x = L$: $\eta = (\phi_{el} - \phi_{io})|_{x=L}$.

4.2.5 Model Parameters: Calculation/Estimation of Transport Coefficients and Rate Constants

The equations describing oxygen reduction in Section 4.2.4 require several transport, kinetic and microstructural parameters that must be either calculated (when possible), approximated or estimated through fitting of experimental data. These parameters include:

- Transport parameters: (i) the effective binary gas diffusion coefficient, $D^{eff}_{O_2-N_2}$ (ii) the effective surface diffusion coefficient, D^{eff}_{θ}, and (iii) the effective electronic conductivity, σ^{eff}_{el}.
- Kinetic rate constants: (i) the rate constants of adsorption and desorption, k_{ads} and k_{des} and (ii) the rate constants of the electrochemical reaction, k^0_f and k^0_b.
- Microstructural parameters: (i) the gas-LSM internal surface area, a (ii) the triple phase boundary length, λ_{tpb} (iii) the porosity, ϵ, (iv) the average pore size, p_{avg} and (v) the tortuosity, τ.

The triple phase boundary length and porosity were estimated from SEM images of porous LSM electrodes, as described in Section 2.2.3 (page 53) and the gas/LSM internal surface area and average pore size were calculated from numerical construction of the porous electrode, described in [20]. The calculation/estimation of the transport and kinetic parameters are described in the following subsections.

Gas transport coefficient, $D^{eff}_{O_2-N_2}$

The binary diffusion coefficient can be derived from kinetic theory assuming rigid spherical gas molecules and is given by:

$$D_{AB} = \frac{2}{3}\sqrt{\frac{\kappa T}{\pi}}\sqrt{\frac{1}{2}\left(\frac{1}{m_A}+\frac{1}{m_B}\right)}\frac{1}{\pi(0.5(d_A+d_B))^2}\frac{1}{n} \tag{4.17}$$

A detailed discussion of the derivation can be found in [21] (pg 514-528).

The effective binary diffusivity through porous media arises from volume averaging and by accounting for the enhanced transport path lengths in a porous structure. The effective gas transport coefficient is

$$D^{eff}_{O_2-N_2} = D_{O_2-N_2}\frac{\epsilon}{\tau} \tag{4.18}$$

where ϵ is the porosity and τ is the tortuosity. The tortuosity of a cathode with particle size distributions and porosities equal to those used in this work has been calculated to be 2 using both the Monte Carlo technique and a finite volume technique on numerically constructed electrodes [22]. A tortuosity of 2 was also found by Wilson *et al.* [23] for the SOFC anode.

In the case of the electrode pore size being comparable to the mean free path of the oxygen molecule, Knudsen diffusivity must also be considered. Knudsen diffusion dominates when the gas molecule collides with the pore walls more frequently than with other gas molecules. Frequently it is assumed that the pore size for SOFC electrodes is between 0.5 and $1 \mu m$ such as in [24, 25], however, Cannarozzo *et al.* [26] calculated the pore size in a composite electrode as a function of volume fraction and particle size. These studies place gas diffusion in the transition regime for SOFC operating temperatures above 750°C. In the transition regime, both molecular and Knudsen diffusion become important. In such a case, the Bosanquet equation can be employed to calculate the overall effective gas diffusivity from the effective binary gas diffusivity and the Knudsen diffusivity.

Whether or not the transition regime approximation is valid depends on the Knudsen number defined by Equation 4.19a which is calculated from the mean free path length (MFPL) of the gas molecule (Equation 4.19b) and the average pore diameter (p_{avg}),

$$Kn = \frac{MFPL}{p_{avg}} \tag{4.19a}$$

$$MFPL = \frac{RT}{\sqrt{2}\pi d_{gas}^2 N_A P} \tag{4.19b}$$

where d_{gas} is the diameter of the gas molecule, N_A is Avogadro's number and P is the gas pressure. Knudsen numbers below 0.1 place gas transport in the continuum regime where the Knudsen diffusivity is not required, however, for Knudsen numbers roughly between 0.1 and 10, gas transport is in the transition regime which requires the use of a Knudsen diffusion coefficient. For Knudsen numbers above 10, the free molecular flow regime dominates and using volume average techniques are difficult to justify. It is therefore important to have an accurate estimator/measurement of the pore size and how it is distributed throughout the electrode. Using techniques developed in [20], the average pore size (p_{avg}) was estimated to be 250nm which makes the Knudsen number 1.36, placing gas transport in the transitional regime.

The effective Knudsen diffusivity can be calculated from [27]:

$$D_K^{eff} = \frac{1}{3} d_{pore} \sqrt{\frac{8RT}{\pi M_w}} \frac{\epsilon}{\tau} \tag{4.20}$$

and the total gas diffusivity in the transitional regime is a harmonic average of the effective gas diffusivity and the effective Knudsen diffusivity:

$$D_{O_2-N_2}^{eff,tot} = \left(\frac{1}{D_{O_2-N_2}^{eff}} + \frac{1}{D_K^{eff}} \right)^{-1} \tag{4.21}$$

The range of effective gas diffusivities are presented in Table 4.3:

Table 4.3: Effective binary ($O_2 - N_2$) gas diffusivity for various microstructures and temperatures.

Temperature $^\circ C$	Porosity	Pore Size μm	K_N	$D^{eff,tot}_{O_2-N_2}$ m^2/s
750	0.3	0.25	1.36	6.34×10^{-7}
750	0.4	0.25	1.36	8.45×10^{-7}
750	0.3	0.50	0.68	1.24×10^{-6}
800	0.3	0.25	1.42	6.50×10^{-7}
800	0.4	0.25	1.42	8.67×10^{-7}
800	0.3	0.50	0.71	1.27×10^{-6}
850	0.3	0.25	1.49	6.65×10^{-7}
850	0.4	0.25	1.49	8.87×10^{-7}
850	0.3	0.50	0.75	1.30×10^{-6}

Surface diffusion coefficient, D_θ

The surface diffusion coefficient, D_θ, is difficult to measure and estimation/calculation of this parameter from O_{ads} diffusion on the LSM surface has not been attempted through theoretical work. The surface diffusion coefficient for small molecules on metals has been measured and provides a range, perhaps wide, for use in modelling work.

For O_{ads} on Pt electrodes, Mitterdorfer and Gauckler [16] estimated the surface diffusion coefficient to be on the order 10^{-12} m^2/s at 700°C and for O_{ads} on the Ni surface. Vogler *et al.* [17] used a value on the order of 10^{-10} m^2/s at 700°C while Goodwin *et al.* [18] used a surface diffusion coefficient of 10^{-8} m^2/s for H_2 on Ni at $700^\circ C$. An experimental study of CO surface diffusion on Pt particles for PEM fuel cells [28] found coverage dependent surface diffusion coefficients on the order of $10^{-12} - 10^{-14}$ m^2/s at $750^\circ C$ (extrapolated to $750^\circ C$) and a number of experimentally obtained surface diffusion coefficients are reported in [29]. For example, surface diffusion of O_{ads} on the tungsten (110) surface can range from 10^{-14} m^2/s to 10^{-8} m^2/s between $750^\circ C$ and $900^\circ C$.

Most experimental studies find the surface diffusion coefficient to depend on surface coverage [30]. Although some studies show that the surface diffusion coefficient increases with increasing coverage, Wieckowski *et al.* [28] report a decrease with increasing surface coverage. A decrease in the surface diffusion coefficient with increasing surface coverage is intuitive since adsorbed species are less mobile due to self-interactions at the surface.

In this work, the effective surface diffusion coefficient was considered to be a fitting parameter and bound within a range of $D_\theta^{eff} = 10^{-13} - 10^{-8}\ m^2/s$. For a porous structure involving solid spheres [31], the surface tortuosity has been estimated to be of similar order of magnitude as the gas phase tortuosity ($\tau \approx 3$ in [31]) for porosities less than 40%. Therefore, compared to the possible range of D_θ, the uncertainty around the tortuosity of the solid LSM phase is not significant.

Gas permeability

The gas permeability, κ, of the porous cathode plays a direct role in determining the pressure drop within the porous electrode and hence, the contribution of convection to gas transport. Typically it is assumed that the permeability depends only on the porosity and the solid particle size of the electrode. Under these assumptions, and assuming spherical particles, the permeability can be calculated from the Carman-Kozeny equation [32]:

$$\kappa = \frac{d^2\epsilon^2}{180(1-\epsilon)^2} \tag{4.22}$$

where d is the average particle size ($\sim 0.5\mu m$) and ϵ is the electrode porosity. This results in a permeability on the order of $10^{-16}\ m^2$. It should be noted that the permeability is also expected to be a function of temperature due to the temperature dependence of the mean free path of a gas. Resch [33] obtained experimental permeability values of O_2 gas through tape-cast porous SOFC anodes and found permeabilities on the order of $10^{-15}\ m^2$ at temperatures of $\sim 500°C$. These permeabilities increased with increasing Knudsen number (or with increasing temperature).

Adsorption and desorption rate constants, k_{ads} and k_{des}

Adsorption rate constant In this work we have used collision theory to describe the kinetics of the adsorption reaction. Collision theory can be used to define the rate of an adsorption process in terms of the number of gas-phase molecules colliding with a surface per unit area per unit time [34,35]. The fraction of these collisions resulting in an adsorbed species is defined by the sticking coefficient (S), which represents the probability that a collision with the surface leads to adsorption. From kinetic theory, the rate of gas molecules colliding with a solid surface is [34]:

$$Z_w = \left(\frac{k_B T}{2\pi M}\right)^{0.5} \left(\frac{N}{V}\right) \tag{4.23}$$

where k_B is Boltzmann's constant, M is the molecular mass of the gas and N/V is the number density of gas molecules.The sticking coefficient, S can be related to the standard rate constant of adsorption (shown in Equation 4.8) by [34]:

$$S = \frac{N^m k_{ads}}{Z_w} \frac{RT}{101325} \tag{4.24}$$

where k_{ads} has units of $m^2/mol/atm/s$, N is the total number of adsorption sites, m is the sum of all the surface reactants stoichiometric coefficients and the factor $RT/101325$ converts the adsorption rate constant from pressure units into the required concentration units. Since the sticking coefficient is a probability, it must fall between values of 0 and 1 and the sticking coefficient, S, must be obtained by fitting to experimental data.

Through the derivation of equations presented in Section 4.2.4, the laws of mass action were used to derive the rate of adsorption and desorption. If the rate constants of adsorption and desorption remain in their standard form presented by Equation 4.8, then this is equivalent to Langmuir type adsorption, however, many metals are known to deviate from Langmuir adsorption [36]. Deviations from Langmuir adsorption kinetics may be caused by several reasons such as: 1) interactions between gas molecules and adsorbates 2) gas molecules adsorbing onto other adsorbates before settling onto the surface 3) gas species binding to more than a single adsorption site at the same time. The most common of these are interactions between gas molecules and adsorbates. Kisliuk [37] derived the following expression to describe various shapes of the sticking coefficient vs surface coverage that have been experimentally observed for adsorption on metal surfaces:

$$S = S^0 \left(1 + \frac{\theta}{1-\theta}\wp\right)^{-1} \tag{4.25}$$

where $\wp$ is a parameter ($\wp \geq 0$) describing the shape of the sticking coefficient vs surface coverage relationship. For all values of $\wp$, Equation 4.25 shows a decrease in S as θ increases, which is consistent with adsorbates hindering the adsorption of gas molecules. For values of $\wp \ll 1$, the sticking coefficient decreases quickly at high values of θ whereas for $\wp \gg 1$, the sticking coefficient decreases quickly at low values of θ and for $\wp = 1$, the sticking coefficient decreases linearly as θ increases. Therefore, to describe deviations away from typical Langmuir adsorption kinetics, it is possible to consider the sticking coefficient to be a function of the surface coverage.

Neither the adsorption rate constant or the sticking coefficient has been measured for oxygen adsorption on the LSM surface. However, a model by Svensson *et al.* [10] considered k_{ads} for this reaction to range from 10^4 to 10^{10} $m^2/mol/atm/s$ which corresponds to a sticking coefficient between $S = 10^{-8}$ and $S = 0.01$. In other work for the SOFC anode, for dissociative H_2 adsorption onto the Ni surface, Vogler *et al.* [17] used $S = 0.01$ whereas Goodwin *et al.* [18] used $S = 4 \times 10^{-9}$ at $750°C$ for H_2O adsorption on Ni. In this work, the sticking coefficient was used as a fitting parameter and a valid range was considered to be between 10^{-9} and 1.0.

Desorption rate constant To describe the rate of the desorption reaction, two methods were used. The first method describes the desorption rate constant by assuming an energy barrier for desorption, used by some authors such as Goodwin [38]:

$$k_{des} = \frac{N k_B T}{h} \exp\left(\frac{-E_{des}}{RT}\right) \tag{4.26}$$

where E_{des} is the activation energy of the desorption process, h is Planck's constant, k_B is Boltzmann's constant and N is the maximum number of surface sites. It is sometimes assumed that in collision theory, the adsorption process is barrier-less so that the activation energy of the adsorption process is zero.

The second method of calculating the desorption rate constant is to obtain the desorption rate constant by enforcing thermodynamic consistency. For a chemical reaction at equilibrium, the forward and reverse rate constants are related to the Gibbs energy of the reaction by:

$$\frac{k_f}{k_b} = \exp\left(-\frac{\Delta G^{\ominus}}{RT}\right) \tag{4.27}$$

where k_f and k_b are rate constants of the forward and reverse reactions. Since the right hand side of Equation 4.27 is unitless, the units of k_f and k_b must be the same. This method requires careful consideration of the form of the rate equation of adsorption and desorption. There are two approaches to dealing with the rate of adsorption and desorption. The first involves the derivation of the rate of adsorption/desorption in terms of activities:

$$N\frac{d\theta}{dt} = k^{\dagger}_{ads}\frac{pO_2}{P^o}N(1-\theta)^2 - k^{\dagger}_{des}N\theta^2 \tag{4.28}$$

where the reference state of surface species is full coverage so θ and $(1-\theta)$ represent the activity of surface species. The units of both $k^{\dagger}_{ads}$ and $k^{\dagger}_{des}$ are $1/s$. The second approach (which was used to describe the net rate of adsorption in Equation 4.8) is to start with the concentration of adsorbates with units of mol/m^2 and then convert into surface coverage, resulting in:

$$N\frac{d\theta}{dt} = k_{ads}pO_2N^2(1-\theta)^2 - k_{des}N^2\theta^2 \tag{4.29}$$

where k_{ads} has units of $m^2/mol/atm/s$ and k_{des} has units of $m^2/mol/s$. In this case the units of the rate constants are different, therefore, when imposing thermodynamic consistency, it is best to use the form in Equation 4.28, however, in terms of ensuring unit consistency in the flux balance of both oxygen gas and oxygen adsorbates, it is easier to use the form presented in Equation 4.29. The rate constants k_{ads}, $k^{\dagger}_{ads}$ and k_{des}, $k^{\dagger}_{des}$ are related through:

$$k_{ads} = k^{\dagger}_{ads}\frac{1}{P^o}\frac{1}{N} \tag{4.30a}$$

$$k_{des} = k^{\dagger}_{des}\frac{1}{N} \tag{4.30b}$$

Thermodynamic consistency can then be enforced by combining Equations 4.27 with 4.30, which results in:

$$k_{des} = k_{ads}P^0\exp\left(\frac{\Delta G^{\ominus}}{RT}\right) \tag{4.31}$$

where P^0 is the reference pressure, $1atm$.

When using Equation 4.31 to calculate the desorption rate constant, the Gibbs energy of the adsorption/desorption reaction must be known. For typical chemical reactions, this can be easily computed based on tabulated thermodynamic properties, however, adsorption reactions involve solids which do not have known thermodynamic properties. In this case, quantum mechanics calculations based on density functional theory (DFT) can yield energies of the adsorption reaction at the zero point energy state (at 0K and in vacuum). A recent DFT study [39] investigated oxygen adsorption on $LaMnO_3$ crystals and determined that the most favorable oxygen adsorption pathway (ie. the pathway with the lowest energy) was dissociative adsorption on a Mn surface site. The adsorption energy for this pathway was -2.14eV.

Since energies obtained from the DFT method are calculated at the zero-point condition (i.e., 0K and 0atm), in order to apply them to realistic temperatures and pressures, appropriate corrections should be made. Kotomin *et al.* [39] considered the following oxygen adsorption reaction:

$$O_2(g) + LaMnO_{3,surface} \rightarrow 2O - LaMnO_{3,surface} \tag{4.32}$$

with a computed energy of $\Delta E_{dft} = \Delta G_{rxn}(0K, 0atm) = -2.14eV$. Mathematically, this energy can be expressed as:

$$\Delta G_{rxn}(0K, 0atm) = \Delta E_{dft} = 2G_{O-LMO} - G_{LMO} - G_{O_2} \tag{4.33}$$

where G_i is the Gibbs energy of species i where LMO is the $LaMnO_3$ surface without adsorbed oxygen, $O-LMO$ is the surface with an adsorbed oxygen atom and O_2 is an oxygen gas molecule. It is common to assume that the difference in the Gibbs energy of the solid surface between operating conditions and the zero-point energy is small when compared to the Gibbs energy change of the gas [40] and therefore, only the Gibbs energy change of the gas phase is considered. This allows for the following method of calculating $\Delta G_{rxn}(T, P)$:

$$\Delta G_{rxn}(T, P) = \underbrace{2G_{O-LMO} - G_{LMO} - [G_{O_2}(0K, 0atm)}_{\Delta E_{dft}} + G_{O_2}(0 \rightarrow T, P^o)] \tag{4.34}$$

Therefore, we must only concern ourselves with calculating the Gibbs energy change of the gas from zero-point conditions to operating conditions. This change can be calculated for an ideal gas using the following thermodynamic properties:

$$\Delta G^{ig}(0 \rightarrow T, P) = \Delta H^{ig}(T) - T\Delta S^{ig}(T, P^o) \tag{4.35}$$

$$\Delta H^{ig}(T) = \int_{T_1}^{T_2} C_P dT \tag{4.36}$$

$$\Delta S^{ig}(T,P) = \int_{T_1}^{T_2} \frac{C_P}{T} dT - R \int_{1}^{P^o} \frac{dP}{P} \tag{4.37}$$

The constant pressure heat capacity as a function of temperature (C_P) valid for temperatures greater than 298K as well as the enthalpy (ΔH) and the entropy (ΔS) change between 0K and 298K for oxygen gas is documented in a thermodynamic database available from NASA [41].

When fitting the adsorption and desorption rate constants, it is desirable to be thermodynamically consistent, which means enforcing Equation 4.27 and using zero point energies along with the appropriate correction to account for operating temperatures. As will be discussed later in Section 4.4, thermodynamic consistency was possible when fitting the model against experimental polarization curves, however, it was not possible when fitting the model against the experimental impedance response. Therefore, when fitting impedance data, the desorption rate constant was defined by Equation 4.26 with E_{des} used as a fitting parameter but when fitting steady state data, the desorption rate constant was defined by Equation 4.31 with ΔE_{dft} used as a fitting parameter.

Electrochemical rate constants, k_f^0 and k_b^0

The chemical component of the forward and reverse electrochemical rate constants, k_f^0 and k_b^0, are simply treated here as fitting parameters to experimental data. Since the triple phase boundary length is known to be relatively high ($\lambda_{tpb} = 3.5 \times 10^6 m/m^2$) and k_f^0 and k_b^0 influence the exchange current density/charge transfer resistance, their contribution can be verified against experimentally obtained values of i_0 and R_{ct} from impedance spectroscopy. It should be noted that mathematically, the parameters k_f^0 and k_b^0 can be treated as lumped since their independent variation only affects the magnitude of i_0. Therefore, for fitting purposes, $k_{ct} = k_f^0 = k_b^0$ and only k_{ct} is required as a fitting parameter to experimental data. The expression for i_0 was then:

$$i_0 = nF[\lambda_{tpb} k_{ct} N (1 - \theta^{eq}) C_{O_{\ddot{O}}^x}]^{\beta} [\lambda_{tpb} k_{ct} N \theta^{eq} C_{V_{\ddot{O}}}]^{(1-\beta)} \tag{4.38}$$

Other parameters

A number of other parameters are required by the model. These were either calculated or taken from the literature. Table 4.4 lists these other parameters and their values.

Table 4.4: Model parameters obtained by methods other than fitting

Parameter	Description	Value	Units	Ref
λ_{tpb}	Triple phase boundary length	3.16	$\mu m\ \mu m^{-2}$	Measured
ϵ	Porosity	0.32		Measured
a	Gas-LSM internal surface area	3.49×10^6	$m^2\ m^{-3}$	[20]
τ	Tortuosity	2		[22, 23]
p_{size}	Pore size	0.25	μm	[20]
$C_{V_{\ddot{O}}}$	Oxygen vacancy concentration in YSZ	4.65×10^3	$mol\ m^{-3}$	[16]
$C_{O^x_{\ddot{O}}}$	Oxygen lattice concentration in YSZ	4.45×10^4	$mol\ m^{-3}$	[16]
N	Maximum surface site concentration	10^{-5}	$mol\ m^{-2}$	[10]
β	Symmetry coefficient	0.5		
$Q^{\ddagger}_{cpe}$	Constant phase element parameter	40-60	$Sm^{-2} \cdot s^{P_{cpe}}$	Measured
$P^{\ddagger}_{cpe}$	Constant phase element parameter	$T^{-0.21}\exp(0.1eV/R/T)$		Measured

‡ Only required for transient simulations

For transient calculations, the double layer capacitance, C_{dl}, is also required. This was obtained from impedance measurements and was reported in Section 3.3.2 (page 116) of Chapter 3.

4.2.6 Solution Methodology

Numerical Method

The model presented here contains a number of coupled transport equations and associated boundary and initial conditions. These transport equations are all partial differential equations which as a system, do not have an analytical solution and so the solution must be approximated using a numerical technique. The equations stated above were initially solved in two different ways: 1) by programming the finite volume technique in Matlab 2) by using the commercial software package Comsol Multiphysics with the Matlab interface which uses the finite element method to solve systems of partial differential equations. Since some of the parameters were estimated using a fitting algorithm, the speed of the solution was important and for this reason, Comsol Multiphysics was used for the majority of the simulations. Using Comsol, a full polarization curve with ~30 potentials/current densities could be simulated in ~30 seconds compared to ~50 seconds using in-house Matlab finite volume code on a 2.16GHz processor with 2GB RAM. Over the entire fitting process, this resulted in a time advantage on the order of days.

Using both Matlab and Comsol, the set of partial differential equations was discretized over the domain. Discretization converts the continuous PDEs into a series of algebraic equations that rely on the species concentration at each grid point. The set of algebraic equations can be formulated into a general system of $\mathbf{Ax} = \mathbf{b}$ where $\mathbf{x}$ is a vector containing the desired species concentration/potentials at each grid point, $\mathbf{A}$ is a matrix and $\mathbf{b}$ is a vector both populated by coefficients of the discretization scheme. Since the solution for vector $\mathbf{x}$ requires an iterative solution, an initial guess was provided. Once the initial guess was provided, the $\mathbf{A}$ and $\mathbf{b}$ matrices were populated and a new solution vector $\mathbf{x}$ was found. This process continued until a desired convergence was achieved. In both Matlab and Comsol, the UMFPACK direct solver was used to invert the $\mathbf{A}$ matrix.

Steady state calculation For the steady state calculations, a parametric solver was used in Comsol which allowed the electrode potential to be varied stepwise from low to high values. Typically, a set of 30 potentials was applied between $\Delta\phi_{el}^{applied} = 0V$ and $\Delta\phi_{el}^{applied} = -0.6V$ at the boundary $x = 0$. After each potential had converged to the desired tolerance, the solution was used as the initial value for subsequent potentials. Starting at low potentials where the solution was known to be close to equilibrium values and slowly updating the initial value for each potential ensured that the desired solution was achieved.

Transient calculation For the transient calculations, a frequency and time-dependent sinusoidal potential was applied to the boundary $x = 0$. This potential was:

$$\Delta\phi_{el}^{applied} = \Delta\phi_{s.s.} + \eta_{var}\sin(\omega t) \tag{4.39}$$

where η_{var} is the amplitude of the sinusoidal component of the applied potential, $\Delta\phi_{s.s.}$ is the steady state component of the potential and $\omega = 2\pi f$ is the angular frequency, with f equalling the frequency in Hz. In this case, there are a number of factors which can influence the solution such as the number of time steps as well as the total simulation time. The number of time steps was quantified in terms of the number of time steps per period of the sinusoidal input signal and the total simulation time was quantified in terms of the total number of periods simulated. For all transient simulations, the number of time steps per period was set to 100 and the total number of periods was at least 8.

Convergence/Mesh Independence

Using Comsol, a converged solution was assumed when the error after each iteration was smaller than a specified tolerance, defined as [42]:

$$tol = \frac{1}{N_f}\sum_i |E_i| \tag{4.40}$$

where N_f is the number of degrees of freedom and $\mathbf{E} = \mathbf{b} - \mathbf{A}\mathbf{x}$ is the error, or residual, which was forced close to 0. The tolerance, or tol, was manually set to 10^{-12}. Figure 4.4 shows an example of a typical convergence plot showing the residual vs total iteration number. When a potential was initially applied, the residual decreased until it reached the tolerance level and then a new potential was applied causing the residual to increase before falling again to below the desired tolerance. It should also be noted that double precision was used in all numerical simulations.

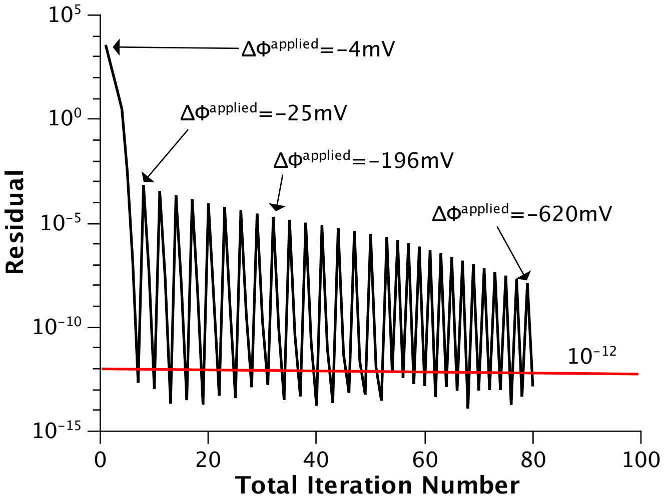

Figure 4.4: Example convergence plot showing the residual vs total iteration number. The abrupt increase in residual followed by its decrease is caused by the application of a new potential.

The conservation of species was verified by calculating the fluxes at the boundaries of the domain. Since the flux of oxygen gas and surface species as well as electronic potential is related to the current density by Faraday's law, a number of methods can be used to calculate the current and ensure that the flux balance was consistent:

1. Using the flux of oxygen gas entering the domain multiplied by 4F ($i = 4FJ_{O_2}$)

2. Using the flux of oxygen adsorbates leaving the domain multiplied by 2F ($i = 2FJ_\theta$)
3. Using the flux of electronic charge entering or leaving the domain ($i = J_{\phi_{el}}$)
4. Obtaining the current directly from the Butler-Volmer equation at the LSM/YSZ interface ($i = i_{anodic} - i_{cathodic}$)

In addition, it is also important to ensure that the solution is independent of the mesh size. Since large gradients could exist close to the triple phase boundary, the mesh density was highest at a distance of $5\mu m$ from the electrode/electrolyte interface (considered to be an approximate range for the "active" thickness). In this "active" region, the maximum mesh density was set to 5 nm and this mesh density decreased linearly away from the "active" region. This technique for placing the mesh ensured both mesh independence and maintained the number of grid points to a reasonable number (for a $20\mu m$ electrode, the number of 1D elements, or grid points, was 1230) allowing for relatively fast solution. It should be noted that this grid size was selected for the parameter sets that were expected to generate the largest gradients (essentially those parameter sets that had the lowest surface diffusion coefficient, equal to $10^{-13}\ m^2/s$). This allowed the assumption of grid independence to be made while fitting the parameters. Table 4.5 shows an example of the current calculated from various fluxes as a function of the mesh size.

Table 4.5: Grid dependency of the current density for various methods of calculating the current at $\Delta\phi_{el} = -0.4V$ with $D_\theta^{eff} = 10^{-13}\ m^2/s$.

Minimum mesh size* μm	Current density calculated from:					Difference** %
	$J_{O_2}\|_{x=0}$ mA/cm^2	$J_\theta\|_{x=L}$ mA/cm^2	$J_{\phi_{el}}\|_{x=0}$ mA/cm^2	$J_{\phi_{el}}\|_{x=L}$ mA/cm^2	i_{far} mA/cm^2	
0.47	-0.1728	-0.1582	-0.1728	-0.1728	-0.1728	-
0.12	-0.1727	-0.1726	-0.1727	-0.1727	-0.1727	1.64
0.005	-0.1727	-0.1727	-0.1727	-0.1727	-0.1727	0.01

* Non uniform mesh shown in Figure 4.2b with a grid growth ratio of 1.02

** Percent difference between the average of the current densities for each mesh size

Parameter Estimation

The unknown parameters, D_θ^{eff} (surface diffusion coefficient), S (sticking coefficient), E_{des} (desorption energy barrier) or ΔE_{dft} (zero point adsorption/desorption reaction energy) and k_{ct} (electrochemical rate constant) were estimated by fitting the model to the experimental steady state polarization curves and to the experimental impedance response. All parameter fits were performed for experimental data at a single temperature over multiple oxygen concentrations. The Matlab optimization routine *fminsearchcon* (a version of *fminsearch* capable of applying parameter constraints) was used to minimize the sum of squares between the experimental data and the model. The *fminsearchcon* routine is a simplex algorithm [43,44] which is commonly used for nonlinear optimization. For the steady state case, the polarization response was simulated using a given parameter set in 10^{-4}atm, 2.5×10^{-4}atm, 5.0×10^{-4}atm and 10^{-3}atm O_2. The fitting error for each polarization curve was calculated from the deviation of the current density at each experimental overpotential. The objective function being minimized was then the normalized sum of the fitting error at each oxygen concentration:

$$\chi^{ss} = \sum_{pO_2}^{p} \sum_{\Delta V}^{V} \left(\frac{(i_v^{exp} - i_v^{mod})^2}{variance(i_v^{exp})} \right)_p \tag{4.41}$$

where i_v is a current density at potential V, p refers to a specific oxygen partial pressure and ss refers to steady-state. In some cases, only the experimental polarization resistance at OCV was fit to experimental data. In these cases, steady state polarization curves were simulated up to an overpotential of -50mV. The polarization resistance from the model was calculated from the slope of the i-η curve using the low field approximation (see Section 2.4.1). For this case, the minimized objective function was:

$$\chi^{Rp} = \sum_{pO_2}^{p} \frac{(R_p^{exp} - R_p^{mod})^2}{variance(R_p^{exp})} \tag{4.42}$$

For impedance simulations, most of the model fitting was performed by hand, and the features that were considered to be important were the values of R_{ct}, R_{chem} and the phase shift. The goodness of fit was calculated from:

$$\chi^{imp} = \sum_{f} (Z_f^{exp} - Z_f^{mod})^2 \tag{4.43}$$

where Z_f is the impedance at frequency f.

The fitting algorithm required initial values for the parameters S, ΔE_{dft} (or E_{des}), D_θ^{eff} and k_{ct}. For the adsorption reaction, the initial guesses ΔE_{dft} was obtained from DFT studies such as [39,45] and S from models developed by Svensson *et al.* [10,19]. The initial value of the surface diffusion coefficient was obtained from known transport properties on metals and the electrochemical rate constant k_{ct} was first estimated by fitting it to experimental R_{ct} values obtained from impedance spectroscopy with an estimated θ^{eq}.

Calculation of the Impedance Response

During impedance spectroscopy measurements, a time-dependent, sinusoidal potential is applied between the reference electrode and the working electrode and the resulting time-dependent sinusoidal current density is measured. In a similar manner, the impedance response was calculated by applying a time-dependent sinusoidal potential and calculating the time-dependent current response. Following the method used by Bessler [46], Equation 4.39 was imposed at the boundary $x = 0$ (gas-current collector/electrode interface). This boundary condition was applied for a range of frequencies, typically matching experimental conditions which were 71 frequency points between 100kHz and 0.01Hz. Assuming that η_{var} is low enough so that nonlinearity between the potential input and current response is not observed, the resulting current density is:

$$i = i_{s.s.} + i_{var} \sin(\omega t + \bar{\theta}) \tag{4.44}$$

where $\bar{\theta}$ is a frequency dependent phase shift between the potential and the current. With the time dependent input signal (such as the sinusoidal potential) and the time dependent output signal (such as the phase shifted sinusoidal current response), the impedance can be calculated from the knowledge of the phase shift $\bar{\theta}$ and the input/output amplitudes. This can be accomplished using a number of techniques described in [47]. The methods used by frequency response analyzers are the single-frequency Fourier analysis (used by instruments such as the Solartron 1260) and the multiple-frequency Fourier analysis (used by newer instruments such as the Solartron 145x series).

In this work, the single-frequency Fourier analysis was used to calculate the impedance from knowledge of the time dependent potential input and time dependent current output signals. A detailed derivation of the calculation can be found in [46, 47]. The real and complex parts of the admittance, assuming linear sinusoidal input and output signals, are:

$$Y' = \frac{2}{\eta_{var}\tau_p}\int_0^{\tau_p} i(t)\sin(\omega t)dt \tag{4.45a}$$

$$Y'' = \frac{2}{\eta_{var}\tau_p}\int_0^{\tau_p} i(t)\cos(\omega t)dt \tag{4.45b}$$

where $Y = Y' + \sqrt{-1}Y''$ is the admittance and $\tau_p = 2\pi/\omega$ is the periodicity (the number of periodic cycles of the applied potential). For typical simulations, $\tau_p = 8$. The impedance is then $Z = 1/Y$ and the phase shift and magnitude can be calculated from:

$$\tan\bar{\theta} = \frac{Real(Z)}{Imag(Z)} \tag{4.46a}$$

$$|Z| = \sqrt{Real(Z)^2 + Imag(Z)^2} \tag{4.46b}$$

When the current, $i(t)$, in Equation 4.45 is the Faradaic current, i_{far}, described by Equation 4.14, the resulting impedance is the Faradaic impedance, Z_{far}. However, when the current used in Equation 4.45 is the total current i_{tot} described by Equation 4.16, the resulting impedance is the total impedance, Z_{tot}.

Special consideration was required to model the constant phase element (CPE) observed in the experimental impedance data. While the charge double layer could be modelled directly for an ideal capacitor, we were unable to directly model the distributed behavior of the capacitance (ie. the constant phase element) observed in the experimental data. To model the constant phase element, first, the Faradaic impedance was calculated assuming that the double layer behaved like an ideal capacitor (ie. with the total current defined by Equation 4.16), then, equivalent circuits were used to add a constant phase element in parallel to the Faradaic impedance. Figure 4.5 shows the equivalent circuit and Equation 4.47 [47] was used to calculate the total impedance based on this equivalent circuit.

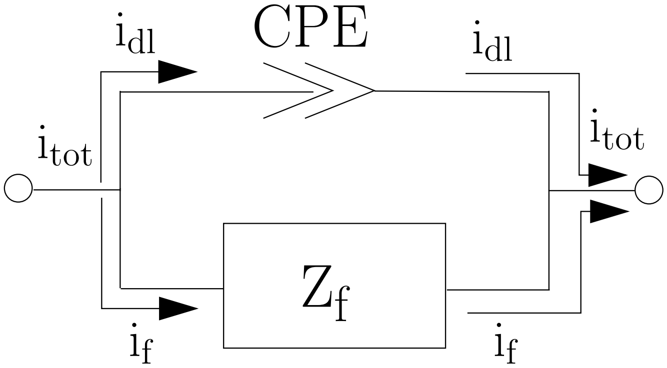

Figure 4.5: Equivalent circuit used to model the constant phase element observed in the experimental impedance response. Z_f was calculated directly from the model and non-ideal capacitative behavior was calculated using this circuit. Arrows represent the separation of double layer and faradaic currents.

$$Z_{tot}(\omega) = \frac{Z_f(\omega)}{(1 + j\omega)^P Q Z_f(\omega)} \tag{4.47}$$

where $Z_{tot}(\omega)$ is the total impedance at a specified angular frequency, ω, $Z_f(\omega)$ is the Faradaic impedance calculated directly by the model at a specified angular frequency, j is $\sqrt{-1}$, P is a number between 0 and 1 describing the deviation of the constant phase element away from a pure capacitor (where $P = 1$ is a pure capacitor) and Q is a type of capacitance associated with the constant phase element (Note: if $P = 1$, then $Q = C_{dl}$).

4.3 General Model Behavior

This section discusses the general behavior of the steady state model and the impedance model. Changes in the polarization curves, reaction orders and in the impedance are compared as various kinetic rate constants and structural parameters are systematically varied.

- Section 4.3.1 discusses how the polarization curve and species distributions can be influenced by changes in adsorption kinetics and the electrode permeability and how pO_2 dependencies can vary depending on various kinetic rate constants

- Section 4.3.2 discusses how the impedance changes with variations in the sticking coefficient, surface diffusion coefficient and average pore size

4.3.1 Steady State Model Behavior

The set of five coupled partial differential equations shown in Table 4.1 with boundary conditions in Table 4.2 were solved simultaneously for the steady state case by setting the accumulation terms of the partial differential equations equal to zero. A cell potential was applied to the boundary $x = 0$ which physically represents a potential being applied between the working electrode and reference electrode and the current was calculated at the triple phase boundary based on local compositions of surface species. The cell current and overpotential depends on the rates of the various processes, which determine the distribution of species through the electrode. To investigate the general behavior of the steady state model, a set of initial parameters were chosen based on the ranges of possible values given in Section 4.2.5. These parameters are shown in Table 4.6.

Table 4.6: Base parameter set chosen for model behavior study

Parameter	Value	Units	Eq.
S	2.5×10^{-5}	-	4.24
$\wp$	0	-	4.25
E_{des}	0.42	eV	4.26
D_{θ}^{eff}	4×10^{-9}	$m^2\ s^{-1}$	
$k_{ct} = k_f^0 = k_b^0$	7×10^{-10}	$m^4\ mol^{-1}\ s^{-1}$	4.38
$Q_{cpe}^{\ddagger}$	40-60	$Sm^{-2} \cdot s^{P_{cpe}}$	4.47
$P_{cpe}^{\ddagger}$	$T^{-0.21} \exp(0.1eV/R/T)$		4.47

‡ Only used in impedance simulations
‡ Values are for CPE of impedance

The mathematical model can be solved for the species concentration distributions of ρ_{O_2}, θ, ϕ_{el} and P_{tot} throughout the electrode. These species distributions were then used to calculate a steady state polarization curve. Figures 4.6a, 4.6b and 4.6c show examples of the distributions of θ, ρ_{O_2} and ϕ_{el} as a function of current density along the thickness of the cathode, where $x = 0$ is the gas-current collector/electrode interface and $x = 20\mu m$ is the electrode/electrolyte interface (for a $20\mu m$ thick electrode). As the current density is increased, gradients in the relevant potential become larger, however, these gradients depend on the respective effective transport coefficient. In the case of the electronic phase potential, the gradients are very small because the effective electronic conductivity is very high. These species distributions are coupled to the current density. Figure 4.6d shows examples of the steady state polarization curve calculated at $750°C$ in oxygen concentrations between 10^{-4}atm and 1atm. As expected, as the pO_2 increases, more current is produced, however, for low pO_2 conditions, limiting currents are observed at high potentials where the reactant concentrations approach zero.

In addition to the species distribution, Figure 4.7 plots the fraction of the atomic oxygen flux from oxygen in the gas phase and oxygen on the LSM surface. The flux of oxygen can be calculated from Equation 4.7 and the flux of adsorbed oxygen can be calculated from Equation 4.9. The fraction of the oxygen flux due to adsorbed oxygen is:

$$J_\theta^{fraction} = \frac{J_\theta}{J_\theta + 2J_{O_2}} \tag{4.48}$$

where J_i represents the flux of species i and the factor 2 accounts for the fact that the gas species is molecular oxygen whereas the surface species is atomic oxygen. A similar expression can be used to calculate the fraction of oxygen in the gas phase. As Figure 4.7 shows, for low values of D_θ^{eff}, the flux of adsorbed oxygen relative to the total oxygen flux is low until about $5\mu m$ from the electrode/electrolyte interface. This indicates that the gas transport pathway for providing oxygen to the electrode/electrolyte interface is preferred over the surface pathway because it provides less resistance to oxygen transport. However, for the high value of D_θ^{eff} shown in Figure 4.7, the contribution of the two pathways is roughly equal. This highlights one of the main advantages of a physical based model when analyzing the complex oxygen reduction reaction: parallel pathways can be modelled and their individual contributions can be calculated based on the kinetics and transport properties of the electrode processes.

Since each process of the oxygen reduction mechanism is coupled to one another, the distribution of species and their fluxes shown in Figures 4.6 and 4.7 depend on the rates of the individual processes. This is illustrated in Figures 4.8 and 4.9 which show how changing the sticking coefficient and the electrode permeability can affect the steady state polarization curve as well as the species

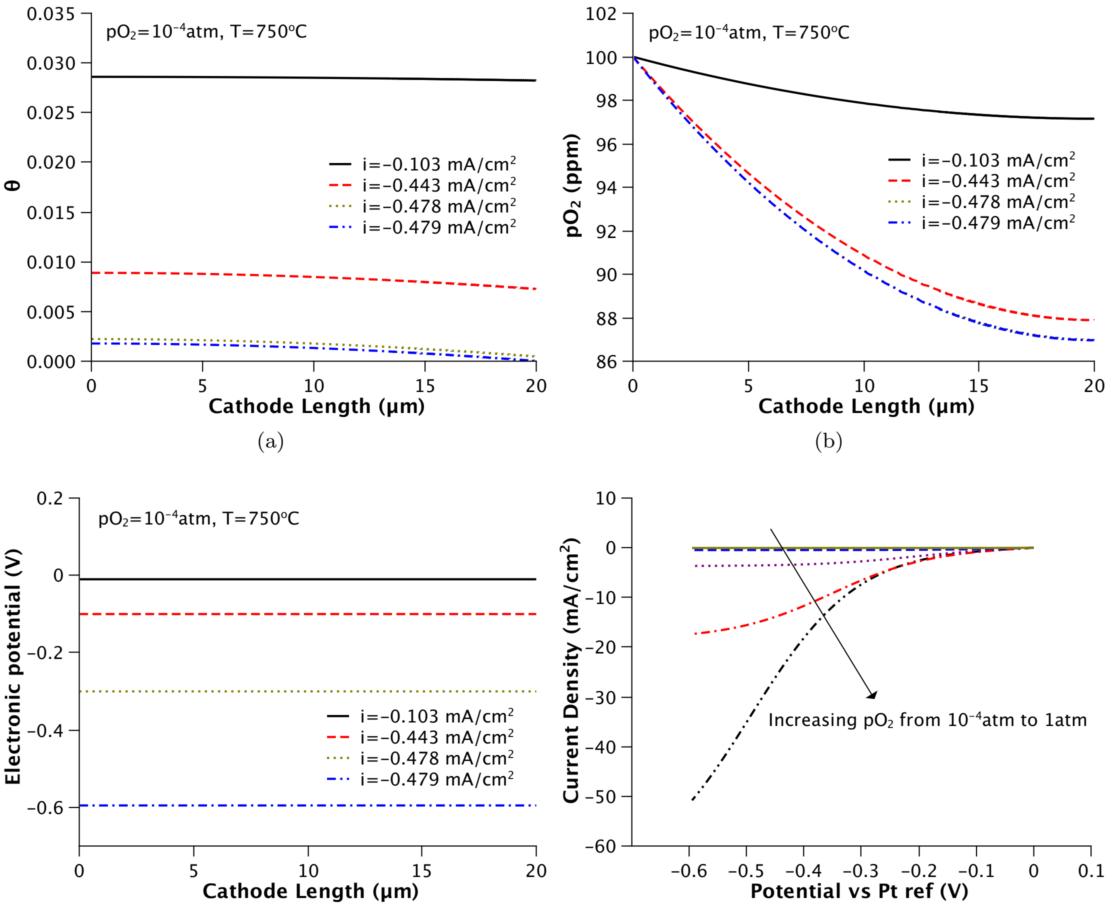

(a) (b)

(c) (d)

Figure 4.6: Example of the distribution of various species throughout the porous cathode at $750°C$: (a) Distribution of surface coverage, θ for $pO_2 = 10^{-4}atm$ (b) Distribution of oxygen gas for $pO_2 = 10^{-4}atm$ (c) Electronic potential, ϕ_{el} for $pO_2 = 10^{-4}atm$ (d) Example steady state polarization curves in $10^{-4}atm \leq pO_2 \leq 1atm$. The parameter set used to obtain these results is shown in Table 4.6.

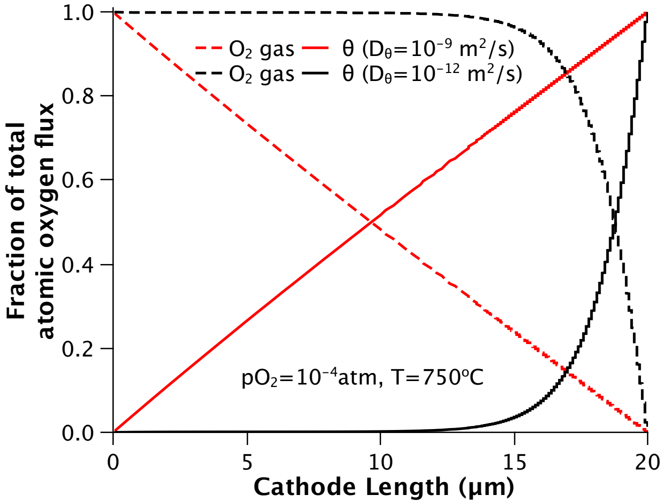

Figure 4.7: Fraction of oxygen flux from gas phase and surface phase (in terms of atomic oxygen) for $D_\theta^{eff} = 4 \times 10^{-9}$ and $D_\theta^{eff} = 4 \times 10^{-12}\ m^2/s$. The parameter set used to obtain these results is shown in Table 4.6.

distributions within the electrode.

Influence of adsorption Figure 4.8a shows that as the sticking coefficient is increased from $S = 2.5 \times 10^{-5}$ to $S = 2.5 \times 10^{-3}$, the electrode current increases for the same electrode potential. In addition, the limiting current density increases and forms at higher electrode potentials. The associated species distributions shown in Figure 4.8b for a constant current density of $i = -4.6 mA/cm^2$ indicate that this increase in current as the sticking coefficient increases is a result of an increase in the surface coverage, while the O_2 gas distribution remains relatively constant for these three cases. As the sticking coefficient is increased from $S = 2.5 \times 10^{-5}$ to $S = 2.5 \times 10^{-3}$, the equilibrium surface coverage in $pO_2 = 0.001$ increases from $\theta^{eq} = 0.08$ to $\theta^{eq} = 0.47$ which results in higher surface coverage at the LSM/YSZ interface. Although the surface coverage at the LSM/YSZ interface is higher, it is not the sole reason for increased currents. The exchange current density, i_0, defined in Equation 4.13, depends on θ^{eq} and so i_0 also increases. The fact that changing the sticking coefficient influences both the adsorption and charge transfer reactions illustrates the close coupling of electrode processes in the porous LSM cathode.

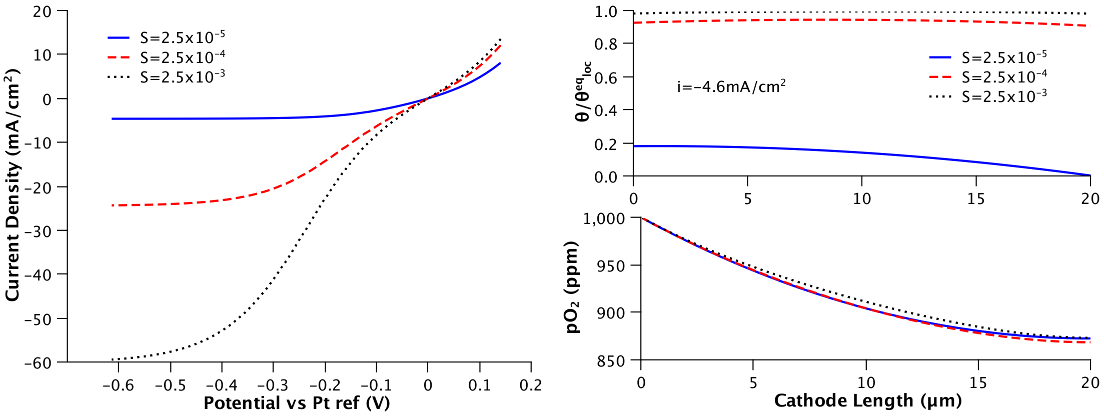

(a) (b)

Figure 4.8: Influence of adsorption on the steady state (a) polarization curve and (b) oxygen gas and adsorbed oxygen distributions in 0.001atm O_2 at a current of $i = -4.6mA/cm^2$. θ^{eq}_{loc} is the surface coverage in equilibrium with the local pO_2. The parameter set used to obtain these results is shown in Table 4.6.

Influence of gas permeability Although it is not commonly considered, another factor that may affect the species distribution within the electrode and, hence, the current/overpotential relationship is the gradient of total pressure within the electrode. As oxygen gas is consumed by the adsorption reaction at the pore/LSM interface, the sink of oxygen species can cause a decrease in the total electrode pressure. This pressure gradient is proportional to the electrode permeability, κ, and helps drive the transport of oxygen gas through a convective flux. Figure 4.9a shows the polarization curve and Figure 4.9b shows the O_2 mole fraction (y_{O_2}) and total pressure distributions within the electrode for electrode permeabilities ranging from $\kappa = 10^{-17}\ m^2$ to $\kappa = 10^{-15}\ m^2$. Figure 4.9b indicates that as the permeability decreases, the pressure gradient increases which results in a slightly higher O_2 mole fraction caused by a larger convective flux through the porous electrode. For $\kappa = 10^{-17}\ m^2$, the total pressure decreases from 1atm to 0.995atm and is constant for $\kappa = 10^{-15}\ m^2$. Even for a low permeability ($\kappa = 10^{-17}\ m^2$), the differences in the total pressure are small and do not translate into significant changes in the current density or in surface coverages. The pressure gradient is also related to the electrode thickness, and accordingly it would be expected that as the electrode thickness is increased, the contribution from gas phase convection would also increase. For typical cathode thicknesses of $20\mu m$ though, with $\kappa = 10^{-15}\ m^2$ in Figure 4.9b, the highest Peclet number is on the order of 10^{-7} which indicates that the diffusive flux is much higher than the convective flux for the transport of oxygen gas.

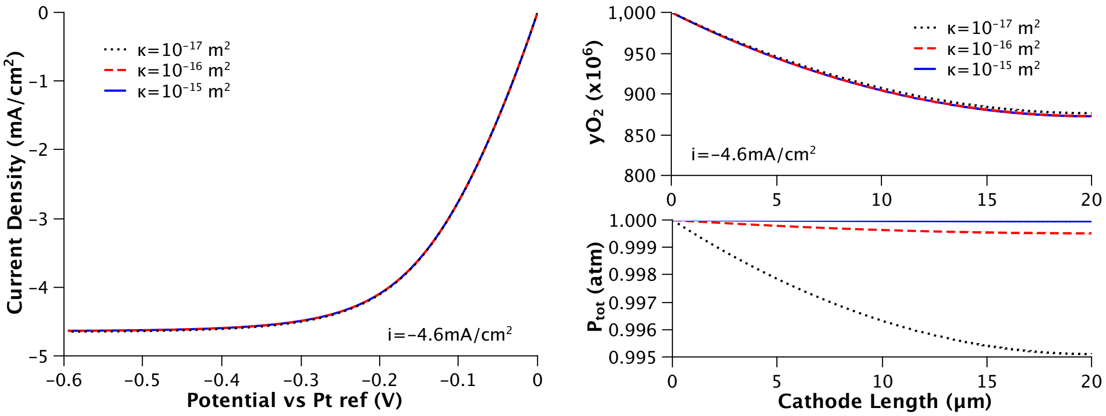

(a) (b)

Figure 4.9: Influence of gas phase convection on the steady state (a) polarization curve and (b) oxygen partial pressure and total pressure for $pO_2^{bulk} = 0.001atm$ at a current of $i = -4.6mA/cm^2$. The parameter set used to obtain these results is shown in Table 4.6.

Influence of kinetics on reaction order It is often observed that the electrode resistance depends on the oxygen partial pressure according to $R \propto pO_2^{-\gamma}$ where γ is the oxygen gas reaction order. The reaction order can sometimes be related to the rate determining step of the overall oxygen reduction reaction. However, as discussed in Section 3.3.2 (Chapter 3), when analyzing the reaction orders of experimental data, a single rate determining step may not exist for the oxygen reduction reaction. In fact, the concept of a rate determining step may be difficult to justify in the context of parallel pathways because the dominant pathway is the one with the least resistance. For this reason, it is not obvious how the reaction orders can be influenced by the various pathways and mixed controlled kinetics that may exist.

In this analysis, the reaction order was calculated from the electrode resistance for various kinetic rate constants of the adsorption reaction. The electrode resistance can be determined from the polarization curve using the low field approximation (described in Section 2.4.1) but with the additional details of the model, it is also possible to calculate the charge transfer resistance, R_{ct}, and the chemical resistance, R_{chem}, which experimentally are only possible to measure using impedance spectroscopy. The polarization resistance can be calculated from the polarization curve around some operating point (such as OCV conditions) from the relationship $R_p = \partial\eta/\partial i$, as was done previously when analyzing the experimental data. With the knowledge of the exchange current density, i_0, the charge transfer resistance can be calculated from:

$$R_{ct} = \frac{RT}{nF}\frac{1}{i_0} \tag{4.49}$$

where in this case, $n = 2$ and i_0 is the exchange current density (Equation 4.13). The chemical resistance, R_{chem}, can then be calculated simply from its definition, $R_{chem} = R_p - R_{ct}$.

In a previous study, Svensson *et al.* [10] showed how the reaction order of R_p and of the limiting current can vary depending on the values of the rate constants and transport coefficients. However, it is also possible to show how the reaction order changes for R_{ct} and R_{chem}. The change in the reaction order is especially interesting for the case where adsorbates influence the adsorption kinetics, as described in Section 4.2.5. To investigate this behavior, the model developed by Kisliuk [37] was used to describe how the sticking coefficient changes with surface coverage:

$$S = S^0\left(1 + \frac{\theta}{1-\theta}\wp\right)^{-1} \tag{4.50}$$

where $\wp$ is a parameter describing the shape of the sticking coefficient vs. surface coverage relationship. For all values of $\wp$, Equation 4.50 shows a decrease in S as θ increases, which is consistent with adsorbates blocking adsorption sites on the surface. For values of $\wp \ll 1$, the sticking coefficient decreases quickly at higher values of θ whereas for $\wp \gg 1$, the sticking coefficient decreases quickly at lower values of θ and for $\wp = 1$, the sticking coefficient decreases linearly as θ increases.

Table 4.7 shows how the nature of the adsorption reaction, defined by the parameter $\wp$ in Equation 4.50, can influence the reaction order of R_{ct}, R_{chem} and of R_p. For low values of $\wp$, the reaction orders remain relatively independent of the nature of the adsorption reaction since the surface coverage does not reach high enough values for Equation 4.50 to take effect. However, as the value of $\wp$ increases above 1, indicating adsorbate/gas molecule interaction at low surface coverages, then the reaction orders of each resistance vary enough to make a simple analysis such as that using γ values in Table 3.2 (page 104) unreliable. For example, for $\wp = 1000$, the reaction order of R_{ct} with respect to pO_2 is $\gamma = 0.16$. However, for the same mechanism, Table 3.2 predicts $\gamma = 0.25$ for R_{ct}. This reaction order may also be mistaken for a completely different step in a different Mechanism, sk,uch as the charge transfer step in Mechanism 2 of Table 3.2 which has $\gamma = 0.125$.

Table 4.7: Variation in reaction order of R_{ct}, R_{chem} and R_p with various values of $\wp$ to describe $S = S(\theta)$ using Equation 4.50

	γ		
$\wp$	R_{ct}	R_{chem}	R_p
0	0.22	0.91	0.51
0.1	0.22	0.91	0.51
1	0.21	0.89	0.50
10	0.19	0.79	0.48
100	0.17	0.67	0.49
1000	0.16	0.65	0.57

Where $R \propto pO_2^{-\gamma}$

The fact that the reaction orders are greatly influenced by the rate constants of each process highlights the need for estimating those rate constants directly instead of relying on simple analysis that are often only valid for the most simple cases of pure rate limiting steps. Only by using modelling techniques, which can implement various features such as gas molecule-adsorbate interaction, can the contributions from each process be delineated.

4.3.2 Impedance Model Behavior

While steady state simulations can predict the shape of the polarization curve as well as the oxygen reaction orders of R_p and R_{ct} and indirectly R_{chem}, impedance simulations result in a direct calculation of R_{chem} (as well as R_{ct} and R_p). In addition to the calculation of these resistances, impedance spectroscopy modelling allows for the calculation of frequency dependent phase shifts which arise from the dynamics of each process. To calculate the electrochemical impedance response, the partial differential equations derived in Section 4.2.4 were solved simultaneously in the time domain to obtain time dependent sinusoidal current densities resulting from the sinusoidal potential boundary condition of Equation 4.39.

Figure 4.10 shows the applied sinusoidal potential and the resulting sinusoidal current density as well as the surface coverage for frequencies of 10kHz, 1Hz and 0.1Hz at the LSM/YSZ interface

($x = L$). The phase shift between the applied potential and the resulting current density can be used to calculate the impedance directly. This phase shift is larger for slow kinetics and transport processes and is also frequency dependent. An example of this phase shift between the current density and applied potential can be observed in Figures 4.10c and 4.10e. As Figures 4.10b, 4.10d and 4.10f also show, the sinusoidal potential induces sinusoidal responses in the species involved in the electrode reactions. As the applied potential becomes positive, the anodic current drives the production of surface species and as the applied potential becomes negative, the cathodic current consumes surface species.

The impedance response was calculated directly from the current/voltage behavior shown in Figure 4.10 using Equation 4.45. To investigate the general behavior of the impedance response, the same base set of kinetic parameters that were used for the steady state model were adopted (see Table 4.6). The influence of adsorption, surface diffusion and gas phase diffusion on the shape of the impedance response was investigated by changing the sticking factor (S), surface diffusion transport coefficient (D_θ^{eff}) and the cathode pore size (p_{avg}). These effects are shown in Figures 4.11, 4.12 and 4.13.

Influence of adsorption Figure 4.11 shows the calculated Nyquist and Bode plots of the total impedance (Z_{tot}) and Faradaic impedance (Z_{far}) for various values of the sticking coefficient at $750°C$ in $pO_2 = 10^{-4} atm$. It must be recalled that the Faradaic impedance is the electrode impedance in the absence of a double layer current. When the rate of adsorption decreases (due to a decrease in the sticking coefficient, S), the total impedance increases. This decrease in total impedance is caused by two main factors: 1) an increase in the Faradaic impedance due to the fact that the equilibrium surface coverage is decreased resulting in lower concentrations of surface species at the triple phase boundary and 2) an increase in the charge transfer resistance, attributed to the fact that the equilibrium surface coverage decreases. Both of these effects can be observed in the Faradaic impedance plots shown in Figure 4.11c where an increase in the high frequency intercept results from higher R_{ct} values and the difference between the low and high frequency intercepts is R_{chem}. For purely adsorption limited mechanisms, the shape of the Faradaic impedance Nyquist plot is a semi-circle, which is predicted by this impedance model as well as theoretical derivations of equivalent circuits. When other factors such as diffusion processes influence the kinetics of the

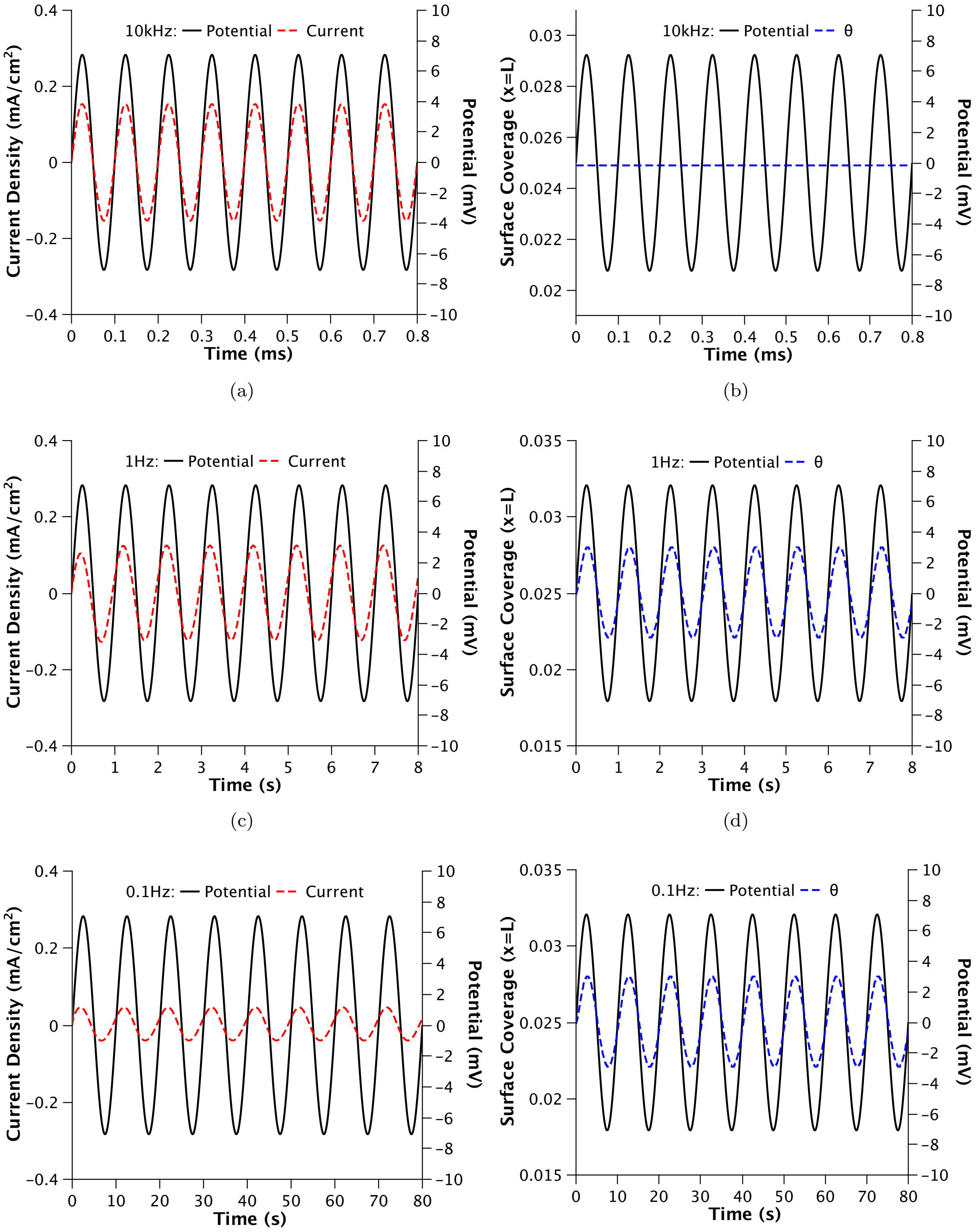

(a) (b)

(c) (d)

(e) (f)

Figure 4.10: Sinusoidal currents and surface coverages (at LSM/YSZ interface, $x = L$) vs applied potential: (a)-(b) Current and surface coverage at a frequency of 10kHz (c)-(d) Current and surface coverage at a frequency of 1Hz (e)-(f) Current and surface coverage at a frequency of 0.1Hz. The parameter set used to obtain these results is shown in Table 4.6.

mechanism, the shape of the Faradaic impedance can deviate from a semi-circle. Figure 4.11c shows that for the most part, the shape is semi-circular, due to the fact that for the chosen parameters, adsorption processes limit the electrode behavior. The shape of the Faradaic impedance at high frequencies in Figure 4.11c is due to a small, but non-negligible diffusion process.

In the Faradaic impedance Nyquist plot (Figure 4.11c), it is also interesting to note the shift in the high frequency intercept, which is related to the charge transfer resistance. As the rate of adsorption increases, the charge transfer resistance decreases. This is due to the dependence of the exchange current density (which dictates the charge transfer resistance) on the equilibrium surface coverage, as shown in Equation 4.13:

The shape of the phase shift vs frequency plot (a Bode plot) can also give valuable insight when analyzing impedance data. Figure 4.11b shows the phase shift of the total impedance and Figure 4.11d shows the phase shift of just the Faradaic impedance. As the rate of adsorption decreases, a large peak forms in Figure 4.11b at low frequencies. Generally the phase shift, like the total impedance, is masked by the double layer current; but, as the adsorption process becomes slow, a second peak at low frequencies associated with adsorption becomes apparent. The reason for the formation of the low frequency peak in the total impedance is evident by observing the phase shift of the Faradaic impedance (Figure 4.11d) as the adsorption rate constant decreases. From these Bode plots, we can determine that the adsorption process has a resonant frequency of between 0.2Hz and 0.4Hz. In Figure 4.11, as the adsorption rate constant increases, the equilibrium surface coverage increases from $\theta^{eq} = 0.023$ to $\theta^{eq} = 0.09$. The frequency at which the adsorption process responds therefore depends on the equilibrium surface coverage while the phase shift depends on the net rate of adsorption (the magnitudes of k_{ads} and k_{des}).

Influence of surface diffusion While the adsorption process influences both R_{ct} and R_{chem}, Figure 4.12 shows that surface diffusion only has an impact on the R_{chem} component. As expected, decreasing the surface diffusion coefficient results in an increase in the total impedance, shown in Figures 4.12a and 4.12b due to the fact that lower diffusion coefficients result in transport limitations which reduce the concentration of adsorbates at the triple phase boundary interface. The shape of the Nyquist plot for a surface diffusion limited Faradaic impedance is quite different from that of an adsorption limited Faradaic impedance though. Figure 4.12c shows that as the surface diffusion

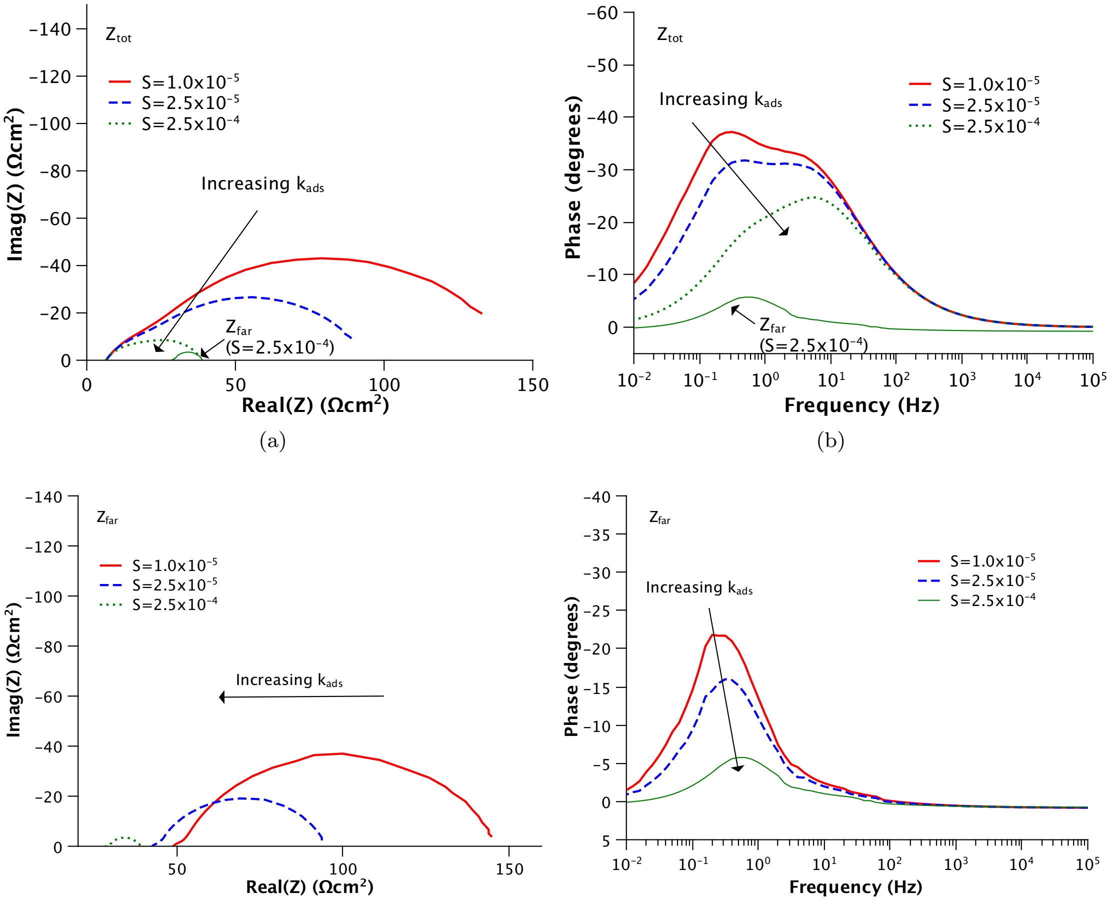

(a) (b)

(c) (d)

Figure 4.11: Influence of adsorption on the impedance response: Total impedance (a) Nyquist plot (b) Bode plot and Faradaic impedance (c) Nyquist plot (d) Bode plot. The parameter set used to obtain these results is shown in Table 4.6 and simulation conditions were at 750°C in $pO_2 = 10^{-4} atm$.

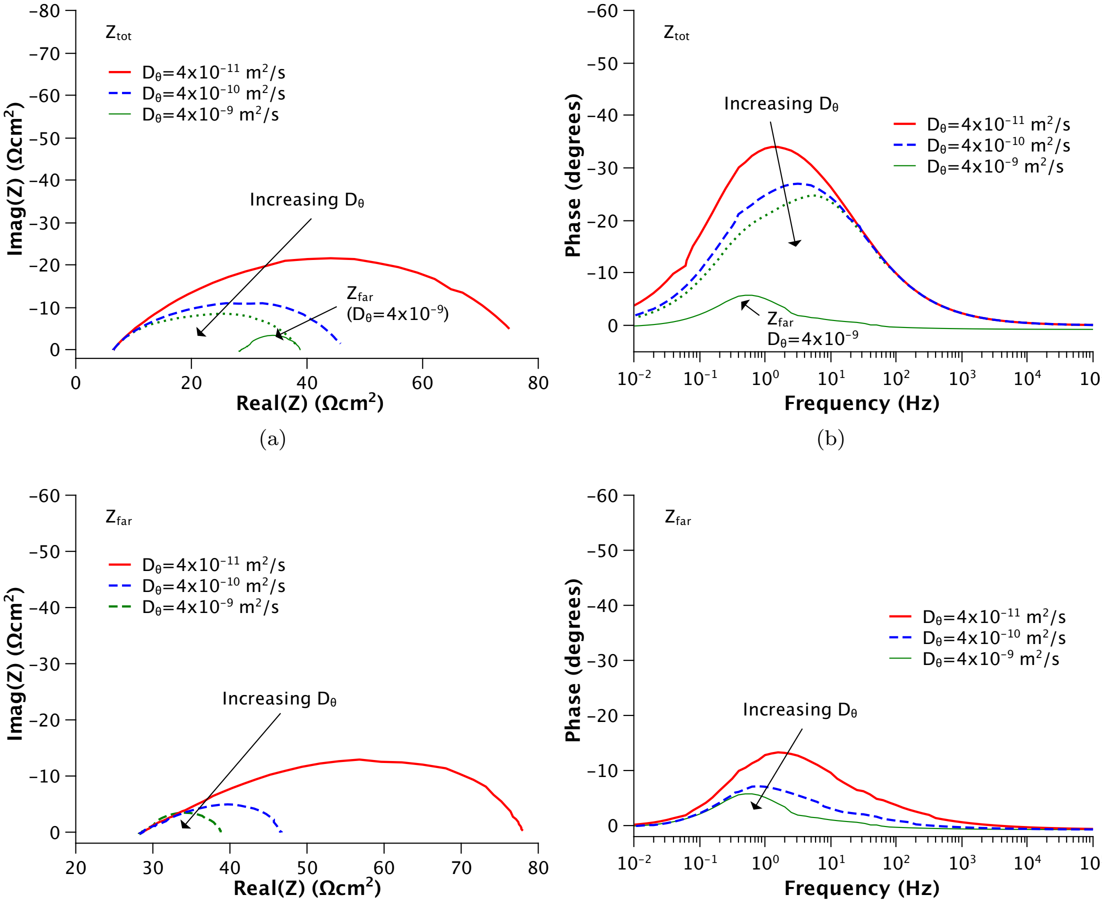

(a) (b)

(c) (d)

Figure 4.12: Influence of surface diffusion on the impedance response: Total impedance (a) Nyquist plot (b) Bode plot and Faradaic impedance (c) Nyquist plot (d) Bode plot. The parameter set used to obtain these results is shown in Table 4.6 and simulation conditions were at 750°C in $pO_2 = 10^{-4} atm$.

coefficient decreases, the shape of the Nyquist plot becomes more "tear-drop" like and resembles a Warburg or Gerischer impedance. Figure 4.12c shows that the high frequency intercept is independent of the surface diffusion coefficient. This is because the surface diffusion coefficient does not impact the equilibrium concentration of adsorbates; therefore, it has no impact on the exchange current density or R_{ct}. As the surface diffusion coefficient decreases, the phase shift increases, as expected, but the Faradaic impedance phase shift is shifted towards higher frequencies, unlike the adsorption process which shifts towards lower frequencies as adsorption is decreased. Figure 4.12d shows that the resonant frequency of the phase shift is between 1Hz and 4Hz.

Influence of pore size In addition to surface diffusion, gas phase diffusion may become important under certain operating conditions. At temperatures relevant to SOFC operating conditions and pore sizes on the order of 0.25-0.5μm [20], gas phase diffusion is in the transitional regime, which means that Knudsen diffusion has an impact on the total gas transport coefficient. Figure 4.13 shows the influence of gas phase diffusion on the impedance for pore sizes of 100 to 25nm, corresponding to a total gas phase diffusivity between 2.57×10^{-7} - 6.5×10^{-8} m^2/s respectively (at a porosity of 30% and 750$°C$). Again, as expected, when the pore size decreases, the total impedance increases. Similar to adsorption limiting kinetics and unlike surface diffusion limiting kinetics, the phase shift of gas phase diffusion limiting processes (Figure 4.13b) has a low frequency peak as a result of the low frequency response of the gas diffusion process. In observing the phase shift of the Faradaic impedance, Figure 4.13d, the resonant frequency is slightly lower, roughly 0.1Hz to 0.3Hz, but overlaps that of the adsorption process. Adsorption and gas phase diffusion are related since the equilibrium surface coverage is a function of the oxygen concentration. The major difference between adsorption and gas phase diffusion is in the Nyquist plot of the Faradaic impedance, Figure 4.13d, which shows a similar "tear-drop" shape as the surface diffusion case, again, indicating a diffusion controlled process. When comparing the Faradaic impedance phase shift for both gas phase diffusion and surface diffusion it is also interesting to note that for the diffusion processes, the phase shift is higher at high frequencies compared to the adsorption reaction which has a phase shift close to 0 at high frequencies.

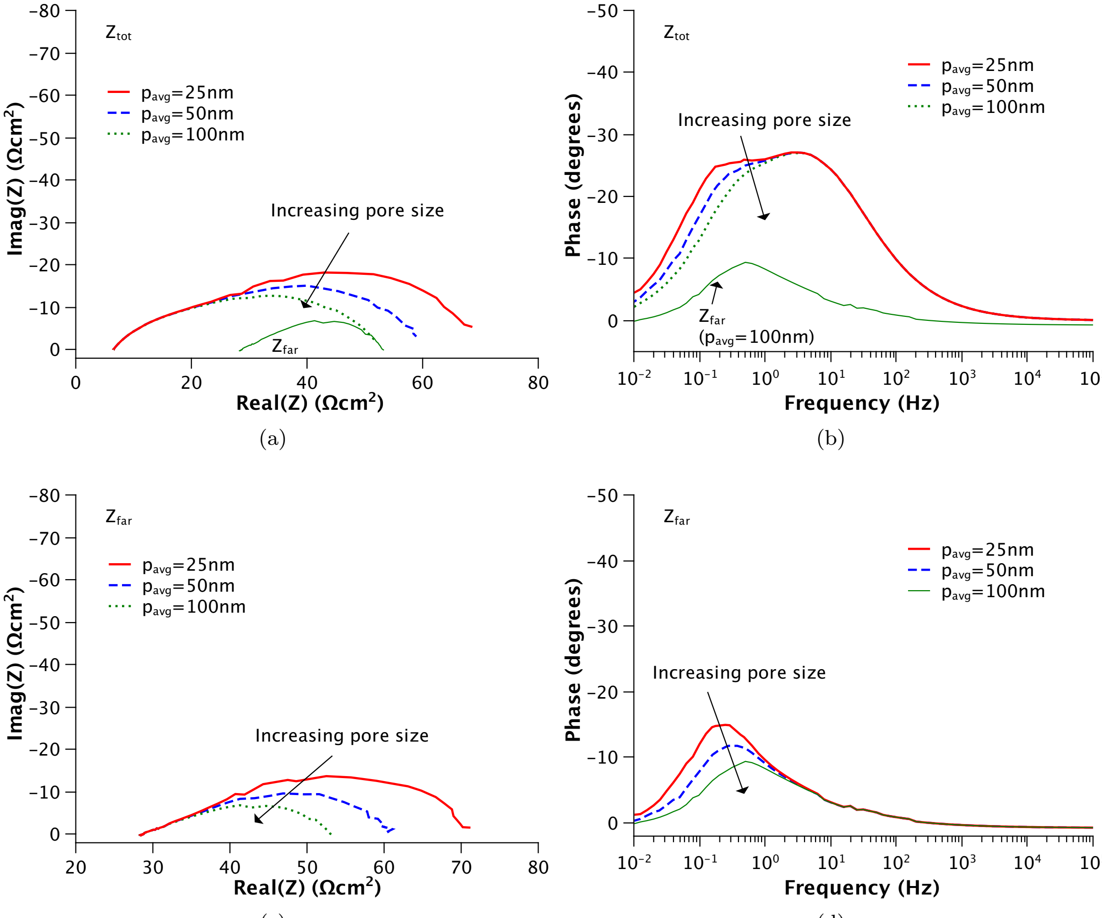

(a) (b)

(c) (d)

Figure 4.13: Influence of gas diffusion on the impedance response: Total impedance (a) Nyquist plot (b) Bode plot and Faradaic impedance (c) Nyquist plot (d) Bode plot. The parameter set used to obtain these results is shown in Table 4.6 and simulation conditions were at 750°C in $pO_2 = 10^{-4} atm$.

4.3.3 Summary of General Model Behavior

Section 4.3 discussed the general behavior of the steady state and impedance models. From the steady state model behavior, Section 4.3.1, the following observations were made:

1. The convective flux portion of gas transport is insignificant compared to the diffusive flux for electrode permeabilities higher than $\kappa = 10^{-17}\ m^2$.
2. Limiting currents occur when the surface coverage at the LSM/YSZ interface tends to 0.
3. Chemical and electrochemical processes are highly coupled and changes to one process can influence another.
4. Oxygen reaction orders depend to a large extent on the rate constants and transport coefficients of the various processes. Adsorbate interactions with gas molecules which influence the sticking coefficient can change the reaction order of both R_{ct} and R_{chem} significantly, which complicates a simple reaction order analysis of experimental data.

From the impedance model behavior, Section 4.3.2, the following observations were made:

1. The resonant frequency of the adsorption/desorption reaction is between 0.2Hz and 0.4Hz, the resonant frequency of surface diffusion is 1Hz to 4Hz and the resonant frequency of gas phase diffusion limitations is 0.1Hz to 0.3Hz but highly coupled to adsorption/desorption.
2. The charge transfer resistance is affected by the rate of the charge transfer reaction and the adsorption/desorption rate constants. The triple phase boundary length and the electrolyte composition also affect R_{ct} however they are generally considered to be constant for a given electrode.
3. Warburg like Faradaic impedances can be modelled from surface diffusion as well as gas diffusion limiting reactions.
4. The shape of the Faradaic impedance for an adsorption limiting process is a semi-circle whereas the shape of the Faradaic impedance for a diffusion reaction is “tear-dropped”.

4.4 Model Fit to Experimental Data

A number of kinetic and transport parameters for oxygen reduction processes in the LSM cathode are unknown and must be estimated by fitting to experimental data. These parameters are: (i) the sticking coefficient, S (ii) the zero-point energy of the adsorption/desorption reaction, ΔE_{dft}, or the desorption activation energy E_{des} (iii) the surface diffusion coefficient, D_{θ}^{eff} and (iv) the electrochemical rate constant $k_{ct} = k_f^0 = k_b^0$. When fitting the experimental data, the steady state polarization curves and the impedance spectroscopy experiments were fit separately. Ideally, there are a number of experimental features that can be used to determine the proper parameter set. For the steady state case, these features include:

1. The reaction order of the polarization resistance (R_p)
2. The full steady state polarization curve over a range of oxygen partial pressures
3. The presence or lack of limiting currents

The advantage of using impedance spectroscopy compared to steady state polarization measurements is that there are a number of additional experimental features that can be useful in determining the proper parameter set. These additional experimental features are what make EIS so powerful when performing kinetic studies. Moreover, the traditional equivalent circuit analysis of impedance data can also be used to complement the impedance model presented in this work. The experimental features that can be used to validate the impedance model include:

1. The polarization resistance (R_p), charge transfer resistance (R_{ct}) and chemical resistance (R_{chem}) of the impedance determined from equivalent circuit fitting
2. The reaction order with respect to oxygen of R_p, R_{ct} and R_{chem}
3. The phase shift of the total impedance (Z_{tot}) as well as the phase shift of the Faradaic impedance (Z_{far}) determined from equivalent circuit fitting
4. Any experimental non-linear behavior with respect to the AC amplitude (η_{var} in Equation 4.39) of the applied sinusoidal potential

5. The impedance response under DC bias conditions

Combining equivalent circuits with a physical impedance model allows us to fit not just the polarization resistance and the phase shift of the total impedance but also the components of the total polarization resistance, i.e., R_{ct} and R_{chem}. In addition to the impedance response, it is also possible to simulate the dynamic response of a step change in the current or gas concentration and compare against experimental behavior. With a time dependent model, these step changes can be easily calculated, however, their experimental counterpart is more difficult to obtain due to the difficulty of changing the bulk pO_2 instantaneously. Along with fitting the experimental features mentioned above, it is desirable to obtain high quality experimental data. For reasons previously discussed, it was easier to fit the experimental data in low pO_2s between 10^{-4}atm and 10^{-3}atm O_2 due to the fact that these conditions exaggerate certain experimental features such as limiting currents and the low frequency phase shift. In addition, there is more evidence to support a mechanism in which neutral oxygen atom is transported along the LSM surface for these low pO_2 conditions as opposed to high pO_2 conditions.

The fitting process involved the following steps: 1) model parameters were fit to experimental steady state data, ensuring that experimental features were reproduced as best as possible 2) from the steady state parameter fits, the impedance spectra at OCV was fit, with a particular focus on ensuring that the phase shift as well as the polarization resistance matched experimental data as best as possible.

It should be noted that at this point, it is unknown whether or not the parameter set estimated by fitting against experimental data is unique. This model requires four fitting parameters and the uniqueness of the solution was considered to be outside the scope of this thesis. It should also be pointed out though that techniques such as the analysis of EIS data using equivalent circuits also may not be unique solutions since various equivalent circuit models are known to fit the same experimental data. The following sections discuss the parameter estimates that were found to give the best fit to the experimental data collected in $10^{-4}atm \leq pO_2 \leq 10^{-3}atm$ within the parameter constraints.

- Section 4.4.1 discusses the model parameters obtained by fitting against steady state polarization data

- Section 4.4.2 discusses the model parameters obtained by fitting against impedance data at OCV

4.4.1 Fitting Model Parameters to Steady-State Polarization Data

The steady state model was fit to combined polarization data collected for pO_2s of 10^{-4}atm, 2.5×10^{-4}atm, 5.0×10^{-4}atm and 10^{-3}atm, but one temperature at a time using the Matlab optimization routine '*fminsearchcon*' with the objective function defined by Equation 4.41. Table 4.8 shows the parameter set obtained after fitting the model to experimental polarization curves at each temperature and Figures 4.14a, 4.14c and 4.14e show the comparison of the model and experimental polarization curves using the parameter set shown in Table 4.8.

Table 4.8: Model fitting parameters for steady state polarization curve

Parameter	$750°C$	$800°C$	$850°C$	Eq.
S	1.28×10^{-4}	1.52×10^{-4}	1.68×10^{-4}	4.24
ΔE_{dft} (eV)*	-2.62	-2.62	-2.62	4.33
D_θ^{eff} $(m^2\ s^{-1})$	2.62×10^{-9}	2.85×10^{-9}	6.89×10^{-8}	
k_{ct} $(m^4\ mol^{-1}\ s^{-1})$	4.99×10^{-11}	1.70×10^{-10}	1.36×10^{-9}	4.38
$S = 2.8 \times 10^{-3} \exp(-0.27eV/R/T)$				
$D_\theta^{eff} = 7.8 \times 10^{6} \exp(-3.19eV/R/T)$				
$k_{ct} = 4.9 \times 10^{5} \exp(-3.26eV/R/T)$				

* Kept constant after $750°C$ fitting

At $750°C$, the combined model fit of the polarization curve for the four oxygen concentrations had a χ^{ss} value (defined by Equation 4.41) of 0.093, while that at $800°C$ had a $\chi^{ss} = 0.132$ and at $850°C$, $\chi^{ss} = 0.197$. The model fit was more accurate at high potentials compared to low potentials. The reaction order of R_p at OCV predicted by the model was 0.20, 0.25 and 0.28 at $750°C$, $800°C$ and $850°C$ respectively while that of the experimental data was 0.40, 0.43 and 0.44 over the same temperature range. The reaction order of the limiting current predicted by the model was 0.93, 0.89 and 0.85 at $750°C$, $800°C$ and $850°C$ respectively compared to 1.0 for the experimental data over the same temperature range.

The model fit at low potentials matched experimental data better at pO_2s of 10^{-4}atm and 2.5×10^{-4}atm compared to 5.0×10^{-4}atm and 10^{-3}atm. At $750°C$, the model R_p at OCV in

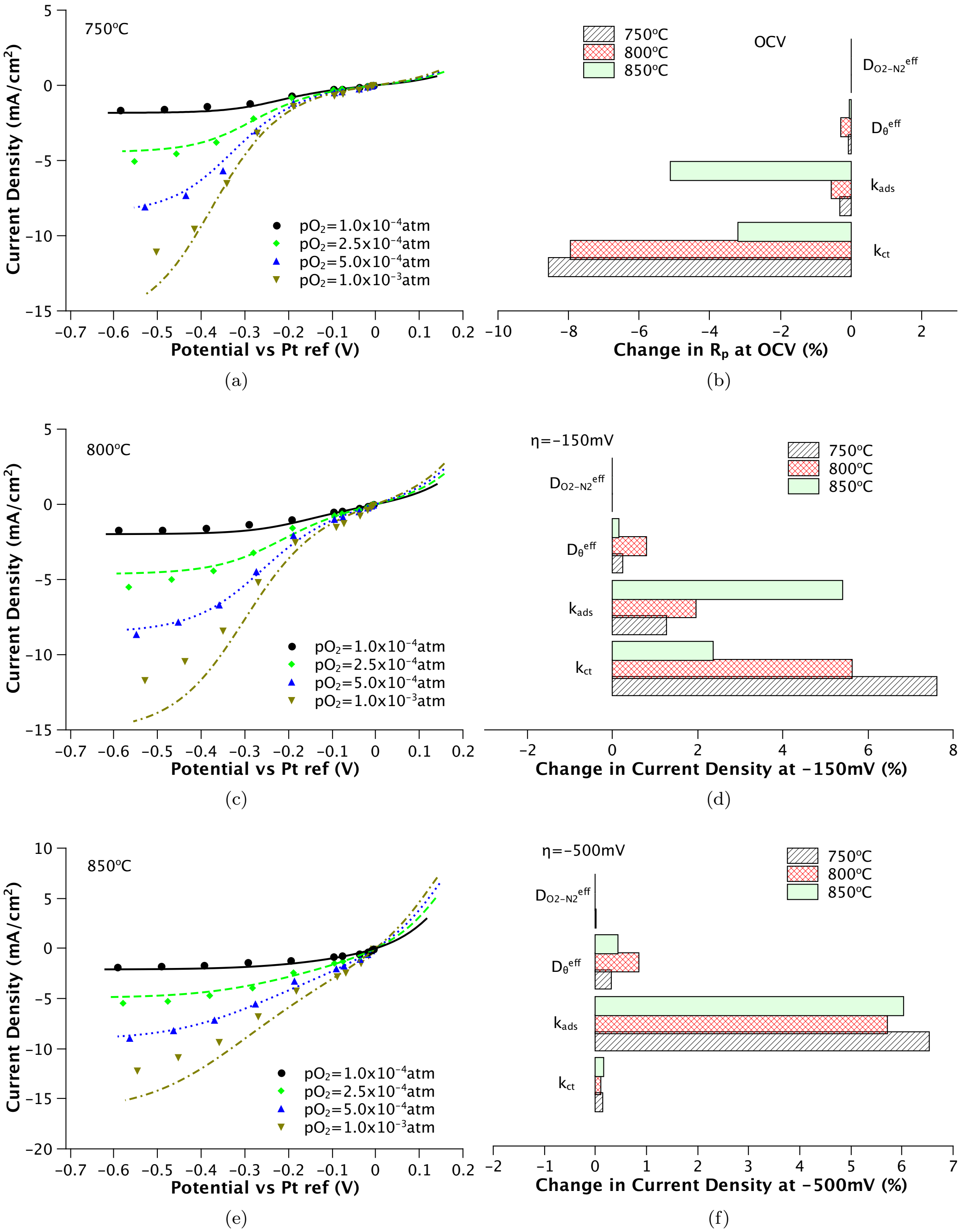

(a) (b)

(c) (d)

(e) (f)

Figure 4.14: (a), (c), (e) Comparison of model (lines) and experimental (data points) polarization curves in 750, 800 and 850°C respectively (b), (d), (f) Sensitivity of parameters with respect to R_p at OCV, with respect to current density at $\eta = -150mV$ and with respect to current density at $\eta = -500mV$ respectively in $pO_2 = 10^{-4}$atm. The sensitivity analysis shows the deviation of R_p or current density at the indicated potential when each parameter is increased by +10%. The parameter set is given in Table 4.8.

10^{-4}atm and 2.5×10^{-4}atm were both within 5% of the experimental data however, this error increased to 25% and 40% in 5.0×10^{-4}atm and 10^{-3}atm respectively. It should be noted that it was possible to find a parameter set that could fit the polarization resistance at OCV, however, the parameter set that matched R_p also predicted much lower limiting currents over each pO_2 and ultimately had a much larger χ value over the full polarization curve.

Sensitivity analysis While the parameter values in Table 4.8 can provide quantitative comparisons of the rates of the various processes, they do not directly give information about their relative contributions towards the oxygen reduction reaction. To compare each of their respective contributions to the ORR, a sensitivity analysis was performed by increasing the rate constant or transport coefficient of each process by 10% and calculating the resulting change in the polarization curve. This way, the relative contributions of each process can be gauged and a qualitative opinion can be formed on the importance of each process towards oxygen reduction. The sensitivity of parameters in Table 4.8 are shown in Figures 4.14b with respect to the polarization resistance, R_p, at OCV and Figures 4.14d and 4.14f show the sensitivity of the parameters with respect to the current density at $\eta = -150mV$ and $\eta = -500mV$ in $pO_2 = 10^{-4}$atm. Parameters k_{ct}, k_{ads}, D_{θ}^{eff} and $D_{O_2-N_2}^{eff}$ represent the rate constant of the electrochemical reaction at the LSM/YSZ interface, the rate constant of adsorption, the surface diffusion transport coefficient and the gas transport coefficient, respectively. Parameter increases that result in a comparatively large decrease in R_p or increases in current density represent slow processes in the mechanism.

Figure 4.14b indicates that for near OCV conditions, at $750°C$ and $800°C$, the electrochemical rate constant is the parameter most sensitive to R_p however, at $850°C$, both the electrochemical reaction and adsorption impact R_p at OCV. The reason why adsorption can be influential even at OCV is because adsorption can also influence i_0 through the equilibrium surface coverage. As expected, at OCV conditions, the surface diffusion coefficient and the gas transport coefficient have a negligible impact on R_p at OCV owing to the fact that the flux of these species is small at OCV. Away from OCV conditions, Figures 4.14d and 4.14f indicate that the electrochemical reaction at the TPB is still an important process in the mechanism, even at $\eta = -150mV$, however, as the overpotential increases further to $\eta = -500mV$, adsorption clearly limits the oxygen reduction reaction. Surprisingly, the current density is not sensitive to 10% increases in the gas transport

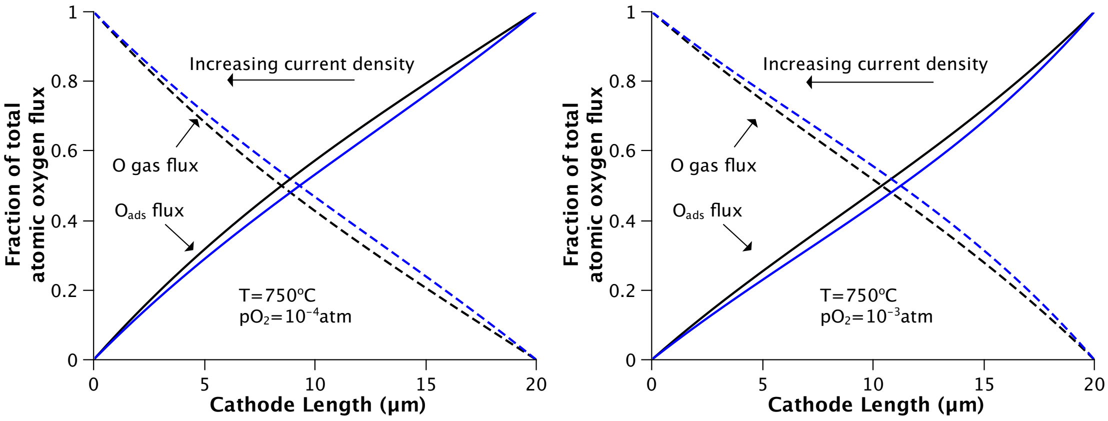

(a) (b)

Figure 4.15: Fraction of oxygen flux from gas phase and surface phase (in terms of atomic oxygen) at a temperature of 750°C and (a) $pO_2 = 10^{-4}$atm (b) $pO_2 = 10^{-3}$atm. The parameter set used to obtain these results is shown in Table 4.8.

coefficient even at high overpotentials and only slightly sensitive to a 10% increase in the surface diffusion coefficient. This is because both the gas phase pathway and the surface transport pathways are limited by the slow kinetics of the adsorption reaction.

The sensitivity analysis can provide information about limiting processes in the oxygen reduction reaction, however, it does not provide information about the preference between the two pathways that are considered: 1) the gas phase pathway 2) the surface pathway. Figures 4.15a and 4.15b show the relative contributions of the flux of gas phase oxygen (atomic oxygen) and surface oxygen species throughout the electrode for a $pO_2 = 10^{-4}$atm and $pO_2 = 10^{-3}$atm at 750°C. These fluxes were calculated using Equation 4.48. For a $pO_2 = 10^{-4}$atm, the surface oxygen flux was larger than the gas phase flux after 8μm of the 20μm thick electrode. This indicates that the surface pathway was more favorable than the gas phase pathway over the majority of the electrode thickness. However, as the pO_2 was increased to 10^{-3}atm, the gas phase pathway became more favorable since the gas phase flux was larger than the surface oxygen flux over the majority of the electrode thickness. Figures 4.15a and 4.15b also show the flux contributions for low and high current densities. As the current density increased, the surface diffusion pathway became slightly more favorable compared to the gas phase pathway.

It should be noted that the gas transport coefficient was not treated as a fitting parameter and was calculated based on the method described in Section 4.2.5 (page 164). In the transition regime for gas transport, $D_{O_2-N_2}^{eff}$ is primarily influenced by the average pore size (or the Knudsen number) in the electrode which we calculated [20] to be $p_{avg} = 0.25\mu m$. To further explore the influence of gas phase transport, another parameter fit was performed, this time taking the average pore size to be $p_{avg} = 0.5\mu m$ instead of $p_{avg} = 0.25\mu m$, which represents a 90% increase in $D_{O_2-N_2}^{eff}$ from $6.3 \times 10^{-7}\ m^2/s$ to $1.2 \times 10^{-6}\ m^2/s$. This second fitting routine resulted in only a 4% decrease in D_{θ}^{eff}. This indicates that any limitations from the gas phase are not caused by the small pore size but instead from the low bulk pO_2 values.

Predicted species distributions Figure 4.16 shows the concentration of adsorbates (in terms of normalized surface coverage, θ/θ^{eq} where θ^{eq} is calculated with the bulk concentration of oxygen gas, not the local oxygen gas concentration) and the oxygen partial pressure (in terms of normalized partial pressure, pO_2^{loc}/pO_2^{eq}) along the thickness of the electrode for temperatures of $750°C$, $800°C$ and $850°C$ and pO_2s between 10^{-4}atm and 10^{-3}atm at a current density equal to the limiting current in 10^{-4}atm O_2: $i_L(750°C) = -1.83mA/cm^2$, $i_L(800°C) = -1.98mA/cm^2$ and $i_L(850°C) = -2.10mA/cm^2$. The gradient in surface coverages indicate that either surface species are diffusing towards the LSM-YSZ interface or that locally the equilibrium between oxygen gas and surface is affected by the local oxygen concentration varying from its bulk, or equilibrium level. Although gradients in the oxygen concentration exist, as shown in Figure 4.16b, the limiting currents shown in the polarization curve are caused by the depletion of adsorbed oxygen at the LSM/YSZ surface because of the slow adsorption kinetics.

The slow adsorption kinetics and low pO_2s also result in low equilibrium surface coverages. Figure 4.17a plots the surface coverage and Figure 4.17b plots the oxygen partial pressure at the LSM/YSZ interface with respect to the current density for $pO_2 = 10^{-4}$atm at various temperatures. As the current increases, both oxygen adsorbates and oxygen gas are depleted near the LSM/YSZ interface until the surface coverage drops to 0 at the limiting current. The fact that the oxygen gas concentration drops by only half indicates that it is not the direct cause of the limiting currents observed in the polarization curves, although, since the local pO_2 is coupled to the rate of adsorption, it does contribute. Figure 4.17a also indicates the equilibrium surface coverage, which is the surface coverage when no net current flows through the cell ($i = 0$). The values for the equilibrium surface

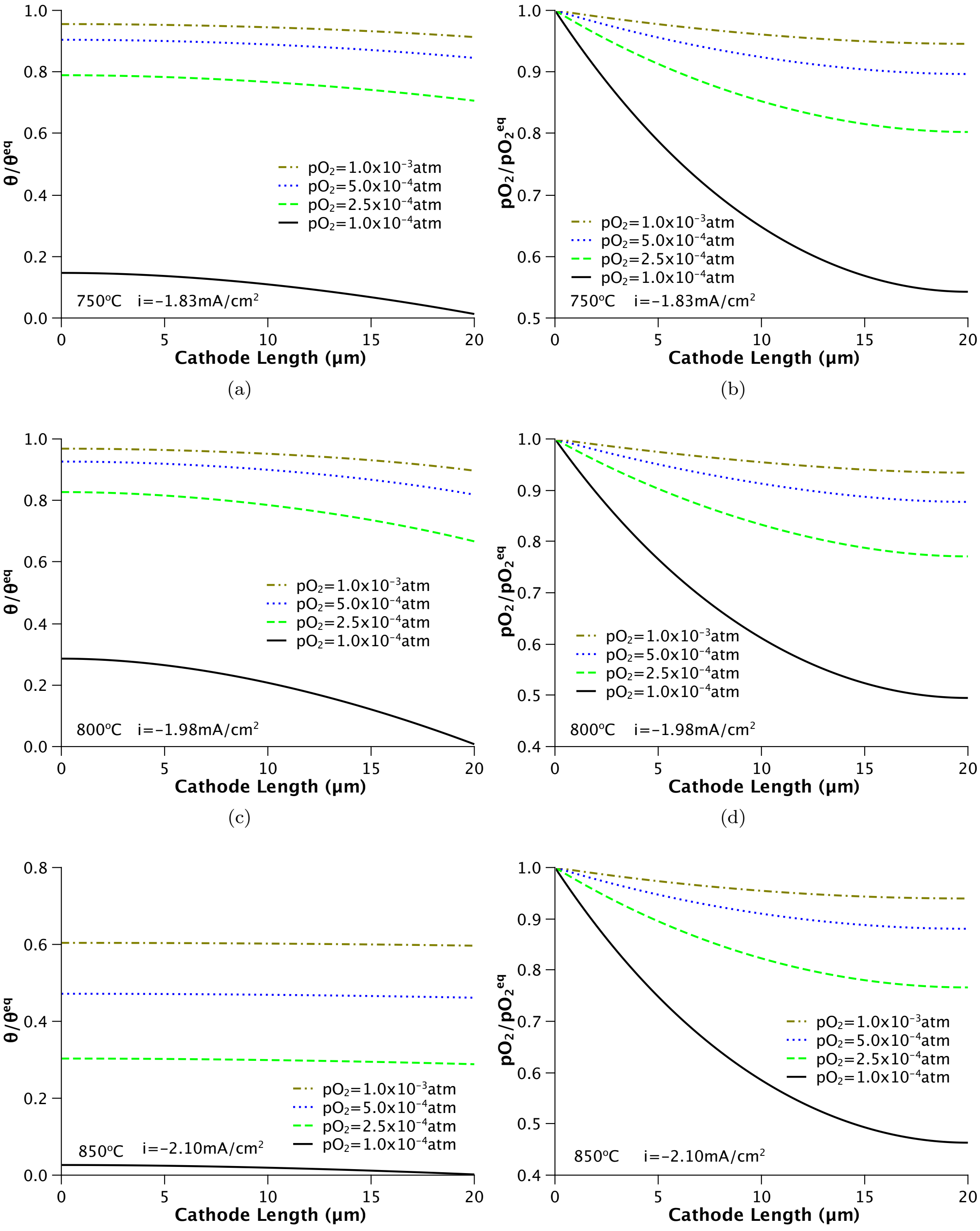

(a) (b)

(c) (d)

(e) (f)

Figure 4.16: Surface coverage and pO_2 distribution at 10^{-4}atm limiting current densities: (a), (c), (e) Surface coverage at 750, 800 and 850$°C$ respectively (b), (d), (f) Oxygen gas distribution at 750, 800 and 850$°C$ respectively. The current density at each temperature was taken to be the limiting current density in 10^{-4}atm O_2 which was $i(750°C) = -1.83mA/cm^2$, $i(800°C) = -1.98mA/cm^2$, $i(850°C) = -2.10mA/cm^2$. The parameter set used to obtain these results is shown in Table 4.8.

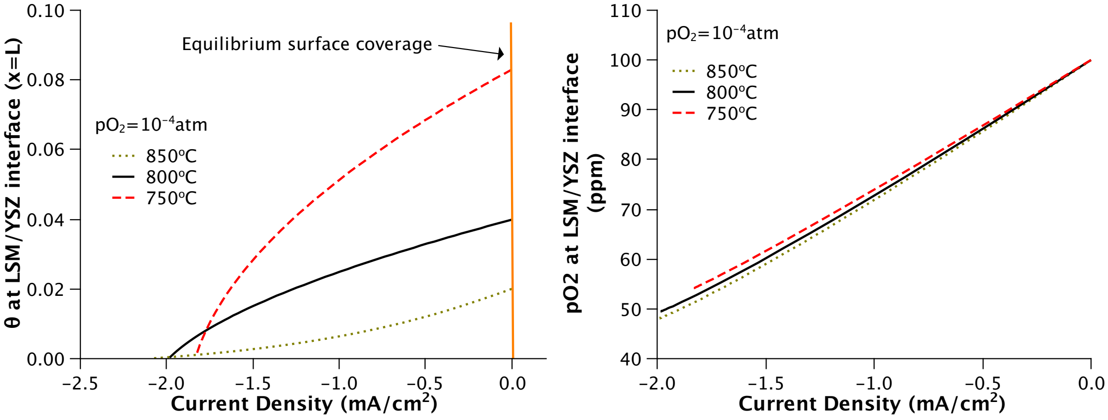

(a) (b)

Figure 4.17: (a) Surface coverage at LSM/YSZ interface ($x = L$) with respect to current density (b) Oxygen concentration at LSM/YSZ interface ($x = L$) with respect to current density. The parameter set used to obtain these results is shown in Table 4.8.

coverage for $pO_2 = 10^{-4}$atm were: $\theta^{eq}(750°C) = 0.082$, $\theta^{eq}(800°C) = 0.040$ and $\theta^{eq}(850°C) = 0.020$. The reason why the equilibrium surface coverage decreases with increasing temperature is a result of thermodynamic consistency in the adsorption/desorption reaction and occurs because the heat of an adsorption reaction ($\Delta_{ad}H^{\ominus}$) is typically negative, resulting in a decrease in the ratio $K_{ad} = k_{ads}/k_{des}$ as temperature increases. Experimental evidence for this is also reflected in the experimental CV plots of Figure 3.24 (page 141) discussed in Section 3.3.3.

Impedance simulation using steady state parameters As previously mentioned, the parameters obtained from the polarization curve fitting were able to fit high overpotentials better than low overpotentials. For a better understanding of why this is, the impedance response at OCV can be simulated and compared to experimental data. Figure 4.18 shows the impedance response calculated using the steady state parameter set at 750°C and in pO_2s of 10^{-4}atm and 10^{-3}atm. The experimental impedance data shown in Figure 4.18 is for an unpolarized electrode, that is, an electrode that has not been exposed to a net cathodic current. As mentioned in Chapter 3, polarized and unpolarized electrode behave differently, which is one reason contributing to the poor fit between the model and experimental impedance data. However, of particular note is the very small contribution of the Faradaic impedance to the total impedance (shown for 10^{-3}atm O_2), which indicates that the

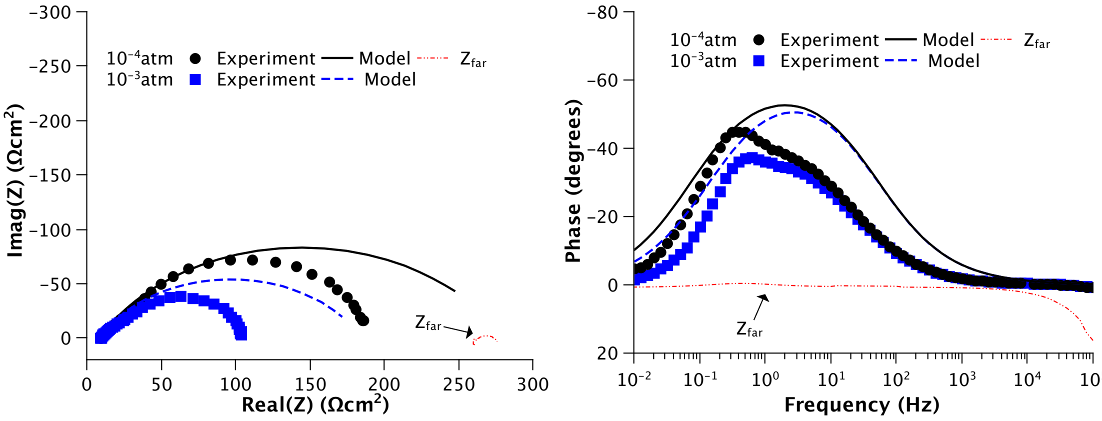

(a) (b)

Figure 4.18: Impedance simulation using steady state fitting parameters at 750°C in 10^{-4}atm and 10^{-3}atm O_2: (a) Nyquist (b) Bode plot.

parameter set estimates values of R_{chem} that are much too small at open circuit conditions. This is also evident in the Bode plot where the model only predicts a single peak however, the experimental data has two peaks at lower frequencies. The low frequency peak observed in the impedance experiments is not predicted by the model using the steady state parameters because the R_{chem} contribution is too small. Experimentally, the ratio of R_{chem}/R_p at 750°C is equal to 0.75 at 750°C and 10^{-4}atm (see Figure 3.8 page 107 in Section 3.3.2) whereas the model predicts R_{chem}/R_p equal to only 0.05. The fact that the parameters which fit high overpotentials predict much lower R_{chem} values at OCV may indicate that R_{chem} is enhanced as the overpotential increases, which could point towards an electrochemical adsorption reaction.

4.4.2 Fitting Model Parameters to Impedance Data

In Chapter 3 the differences between polarized and pre-polarized electrodes were discussed. Due to the seemingly different behavior between polarized electrodes and pre-polarized electrodes, it was of interest to fit the impedance data of pre-polarized electrodes so as to gain insight into what processes/parameters were responsible for the different behavior within the framework of the chosen mechanism. For this reason, it was necessary to fit the impedance response separately from the steady state polarization curve. To achieve this, the steady state parameter set provided initial guesses for the impedance response fitting. The experimental features that were considered to be most important while fitting the impedance data were: 1) the phase shift which showed two distinct peaks at low pO_2 2) the charge transfer resistance, R_{ct}, determined from equivalent circuit fitting and 3) the chemical resistance, R_{chem}, determined from equivalent circuit fitting. The determination of experimental values of R_{ct} and R_{chem} from equivalent circuits was described in Chapter 3.

Fitting parameters Table 4.9 lists the parameters obtained from the impedance fitting procedure. It was not possible to fit all three features simultaneously with a single parameter set, however, the fit became better as the temperature increased. At $750°C$ and $800°C$, it was necessary to make the sticking coefficient a function of pO_2 in such a way so that $S = S^0 \times pO_2^{\delta}$, where δ was a constant determined after fitting the individual pO_2s. The fact that the sticking coefficient changed with pO_2 likely indicates that it depends on the surface coverage, meaning that there are interactions between the reactant oxygen gas molecules and the surface species. At both $750°C$ and $800°C$, as the pO_2 increased, the sticking coefficient decreased which is consistent with surface species blocking molecules from adsorbing onto the electrode surface. As explained in Section 4.2.5, it is possible for the sticking coefficient to be a complex function of surface coverage, which is a deviation away from Langmuir adsorption kinetics. To mathematically describe these deviations away from typical Langmuir behavior, Kisliuk [37] derived the following expression to describe various shapes of the sticking coefficient vs surface coverage that have been observed for adsorption on metal surfaces:

$$S = S^0 \left(1 + \frac{\theta}{1-\theta}\wp\right)^{-1}$$

where $\wp$ is a parameter describing the shape of the sticking coefficient vs surface coverage relationship. For all values of $\wp$, Equation 4.50 shows a decrease in S as θ increases, which is consistent with the fitting results found in Table 4.9. This type of surface coverage dependent sticking coefficient is currently being implemented in an attempt to describe the parameter sets at $750°C$ and $800°C$.

Another adsorption model which accounts for interactions between adsorbates is Temkin adsorption and assumes that the heat of adsorption is a linear function of coverage. As explained in [48,49], assuming a linear surface dependent heat of adsorption results in the rate of adsorption/desorption

Table 4.9: Model fitting parameters for impedance at OCV

Parameter	$750°C$	$800°C$	$850°C$	Eq.
S	$4 \times 10^{-8} pO_2^{-0.573}$	$8 \times 10^{-7} pO_2^{-0.371}$	7.36×10^{-5}	4.24
E^*_{des} (eV)	0.38	0.33	0.48	4.26
D^{eff}_{θ} $(m^2\ s^{-1})$	2.62×10^{-9}	2.85×10^{-9}	6.89×10^{-8}	
k_{ct} $(m^4\ mol^{-1}\ s^{-1})$	1×10^{-9}	1.2×10^{-9}	1.3×10^{-9}	4.13
Q^*_{cpe} $(Sm^{-2} \cdot s^{P_{cpe}})$	37-40	45-50	57-60	4.47
P^*_{cpe}	0.77	0.72	0.68	4.47

* Based on collision theory

being exponentially dependent on the surface coverage so that

$$r_{ads} = k_{ads} pO_2 (1-\theta)^2 \exp\left(-\frac{\varpi r \theta}{RT}\right) \tag{4.51a}$$

$$r_{des} = k_{des} \theta^2 \exp\left(\frac{(1-\varpi) r \theta}{RT}\right) \tag{4.51b}$$

where ϖ is a type of symmetry factor and r is a coefficient determining the variation of heat of adsorption with coverage. Temkin adsorption is typically valid for intermediate surface coverages between $0.2 < \theta < 0.8$ [48].

A model incorporating Temkin adsorption was explored however for values of r that make Temkin contributions significant relative to typical Langmuir kinetics, the oscillations in θ with time at low frequencies are such that the the impedance calculation becomes unstable. For the time being, the sticking coefficient at temperatures of $750°C$ and $800°C$ have been left as a function of pO_2.

Model comparison to experiments Figures 4.19 and 4.20 show the impedance model comparison against experimental data at temperatures of $750°C$, $800°C$ and $850°C$ using the parameter sets shown in Table 4.9. Figure 4.19 plots the total impedance and total phase shift against experimental data while Figure 4.20 compares the values of R_{ct}, R_{chem} and R_p of the model to the experimental data. The quality of fit of the total impedance as well as the individual resistances and the reaction orders, γ, are summarized in Table 4.10. The quality of fit for the impedance simulation, χ^{imp}, was calculated for each pO_2 using Equation 4.43 and averaged over those pO_2s at $750°C$, $800°C$ and

850°C while the quality of fit for the individual resistances, χ^R, was calculated from Equation 4.42. Compared against the steady state fitting, the reaction orders of the impedance model were much closer to the experimental data, however, this is expected since the impedance model is focused only on a single operating point, open circuit conditions, compared to the full polarization curve for the steady state fitting.

Table 4.10: Quality of fit and pO_2 dependencies of impedance model parameters compared to experimental data

Temperature	χ^{imp} *	χ^R			γ^{mod} (γ^{exp})		
(°C)		R_{ct}	R_{chem}	R_p	R_{ct}	R_{chem}	R_p
750	249	1.06	2.34	0.85	0.10 (0.15)	0.41 (0.34)	0.32 (0.28)
800	29.8	0.56	4.73	1.21	0.15 (0.22)	0.59 (0.50)	0.37 (0.35)
850	8.9	0.60	0.89	0.11	0.20 (0.22)	0.77 (0.93)	0.46 (0.42)

* Averaged over the pO_2s for each temperature

γ^{mod}: model reaction order, γ^{exp}: experimental reaction order where $R \propto pO_2^{-\gamma}$

Model parameters shown in Table 4.9

In observing the reaction orders shown in Table 4.10, one pitfall of a basic mechanistic analysis using theoretically derived reaction orders becomes evident: for processes that are mixed (such as adsorption and surface diffusion), the observed reaction order can have a large range which makes it difficult to pinpoint exact processes. This is easily shown by comparing the reaction orders in Table 4.10 with those previously derived by assuming a single rate determining step in Table 3.2 (page 104) of Chapter 3. For a mechanism involving surface diffusion of neutral adsorbates (Mechanism 1, Table 3.2), the reaction order of an adsorption rate determining step was found to be $\gamma = 1$, whereas for a surface diffusion limiting process, $\gamma = 0.5$ and for a charge transfer limiting process, $\gamma = 0.25$. Table 4.10 shows that the observed reaction order of R_{chem} can range from 0.41 to 0.77 and depends on the values of D_θ, k_{ads} and k_{des}. The variation in the reaction order of R_{ct} shown in Table 4.10 is solely due to the change in θ^{eq} which is caused by interactions between surface species and gas molecules.

Apart from the variation in the reaction orders of the impedance simulations, one of the most interesting features of the experimental impedance data is the low frequency peak in the Bode plot, shown in Figures 4.19b, 4.19d and 4.19f. This low frequency peak is caused entirely by the

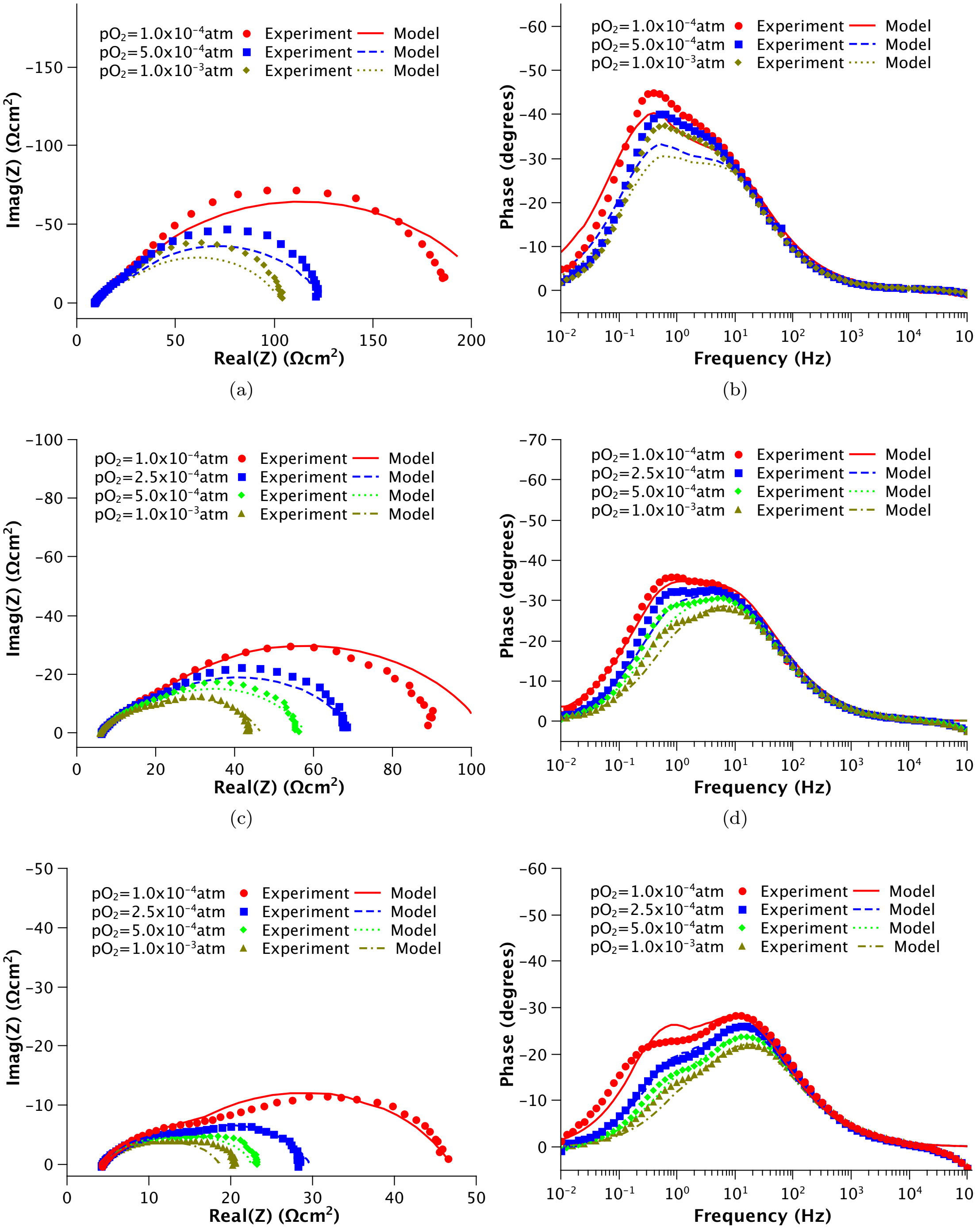

(a)

(b)

(c)

(d)

(e)

(f)

Figure 4.19: Comparison of impedance model to experimental data: (a)-(b) Nyquist and Bode plots at 750°C and pO_2's between 10^{-4}atm and 10^{-3}atm (c)-(d) Nyquist and Bode plots at 800°C and pO_2's between 10^{-4}atm and 10^{-3}atm (c)-(d) Nyquist and Bode plots at 850°C and pO_2's between 10^{-4}atm and 10^{-3}atm. The parameter set used to obtain these results is shown in Table 4.9.

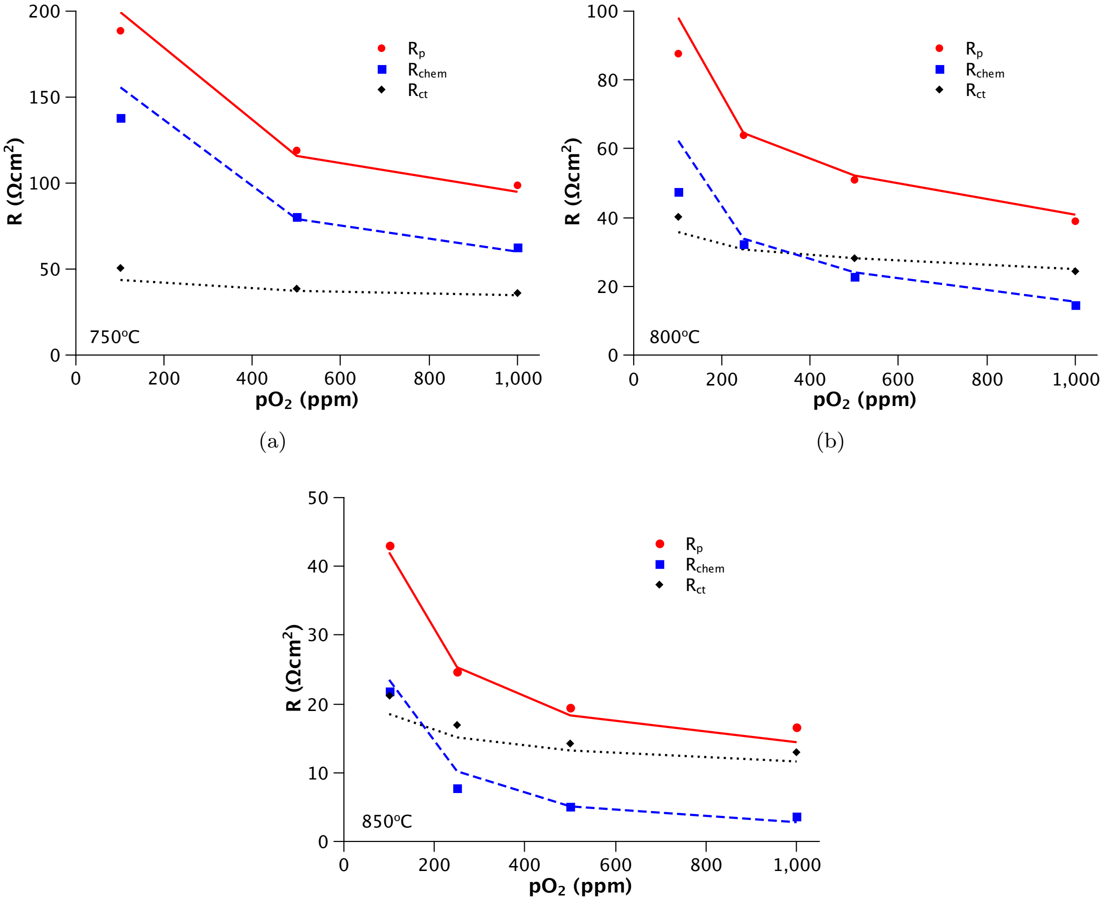

(a)

(b)

(c)

Figure 4.20: Comparison of model (lines) and R_{ct}, R_{chem} and R_p values obtained from equivalent circuits (dots): (a) 750°C (b) 800°C (c) 850°C. The parameter set used to obtain these results is shown in Table 4.9.

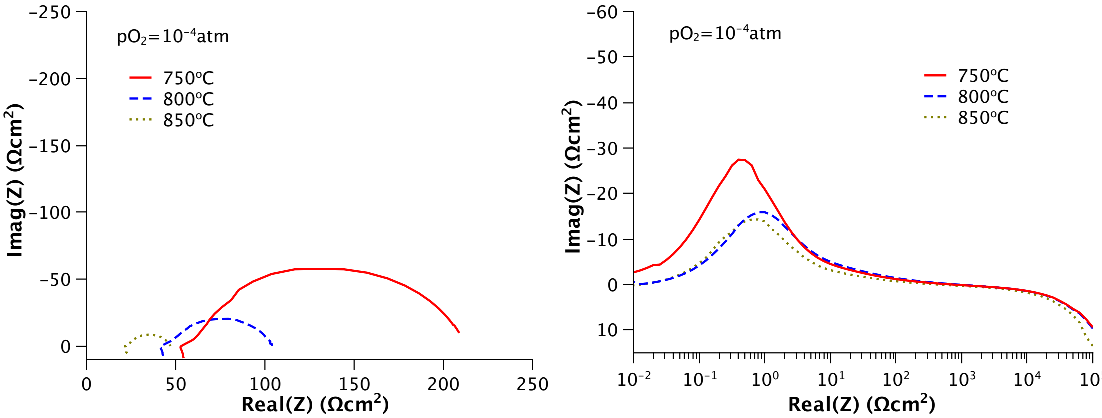

(a)

(b)

Figure 4.21: Faradaic impedance in 10^{-4}atm and at 750, 800 and 850°C from impedance fitting: (a) Nyquist (b) Bode plot.

Faradaic impedance and is, for the most part, not influenced by the double layer capacitance. An interesting observation from the phase shift of the experimental data is that for a given temperature, the phase shift of this low frequency peak decreases as the pO_2 increases, however, its characteristic frequency remains relatively constant. This low frequency peak is most sensitive to the adsorption and desorption rate constants and are related not only to the net rate of adsorption, dictated by the magnitude of k_{ads}, k_{des} and pO_2, but also to the ratio k_{ads}/k_{des}, which along with the pO_2, sets the equilibrium surface coverage. As explained in Section 4.3.2 by Figure 4.11, for typical Langmuir type adsorption, it is expected that this low frequency peak should 1) decrease in the phase shift and 2) increase in the frequency at a constant temperature when the pO_2 is increased. Theoretically this behavior is caused by an increase in the equilibrium surface coverage of atomic oxygen, θ^{eq}, as well as an increase in the net rate of adsorption, both due to the higher pO_2.

Table 4.11 lists the phase shift and the characteristic frequency of the low frequency peak from the experimental data and shows that although the phase shift decreases with pO_2, which is consistent with an increase in the net rate of adsorption due to an increase in the pO_2, the characteristic frequency remains relatively constant over the pO_2 range and the temperature range. As a consequence of this relatively constant characteristic frequency, the parameters that fit this data predict an equilibrium surface coverage that increases with temperature, with $\theta^{eq}(750^oC, 10^{-4}atm) = 0.014$,

Table 4.11: Characteristics of the low frequency peak of the Bode plot shown for experimental data in Figure 4.19

Temperature ($^\circ C$)	pO_2 (atm)	Phase (degrees)	Frequency (Hz)
750	1×10^{-4}	-44.6	0.398
	5×10^{-4}	-39.4	0.631
	1×10^{-3}	-36.5	0.631
800	1×10^{-4}	-35.8	0.794
	2.5×10^{-4}	-32.3	0.794
	5×10^{-4}	-28.3	0.794
	1×10^{-3}	-23.6	0.794
850	1×10^{-4}	-21.5	0.316
	2.5×10^{-4}	-16.9	0.501
	5×10^{-4}	-13.5	0.501
	1×10^{-3}	-13.1	0.794

$\theta^{eq}(800^oC, 10^{-4}atm) = 0.017$ and $\theta^{eq}(850^oC, 10^{-4}atm) = 0.056$. As previously mentioned, the change in equilibrium surface coverage with temperature can be described by the van 't Hoff equation [50]:

$$\left(\frac{\partial \ln K}{\partial T}\right)_\theta = \frac{\Delta_{ad}H^\ominus}{RT^2} \tag{4.52}$$

where K is the ratio k_{ads}/k_{des} and $\Delta_{ad}H^\ominus$ is the enthalpy of adsorption. For almost all adsorption reactions on metal surfaces, $\Delta_{ad}H^\ominus < 0$ (and $\Delta_{ad}S < 0$) [50] which means that K, and by extension, θ^{eq}, should decrease as the temperature increases. As noted in [50], some exceptions to $\Delta_{ad}H^\ominus < 0$ have been observed if the adsorbate dissociates and has high translational mobility on the surface, such as the adsorption of H_2 on glass. In such a case, the entropy change of the process is sufficiently positive to overcome the small positive enthalpy change and maintain the spontaneity requirement that $\Delta_{ad}G < 0$. Recent DFT results by Choi *et al.* [45] show that oxygen vacancies are expected to enhance the rate of adsorption significantly. Although it is expected that the oxygen vacancy concentration in LSM is low, the concentration of point defects in a perovskite material can increase with temperature by $n_d \approx N\exp(-\Delta H/R/T)$ [51]. This implies that it may be possible that the surface of LSM changes with temperature such that an increase in the adsorption rate constant occurs through the formation of defects such as oxygen vacancies which may be sufficient to increase

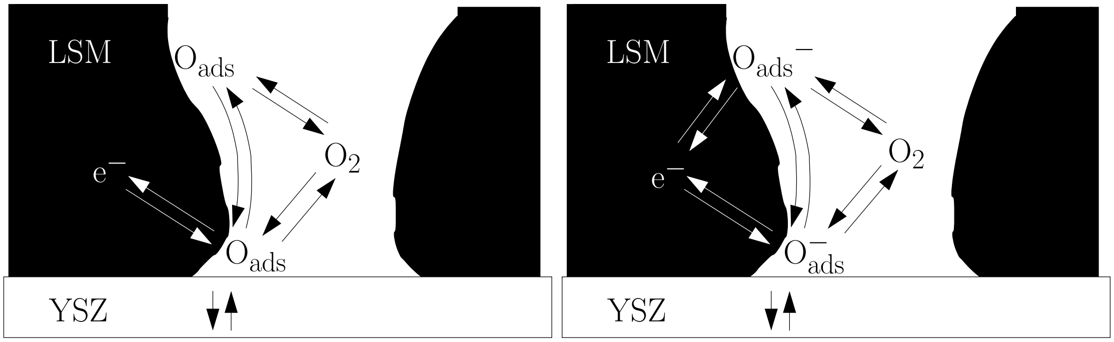

(a)

(b)

Figure 4.22: (a) Mechanism considered in this study (b) Proposed mechanism.

the ratio k_{ads}/k_{des}, resulting in higher θ^{eq}. This result highlights a major difference between metals such as Pt and perovskites such as LSM, i.e., the surface of a perovskite is dynamic and can change with both pO_2 and temperature.

4.4.3 Differences Between Steady State and Impedance Data Fitting

One of the main differences between the parameter set obtained from the steady state polarization curve fitting (shown in Table 4.8) and the impedance fitting (shown in Table 4.9) was in the adsorption/desorption rate constants. The sticking coefficient S was nearly two orders of magnitude smaller for the impedance fitting than for steady state fitting, resulting in lower R_{chem} values at higher overpotentials. The fact that steady state fitting resulted in R_{chem} values at OCV which were too low, while impedance fitting resulted in R_{chem} values under polarized conditions which were too high, may suggest that a potential dependent adsorption/desorption reaction exists. If adsorption/desorption rate constants were potential dependent, then their values would be small at low potentials (similar to what was observed in the impedance fitting) and high at higher potentials (similar to what was observed during polarization curve fitting), resulting in the required high R_{chem} values at low potentials and low R_{chem} values at high potentials. A graphical depiction of this mechanism compared to the mechanism that was considered here is shown in Figure 4.22.

A model involving an electrochemical reaction between the gas/LSM interface requires a new definition of the overpotential at the gas/LSM interface, as described by Fleig [52]. A detailed derivation of the model equations for the transport of charged adsorbates is given in Appendix A.2 and is currently in the process of being implemented. One difficulty that arises with this mechanism, however, is that as the potential is increased, the rate of adsorption increases and the rate of desorption decreases. This situation does not result in limiting currents and so may not be appropriate to describe low pO_2 behavior. An alternative mechanism that has been suggested by Kotomin *et al.* [39] is the transport of oxygen via oxygen vacancies along the surface of LSM. In order to model this type of mechanism, the LSM vacancy concentration at the surface must be known.

4.4.4 Modelling of High pO_2 Experimental Data

As previously mentioned, based on the experimental evaluation of LSM cathodes in Chapter 3, it is likely that the mechanism for oxygen reduction in LSM cathodes for $pO_2 \geq 0.01atm$ involves an electrochemical reaction at the gas-LSM interface. The mechanism relevant to high pO_2 operation was not considered in this modelling work, however, the equations describing such a mechanism are presented in Appendix A. Nevertheless, Figure 4.23 shows the simulated polarization curves in pO_2s of 0.01atm, 0.05atm and 0.21atm at $750°C$ using the parameter set found from low pO_2 fitting, shown in Table 4.8, as well as the polarization curves resulting from fitting to the high pO_2 experimental data whose parameter set is shown in Table 4.12.

Table 4.12: Model fitting parameters for steady state polarization curve in $pO_2 \geq 0.01atm$.

Parameter	$750°C$	Eq.
S	3.92×10^{-5}	4.24
ΔE_{dft} (eV)*	-1.36	4.33
D_{θ}^{eff} ($m^2\ s^{-1}$)	4.10×10^{-7}	
k_{ct} ($m^4\ mol^{-1}\ s^{-1}$)	1.56×10^{-8}	4.38

Figure 4.23a shows the comparison of polarization data with model parameters obtained in $pO_2 \geq 0.01atm$ using parameter sets found by fitting against $pO_2 \leq 0.001atm$. An important difference between the model behavior and experimental data for this case is the oxygen reaction order of R_{ct}. For $10^{-4}atm \leq pO_2 \leq 10^{-3}atm$, the model predicted a reaction order (γ) for R_{ct} between 0.10 and 0.22, consistent with experimental data in low pO_2. However, for $0.01atm \leq pO_2 \leq 0.21atm$, the

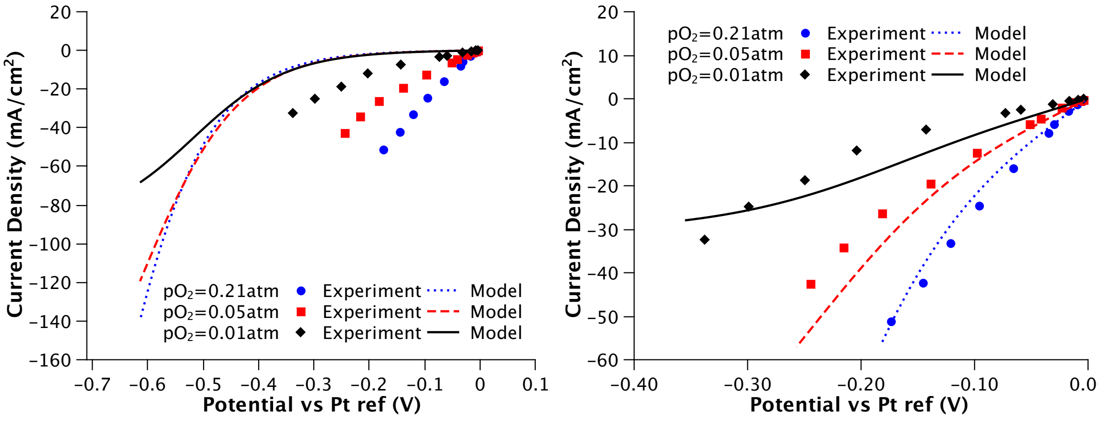

(a) (b)

Figure 4.23: Comparison of simulated polarization curves and experimental data in pO_2 of 0.01atm, 0.05atm and 0.21atm at $750°C$: (a) using the low pO_2 parameter set shown in Table 4.8 (b) using a new parameter fit shown in Table 4.12.

model predicted a reaction order of $\gamma = -0.12$, which suggests higher charge transfer resistances at higher pO_2 values. This is not observed experimentally. Experimentally, the reaction order of R_{ct} in $pO_2 \geq 0.01atm$ was found to be $\gamma = 0.33$. Since R_{ct} is related to the exchange current density which is a function of θ^{eq}, the rate constants of the adsorption and desorption reaction are important in determining the reaction order of R_{ct}. The mechanism involving neutral adsorbed oxygen and a charge transfer reaction at the LSM/YSZ interface can only predict $\gamma > 0$ for $pO_2 > 0.01atm$ if $k_{des} \gg k_{ads}$, however, the low pO_2 fitting found $k_{ads} > k_{des}$ ($k_{ads}/k_{des} = 88$) which results in $\gamma < 0$ at high pO_2. This is one reason explaining the deviation between the simulated and experimental polarization curves in Figure 4.23a. After fitting the model parameters to experimental data in high pO_2, shown in Figure 4.23b, the reaction order of R_{ct} for $pO_2 \geq 0.01atm$ was $\gamma = 0.25$ because the new parameter set, given in Table 4.12, resulted in $k_{des} \gg k_{ads}$ ($k_{ads}/k_{des} = 5 \times 10^{-5}$). The most important difference between the parameter sets obtained by fitting in low pO_2 and in high pO_2 was the energy of the adsorption/desorption reaction which dropped from $\Delta E_{dft} = -2.62eV$ to $\Delta E_{dft} = -1.36eV$, resulting in k_{des} increasing from 10^6 to 10^{12} $m^2/mol/s/atm$. Although this new parameter set could fit the shapes of the polarization data in 0.21atm and 0.05atm O_2, it predicted limiting currents in 1% O_2 which were not observed experimentally.

In addition to the shortcoming of the mechanism when fitting to $pO_2 \geq 0.01atm$, the model also does not account for the influence of current density on the LSM structure. As explained in Chapter 3, the LSM lattice may undergo a chemical change as a result of cation diffusion during polarization which considerably reduces the resistance of polarized LSM electrodes. This behavior is difficult to model and has not been captured, contributing to the deviations between the model and experimental data shown in Figure 4.23a.

4.4.5 Summary of Model Fitting

In Section 4.4, fitting of model kinetic and transport parameters to experimental data in $pO_2 \ll 0.001atm$ for the steady state polarization curve and for experimental impedance curves were discussed. Low pO_2 data was used for fitting for two main reasons: 1) in low pO_2, certain experimental features such as limiting currents and separation of peaks in the phase shift of Bode plots become more noticeable, making the fitting process easier 2) from the experimental evaluation, the reaction order of the charge transfer reaction may indicate a surface diffusion type mechanism which is the mechanism being modelled in this section.

The model parameters that were used to fit against experimental data were (i) the sticking coefficient (S) (ii) either the zero point energy of the adsorption reaction (ΔE_{dft}) or the desorption energy barrier (E_{des}) (iii) the surface diffusion coefficient (D_{θ}^{eff}) and (iv) the chemical component of the electrochemical rate constant ($k_{ct} = k_f^0 = k_b^0$). Ideally, the model parameters would be able to fit the polarization curves as well as the impedance response and match experimental oxygen reaction orders for not only R_p but also for R_{ct} and R_{chem}. It was not possible to adequately fit some of these features and it was necessary to fit the steady-state polarization curve and the impedance curves (at OCV) separately. The experimentally observed differences between polarized electrodes and pre-polarized electrodes indicate that the system or electrode in itself behaves differently under these two different conditions. The fit of EIS and steady state polarization data separately sheds light on what could be the possible source for these differences, within the framework of the mechanism analyzed.

The difference between these two cases is essentially the difference between polarized and unpolarized behavior in LSM and may also be a result of: 1) an oxygen reduction reaction mechanism that may not be fully representative of the true mechanism or one which changes with applied potential

2) the possibility that the surface composition of LSM is dynamic and changes with temperature, potential and pO_2.

From the steady state polarization curve fitting, the following was observed:

1. Limiting currents were related to atomic oxygen surface coverage at the LSM/YSZ interface, which was more strongly influenced by the rate of adsorption than by the surface diffusion coefficient.
2. From a sensitivity analysis on the model parameters at low pO_2 and high overpotentials, adsorption clearly limited the oxygen reduction reaction but at low overpotentials, charge transfer was more limiting.
3. The relative contribution of the surface pathway and the gas phase pathway was confirmed from an analysis of the flux contributions which showed that at $pO_2 = 10^{-4} atm$, the surface pathway was slightly favored over the gas phase pathway however, both contributed to the total flux of oxygen through the porous electrode. At a higher $pO_2 = 10^{-3} atm$, the gas phase pathway had slightly higher contributions compared to the surface pathway.
4. Increasing the average pore size of the electrode from $p_{avg} = 0.25 \mu m$ to $p_{avg} = 0.50 \mu m$ did not appreciably change the pathway to which oxygen was transported to the LSM/YSZ interface.
5. The model parameter set obtained from steady state polarization data fit predicted an equilibrium surface coverage (θ^{eq}) that decreased with temperature, consistent with metallic behavior and with the interpretation of steady state experimental results from Chapter 3.
6. The steady state parameter set could not predict the phase shift in the impedance response at OCV due to an R_{chem} contribution that was too small.

From the impedance fitting, the following was observed:

1. The low frequency peak observed in the Bode plots of experimental impedance data at low pO_2 was caused by high values of R_{chem}, primarily as a result of the adsorption/desorption process.

2. The low frequency peak in the Bode plots could only be fit by modifying the adsorption and desorption rate constants.
3. In order to fit experimentally obtained R_{ct} and R_{chem} values and their pO_2 dependencies along with the peaks in the Bode plot at 750 and $800°C$, it was necessary to make the sticking coefficient a function of pO_2. Theoretically, this could correspond to a situation in which adsorbates hinder the adsorption of gas molecules.
4. The parameter set from impedance fitting at OCV resulted in an equilibrium surface coverage (θ^{eq}) that increased with temperature. This situation may be caused by a dynamic LSM surface whose composition changes with both temperature and pO_2, creating defects such as oxygen vacancies which can accelerate the kinetics of adsorption.

4.5 Summary/Conclusion

In this chapter, a detailed mathematical model of oxygen reduction in porous LSM cathodes was developed which accounted for a parallel pathway for the transport of oxygen species through either 1) transport of oxygen gas to the LSM/YSZ interface followed by adsorption and charge transfer 2) transport of adsorbed oxygen along the LSM solid surface towards the LSM/YSZ interface followed by adsorption and charge transfer. This model was used to help analyze steady state polarization curves as well as the impedance response of experimental data for porous LSM electrodes collected in low oxygen partial pressures between $pO_2 = 10^{-4} atm$ to $pO_2 = 10^{-3} atm$. The model was fit against experimental data to obtain microstructure independent kinetic and transport parameters for each of the steps modelled.

In this chapter, it was found that:

1. Parameters that could fit the steady state polarization curve could not predict open circuit behavior and especially were not able to fit the phase shift in the impedance response at OCV.
2. In order to fit the impedance data at OCV, a shift away from Langmuir adsorption kinetics was required, indicating that adsorbates may interact with molecular oxygen species.

3. After analyzing the equilibrium surface coverages predicted by steady state and impedance data fitting, it was hypothesized that at open circuit conditions, the LSM surface is dynamic and its composition and defect concentration may depend on temperature whereas under polarized conditions, the LSM surface behaves more metallic, perhaps as a result of cation diffusion from the bulk to the surface as observed in Chapter 3.

4. Compared to the other processes being considered, adsorption was slow, especially at high overpotentials.

5. Steady state parameter fitting resulted in R_{chem} values that were too small at OCV but impedance parameter fitting resulted in R_{chem} values that were too large under polarized conditions. This may indicate that the adsorption reaction is electrochemical in nature, although this likely cannot explain all features of the experimental data.

4.6 List of symbols

Greek symbols	Description	Units
χ	Factor accounting for porous nature of CV	
Ψ	Concentration of species	various
ϵ	Porosity	-
ρ	Density	kg/m^3
Γ	General transport coefficient	various
τ	Gas phase tortuosity	-
θ	Surface coverage	-
λ_{tpb}	Triple phase boundary length	m/m^2
$\phi_{el,io}$	Electronic and ionic phase potentials	V
κ	Permeability	m^2
μ	Viscosity	Pa s
$\sigma_{el,io}$	Electronic or ionic conductivity	S/m
β	Symmetry coefficient	-
η	Overpotential	V
η_{var}	Amplitude of applied sinusoidal potential	V
ω	Angular frequency	1/s
χ	Least squares fitting function	-
$\bar{\theta}$	Impedance phase shift	radians
τ_p	Periodicity of applied sinusoidal potential	-
γ	Reaction order wrt oxygen gas	-
$\wp$	Sticking coefficient as a function of surface coverage	-

Symbol	Description	Units
x	Position along cathode length	m
A	Geometric area	m^2
V	Geometric volume	m^3
J	Species flux	$mol/m^2/s$
a	Gas-solid internal surface area	m^2/m^3
u	Pore velocity	m/s
$D_{O_2-N_2}$	Binary gas diffusion coefficient	m^2/s
D_K	Knudsen diffusion coefficient	m^2/s
k_{ads}	Rate constant of adsorption	$m^2/mol/s/atm$
k_{des}	Rate constant of desorption	$m^2/mol/s$
N	Maximum number of adsorption sites	mol/m^2
M_{O_2}	Molar mass of O_2	kg/mol
F	Faraday constant	C/mol
n	Number of electrons in charge transfer step	-
$C_{V_{\ddot{O}}}$	Concentration of oxygen vacancies in YSZ	mol/m^2
$C_{O_O^x}$	Concentration of oxygen in YSZ	mol/m^2
s	Free adsorption site	mol/m^2
P_{tot}	Total pressure	Pa
R	Gas constant	$J/mol/K$
T	Temperature	K
k_f^0, k_b^0	Forward and backward charge transfer rate constant	$m^4/mol/s$
i	Current density	A/m^2
C_{dl}	Double layer capacitance	F/m^2
S	Sticking coefficient	-
E_{des}	Desorption activation energy	eV
ΔE_{dft}	Energy of adsorption at 0K, 0atm	eV
k_{ct}	Charge transfer rate constant	$m^4/mol/s$
p_{size}	Average pore size	m
Q_{cpe}, P_{cpe}	Constant phase element parameters	-
D_θ^{eff}	Effective surface diffusion coefficient	m^2/s
R_i	Resistance of component i	Ωm^2

Superscript	Description	Subscript	Description
eff	effective	tot	total
eq	equilibrium	conv	convective
ed	electrode	diff	diffusive
el	electrolyte	dl	double layer
bulk	bulk value or equilibrium value	ct	charge transfer
ss	steady state	chem	chemical
imp	impedance	P	polarization
mod	model	far	Faradaic
exp	experimental		

References

[1] Y. Takeda, R. Kanno, M. Noda, Y.Tomida, and O. Yamamoto. Cathodic Polarization Phenomena of Perovskite Oxide Electrodes with Stabilized Zirconia. *Journal of the Electrochemical Society*, 134(11):2656–2661, 1987.

[2] J-D. Kim, G-D. Kim, J-W. Moon, Y. Park, W-H. Lee, K. Kobayashi, M. Nagai, and C-E. Kim. Characterization of LSM-YSZ composite electrode by ac impedance spectroscopy. *Solid State Ionics*, 143:379–389, 2001.

[3] E. Siebert, A. Hammouche, and M. Kleitz. Impedance Spectroscopy Analysis of $La_{1-x}Sr_xMnO_3$-Yttria-Stabilized Zirconia Electrode Kinetics. *Electrochimica Acta*, 40(11):1741–1753, 1995.

[4] J. Divisek, L.G.J. de Haart, P. Holtappels, T. Lennartz, W. Mallener, U. Stimming, and K. Wippermann. The kinetics of electrochemical reactions on high temperature fuel cell electrodes. *Journal of Power Sources*, 49:257–270, 1994.

[5] M. Ostergard and M. Mogensen. ac Impedance Study of the Oxygen Reduction Mechanism on $La_{1-x}Sr_xMnO_3$ in Solid Oxide Fuel Cells. *Electrochimica Acta*, 38(14):2015–2020, 1993.

[6] A. Esquirol, N. Brandon, J. Kilner, and M. Mogensen. Electrochemical Characterization of $La_{0.6}Sr_{0.4}Co_{0.2}Fe_{0.8}O_3$ Cathodes for Intermediate-Temperature SOFCs. *Journal of the Electrochemical Society*, 151(11):A1847–A1855, 2004.

[7] A.C. Co and V. Birss. Mechanistic Analysis of the Oxygen Reduction Reaction at $(La, Sr)MnO_3$ Cathode in Solid Oxide Fuel Cells. *Journal of Physical Chemistry B*, 110:11299–11309, 2006.

[8] F.H. van Heuveln and H.J.M. Bouwmeester. Electrode Properties of Sr-Doped $LaMnO_3$ on Yttria-Stabilized Zirconia: II. Electrode Kinetics. *Journal of the Electrochemical Society*, 144(1):134–140, 1997.

[9] X.J. Chen, K.A. Khor, and S.H. Chan. Identification of O_2 reduction processes at yttria stabilized zirconia—doped lanthanum manganite interface. *Journal of Power Sources*, 123:17–25, 2003.

[10] A. Svensson, S. Sunde, and K. Nisancioglu. Mathematical modeling of oxygen exchange and transport in air-perovskite-YSZ interface regions. 1. Reduction of intermediately adsorbed oxygen. *Journal of the Electrochemical Society*, 144(8):2719–2732, 1997.

[11] M. Mogensen, S. Primdahl, and M. Juhl. Revealing the mechanisms of SOFC electrodes using a combination of AC and DC methods. *Electrochemical Proceedings*, 97-18:385–393, 1997.

[12] B. Kenney and K. Karan. Impact of Nonuniform Potential in SOFC Composite Cathodes on the Determination of Electrochemical Kinetic Parameters: A Numerical Analysis. *Journal of the Electrochemical Society*, 153(6):A1172–A1180, 2006.

[13] B.A. van Hassel, B.A. Boukamp, and A.J. Burggraaf. Electrode polarization at the $Au, O_2(g)$/yttria stabilized zirconia interface. Part I: Theoretical considerations of reaction model. *Solid State Ionics*, 48:139–154, 1991.

[14] B.A. van Hassel, B.A. Boukamp, and A.J. Burggraaf. Electrode polarization at the $Au, O_2(g)$ / yttria stabilized zirconia interface. Part II: electrochemical measurements and analysis. *Solid State Ionics*, 48:155–171, 1991.

[15] A. Mitterdorfer and L.J. Gauckler. Identification of the reaction mechanism of Pt, O2(g)/YSZ system Part 1: General framework, modeling and structural investigation. *Solid State Ionics*, 117:187–202, 1999.

[16] A. Mitterdorfer and L.J. Gauckler. Identification of the reaction mechanism of the $Pt, O_{2(g)}/YSZ$ system Part 2: Model implementation, parameter estimation, and validation. *Solid State Ionics*, 117:203–217, 1999.

[17] Marcel Vogler, Anja Bieberle-Hutter, Ludwig Gauckler, Jurgen Warnatz, and Wolfgang Bessler. Modelling Study of Surface Reactions, Diffusion, and Spillover at a Ni/YSZ Patterned Anode. *Journal of the Electrochemical Society*, 156(5):xxx–xxx, 2009.

[18] David G. Goodwin, Huayang Zhu, Andrew M. Colclasure, and Robert J. Kee. Modeling Electrochemical Oxidation of Hydrogen on Ni-YSZ Pattern Anodes. *Journal of the Electrochemical Society*, 156(9):B1004–B1021, 2009.

[19] A. Svensson, S. Sunde, and K. Nisancioglu. Mathematical modeling of oxygen exchange and transport in air-perovskite-YSZ interface regions. 2. Direct exchange of oxygen vacancies. *Journal of the Electrochemical Society*, 145(4):1390–1400, 1998.

[20] Ben Kenney, Mikelis Valdmanis, Craig Baker, J.G. Pharoah, and Kunal Karan. Computation of TPB length, surface area and pore size from numerical reconstruction of composite solid oxide fuel cell electrodes. *Journal of Power Sources*, 128(2):1051–1059, 2009.

[21] R. Byron Bird, Warren E. Stewart, and Edwin N. Lightfoot. *Transport Phenomena*. John Wiley & Sons, 2 edition, 2002.

[22] Hae-Won Choi, Arganthael Berson, Ben Kenney, Jon G. Pharoah, Steven Beale, and Kunal Karan. Effective transport coefficients for porous microstructures in solid oxide fuel cells. In *Electrochemical Society?s 216th meeting (SOFC-XI)*, 2009.

[23] James R. Wilson, Worawarit Kobsiriphat, Roberto Mendoza, Hsun-Yi Chen, Jon M. Hiller, Dean J. Miller, Katsuyo Thornton, Peter W. Voorhees, Stuart B. Adler, and Scott A. Barnett. Three-dimensional reconstruction of a solid-oxide fuel cell anode. *Nature*, 5:541–544, 2006.

[24] H. Zhu, R. Kee, V. Janardhanan, O. Deutschmann, and D. Goodwin. Modeling Elementary Heterogeneous Chemistry and Electrochemistry in Solid-Oxide Fuel Cells. *Journal of the Electrochemical Society*, 152(12):A2427–A2440, 2005.

[25] R. Suwanwarangkul, E. Croiset, M.W. Fowler, P.L. Douglas, E. Entchev, and M.A. Douglas. Performance comparison of Fick's, dusty-gas and Stefan-Maxwell models to predict the concentration overpotential of a SOFC anode. *Journal of Power Sources*, 122:9–18, 2003.

[26] Marco Cannarozzo, Adriana Del Borghi, and Paola Costamagna. Simulation of mass transport in SOFC composite electrodes. *Journal of Applied Electrochemistry*, 38:1011–1018, 2008.

[27] F. Zhao, T. Armstrong, and A. Virkar. Measurement of $O_2 - N_2$ Effective Diffusivity in Porous Media at High Temperatures Using an Electrochemical Cell. *Journal of the Electrochemical Society*, 150(3):A249–A256, 2003.

[28] Andrzej Wieckowski, Takeshi Kobayashi, Panakkattu K Babu, Jong Ho Chung, and Eric Oldfield. Coverage Dependence of CO Surface Diffusion on Pt Nanoparticles - an EC-NMR Study. In *Meterials Research Society Proceedings*, volume 984, 2007.

[29] Gabor A. Somorjai. *Introduction to surface chemistry and catalysis*. John Wiley & Sons, Inc, 1994.

[30] Robert Gomer. Diffusion of adsorbates on metal surfaces. *Reports on Progress in Physics*, 53:917–1002, 1990.

[31] J.M. Zalc, S.C. Reyes, and E. Iglesia. Monte-Carlo simulations of surface and gas phase diffusion in complex porous structures. *Chemical Engineering Science*, 58:4605–4617, 2003.

[32] D.A. Nield and A. Bejan. *Convection in Porous Media*. Springer-Verlag, 1992.

[33] Emmanuel Resch. Numerical and Experimental Characterisation of Convective Transport in Solid Oxide Fuel Cells. Master's thesis, Queen's University, October 2008.

[34] Robert J. Kee, Michael E. Coltrin, and Peter Glarborg. *Chemically Reactive Flow: Theory and Practice*. Wiley Interscience, 2003.

[35] R.D. Cortright and J.A. Dumesic. Kinetics of Heterogenous Catalytic Reactions: Analysis of Reaction Schemes. *Advances in Catalysis*, 46:161–264, 2001.

[36] Richard I. Masel. *Principles of Adsorption and Reaction on Solid Surfaces*. John Wiley and Sons, 1996.

[37] P. Kisliuk. The Sticking Probabilities of Gases Chemisorbed on the Surfaces of Solids. *Journal of Physical Chemistry of Solids*, 3:95–101, 1957.

[38] David G. Goodwin. A Patterned Anode Model With Detailed Chemistry. In *Solid Oxide Fuel Cells IX (SOFC-IX)*, volume 1, 2005.

[39] Eugene A. Kotomin, Yuri A. Mastrikov, Eugene Heifets, and Joachim Maier. Adsorption of atomic and molecular oxygen on the $LaMnO_3$ (001) surface: ab initio supercell calculations and thermodynamics. *Physical Chemistry Chemical Physics*, 10:4644–4649, 2008.

[40] J.R. Smith, A. Chen, D. Gostovic, D. Hickey, D. Kundinger, K.L. Duncan, R.T. DeHoff, K.S. Jones, and E.D. Wachsman. Evaluation of the relationship between cathode microstructure and electrochemical behavior for SOFCs. *Solid State Ionics*, 180:90–98, 2009.

[41] Bonnie J. McBride, Michael J. Zehe, and Sanford Gordon. Nasa glenn coefficients for calculating thermodynamic properties of individual species.

[42] *FEMLAB Modeling Guide.* COMSOL AB, 2004.

[43] J. A. Nelder and R. Mead. A Simplex Method for Function Minimization. *The Computer Journal*, 7(4):308–313, 1965.

[44] Kenneth J. Beers. *Numerical Methods for Chemical Engineering: Applications in MatLab.* Cambridge University Press, 2007.

[45] YongMan Choi, Matthew E. Lynch, M.C. Lin, and Meilin Liu. Prediction of O_2 Dissociation Kinetics on $LaMnO_3$-Based Cathode Materials for Solid Oxide Fuel Cells. *Journal of Physical Chemistry C*, 113:7290–7297, 2009.

[46] W.G. Bessler. A new computation approach for SOFC impedance from detailed electrochemical reaction-diffusion models. *Solid State Ionics*, 176:997–1011, 2005.

[47] Mark E. Orazem and Bernard Tribollet. *Electrochemical Impedance Spectroscopy.* Wiley, 2008.

[48] B.E. Conway and E. Gileadi. Kinetic Theory of Pseudo-Capacitance and Electrode Reactions at Appreciable Surface Coverage. *Transactions of the Farraday Society*, 58:2493–2509, 1962.

[49] J. Bockris and S. Srinivasan. *Fuel Cells: Their Electrochemistry.* McGraw-Hill Book Company, 1969.

[50] Peter Atkins and Julio De Paula. *Atkins' Physical Chemistry*. W.H. Freeman and Company, 8 edition, 2006.

[51] Richard Tilley. *Understanding Solids: The Science of Materials*. Wiley, 2004.

[52] J. Fleig. On the current-voltage characteristics of charge transfer reactions at mixed conducting electrodes on solid electrolytes. *Physical Chemistry Chemical Physics*, 7:2027–2037, 2005.

Chapter 5

A Study of Porous LSM/YSZ Composite Cathodes

Note

The model reported in this chapter was developed prior to the experimental and modelling studies reported in Chapter 3 and Chapter 4 of this thesis. Accordingly, the treatment of chemical and electrochemical kinetics was simplified.

5.1 Introduction

A large part of the resistance of a solid oxide fuel cell (SOFC) can be attributed to the electrochemical losses associated with the cathode processes, which lead to the reduction of gaseous oxygen into oxide ions [1]. It is generally thought that charge transfer at the triple phase boundary (TPB) plays an important role in limiting the overall oxygen reduction reaction and one strategy for improving the electrochemical performance of an SOFC cathode is to enhance the number of active TPBs by creating a porous composite structure comprising of a solid phase mixture of an electro-catalyst and an oxygen-ion conducting material. In doing so, composite cathodes extend the electrochemically active region from the electrode/bulk electrolyte interface, as in the case of conventional cathodes, to throughout the porous composite cathode structure.

The actual rate of the oxygen reduction reaction at the TPB is influenced by the potentials associated with the three participating species, namely the chemical potential of oxygen, the electronic potential of the electron-conducting phase, and the ionic potential of the oxygen-ion conducting phase. Moreover, the distribution of the phase potentials is influenced by the pathways undertaken by the three participating species, as well as the relevant transport coefficients such as the effective gas phase diffusivity and the electronic/ionic conductivity. Thus, the overall electrochemical performance of a composite cathode depends on the active TPB sites as well as the pathways taken by the participating species to get to the active site and the geometrical factors such as the cathode thickness. The total number of TPB sites in a porous composite electrode is a strong function of electrode parameters such as particle size, porosity and the volume fraction of the solid phases. Further, these parameters also influence the percolation of each phase and thus, the effective transport coefficients. For high electrochemical performance of composite electrodes, both sufficiently large number of sites and facile transport of reacting species must concurrently be realized. In other words, the goal of the engineering of composite electrodes should not merely be to maximize the TPB but to find the optimum electrode structure/composition that finds the right balance between active sites and species transport.

Clearly, a large number of parameters need to be optimized to design an efficient cathode. This has led to several experimental [2–12] and modelling [13–16] studies on composite cathodes. A common experimental method of quantifying the SOFC cathode performance involves the measurement of the cathode polarization resistance (R_p) which typically follows a power law relationship with respect to the oxygen concentration by $R_p \propto pO_2^{-\gamma}$ where γ is the oxygen reaction order. The reaction order of the polarization resistance can be useful in kinetic studies to examine the rate determining step(s) of the oxygen reduction reaction.

In analyzing the experimental data for R_p, a number of assumptions must be made since only a limited number of experimental variables are accessible. Commonly made assumptions include - (i) oxygen partial pressure at the reaction site is equal to the bulk oxygen partial pressure, (ii) a uniform and single overpotential exists at all locations within the porous electrode. It is generally thought that by conducting experiments under low overpotentials, the corresponding low currents or oxygen consumption rates may lead to low gradients in oxygen partial pressure. However, the assumption of a uniform distribution of the ionic and electronic phase potentials may not hold true and as will be shown in this paper, may lead to erroneous determination of electrochemical kinetic parameters.

In this work, a mathematical model developed for the LSM-YSZ composite cathode is compared against experimental results and used to determine the gradients in species within the composite cathode. In addition, the relationship between the microstructure of the composite cathode and the total resistance of the cathode is examined and predicted using microstructural parameters obtained from numerical construction of composite cathodes [17].

5.2 Experimental

2-electrode symmetrical cell tests 2-electrode symmetrical composite cathode cells of various functional layer thicknesses were fabricated using the techniques described in Section 2.2 of Chapter 2 (page 43). The cathode functional layers (CFLs) consisted of 50 vol% LSM-50 vol% YSZ and the current collector layer (CCL) was $\sim 20\mu m$ porous LSM. The impedance of these 2-electrode cells was measured near OCV in oxygen partial pressures ranging between 0.01atm and 0.21atm. From these impedance measurements, the reaction order, γ, of the electrode resistance was calculated, $R_p = kpO_2^{-\gamma}$.

van der Pauw conductivity measurements In addition to the symmetrical cells, single electrode cathode samples were fabricated for LSM volume fractions between 50 vol % LSM and 100 vol % LSM (with respect to the solid content) as well as dense LSM pellets. These samples were used for electrical conductivity measurements using the van der Pauw technique [18]. Four Pt contact points, A, B, C, D, were arranged on the thin cathode samples in a virtual square and a small current was passed between points A and B and the voltage was measured between the points C and D resulting in a resistance $R_{AB,CD}$. Then, the current lead wires were rotated so that the current was passed through the points A and C and the voltage was measured between points B and D, resulting in the resistance $R_{AC,BD}$. The electrical conductivity, σ was then calculated from:

$$\exp\left(-\pi R_{AB,CD} L\sigma\right) + \exp\left(-\pi R_{AC,BD} L\sigma\right) = 1 \tag{5.1}$$

where L is the thickness of the cathode samples, measured from SEM.

Particle size measurements The composite cathodes were fabricated using LSM powder (Praxair, USA) and YSZ powder (Tosoh, USA). The particle size distribution was measured using a Malvern Mastersizer 2000 particle size analyzer using the light scattering method. The particle sizes of the LSM and YSZ powders were approximated using a normal distribution for the purpose of using them with a numerical reconstruction technique of the porous electrode [17]. For the LSM powder, the mean particle size was $d_{LSM} = 0.73\mu m$ and the standard deviation in the particle size was $0.3\mu m$ whereas for the YSZ powder, the mean particle size was $d_{YSZ} = 0.51\mu m$ and the standard deviation in the particle size was $0.35\mu m$. The actual distribution of the LSM powder was $d_{10} = 0.41\mu m$, $d_{50} = 0.68\mu m$ and $d_{90} = 1.13\mu m$ and for the YSZ powder, the distribution was $d_{10} = 0.23\mu m$, $d_{50} = 0.34\mu m$ and $d_{90} = 1.08\mu m$ where d_{10} indicates that 10% of the particles, by volume, were smaller than the given size.

SEM image analysis Figure 5.1 shows example cross section SEM images of composite cathodes with $2.7\mu m$ CFL thickness and $26\mu m$ CFL thickness fabricated without and with a current collector layer. The thickness of the layers were estimated using SEM images and the ImageJ (NIH, USA) software. Based on the electrode thickness, the bulk density of LSM and YSZ and the deposit weight of the composite cathode, the porosity was estimated for each sample. The porosity was approximately $\epsilon \approx 0.35$.

5.3 Composite Cathode Model

A one-dimensional steady-state composite cathode mathematical model was developed based on the consideration of various physical, chemical, and electro-chemical processes that occur in the porous cathode. The model is isothermal and it was assumed that the various electrochemical processes such as adsorption, surface diffusion and the electrochemical reaction could be captured by the reaction order of the overall oxygen reduction reaction. To simplify the model, it was also assumed

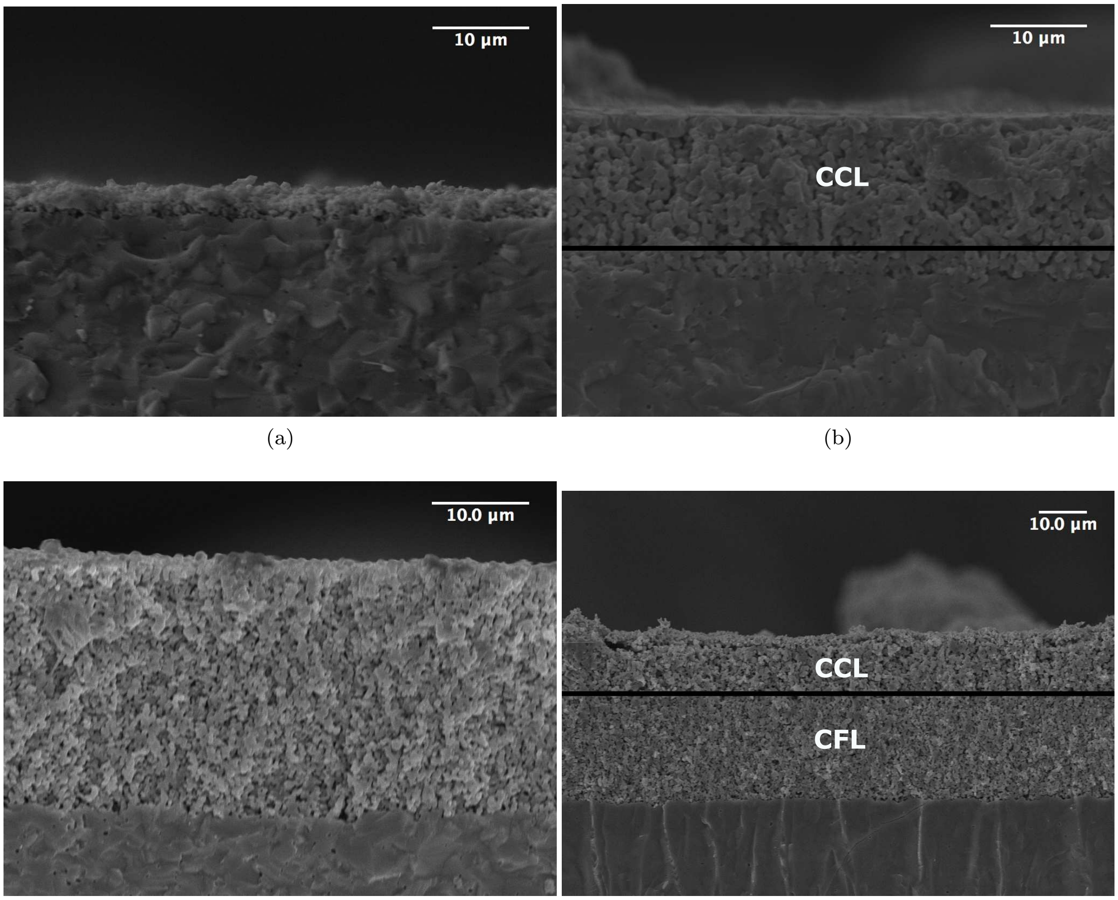

(a) (b)

(c) (d)

Figure 5.1: Cross section of 50 vol% LSM-50 vol% YSZ composite cathodes fabricated by wet spraying: (a)-(b) $2.7\mu m$ CFL without and with CCL (c)-(d) $26\mu m$ CFL without and with CCL

that the electrochemical reactions occurred within the bulk of the composite cathode and not at the interface between the cathode/bulk electrolyte where some TPBs may exist. This model was limited to low overpotentials where reactant and product concentrations did not vary from their equilibrium values. The primary goal was to determine the cathode polarization resistance at OCV, R_p.

5.3.1 Model Domain

Figure 5.2 is a representation of the computational domain employed for the composite cathode model. The top boundary of $x = 0$ represents the electrode surface, which is permeable to gas and is also the interface between the current collector and the electrode. There is a porous current collector layer (CCL) from $x = 0$ to $x = L_{ccl}$ which is composed of pure LSM followed by the cathode functional layer which is a mixture of LSM and YSZ particles. The thickness of the CCL was $20\mu m$ and the thickness of the CFL was varied between 1 and $50\mu m$.

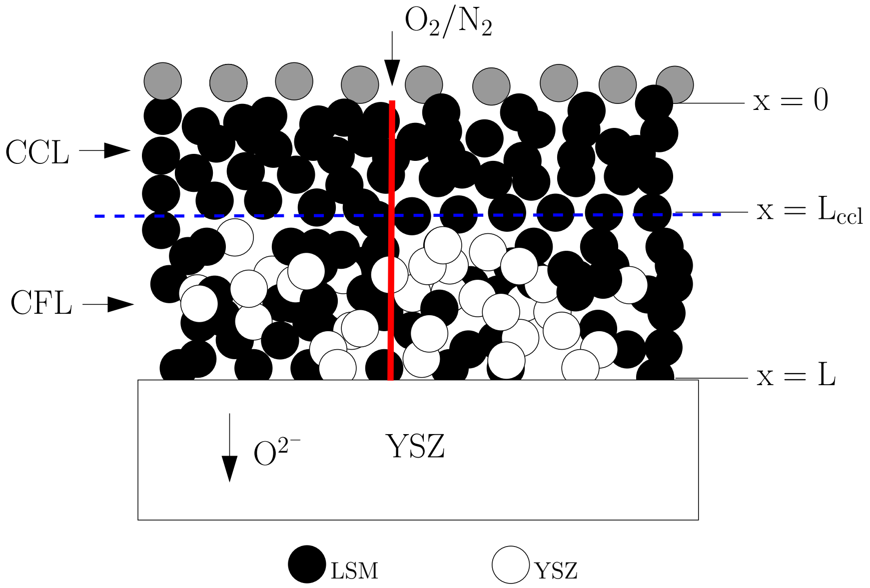

Figure 5.2: Representation of composite cathode simulated in model. The cathode includes a porous current collector layer (CCL) composed of pure LSM and a porous cathode functional layer (CFL) composed of a mixture of LSM and YSZ particles. The model domain is a line drawn from $x = 0$ to $x = L$.

5.3.2 Composite Cathode Model Equations

Charge transport The flux of electronic and ionic charge through the porous electrode represents the electronic and ionic current densities. In the porous CCL, there are no electrochemical reactions and the transport of electronic charge is given by:

$$-\frac{di_{LSM}}{dx}=0 \tag{5.2}$$

The governing equations for steady-state transport of electronic and ionic charge in the composite cathode functional layer are coupled to the rate of the oxygen reduction reaction:

$$-\frac{di_{LSM}}{dx}=\frac{di_{YSZ}}{dx}=\lambda_{tpb}(i_{anodic}-i_{cathodic}) \tag{5.3}$$

where, subscripts LSM and YSZ represent the electronic phase and ionic phase respectively, i, is the current density (A/m^2) and λ_{tpb} is the active triple phase boundary line length per geometric volume (m/m^3). The ionic/electronic current is associated with a corresponding gradient in ionic/electronic potential of the relevant phase and can be expressed via Ohms Law:

$$\sigma_k^{eff}\frac{d\phi_{io}}{dx}=-i_k \tag{5.4}$$

where, k is either LSM or YSZ phase and σ^{eff} is the effective conductivity. Substituting Equation 5.4 into Equation 5.3, the electronic and ionic charge balance is obtained:

$$\sigma_{LSM}^{eff}\frac{d^2\phi_{LSM}}{dx^2}=-\sigma_{YSZ}^{eff}\frac{d^2\phi_{YSZ}}{dx^2}=\lambda_{tpb}(i_{anodic}-i_{cathodic}) \tag{5.5}$$

Chemical species transport It is assumed that the transport of oxygen gas in the porous cathode can be described by Ficks Law of diffusion. In the CCL, no reaction takes place, resulting in Equation 5.6a, however, in the CFL, Ficks Law is coupled via the rate of consumption of oxygen resulting in Equation 5.6b:

$$-D^{eff}_{O_2-N_2}\frac{d^2C_{O_2}}{dx^2}=0 \tag{5.6a}$$

$$-D^{eff}_{O_2-N_2}\frac{d^2C_{O_2}}{dx^2}=\frac{\lambda_{tpb}}{4F}(i_{anodic}-i_{cathodic}) \tag{5.6b}$$

where, $D^{eff}_{O_2-N_2}$ is the effective diffusivity of O_2 and C_{O_2} is the concentration of O_2. The gas phase diffusion of species is corrected for the transport through porous media.

Electrochemical kinetics For a multi-step reaction mechanism, assuming that a single-rate determining step exists, the anodic and cathodic currents can be written in a Butler-Volmer like electrode kinetics expression as follows:

$$i_{anodic}=i_0\exp(\alpha_a f\eta) \tag{5.7a}$$

$$i_{cathodic}=i_0\exp(-\alpha_c f\eta) \tag{5.7b}$$

where $f=F/R/T$ and η is the local overpotential. The local overpotential is defined as the potential drop between the metal phase and the solution, or in this case, the LSM phase and the YSZ phase, making $\eta=\phi_{LSM}-\phi_{YSZ}$. At equilibrium, no net current flows and $i_{anodic}=i_{cathodic}=i_0$. The exchange current density, i_0, can be approximated as:

$$i_0=i_0^{ref}\left(\frac{pO_2}{pO_2^{ref}}\right)^{\gamma} \tag{5.8}$$

where reaction order, γ, can be obtained from the relationship $R_p=kpO_2^{-\gamma}$ between the polarization resistance and the oxygen partial pressure (pO_2). This reaction order contains a contribution from the equilibrium potential as well as chemical processes such as adsorption. The value i_0^{ref} is a reference exchange current density with units of A/m, evaluated at pO_2^{ref}. The reference exchange current density was approximated from the polarization resistance of pure LSM cathodes measured using impedance spectroscopy (see Table 3.5 page 123, Chapter 3):

$$i_0^{ref} = \frac{RT}{2F}\frac{i}{\eta} = \frac{RT}{2F}\frac{1}{R_{p,tpb}} \tag{5.9a}$$

$$i_0^{ref} = 2.2 \times 10^4 \exp\left(\frac{-1.9eV}{RT}\right) \tag{5.9b}$$

The polarization resistance, $R_{p,tpb}$, in Equation 5.9a is the polarization resistance of a pure LSM cathode on a TPB basis, where $R_{p,tpb} = R_p/\lambda_{tpb,i}$. The TPB length at the LSM/YSZ interface for pure LSM cathodes ($\lambda_{tpb,i}$) was determined from SEM images and reported in Section 2.2.3 (page 59 of Chapter 2). It should be noted that this formulation for i_0^{ref} lumps R_{chem} and R_{ct} into a single i_0 value and therefore, R_{chem} and R_{ct} cannot be calculated independently. The contributions of adsorption/surface diffusion are also lumped and so this model can only calculate the total polarization resistance of the composite cathode.

Boundary conditions To solve Equations 5.5 and 5.6, appropriate boundary conditions are required. At the current collector/electrode interface, $x = 0$:

$$\phi_{LSM} = 0 \tag{5.10a}$$

$$C_{O_2} = \frac{pO_2^{bulk}}{RT} \tag{5.10b}$$

at the CCL/CFL interface, $x = L_{ccl}$:

$$\frac{d\phi_{YSZ}}{dx} = 0 \tag{5.11}$$

and at the electrode/electrolyte interface, $x = L$:

$$\frac{d\phi_{LSM}}{dx} = 0 \tag{5.12a}$$

$$\phi_{YSZ} = \eta_{nom} \tag{5.12b}$$

$$\frac{C_{O_2}}{dx} = 0 \tag{5.12c}$$

where η_{nom} is the nominal electrode overpotential or the applied potential between the cathode and the reference electrode located at the LSM/YSZ interface. Nominal refers to the observed quantity and not the local quantity, in this case, η_{nom} is the observed electrode overpotential.

5.3.3 Model Parameters

Several input parameters such as effective electrical conductivities (σ_{LSM}^{eff} and σ_{YSZ}^{eff}), chemical species diffusivity ($D_{O_2-N_2}^{eff}$) as well as the active triple phase boundary length (λ_{tpb}) are required to solve the governing equations. These parameters depend on the microstructure of the cathode and are influenced by the percolation of each phase.

Effective electrical conductivity Unlike the effective ionic conductivity (σ_{YSZ}^{eff}), the effective electronic conductivity (σ_{LSM}^{eff}) can be measured experimentally using the van der Pauw conductivity technique, previously described in Section 5.2. The effective ionic conductivity however is more difficult to obtain. Yamahara *et al.* [19] were able to measure the resistance of porous YSZ pellets and found that the Koh-Fortini [20] relationship held well:

$$\frac{\sigma^{eff}}{\sigma^0} = \frac{1-\zeta}{1+n\zeta^2} \tag{5.13}$$

where σ^0 is the conductivity of the fully dense material and ζ is the volume fraction of material that is not electrically conducting and n is a fitting parameter which Yamahara *et al.* found to be equal to 11. Although this relationship can account for changes in the composition of the composite cathode, such as the volume fraction of the LSM or YSZ phases, it cannot account for changes in the percolation threshold as a result of particle size distributions.

Gas diffusivity The gas diffusivity can be calculated from kinetic theory of gases and was previously described in Section 4.2.5 (page 164).

Triple phase boundary length The triple phase boundary length was estimated based on the numerical construction of porous composite cathodes, described in [17]. The triple phase boundary length depends on microstructural features such as the LSM and YSZ particle size and the cathode porosity. Not all triple phase boundaries are active, however, and so the active triple phase boundary length depends on the percolation of the LSM, YSZ and pore phases. Figure 5.3 plots the triple phase boundary length against the LSM volume fraction. The difference between the total TPB and the active TPB for LSM and YSZ particle sizes of $0.5\mu m$ and an electrode porosity of 0.3 is shown in Figure 5.3a. The active TPB is lower than the total TPB because not all TPB locations belong to a percolating network. Figure 5.3b shows the active triple phase boundary length for a range of LSM and YSZ particle sizes and distributions. For equal LSM and YSZ particle sizes, the TPB length is maximized at an LSM volume fraction of 0.5 but as the ratio between the LSM and YSZ particle size increases, the maximum TPB length is shifted towards higher LSM volume fractions since these volume fractions maximize the percolation of both the LSM and YSZ phases. A summary of the base case parameters used in this model is shown in Table 5.1.

Table 5.1: Base case composite cathode parameters.

Parameter	Description	Value
ϵ	Porosity	0.35
λ_{tpb}	Triple phase boundary length	$3.13\mu m/\mu m^3$ (50 vol% LSM) [17]
σ_{LSM}^{eff}, σ_{YSZ}^{eff}	Effective conductivity	Eqs. 5.13 and 5.14
i_0^{ref}	Reference exchange current density	Eq. 5.9a
α_a, α_c	Charge transfer coefficients	0.5 Eq. 5.7
L_{ccl}	Current collector layer thickness	$20\mu m$
L	Composite cathode thickness	21-$70\mu m$

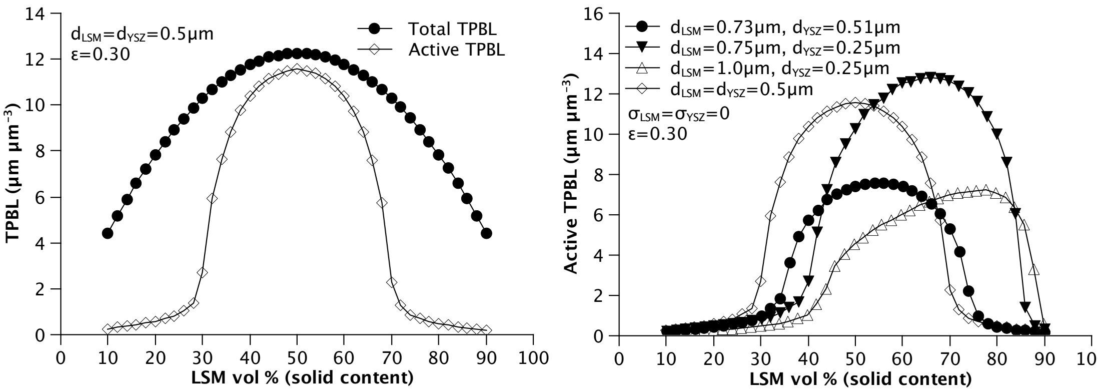

(a) (b)

Figure 5.3: Triple phase boundary length (λ_{tpb}) calculated for composite cathodes of varying LSM and YSZ particle sizes: (a) Total and active triple phase boundary length for LSM and YSZ particle sizes equal to $0.5\mu m$ and electrode porosity of 0.3 (b) Active triple phase boundary length for a range of particle sizes and an electrode porosity of 0.3. Figures taken from [17].

5.4 Experimental Results

5.4.1 Effective Electronic Conductivity Measurements

Figure 5.4a shows the electrical conductivities obtained between temperatures of $400°C$ and $900°C$ using the van der Pauw conductivity method for LSM/YSZ compositions of 50/50, 60/40 and 70/30 and 100/0 vol% (by solids content) at a porosity of $\epsilon \approx 0.35$, as well as the conductivity of fully dense LSM. Owing to the much larger electronic conductivity of LSM compared to the ionic conductivity of YSZ, it is assumed that these electrical conductivities are primarily electronic in nature and not ionic and so these were the values used in the model for σ_{LSM}^{eff}. Figure 5.4a shows that composite cathodes with lower LSM volume fractions had lower electrical conductivities, as expected. At $900°C$, the electrical conductivity of a 50 vol % LSM composite cathode was 10.3 S/cm while that of a 70 vol % LSM composite cathode was 24 S/cm and for a 100 vol % porous LSM cathode, the electrical conductivity was 67 S/cm. A number of samples were also tested to assess the reproducibility of the van der Pauw conductivity. For 100 vol % LSM cathodes at $800°C$, the variability was only 1.56% while the reproducibility of the electrical conductivity measurements on 50 vol % LSM composite cathodes was 0.46% (measured using two different samples).

In comparison to the effective electrical conductivities, the bulk ionic conductivity of the YSZ electrolyte (measured based on the serial resistance from the impedance response) at $900°C$ was 0.1 S/cm and the bulk conductivity of LSM was 211 S/cm. The bulk electronic and ionic conductivities follow the Arrhenius relationship:

$$\sigma^0_{LSM} = 258 \exp\left(\frac{-0.02eV}{RT}\right) \tag{5.14a}$$

$$\sigma^0_{YSZ} = 303 \exp\left(\frac{-0.81eV}{RT}\right) \tag{5.14b}$$

Figure 5.4b shows the normalized effective conductivity of the porous LSM composite electrodes as a function of LSM volume fraction measured using the van der Pauw method. The normalized effective conductivity is the ratio of the effective electronic conductivity to the bulk LSM conductivity. The Koh-Fortini model described in Equation 5.13 is also shown for $n = 11$. It is expected that the normalized ionic conductivity as a function of YSZ volume fraction would behave similarly to that of the normalized electronic conductivity shown in Figure 5.4b. Since the effective ionic conductivity is not easy to measure, the Koh-Fortini model was used in this work to estimate the effective ionic conductivity of the composite electrode, σ^{eff}_{YSZ}.

5.4.2 Impedance Analysis

The impedance response at OCV of a 50 vol % LSM-50 vol % YSZ composite cathode with $26\mu m$ thick CFL is shown in Figure 5.5a at $750°C$ as a function of pO_2 (note: the inductance was removed using equivalent circuits). As expected, as the pO_2 increased, the electrode resistance decreased. In addition to the electrode impedance as a function of pO_2, Figure 5.5b shows the impedance as a function of CFL thickness in air at $750°C$. Interestingly, as the thickness of the cathode functional layer increased from $2.8\mu m$ to $26\mu m$, the electrode resistance decreased from $1.29\Omega cm^2$ to $0.24\Omega cm^2$, a factor of 5. By comparison, the resistance at OCV of a pure LSM electrode (given in Chapter 3) was $9.66\Omega cm^2$ at $750°C$ in air (before polarizing the electrode). This dramatic decrease in resistance between pure LSM cathodes and composite cathodes is commonly assumed to be the result of two contributions [21]: (i) a larger number of active TPBs resulting in an increase in the rate of the

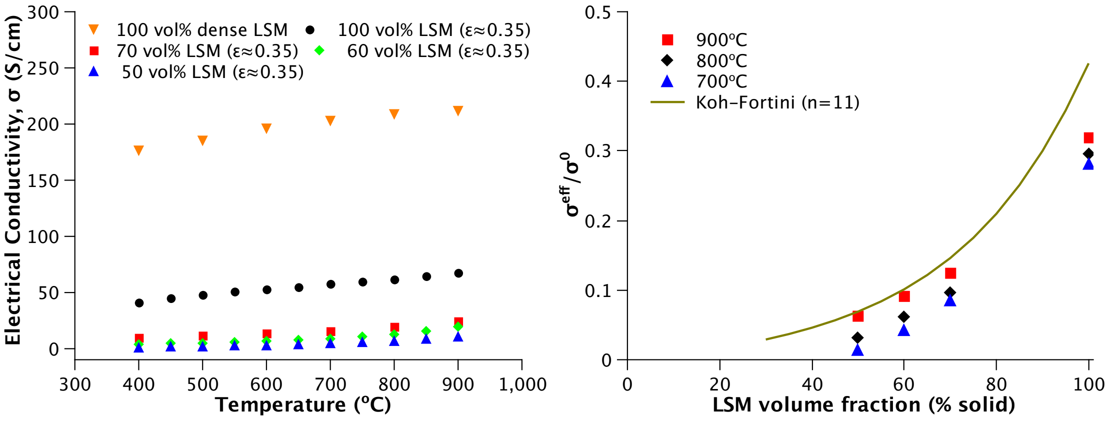

(a) (b)

Figure 5.4: (a) Measured electrical conductivity of cathodes for various LSM/YSZ cathode compositions (b) Comparison of Koh-Fortini model prediction with experimental data. σ^{eff} is the effective electrical conductivity of composite electrodes and σ^0 is the electrical conductivity of dense LSM. All electrical conductivities were measured using the van der Pauw technique.

electrochemical reaction and (ii) better adhesion between the bulk electrolyte and the composite cathode.

Figures 5.5c and 5.5d show the apparent oxygen reaction order with respect to R_p and the inverse of the polarization resistance in air ($1/R_p$) as a function of CFL thickness. The trend shown in Figure 5.5d has been observed by a number of groups before [22–25]. One reason for the decrease in the electrode resistance as the CFL thickness increases is because the total number of TPB sites depends on the volume of the electrode, which increases with thickness. Figure 5.5d indicates that the electrode resistance decreases sharply (or $1/R_p$ increases sharply) with an initial increase in functional layer thickness but further increase results only in a marginal dcrease in R_p. The small decrease in R_p with large increase in thickness indicates that there is an "effective" functional layer thickness above which, the cathode is only marginally utilized. Interestingly, the apparent reaction order of a composite cathode tends to decrease as the CFL thickness is increased.

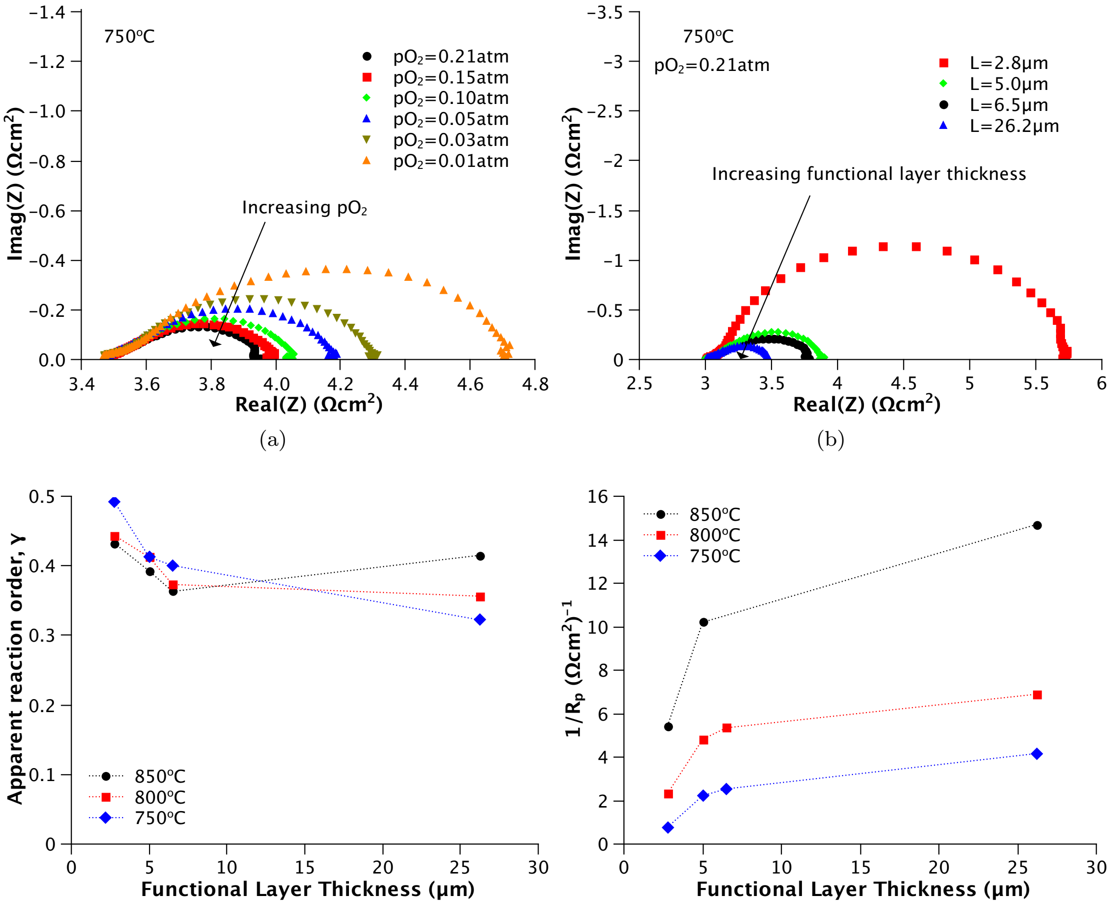

(a) (b)

(c) (d)

Figure 5.5: Impedance of 50 vol% LSM-50 vol% YSZ composite cathodes: (a) Impedance response at OCV as a function of pO_2 for a functional layer thickness of $26\mu m$ and $T = 750°C$ (b) Impedance response at OCV as a function of functional layer thickness in $pO_2 = 0.21atm$ and $T = 750°C$ (c) Apparent reaction order of R_p as a function of functional layer thickness (d) Inverse of polarization resistance (at OCV) as a function of functional layer thickness. Lines through curves are to guide the eye.

5.5 Modelling Results

5.5.1 Comparison of Model to Experimental Data

The mathematical model of the composite cathode presented in Section 5.3.2 was used to help explain the complex relationship between the cathode resistance and its structure. The cathode structure/microstructure such as the LSM/YSZ composition, porosity and particle sizes influence the triple phase boundary length, effective electronic and ionic conductivities and effective gas transport coefficients, which all have an impact on the cathode resistance. Figure 5.6a shows the model predictions for $1/R_p$ vs functional layer thickness and Figure 5.6b shows the model predictions for the apparent reaction order, γ, vs functional layer thickness at a temperature of $750°C$ in air. The base case model parameters, described in Table 5.1, employing triple phase boundary lengths estimated from numerical construction of composite cathodes [17], effective electronic and ionic conductivities using the Koh-Fortini relationship in Equation 5.13 and exchange current densities from pure phase LSM cathodes, predicted the correct trend in terms of R_p and γ vs CFL thickness but the calculated R_p values were too low.

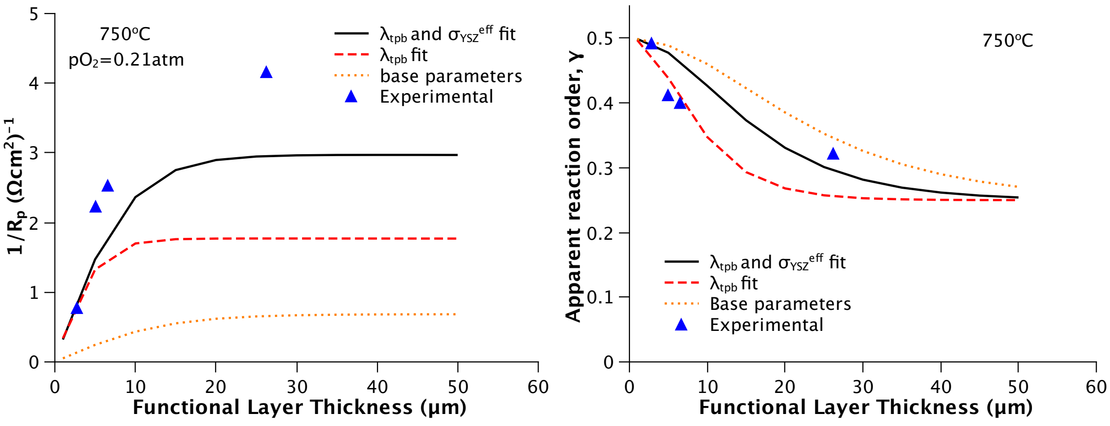

(a) (b)

Figure 5.6: (a) Cathode polarization resistance and (b) apparent reaction order (γ) calculated by model as a function of functional layer thickness. The three model curves represent base case λ_{tpb} and σ_{YSZ}^{eff} values as well as fitted values.

In order to better estimate the R_p values, it was necessary to fit both the λ_{tpb} and σ_{YSZ}^{eff} parameters.These parameters were fit against experimental data of $1/R_p$ vs L and γ vs L simultaneously.

The result of this fitting is also shown in Figure 5.6. It is important to realize that the current density and hence the polarization resistance of composite cathodes is sensitive to the factors appearing in Equation 5.5, however, R_p is much more sensitive to changes in σ_{YSZ}^{eff} than to changes in σ_{LSM}^{eff} because the ionic conductivity is three orders of magnitude smaller than the electronic conductivity. After fitting, the resulting λ_{tpb} value was 6.2 times higher than the estimated λ_{tpb} value and σ_{YSZ}^{eff} was 3 times higher than that predicted by the Koh-Fortini model.

There may be a number of reasons why λ_{tpb} and/or σ_{YSZ}^{eff} predictions were too small. These could include factors such as a variation between the true particle sizes and the particle size distributions used to estimate λ_{tpb}, possibly caused by agglomeration of particles, or a variation in the porosity of the composite cathodes, both of which may impact the percolation of each phase. In addition, it has been suggested [26] that the TPB at the LSM/bulk YSZ interface could contribute to oxygen reduction since there are LSM particles in contact with the bulk YSZ at this interface, however, in the model presented in Section 5.3.2, it was assumed that the triple phase boundaries in the bulk of the cathode were much higher than the triple phase boundaries at the LSM/bulk YSZ interface and electrochemical reactions at this interface were neglected. Also, as previously mentioned, it is thought that a portion of the improvement observed in composite cathodes may be a result of better adhesion between the LSM and YSZ phases due to more intimate contact between LSM particles and YSZ particles within a composite cathode compared to the contact between LSM and YSZ at the cathode/bulk electrolyte interface. This also was not captured by the model. Another possibility is that composite electrodes may provide an additional pathway for the oxygen reduction reaction, one where oxygen gas adsorbs onto the YSZ surface and is transported over a short distance to the LSM/YSZ interface where charge transfer can take place. Unlike in pure LSM cathodes, the gas-YSZ interfacial area within the composite cathode can be high [17] and it has been predicted that oxygen adsorption is accelerated when the surface site involves an oxygen vacancy [27] which may contribute to the improved performance of composite LSM-YSZ cathodes over pure LSM cathodes.

Accounting for the increased TPBs at the cathode/bulk electrolyte interface and better contact between the LSM/YSZ particles would likely impact the rate of the electrochemical reaction, which could explain the increase in λ_{tpb} but not necessarily the increase in σ_{YSZ}^{eff}. Although the Koh-Fortini model predicted σ_{YSZ}^{eff} to be too small, another model that has been used in the literature [28] predicts

σ_{YSZ}^{eff} closer to the fitted value:

$$\sigma_k^{eff} = \sigma_k^0(1-\epsilon)\theta_k P(\theta_k) \tag{5.15}$$

where k is either the LSM or YSZ phase, θ is the volume fraction of phase k and $P(\theta_k)$ is the probability of percolation of phase k which is a function of θ. The probability of percolation can be calculated from numerical construction of porous LSM electrodes [17] and was found to be $P(\theta_{LSM} = 0.50) = 0.95$. Equation 5.15 results in σ_{YSZ}^{eff} 1.4 times larger than the fitted value.

For the purpose of predictions in the composite cathode polarization resistance, the triple phase boundary length and the effective ionic conductivities were increased by factors of 6.2 and 3 respectively, consistent with fitting these parameters to the experimental data.

5.5.2 Distribution of Species Concentration and Potential in Composite Cathodes

A kinetic analysis on SOFC cathodes typically relies on the oxygen reaction order, γ, which can be related to various processes of the overall oxygen reduction reaction. For LSM/YSZ composite cathodes, an interesting result is the behavior of the apparent reaction order, γ, as a function of the cathode functional layer thickness, shown in Figure 5.6b. The value of γ assumed by the model was 0.5, however, when calculating γ from the polarization resistance of the model, significant deviations were observed unless the functional layer thickness was very thin ($L \approx 1\mu m$). This same trend was also observed experimentally and may lead to the wrong interpretation of limiting processes within a composite cathode. This deviation in the apparent reaction order is caused by the distribution of current and potential throughout the thickness of the cathode. Figure 5.7a and 5.7b show the distributions throughout the composite cathode thickness of the local electronic current density and the local overpotential distribution for a nominal overpotential (applied overpotential) of $\eta_{nom} = -1mV$ and for a cathode functional layer thickness of $50\mu m$, $10\mu m$ and $1\mu m$.

The distribution in the electronic current density and overpotential shown in Figure 5.7 are caused by the gradients in the electronic phase and ionic phase potential within the composite cathode functional layer. These gradients are generated as a result of the relatively high electrochemical

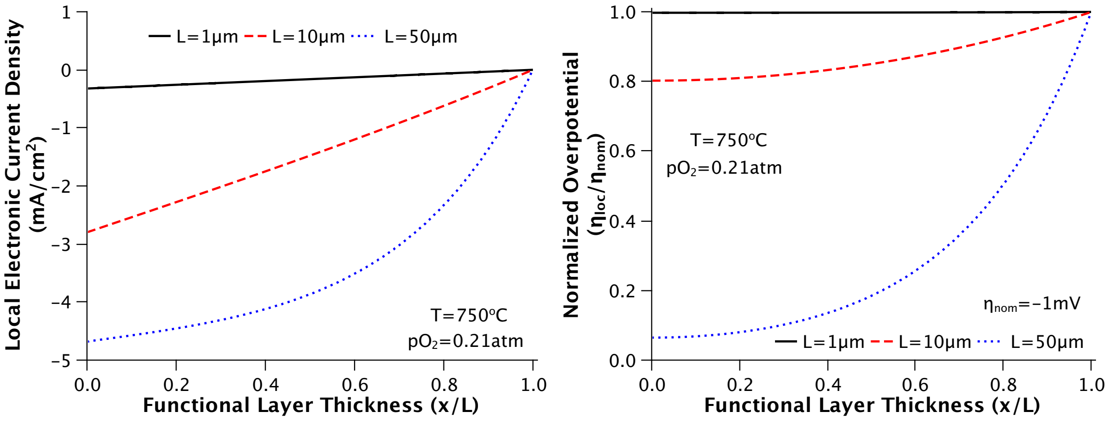

(a) (b)

Figure 5.7: Distribution of (a) local electronic current density at a nominal overpotential of $\eta_{nom} = -1mV$ and (b) local overpotential (normalized against $\eta_{nom} = -1mV$) throughout the thickness of the LSM/YSZ composite cathode for functional layer thicknesses (L) of $50\mu m$, $10\mu m$ and $1\mu m$.

reaction rate coupled with a high resistance to transport of the relevant charged species, especially ionic charge. For a given electro-catalyst/electrolyte system at a fixed temperature and oxygen partial pressure conditions, the rate of the ORR is dependent on the magnitudes of the microstructure dependent quantity λ_{tpb} and the overpotential. Additionally, the resistance to charge transport depends on the resistivity of the constituent material of the composite cathode. Both electrode thickness and electrode microstructural parameters can influence these factors.

Figure 5.8a shows the local distribution of the polarization resistance at OCV along the thickness of the cathode functional layer where the local polarization resistance is calculated using the local overpotential and the total current density, $R_{p,loc} = \partial\eta/\partial i$. The distribution in the electrode resistance is caused by the distribution of the overpotential and hence the variation in the local R_p depends on the same factors: (i) triple phase boundary length, (ii) resistance to charge transport and (iii) the cathode thickness. For the same λ_{tpb} and σ_{YSZ}^{eff}, as the thickness of the composite cathode is reduced, the gradients in the species concentrations decrease and so the distribution in local R_p becomes more uniform. As a result, the local reaction order, shown in Figure 5.8b also becomes more uniform and as $L \to 0$, $\gamma \to 0.5$, which is the true reaction order (specified in the model).

This analysis clearly shows that the reason for the variation in the apparent reaction order

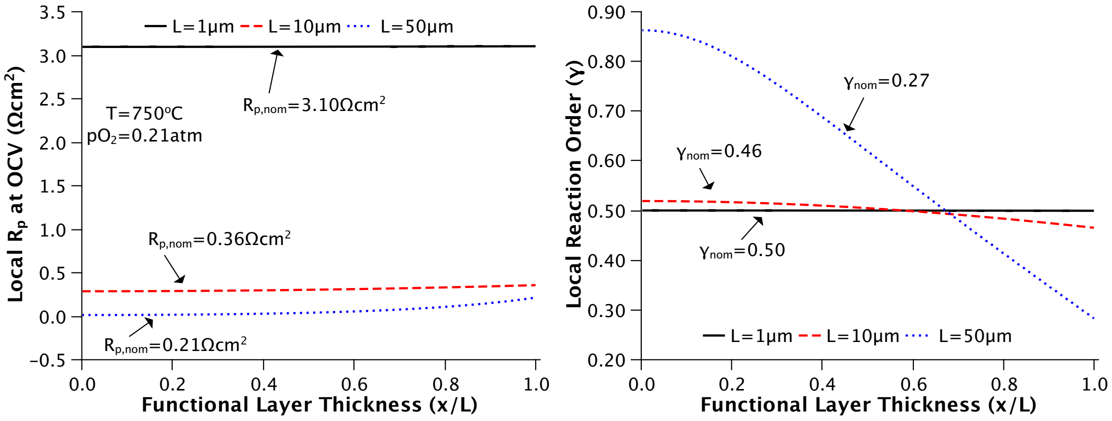

(a) (b)

Figure 5.8: Distribution of (a) local polarization resistance (R_p) at OCV and (b) apparent reaction order throughout the thickness of the LSM/YSZ composite cathode for a functional layer thickness (L) of $50\mu m$, $10\mu m$ and $1\mu m$. Superscript "nom" refers to the nominal value, or observed value calculated from a low field analysis of polarization data.

with composite cathode thickness is due to gradients that exist in the cathode functional layer. Experimentally, since the gradients are unknown, only the nominal values of R_p, η and γ can be known and these nominal values are vastly different than the local values. In order to reduce the gradients and thus ensure that the nominal and local resistances, overpotentials and reaction orders are the same, the thickness of the cathode functional layer can be reduced.

5.5.3 Structure-Performance Prediction of Composite Cathodes

The resistance of a composite cathode and species gradients within the cathode are related to parameters that depend on the cathode structure, such as the thickness of the functional layer, the volume fraction of the LSM, YSZ and pore phase and the particle size. By combining the model for composite cathodes along with a model to calculate the relevant microstructural parameters [17], the performance of various composite cathode designs can be quickly assessed. Figure 5.9 shows the predicted polarization resistance (OCV) at $750°C$ for a composite cathode of porosity 0.35 and LSM volume fractions varying between 0.35 and 0.70 and a functional layer thickness between $1\mu m$ and $50\mu m$. As observed previously, R_p decreases as the CFL thickness increases, however, there is an optimal LSM volume fraction which minimizes R_p. The minimum value of the electrode polarization resistance was found to be $R_p = 0.20\Omega cm^2$ at an LSM volume fraction of 0.45 and a functional layer thickness of $L = 50\mu m$.

The LSM volume fraction influences the percolation of each phase which in turn affects the active triple phase boundary length and the effective electronic/ionic conductivities. For an LSM particle size of $d_{LSM} = 0.73\mu m$ and a YSZ particle size of $d_{YSZ} = 0.51\mu m$, the active TPB length is maximized at an LSM volume fraction of 0.53 (see Figure 5.3b). Although the TPB length is maximized at an LSM volume fraction of 0.53, the effective ionic conductivity, σ_{YSZ}^{eff}, increases as the LSM volume fraction decreases (or as the YSZ volume fraction increases). At $750°C$, for an LSM volume fraction of 0.50, $\sigma_{YSZ}^{eff} = 0.006S/cm$ and $\lambda_{tpb} = 3.1\mu m/\mu m^2$ whereas for an LSM volume fraction of 0.45, $\sigma_{YSZ}^{eff} = 0.008S/cm$ and $\lambda_{tpb} = 3.0\mu m/\mu m^2$. The higher ionic conductivity at an LSM volume fraction of 0.45 compared to an LSM volume fraction of 0.50 results in a lower polarization resistance despite the decrease in the triple phase boundary length. It is important to realize that this optimal composition depends on the ratio of the LSM and YSZ particle sizes. As Figure 5.3b shows, the maximum in λ_{tpb} shifts towards higher volume fractions of LSM as the LSM particle size increases relative to the YSZ particle size. The opposite would be true if the YSZ particle size increased relative to the LSM particle size. If the LSM particle size was much larger than the YSZ particle size, then the LSM composition that minimized R_p (at OCV) would also increase but it would likely still not correspond to the volume fraction that maximizes λ_{tpb}.

Although the cathode polarization resistance is minimized for a functional layer thickness of $L = 50\mu m$ and an LSM volume fraction of 0.45, if the CFL thickness was kept less than $15\mu m$, which is often the case, the optimal LSM/YSZ composition shifts to an LSM volume fraction of 0.50. This is shown in Figure 5.10a which plots the same data as Figure 5.9. At a functional layer thickness of $L = 15\mu m$, $R_p = 0.275\Omega cm^2$ for an LSM volume fraction of 0.50 and $R_p = 0.276\Omega cm^2$ for an LSM volume fraction of 0.45. Figure 5.10a also shows that for low volume fractions of LSM, such as an LSM volume fraction of 0.35 and 0.40, although R_p is high when the functional layer thickness is low, the effective or utilized functional layer thickness is much higher compared to LSM volume fractions above 0.50. For example, the effective functional layer thickness for an LSM volume fraction of 0.65 is $\sim 20\mu m$ whereas the effective functional layer thickness for an LSM volume fraction of 0.35 is $\sim 50\mu m$. In this case, the triple phase boundary length for an LSM

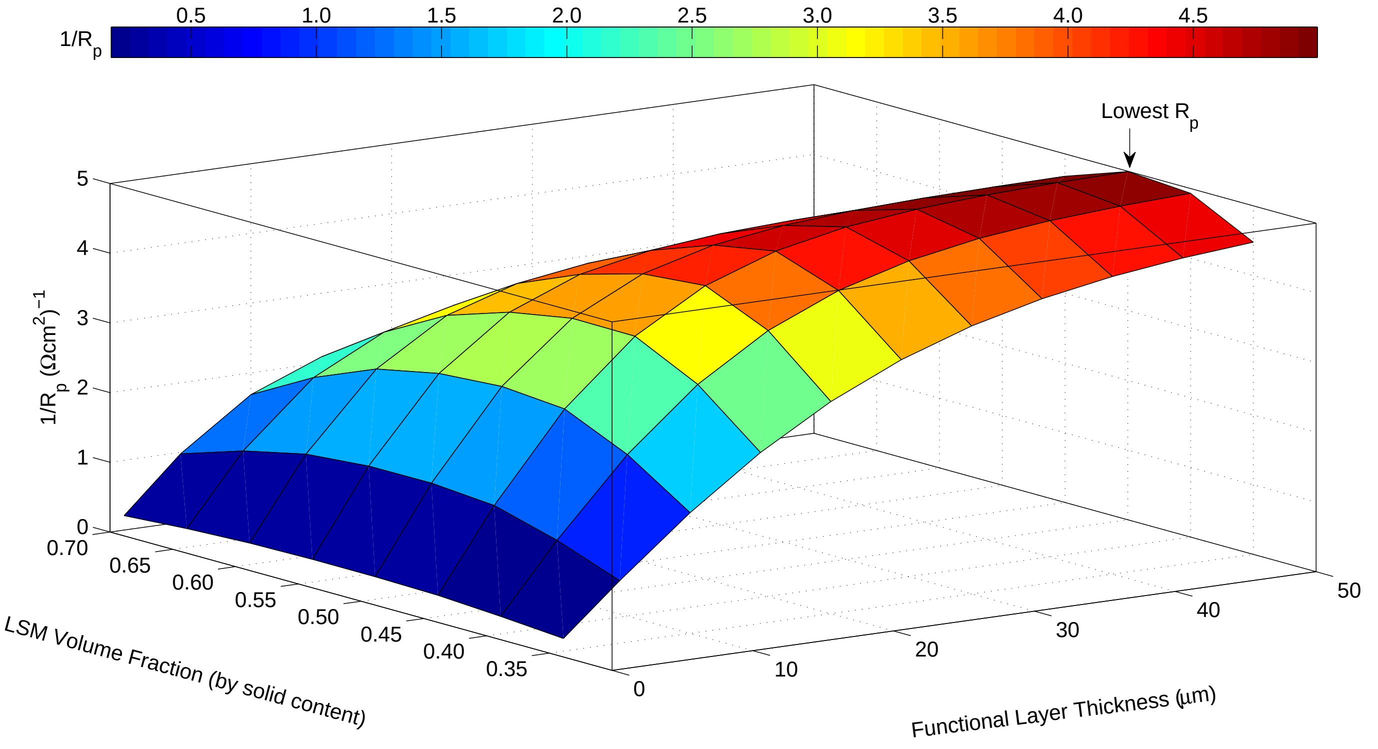

Figure 5.9: 3D surface plot showing the influence of composite cathode composition and functional layer thickness on R_p at OCV at $750°C$ in air.

volume fraction of 0.65 is 1.5 times higher than that of an LSM volume fraction of 0.35 but the effective ionic conductivity is only 1/4 that of an LSM volume fraction of 0.35. Figure 5.10b shows the inverse of the polarization resistance and the triple phase boundary length as a function of LSM volume fraction (by solids content). It is clear that the LSM/YSZ composition which minimizes R_p is not necessarily the composition which maximizes the triple phase boundary length, however, as the thickness of the functional layer decreases, the composition which minimizes R_p shifts towards the composition which maximizes the triple phase boundary length. This is because the electrode is uniformly utilized and the gradients of ionic potential is low within the electrode resulting in an ORR rate being influenced primarily by the number of active sites.

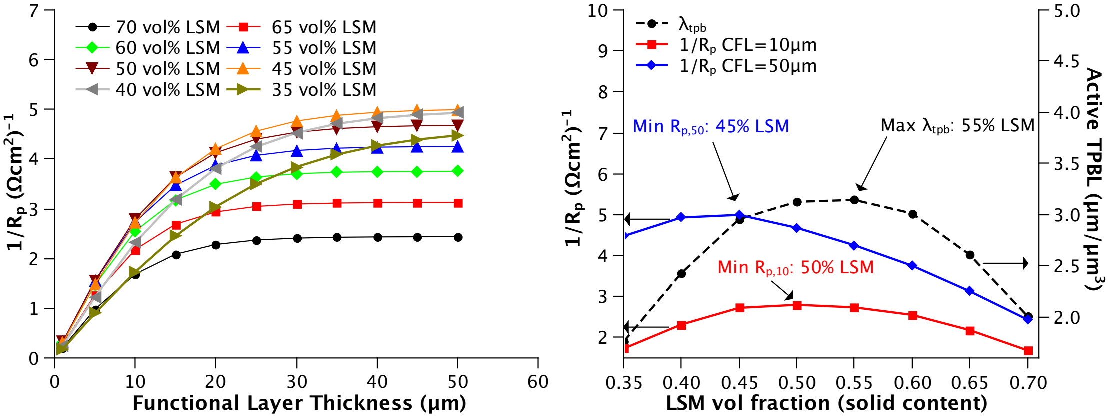

(a) (b)

Figure 5.10: (a) Influence of composite cathode composition and functional layer thickness on R_p at OCV at $750°C$ in air (b) LSM volume fractions that give the minimum R_p and maximum triple phase boundary length for CFL thicknesses of $10\mu m$ and $50\mu m$.

The modelling results discussed above indicate that λ_{tpb}, σ_{YSZ}^{eff} and the functional layer thickness are the most important factors that must be considered when designing composite cathodes. The triple phase boundary length and the effective ionic conductivity are both influenced by microstructural features of the composite cathode such as the LSM and YSZ particle size, which influences the optimal LSM/YSZ composition, and by the LSM/YSZ composition itself. These microstructural features impact the percolation of each phase within the composite cathode as well as the number of LSM and YSZ particles in contact with each other.

5.6 Summary/Conclusion

In this chapter, a numerical model of an LSM-YSZ composite cathode was developed and compared against experimental results of the composite cathode polarization resistance measured on 2-electrode symmetrical cells using impedance spectroscopy at OCV. The experimental results showed:

1. Compared to pure phase LSM cathodes, the polarization resistance of a 50 vol% LSM-50 vol% YSZ composite cathode with a functional layer thickness of $L = 26\mu m$ at $750°C$ in air was lower by a factor of 40 times.
2. An increase in the cathode functional layer thickness from $2.8\mu m$ to $26\mu m$ resulted in a 5 fold decrease in R_p.
3. The oxygen reaction order with respect to R_p was found to decrease as the thickness of the cathode functional layer decreased. For a CFL thickness of $2.8\mu m$, $\gamma = 0.5$ which decreased to $\gamma = 0.3$ for a CFL thickness of $26\mu m$.

These trends observed from experimental studies were also observed in the results of model simulations. The model results showed:

1. The low resistance of a composite cathode is likely not just a result of the extension of the electrochemical reaction away from the LSM/bulk YSZ interface, but also may be caused by additional factors such as better contact between LSM and YSZ phases or an additional pathway such as oxygen adsorption onto the YSZ surface. Evidence for this lies in the fact that exchange current densities measured from pure LSM cathodes were too low to match exchange current densities of LSM/YSZ composite cathodes.
2. The most important parameters influencing the resistance of the composite cathode were: (i) the triple phase boundary length (λ_{tpb}), (ii) the effective ionic conductivity (σ_{YSZ}^{eff}) and (iii) the thickness of the cathode functional layer (L).
3. Local distributions of R_p and γ exist within the cathode functional layer and are related to the gradients of the species concentrations, electronic and ionic charge as well as oxygen gas.

4. As the thickness of the cathode functional layer approaches zero, the species concentration gradients also approach zero and the apparent reaction order measured using a composite cathode approaches the "true" reaction order.
5. For a cathode functional layer thickness larger than $15\mu m$, a lower resistance was found for a composite cathode with an LSM volume fraction of 0.45 compared to an LSM volume fraction of 0.50 despite the fact that λ_{tpb} was lower. This reduced resistance was caused by the fact that σ_{YSZ}^{eff} increases when the LSM volume fraction decreases.
6. For a cathode functional layer thickness smaller than $15\mu m$, an LSM volume fraction of 0.5 minimized the electrode resistance, however, much lower R_p values could be obtained at different compositions by increasing the functional layer thickness.
7. The effective cathode thickness depends primarily on the effective ionic conductivity. For compositions that maximize the effective ionic conductivity, the effective cathode thickness increases.
8. In order to optimize the cathode design, a balance must be found between maximizing the triple phase boundary length and maximizing the effective ionic conductivity.

5.7 List of symbols

Symbol/Term	Description	Units
CCL	Current collector layer	-
CFL	Cathode functional layer	-
i	Current density	A/m^2
x	Position along cathode length	m
λ_{tpb}	Triple phase boundary length	m/m^3
$\sigma_{LSM,YSZ}$	Conductivity of LSM or YSz phase	S/m
$\phi_{el,io}$	Electronic or ionic phase potential	V
$D_{O_2-N_2}$	Binary gas diffusion coefficient	m^2/s
D_K	Knudsen diffusion coefficient	m^2/s
$\alpha_{a,c}$	Anodic or cathodic charge transfer coefficient	-
η	Overpotential	V
$R_{P,tpb}$	Polarization resistance per TPB length	Ωm
L_{ccl}	Current collector layer thickness	m
L	Composite cathode thickness	m
ϵ	Porosity	-
θ_k	Volume fraction of phase k	-
$P(\theta_k)$	Probability of percolation of phase k	-
R	Gas constant	$J/mol/K$
T	Temperature	K

Superscript	Description	Subscript	Description
eff	effective	LSM	LSM phase
0	pure phase	YSZ	YSZ phase
ref	reference	el	electronic
bulk	bulk value or equilibrium value	io	ionic

References

[1] S.B. Adler. Factors Governing Oxygen Reduction in Solid Oxide Fuel Cell Cathodes. *Chemical Reviews*, 104:4791–4843, 2004.

[2] V.A.C. Haanappel, J. Mertens, D. Rutenbeck, C. Tropartz, W. Herzhof, D. Sebold, and F. Tietz. Optimisation of processing and microstructural parameters of LSM cathodes to improve the electrochemical performance of anode-supported SOFCs. *Journal of Power Sources*, 141:216–226, 2005.

[3] V. Dusastre and J.A. Kilner. Optimisation of composite cathodes for intermedita temperature SOFC applications LSCF. *Solid State Ionics*, 126:163–174, 1999.

[4] M. Kleitz and F. Petitbon. Optimized SOFC electrode microstructure. *Solid State Ionics*, 92:65–74, 1996.

[5] M.J. Jorgensen, S. Primdahl, and M. Mogensen. Characterisation of composite SOFC cathodes using electrochemical impedance spectroscopy. *Electrochimica Acta*, 44:4195–4201, 1999.

[6] M.J. Jorgensen and M. Mogensen. Impedance of Solid Oxide Fuel Cell LSM/YSZ Composite Cathodes. *Journal of the Electrochemical Society*, 148(5):A433–A442, 2001.

[7] Y. Jiang, S. Wang, Y. Zhang, J. Yan, and W. Li. Electrochemical reduction of oxygen on a strontium doped lanthanum manganite electrode. *Solid State Ionics*, 110:111–119, 1998.

[8] J-D. Kim, G-D. Kim, J-W. Moon, Y. Park, W-H. Lee, K. Kobayashi, M. Nagai, and C-E. Kim. Characterization of LSM-YSZ composite electrode by ac impedance spectroscopy. *Solid State Ionics*, 143:379–389, 2001.

[9] S. McIntosh, S.B. Adler, J.M. Vohs, and R.J. Gorte. Effect of Polarization on and Implications for Characterization of LSM-YSZ Composite Cathodes. *Electrochemical and Solid State Letters*, 7(5):A111–A114, 2004.

[10] J. Choi, J. Jang, and S. Oh. Microstructure and cathodic performance of $La_{0.9}Sr_{0.1}MnO_3$/yttria-stabilized zirconia composite electrodes. *Electrochimica Acta*, 46:867–874, 2001.

[11] C.W. Tanner, K-Z. Fung, and A.V. Virkar. The effect of porous composite electrode structures on solid oxide fuel cell performance. *Journal of the Electrochemical Society*, 144:21–30, 1997.

[12] James R. Wilson, J. Scott Cronin, Anh T. Duong, Sherri Rukes, Hsun-Yi Chen, Katsuyo Thornton, Daniel R. Mumm, and Scott Barnett. Effect of composition of $(La_{0.8}Sr_{0.2}MnO_3 - Y_2O_3$-stabilized $ZrO_2)$ cathodes: Correlating three-dimensional microstructure and polarization resistance. *Journal of Power Sources*, 195(7):1829–1840, 2009.

[13] J. Deseure, Y. Bultel, L. Dessemond, and E. Siebert. Theoretical optimisation of a SOFC composite cathode. *Electrochimica Acta*, 50:2037–2046, 2005.

[14] S.H. Chan and Z.T. Xia. Polarization effects in electrolyte/electrode-supported solid oxide fuel cells model. *Journal of Applied Electrochemistry*, 32:339–347, 2002.

[15] P. Costamagna, P. Costa, and V. Antonucci. Micro-modelling of solid oxide fuel cell electrodes. *Electrochimica Acta*, 43(3-4):375–394, 1998.

[16] P. Costamagna, P. Costa, and E. Arato. Some more considerations on the optimization of cermet solid oxide fuel cell electrodes. *Electrochimica Acta*, 43(8):967–972, 1998.

[17] Ben Kenney, Mikelis Valdmanis, Craig Baker, J.G. Pharoah, and Kunal Karan. Computation of TPB length, surface area and pore size from numerical reconstruction of composite solid oxide fuel cell electrodes. *Journal of Power Sources*, 128(2):1051–1059, 2009.

[18] L.J. van der Pauw. A method of measuring specific resistivity and hall effect of discs of arbitrary shape. *Philips Research Reports*, 13(1):1–9, 1958.

[19] Keiji Yamahara, Tal Z. Sholklapper, Craig P. Jacobson, Steven J. Visco, and Lutgard C. De Jonghe. Ionic conductivity of stabilized zirconia networks in composite SOFC electrodes. *Solid State Ionics*, 176:1359–1364, 2005.

[20] J.C.Y. Koh and A. Fortini. Prediction of Thermal Conductivity and Electrical Resistivity of Porous Metallic Materials. *International Journal of Heat and Mass Transfer*, 16:2013–1022, 1973.

[21] M. Ostergard, C. Clausen, C. Bagger, and M. Mogensen. Manganite-Zirconia Composite Cathodes for SOFC: Influence of Structure and Composition. *Electrochimica Acta*, 40(12):1971–1981, 1995.

[22] T. Kenjo, S. Osawa, and K. Fujikawa. High Temperature Air Cathodes Containing Ion Conductive Oxides. *Journal of the Electrochemical Society*, 138(2):349–355, 1991.

[23] T. Kenjo and M. Nishiya. $LaMnO_3$ air cathodes containing ZrO_2 electrolyte for high temperature solid oxide fuel cells. *Solid State Ionics*, 57:295–302, 1992.

[24] M. Juhl, S. Primdahl, C. Manon, and M. Mogensen. Performance/structure correlation for composite SOFC cathodes. *Journal of Power Sources*, 61:173–181, 1996.

[25] E.P. Murray, T. Tsai, and S.A. Barnett. Oxygen transfer processes in $(La, Sr)MnO_3/Y_2O_3$-stabilized ZrO_2 cathodes: an impedance spectroscopy study. *Solid State Ionics*, 110:235–243, 1998.

[26] Abbaspour Ali, X. Wen, K. Nandakumar, Jingli Luo, and Karl T. Chuang. Geometrical modeling of microstructure of solid oxide fuel cell composite electrodes. *Journal of Power Sources*, 185(2):961–966, 2008.

[27] YongMan Choi, Matthew E. Lynch, M.C. Lin, and Meilin Liu. Prediction of O_2 Dissociation Kinetics on $LaMnO_3$-Based Cathode Materials for Solid Oxide Fuel Cells. *Journal of Physical Chemistry C*, 113:7290–7297, 2009.

[28] S.H. Chan, X.J. Chen, and K.A. Khor. Cathode micromodel of solid oxide fuel cell. *Journal of the Electrochemical Society*, 151(1):A164–A172, 2004.

Chapter 6

Conclusion

6.1 Overview

In this thesis, a combined experimental and modeling study of the oxygen reduction reaction in a porous LSM solid oxide fuel cell cathode was undertaken. The experimental component of this work focused on the generation of reproducible data over a range of operating conditions, viz. temperature, oxygen partial pressure, and overpotential. Following a strict protocol, experiments were carried out to minimize the influence of electrical history on the measured electrochemical performance. A mathematical framework based on porous electrode theory was developed to describe the electrochemical behavior of porous LSM cathodes. The model explicitly considers the fundamental processes occurring in the porous electrode - gas phase transport in porous media, adsorption/desorption kinetics, surface diffusion of adsorbed oxygen species, and the charge-transfer reaction kinetics. The relevant electrode microstructural parameters were determined either by direct or numerical experimentation. The generalized model developed is a transient model that captures the distributed nature of the porous electrodes. The model was appropriately modified to simulate either steady state polarization or ac impedance experiments.

Combining the modeling work with the experimentation allowed for interpretation of data in terms of rates of specific fundamental processes, and thereby providing improved understanding of the oxygen reduction reaction in LSM cathodes. Previous studies examining the kinetics of LSM cathodes have used the oxygen reaction order or the activation energy of the electrode resistance to determine the rate limiting process, however, the technique developed within this thesis does not assume a single rate determining process and can also be applied to parallel pathways. Further, new insights were gained by conducting studies at low oxygen partial pressure conditions. Although these low oxygen partial pressure measurements are rarely encountered during fuel cell operation, they can be likened to microelectrode studies since they can be used to provide a more fundamental understanding of the LSM/YSZ system. The key scientific observation/findings of the research completed is summarized in Section 6.2 and the original contributions arising from this thesis are highlighted in Section 6.3.

To accomplish the goals of this research, several important tools, presented below, were developed during the thesis.

- Development of an automated spray system for the fabrication of porous electrodes of reproducible thickness and porosity.
- Development of an experimental protocol for the determination of electrode polarization resistances such that measurements were not tainted by differences in electrical history.
- Development of mathematical models of porous electrodes for simulating steady-state polarization and ac impedance experiments.
- Coupling of the porous electrode model with parameter estimation scheme in Matlab for the regression of model parameters, i.e. kinetic rate constants and transport coefficients.

Although these tools were applied specifically to the study of porous LSM electrodes, the framework could be applied to a number of other electrode systems.

6.2 Summary of Scientific Observations/Findings

The observations made from experimental data collected ranged from expected results consistent with previous studies to new findings that have either not been reported at all or only recently reported. The findings of the simulation results were insightful in demonstrating the influence of the electrode microstructure on the electrochemical performance. In addition, the simulation results showed why it is important to consider the distributed nature of porous electrodes in correctly interpreting the electrochemical data.

Experiments conducted in high pO_2 atmospheres exhibited expected steady-state polarization behavior – non-linearly increasing current density with increased overpotential. No limiting current type behavior was observed over the range of overpotentials considered. On the other hand, the experiments conducted in low pO_2 atmosphere ($10^{-4}atm \leq pO_2 \leq 0.001atm$), showed the development of limiting current behavior at high overpotentials. Although limiting current behavior in LSM cathodes has been reported by a few researchers before, its origin had not been explored. From the model fit of low-pO_2 steady-state polarization data, it was found that the primary contributor to the limiting current was a combined effect of thermodynamics and kinetics of adsorption/desorption process. At low pO_2, the equilibrium coverage of oxygen on LSM surface is predicted to be low but more importantly the rate of adsorption is greatly reduced in accordance with collision theory.

One of the most significant experimental observations, previously unreported, is the vastly different and opposite behavior of LSM electrodes after being polarized in two different oxygen atmospheres – low pO_2 (10^{-4} atm) and high-pO_2 (0.01 atm). In high pO_2 atmospheres, the electrode polarization resistance at a cell potential of -600 mV, as expected, was lower than that at the pre-polarized (or unpolarized) condition. On the other hand, in low pO_2 atmospheres (10^{-4} atm of pO_2) the electrode polarization resistance at a cell potential of -600mV was higher than that at the pre-polarized condition. In both cases, upon relaxation to OCV conditions after being polarized to -600 mV, the electrode polarization resistance went back to the pre-polarized level but only after 15-20 hrs. Impedance data collected during the relaxation period identified that while the impedance associated with the charge-transfer process or R_{ct} relaxed relatively quickly, the chemical impedance or R_{chem} (refer to Section 2.4.2, page 77 for definition) relaxed rather slowly.

The analysis of the R_{chem} relaxation process yielded similar time-constants for both low-pO_2 and high-pO_2 conditions despite the fact that in the high-pO_2 environment R_{chem} decreased with polarization while in low-pO_2 environment it increased. It is argued that in both low- and high-pO_2 environments, the composition of the LSM surface is altered upon polarization of LSM and although this surface alteration influences the chemical impedance of the electrode in an opposite manner in low- and high-pO_2 environments, the underlying phenomena is the same – the population of the LSM surface with cation vacancies in high-pO_2 and the removal of cation vacancies from the LSM surface in low-pO_2 environments, consistent with the oxygen nonstoichiometry of LSM. A recent study from Shao-Horn's group at MIT has suggested a similar mechanism based on enhanced chemical activity observed in microelectrode studies in a high pO_2 environment. The original contribution of this thesis is to show an opposite effect in low pO_2 environment.

An important implication of these findings is that the electrode performance based on polarization resistance data at OCV has limited utility for comparison of different electrode materials because the state of the LSM surface and associated chemical/electrochemical property is different at OCV and under polarized conditions. Thus, it would be expected that both the kinetics and thermodynamics of the adsorption/desorption reaction may change with the changing surface composition.

These observations, obviously, add to the complexity of the mechanistic model for oxygen reduction on LSM electrodes. Despite neglecting the polarization-dependent changes in surface property, the low-pO_2 data could be fit reasonably well but not the high-pO_2 data. The adsorption-desorption parameters obtained by fitting the low-pO_2 steady-state polarization data followed the trend consistent with metal surfaces wherein the surface oxygen coverage, and thus the ratio k_{ads}/k_{des}, is observed to decrease with temperature.

Although a different set of kinetic parameters were required to fit the polarization curves and the impedance curves (at OCV), they both indicated that the adsorption process was a major contributor to the overall resistance of the oxygen reduction reaction. Because the adsorption process was so slow compared to surface diffusion, it was found that from the parallel pathways considered for oxygen transport, the gas transport pathway and surface oxygen transport pathways contributed roughly equally to the overall ORR. As the pO_2 increased, the gas transport pathway became slightly more favorable compared to the surface pathway.

In addition to pure LSM electrodes, a study of composite LSM/YSZ cathodes was undertaken. It was observed that compared to pure LSM cathodes at $750°C$ in air, composite cathodes with 50 vol% LSM and with a functional layer thickness of $L = 26\mu m$ resulted in a 40 fold decrease in the polarization resistance. Modelling results attributed this decrease to an increase in the triple phase boundary length as well as enhanced transport of oxygen through the YSZ phase in the composite cathode. The microstructure-performance relationship was examined for composite cathodes and it was determined that LSM-YSZ compositions that maximize the triple phase boundary length may not result in the lowest R_p values since the effective ionic conductivity must also be considered.

6.3 Contributions

The original research contributions of this thesis includes:

1. Development of a transient porous electrode model capable of simulating the impedance experiments while concurrently capturing the distributed nature of the electrode and accounting for adsorption/desorption, surface diffusion and gas transport phenomena. Such a model for LSM cathodes has not been previously presented.

2. Estimation of microstructure independent kinetic parameters from fitting of steady-state and impedance data to a model.

3. A quantitative analysis of the behavior of polarized and unpolarized LSM electrodes in both high and low oxygen partial pressures.

4. Observation of new behavior of LSM electrodes in low-pO_2 environment in that the polarization resistance increased with an increase in the extent of polarization.

5. Hypothesis that the LSM surface when sufficiently polarized undergoes either enrichment or depletion of cations depending on whether the oxygen atmosphere is either at a high-pO_2 or low-pO_2.

6. Analysis of limiting current density in low-pO_2 environment which was found to be caused by the adsorption/desorption ratio.

7. Development of an experimental routine capable of separating the effects of changes in the surface of LSM electrodes and the effects of electrochemical promotion of polarized electrodes.

8. The influence of species gradients within SOFC electrodes, especially for composite electrodes, and the impact these gradients have on the experimental measurements to determine electrochemical kinetic parameters.

6.4 Recommendation for Further Research

Many aspects of oxygen reduction in the state-of-the-art cathode material, LSM, are still unknown. The enhancement in electrode kinetics due to polarization and the apparent dynamic nature of the LSM surface are issues that are not well understood and make accurate prediction of the current/voltage characteristics difficult. At the same time, it is difficult to distinguish some of these phenomena from electrochemical processes such as electrochemical adsorption. It is likely that the mechanism of oxygen reduction involves a charge transfer reaction at the gas/LSM surface and further modelling work should attempt to incorporate this into a physics based model. In an attempt to capture the dynamic behavior of the LSM surface, it may also be interesting to combine a defect chemistry model, which solves for the oxygen stoichiometry and vacancy concentrations within the LSM lattice, with a micro-kinetic and transport model. In addition, there is value in implementing a more detailed physics based model of a composite cathode than what was presented in Chapter 5 of this thesis since there appears to be enhancements in composite cathodes over pure LSM cathodes that are beyond the extension of the triple phase boundary. These enhancements could be related to an additional ORR pathway involving oxygen adsorption and transport on the YSZ surface within the composite electrode. This may be possible since the internal surface area of the YSZ phase within the composite LSM/YSZ cathode is much higher than the YSZ surface area within a pure LSM cathode.

Another area of further research would be to determine if the kinetic rate constants and transport parameters used in the models presented in this work can be estimated uniquely. This can be a complicated problem and was outside the scope of this thesis, however, it is an important issue. The selection of a unique parameter set can also be helped by using quantum mechanical thermodynamic calculations, as was done in this thesis, but these calculations will likely be improved and expanded upon in the near future, especially as it relates to the use in kinetic type modelling studies. In addition, future DFT modelling studies may provide further insight into the kinetics of adsorption onto a cation vacancy as well as the surface diffusion coefficient, D_θ. Another area of improvement could be to increase the efficiency of the impedance calculation, which at the moment is computationally intensive, making fitting of parameters using optimization algorithms impractical. The impedance calculation lends itself well to parallelization and it may be worthwhile to investigate methods such as the multiple-frequency Fourier analysis technique for computing the impedance from time dependent i-V data, which is likely faster than the single-frequency technique used in this work. There are also more efficient optimization techniques which could be implemented to fit kinetic rate constants to experimental data.

Ultimately, in order to understand the true effects of the porous microstructure and performance of porous cathodes, such as the influence of anisotropy of the microstructure, a physics based model should be applied to representative geometries obtained through FIB-SEM reconstruction. Although extremely computationally intensive, theoretically, the impedance as well as the steady state polarization could be computed on such geometries. An interesting study would be to investigate whether the constant phase element behavior observed in the impedance response of LSM electrodes can be captured by such a model. The constant phase element is often said to be caused by a spatial distribution of processes, charges and particle shapes within the electrode. The implementation of local defects in these representative geometries, which influence the kinetics of various reactions, could also be implemented in a semi-empirical way.

Appendix A

Supplemental Material

Note

The raw data collected in this work is available by contacting either the author or Dr. Kunal Karan directly.

A.1 Oxygen Reduction Via Transport of Neutral Adsorbates

A.1.1 Transport of oxygen gas

For the transport of oxygen gas through the porous electrode, the total flux is made up of the diffusive flux and the convective flux. The total flux of oxygen molecules in the x direction is then described by Fick's law of diffusion and also by convection:

$$\Psi_{O_2} = -D_{O_2-N_2}\frac{\epsilon}{\tau}\frac{d\rho_{O_2}}{dx} + \epsilon\rho_{O_2}v_x = -D^{eff}_{O_2-N_2}\frac{d\rho_{O_2}}{dx} + \epsilon\rho_{O_2}v_x \tag{A.1}$$

where $D^{eff}_{O_2-N_2}$ is the effective binary diffusion coefficient, ρ_{O_2} is the density of O_2 (where $\rho_{O_2} = C_{O_2} \times M_{O_2}$) and v_x is the mass averaged velocity in m/s. The mass averaged velocity is used here to remain consistent with any assumptions associated with the continuity equation (mass balance) and the momentum equation.

While oxygen is transported throughout the porous cathode, oxygen may adsorb onto a particle surface to form adsorbed oxygen, or adsorbed oxygen may desorb to form oxygen gas. The adsorption and desorption process represents a consumption and generation of oxygen gas. The rate of adsorption and desorption is described by Equation 4.8. Therefore, the generation and consumption terms in Equation 4.3 become

$$R_g = k_{des} M_{O_2} C^2_{O_{ads}} \tag{A.2a}$$

$$R_c = k_{ads} M_{O_2} pO_2 C^2_s \tag{A.2b}$$

By combining Equations 4.3, A.1, A.2 and generalizing to three dimensions, the oxygen mole balance becomes

$$\epsilon \frac{d\rho_{O_2}}{dt} + \nabla(\epsilon \rho_{O_2} \vec{u}) = \nabla \cdot (D^{eff}_{O_2-N_2} \nabla \rho_{O_2}) + a k_{des} M_{O_2} C^2_{O_{ads}} - a k_{ads} M_{O_2} pO_2 C^2_s \tag{A.3}$$

where a is the internal surface area with units of m^2 surface/m^{-3} total volume. It should be noted that the term $\epsilon \rho_{O_2}$ is an effective concentration averaged over the entire control volume shown in Figure 4.3. $\vec{u}$ is the velocity vector $\vec{u} = [v_x \ v_y \ v_z]$.

A.1.2 Transport of adsorbed oxygen

A balance on adsorbed oxygen is similar to that of oxygen gas, except we assume that the flux of adsorbates is dominated by diffusion only and also the generation of adsorbed oxygen is related to the adsorption process while the consumption of adsorbed oxygen is related to the desorption process. The flux of adsorbed oxygen is

$$\Psi_{O_{ads}} = -a D^{eff}_{O_{ads}} \frac{dC_{O_{ads}}}{dx} \tag{A.4}$$

and the oxygen adsorbate balance becomes

$$a\frac{dC_{O_{ads}}}{dt} = \nabla \cdot (aD^{eff}_{O_{ads}} \nabla C_{O_{ads}}) + 2ak_{ads}pO_2C_s^2 - 2ak_{des}C^2_{O_{ads}} \tag{A.5}$$

Here $C_{O_{ads}}$ is the concentration of adsobates on the LSM surface (mol/m^{-2}) and a is the internal surface area, m^2 surface/m^{-3} total volume and so the term $aC_{O_{ads}}$ is an effective concentration of adsorbates within the control volume.

A.1.3 Transport of total mass

In the SOFC cathode, the electrochemical reaction involves a net consumption of gas molecules which is related to the current density by Farraday's law. As a consequence of the change in the net number of moles, a pressure gradient develops within the electrode causing net motion of gas. This can be described by the volume averaged momentum equation for porous media [1]:

$$\frac{\rho}{\epsilon}\left(\frac{\partial \mathbf{u_D}}{\partial t} + \mathbf{u_D} \cdot \nabla \mathbf{u_D}\right) = -\nabla < p >^{\mathbf{f}} + \rho\mathbf{f} + \frac{\mu}{\epsilon}\nabla^2\mathbf{u_D} - \frac{\mu}{\mathbf{K}}\mathbf{u_D} - \frac{C_E}{\mathbf{K}^{0.5}}\rho|\mathbf{u_D}|\mathbf{u_D} \tag{A.6}$$

If the Reynold's number is less than 1, then the flow is in the creeping flow regime and Equation A.6 can be simplified to

$$\frac{\rho}{\epsilon}\frac{\partial \mathbf{u_D}}{\partial t} = -\nabla < p >^{\mathbf{f}} - \frac{\mu}{\mathbf{K}}\mathbf{u_D} \tag{A.7}$$

which is an expression equivalent to Darcy's Law. The Reynold's number can be calculated from

$$Re = \frac{\rho u_p d}{\mu} = \frac{\rho u_D d}{\mu\epsilon} \tag{A.8}$$

where u_p is the average pore velocity. For typical SOFC operating temperatures between 700-850°C and for an average pore diameter of 0.5μm, pore velocities are required to be less than 7.26m/s to meet this criteria. Here it is assumed that the Reynold's number is much less than 1 so that a simplified version of the momentum equation can be used.

A total mass balance on the gas species within the electrode results in the continuity equation with the flux term being $\Psi_x = \rho u_x$:

$$\frac{d}{dx}(\rho u_x) = aR_g - aR_c \tag{A.9}$$

where the source terms R_g and R_c are defined by Equations A.2. Rearranging Equation A.7 and solving for u and plugging into the continuity equation, Equation A.9 results in an expression for the pressure drop within the electrode:

$$\nabla \cdot \left(-\frac{\rho\kappa}{\mu}\nabla P_{tot}\right) = ak_{des}M_{O_2}C_{O_{ads}}^2 - ak_{ads}M_{O_2}pO_2C_s^2 \tag{A.10}$$

where κ is the permeability in m^2, ρ is the total gas density calculated using the ideal gas law, μ is the gas viscosity and P_{tot} is the total pressure within the electrode. With the knowledge of the pressure gradient, the bulk velocity can be calculated and coupled to the transport of oxygen gas through the convective flux in Equation A.3:

$$u = -\frac{\kappa}{\mu}\frac{dP_{tot}}{dx} \tag{A.11}$$

A.1.4 Transport of charge

The transport of electronic charge is described using Ohm's law using an effective conductivity which was measured experimentally using the van Der Pauw technique. The steady state representation of this equation simply means that the accumulation of charge is accounted for through a double layer current, as will be explained in the next section.

$$0 = \nabla \cdot (\sigma_{el}^{eff}\nabla\phi_{el}) \tag{A.12}$$

A.1.5 Electrochemistry

The derivations above described the transport of species through the porous electrode, however, they are all coupled to the electrochemical reaction at the LSM/YSZ interface. The rate of the charge transfer reaction, Equation 4.10, can be converted into a current by multiplying by the factor nF. The cathodic and anodic currents are

$$i_{cathodic} = \underbrace{nF\lambda_{TPB}k_f^0 C_{O_{ads}} C_{V_{\ddot{O}}} \exp\left(\frac{-\beta nF}{RT}\Delta\phi^{eq}\right)}_{i_{0,c}} \exp\left(\frac{-\beta nF}{RT}\eta\right) \tag{A.13a}$$

$$i_{anodic} = \underbrace{nF\lambda_{TPB}k_b^0 C_{O_O^x} C_s \exp\left(\frac{(1-\beta)nF}{RT}\Delta\phi^{eq}\right)}_{i_{0,a}} \exp\left(\frac{(1-\beta)nF}{RT}\eta\right) \tag{A.13b}$$

If we define θ as the concentration of adsorbates ($C_{O_{ads}}$) divided by the total number of adsorption sites, N, then the concentration of free sites, C_s, can be defined as $N(1-\theta)$, and we can write

$$\frac{C_{O_{ads}}}{C_s} = \frac{N\theta}{N(1-\theta)} \tag{A.14}$$

θ is now a dimensionless quantity called surface coverage and falls between values of 0 and 1 to describe the extent of coverage of adsorbed oxygen on the surface of the LSM electrode. With this definition of surface coverage, Equation A.13 becomes

$$i_{cathodic} = nF\lambda_{TPB}k_f^0 N\theta C_{V_{\ddot{O}}} \exp\left(\frac{-\beta nF}{RT}\Delta\phi^{eq}\right) \exp\left(\frac{-\beta nF}{RT}\eta\right) \tag{A.15a}$$

$$i_{anodic} = nF\lambda_{TPB}k_b^0 C_{O_O^x} N(1-\theta) \exp\left(\frac{(1-\beta)nF}{RT}\Delta\phi^{eq}\right) \exp\left(\frac{(1-\beta)nF}{RT}\eta\right) \tag{A.15b}$$

and the equilibrium potential is

$$\Delta\phi^{eq} = \frac{RT}{nF}\ln\left(\frac{k_f^0}{k_b^0}\right) + \frac{RT}{nF}\ln\left(\frac{\theta^{eq}}{1-\theta^{eq}}\right) + \frac{RT}{nF}\ln\left(\frac{C_{V_{\ddot{O}}}}{C_{O_O^x}}\right) \tag{A.16}$$

Further following the mathematical treatment of Section 2.4.1, the exchange current density is

$$i_0 = nF[\lambda_{TPB}k_b^0 N(1-\theta^{eq})C_{O_O^x}]^{\beta}[\lambda_{TPB}k_f^0 N\theta^{eq} C_{V_{\ddot{O}}}]^{(1-\beta)} \tag{A.17}$$

and the net current is

$$i = i_0\left[\frac{1-\theta}{1-\theta^{eq}}\exp\left(\frac{(1-\beta)nF}{RT}\eta\right) - \frac{\theta}{\theta^{eq}}\exp\left(-\frac{\beta nF}{RT}\eta\right)\right] \tag{A.18}$$

Since i_0 is a function of θ, it is also related to pO_2 through the oxygen adsorption/desorption reaction in Equation 4.8. The current described by Equation A.18 is known as the Faradaic current, or a current resulting from steady state conditions without the influence of a current from the charge double layer. In the transient case, the double layer at the electrode/electrolyte interface is charged and this charging results in a capacitative current, which, for an ideal capacitor, can be described by

$$i_{dl} = A_{dl} C_{dl} \frac{d\eta}{dt} \tag{A.19}$$

where A_{dl} is the contact area between the electrode and the electrolyte with units of m^2 contact area/m^2 total area and C_{dl} is the capacitance of the double layer with units of F/m^2. Under transient conditions such as impedance spectroscopy, the total current at the LSM/YSZ interface is therefore:

$$i_{tot} = i_{far} + i_{dl} = i_0 \left[\frac{1-\theta}{1-\theta^{eq}} \exp\left(\frac{(1-\beta)nF}{RT}\eta \right) - \frac{\theta}{\theta^{eq}} \exp\left(-\frac{\beta nF}{RT}\eta \right) \right] + A_{dl} C_{dl} \frac{d\eta}{dt} \tag{A.20}$$

The electrode overpotential, η, is defined as the difference in the electric potential of the electrode and the electric potential of the electrolyte at the point $x = L$: $\eta = (\phi_{el} - \phi_{io})|_{x=L}$.

A.1.6 Summary of Equations and Boundary Conditions

With $C_{O_{ads}} = N\theta$ and $C_s = N(1-\theta)$, the transport of oxygen gas, oxygen adsorbates, total mass and electronic charge become

$$\epsilon \frac{d\rho_{O_2}}{dt} + \nabla(\epsilon \rho_{O_2} \vec{u}) = \nabla \cdot (D^{eff}_{O_2-N_2} \nabla \rho_{O_2}) + a k_{des} M_{O_2} N^2 \theta^2 - a k_{ads} M_{O_2} pO_2 N^2 (1-\theta)^2 \tag{A.21}$$

$$aN \frac{d\theta}{dt} = \nabla \cdot (aND^{eff}_{\theta} \nabla \theta) + 2ak_{ads} pO_2 N^2 (1-\theta)^2 - 2ak_{des} N^2 \theta^2 \tag{A.22}$$

$$\nabla \cdot \left(-\frac{\rho\kappa}{\mu}\nabla P_{tot}\right) = ak_{des}M_{O_2}N^2\theta^2 - ak_{ads}M_{O_2}pO_2N^2(1-\theta)^2 \tag{A.23}$$

$$0 = \nabla \cdot (\sigma_{el}^{eff}\nabla\phi_{el}) \tag{A.24}$$

Using the geometry definitions outlined in Section 4.2.1 where $x = 0$ is the gas channel/cathode interface and $x = L$ is the cathode/bulk electrolyte interface, then the boundary conditions for Equations A.21, A.22 and A.24 can be defined as follows.

Oxygen gas boundary conditions For the balance on oxygen gas (Equation A.21), we know the mole fraction of oxygen in the bulk and we assume that the electrolyte is perfectly dense such that the flux of oxygen gas through the boundary is 0.

At x=0

$$\rho_{O_2} = \frac{y_{O_2}^{bulk}P_T}{RT}M_{O_2} = \frac{pO_2}{RT}M_{O_2} \tag{A.25}$$

At x=L

$$-\epsilon D_{O_2-N_2}^{eff}\frac{d\rho_{O_2}}{dx} = 0 \tag{A.26}$$

At t=0

$$\rho_{O_2}(t=0) = \frac{y_{O_2}^{bulk}P_T}{RT}M_{O_2} = \frac{pO_2}{RT}M_{O_2} \tag{A.27}$$

Adsorbate boundary conditions For the balance on adsorbed oxygen, adsorbates are blocked at the gas channel/cathode interface, and they are consumed at the cathode/bulk electrolyte interface via the electrochemical reaction whose current is described by Equation A.18. It is also assumed that at $t = 0$, the oxygen gas from the bulk is in equilibrium with adsorbates on the LSM surface.

At x=0

$$-aND_{O_{ads}}^{eff}\frac{d\theta}{dx} = 0 \tag{A.28}$$

At x=L

$$-aND_{O_{ads}}^{eff}\frac{d\theta}{dx} = \frac{i_{far}}{2F} \tag{A.29}$$

At t=0

$$\theta^{eq}(t=0) = \frac{\sqrt{\frac{k_{ads}}{k_{des}}}\sqrt{pO_2^{eq}}}{1+\sqrt{\frac{k_{ads}}{k_{des}}}\sqrt{pO_2^{eq}}} \tag{A.30}$$

Mass transport boundary conditions The transport of mass is represented by the total pressure within the electrode. At the gas/electrode interface, $x = 0$, it is assumed that the pressure is equal to atmospheric pressure, 101325 Pa. At the electrode/electrolyte interface, it is assumed that the gas velocity, u, is equal to zero. From Darcy's Law, this equates to a zero pressure gradient since $u \propto dP/dx$.

At x=0

$$P_{tot} = P \tag{A.31}$$

At x=L

$$-\frac{\rho\kappa}{\mu}\frac{dP_{tot}}{dx} = 0 \tag{A.32}$$

At t=0

$$P_{tot}(t=0) = P \tag{A.33}$$

Electronic potential boundary conditions The potential of the working electrode is applied with respect to the reference electrode. If we set the potential of the reference electrode, which is located both experimentally and in this model on the electrolyte, to be 0, then the potential difference between the working electrode and the reference electrode becomes the potential applied to the current collector of the working electrode. Therefore, numerically, the cathode potential is defined by setting the potential at the gas/electrode interface, $x = 0$. In addition, electronic current is converted into ionic current at the LSM/YSZ interface, representing a flux of charge.

At x=0

$$\phi_{el} = \Delta\phi^{applied} \tag{A.34}$$

At x=L

$$\sigma_{el}^{eff}\frac{d\phi_{el}}{dx} = i_{tot} \tag{A.35}$$

Equations A.21-A.24 and their boundary conditions Equations A.25-A.35 represents a well defined system of equations which, once appropriate parameters are obtained, can be solved using a

PDE solver.

A.2 Oxygen Reduction Via Transport of Charged Adsorbates

The charged adsorbate surface pathway mechanism is characterized by two charge transfer reactions: a charge transfer reaction at the adsorbate/perovskite interface and a second charge transfer reaction at the triple phase boundary. Each of these charge transfer reactions involve a single electron and are similar in that they can both be assumed to obey typical Butler-Volmer kinetics, however, with the caveat that the overpotential at the adsorbate/perovskite interface is not the same as the overpotential at the triple phase boundary, as described by Fleig [2]. In addition, since the adsorbed oxygen is a charged species, its flux may be influenced not only by a concentration gradient but also by the surrounding electric field. The treatment of this additional flux of charged adsorbates can be similar to the treatement of gas convection through porous media using Darcy's Law except instead of being driven by a pressure gradient as in Darcy's Law it is driven by a potential gradient.

The following processes have been assumed to occur:

(i) Electrochemical dissociative adsorption/desorption at gas/perovskite interface:

$$\frac{1}{2}O_2(g) + s + e^- \underset{k_{des}}{\overset{k_{ads}}{\rightleftharpoons}} O^-_{ads}$$

(ii) Surface convection and diffusion:

$$J_{O^-_{ads}} = -D_{O^-_{ads}}\frac{a}{\tau}\frac{dC_{O^-_{ads}}}{dx} + auC_{O^-_{ads}} = -aD^{eff}_{O^-_{ads}}\frac{dC_{O^-_{ads}}}{dx} + auC_{O^-_{ads}}$$

(iii) Charge transfer at the triple phase boundary:

$$O^-_{ads} + (e^-)^{ed} + (V_{\ddot{O}})^{el} \underset{k_b}{\overset{k_f}{\rightleftharpoons}} (O^x_O)^{el} + s$$

The rate of the electrochemical adsorption/desorption reaction is

$$\frac{1}{2}\frac{da_{O^-_{ads}}}{dt} = -\frac{da_{O_2}}{dt} = ak^{\dagger}_{ads}pO_2a_s^2 - ak^{\dagger}_{des}a^2_{O^-_{ads}} \tag{A.36}$$

where $k^{\dagger}_{ads}$ and $k^{\dagger}_{des}$ are electrochemical reaction rate constants. The rate of the charge transfer step at the TPB is

$$\frac{da_{O^-_{ads}}}{dt} = -\lambda_{TPB}k_fa_{O^-_{ads}}a_{V_{\ddot{O}}} + \lambda_{TPB}k_ba_{O^x_O}a_s \tag{A.37}$$

where k_f and k_b are electrochemical rate constants and λ_{TPB} is the triple phase boundary length.

If we assume ideal gas and ideal solution, we can take the activities to be equal to partial pressures of gas (in atm) or their concentrations (in mol/m^3).

A.2.1 Transport of oxygen gas

The transport of oxygen gas follows the same form as for the Surface Pathway 1 mechanism, Equation A.3, except the reaction terms are slightly different due to electrochemical reaction rate constants.

$$R_g^v = ak^{\dagger}_{des}C^2_{O_{ads}} \tag{A.38}$$

$$R_c^v = ak^{\dagger}_{ads}pO_2C_s^2 \tag{A.39}$$

The oxygen mole balance becomes

$$\epsilon\frac{dC_{O_2}}{dt} + \nabla(\epsilon C_{O_2}\vec{u}) = \nabla\cdot(D^{eff}_{O_2-N_2}\nabla C_{O_2}) + ak^{\dagger}_{des}C^2_{O^-_{ads}} - ak^{\dagger}_{ads}pO_2C_s^2 \tag{A.40}$$

A.2.2 Transport of adsorbed oxygen

Now that the adsorbed oxygen is a charged species, it may be possible that its transport is influenced by the surrounding electric field. The flux of adsorbed oxygen is

$$J_{O^-_{ads}} = -D_{O^-_{ads}}\frac{a}{\tau}\frac{dC_{O^-_{ads}}}{dx} + auC_{O^-_{ads}} = -aD^{eff}_{O^-_{ads}}\frac{dC_{O^-_{ads}}}{dx} + auC_{O^-_{ads}} \tag{A.41}$$

and the oxygen adsorbate balance becomes

$$a\frac{dC_{O_{ads}}}{dt} + \nabla \cdot (auC_{O^-_{ads}}) = \nabla \cdot (aD^{eff}_{O^-_{ads}} \nabla C_{O^-_{ads}}) + ak^\dagger_{ads} pO_2 C_s^2 - ak^\dagger_{des} C^2_{O^-_{ads}} \tag{A.42}$$

A.2.3 Transport of charge

Now that electrons are being consumed throughout the electrode, the charge balance requires reaction rate terms describing the anodic and cathodic currents of the electrochemical adsorption/desorption reaction.

$$0 = \nabla \cdot (\sigma^{eff}_{el} \nabla \phi_{el}) + i^{ads}_{anodic} - i^{ads}_{cathodic} \tag{A.43}$$

where superscript *ads* refers to the electrochemical adsorption/desorption reaction.

A.2.4 Electrochemistry

In addition to the electrochemical rate constants at the TPB, k_f and k_b, the adsorption and desorption rate constants, $k^\dagger_{ads}, k^\dagger_{des}$ are now electrochemical rate constants.

$$k_f = k^0_f \exp\left(\frac{-(1-\beta)nF}{RT}\Delta\phi\right) \tag{A.44}$$

$$k_b = k^0_b \exp\left(\frac{\beta nF}{RT}\Delta\phi\right) \tag{A.45}$$

$$k^\dagger_{ads} = k_{ads} \exp\left(\frac{-(1-\beta^{ads})nF}{RT}\Delta\chi\right) \tag{A.46}$$

$$k^\dagger_{des} = k_{des} \exp\left(\frac{\beta^{ads} nF}{RT}\Delta\chi\right) \tag{A.47}$$

where k^0_f and k^0_b are the chemical reaction rate constants at the TPB, β is the symmetry coefficient for the TPB charge transfer reaction, β^{ads} is the symmetry coefficient for the electrochemical adsorption/desorption reaction, $\Delta\phi = \Delta\phi^{eq} + \eta$ is the driving force of the TPB reaction and $\Delta\chi = \Delta\phi - \Delta\phi_{ads}$ is the driving force for the electrochemical adsorption/desorption reaction, as described by Fleig [2]. Fleig derived the following equation for $\Delta\chi$:

$$\Delta\chi = 2\eta - \frac{RT}{F^2} \ln\left(\frac{\theta}{1-\theta}\frac{1-\theta^{eq}}{\theta^{eq}}\right) \tag{A.48}$$

It should be noted that Equation A.48 was derived using chemical and electrochemical potentials and assumes that the electrochemical adsorption/desorption reaction is rate determining. All other equations being described throughout this section do not assume a rate determining step and so we treat Equation A.48 as the best known approximation to the overpotential of the electrochemical adsorption/desorption step. It should also be mentioned that n in Equations A.44-A.47 and throughout the description of the Surface Pathway 2 mechanism is equal to 1.

Electrochemical Adsorption/Desorption Reaction

The electrochemical adsorption/desorption reaction is:

$$\frac{1}{2}O_2(g) + s + e^- \underset{k_{des}}{\overset{k_{ads}}{\rightleftharpoons}} O^-_{ads} \tag{A.49}$$

This reaction can be converted into a current by multiplying its rate, Equation A.36 by the factor nF. The cathodic and anodic currents are described by combining Equations A.36, A.46, A.47 and A.48 . Following the general treatment of electrochemical reactions described in Section 2.4.1 and setting $C_R = pO_2^{0.5}N(1-\theta^-)$ and $C_P = N\theta^-$, we can write the net current and the exchange current density as:

$$i^{ads} = i_0^{ads}\left[\frac{C_P}{C_P^{eq}}\exp\left(\frac{(1-\beta^{ads})nF}{RT}\eta\right) - \frac{C_R}{C_R^{eq}}\exp\left(-\frac{\beta^{ads}nF}{RT}\eta\right)\right] \tag{A.50}$$

where

$$i_0^{ads} = aF(k^0_{ads}C_R^{eq})^{1-\beta}(k^0_{des}C_P^{eq})^{\beta} \tag{A.51}$$

the exchange current density, i_0, is now a function of pO_2 and θ^- as well as the chemical component of the adsorption/desorption rate constants and the gas/LSM surface area, a.

Electrochemical Reaction at TPB

The electrochemical treatment at the TPB for the Surface Pathway 2 mechanism is identical to that of the Surface Pathway 1 mechanism, described in Section A.1.5, except in this case, only 1 electron is transfered ($n = 1$). This current at the triple phase boundary is denoted i^{tpb} to distinguish it from the current at the gas/LSM interface.

A.2.5 Equations and boundary conditions

With $C_{O_{ads}} = N\theta^-$ and $C_s = N(1-\theta^-)$, and defining the volumetric reaction rates in terms of the volumetric current, the transport equations become:

$$\epsilon \frac{dC_{O_2}}{dt} + \nabla(\epsilon C_{O_2} \vec{u}) = \nabla \cdot (D^{eff}_{O_2-N_2} \nabla C_{O_2}) + \frac{i^{ads}}{2F} \tag{A.52}$$

$$aN \frac{d\theta^-}{dt} + \nabla(aN\theta^- \vec{u}) = \nabla \cdot (aND^{eff}_{\theta} \nabla \theta^-) - \frac{i^{ads}}{F} \tag{A.53}$$

$$0 = \nabla \cdot (\sigma^{eff}_{el} \nabla \phi_{el}) + i^{ads} \tag{A.54}$$

If we take $x = 0$ to be the gas channel/cathode interface and $x = L$ to be the cathode/bulk electrolyte interface, then the boundary conditions for Equations A.52, A.53 and A.54 can be defined as follows.

For the balance on oxygen gas (Equation A.52), we know the mole fraction of oxygen in the bulk and we assume that the electrolyte is perfectly dense.

At x=0

$$C_{O_2} = \frac{y^{bulk}_{O_2} P_T}{RT} = \frac{pO_2}{RT} \tag{A.55}$$

At x=L

$$-D^{eff}_{O_2-N_2} \frac{dC_{O_2}}{dx} = 0 \tag{A.56}$$

At t=0

$$C_{O_2}(t=0) = \frac{y^{bulk}_{O_2} P_T}{RT} = \frac{pO_2}{RT} \tag{A.57}$$

For the balance on adsorbed oxygen, adsorbates are blocked at the gas channel/cathode interface, and they react at the TPB interface via the second electrochemical reaction which generates a net current described by Equations A.15a and A.15b with $n = 1$. Also, when the electrochemical adsorption/desorption reaction is at equilibrium, $k^{\dagger}_{ads} = k_{ads}$ and $k^{\dagger}_{des} = k_{des}$ and so the concentration of adsorbates at equilibrium can be described by the Langmuir isotherm.

At x=0

$$-aND^{eff}_{O_{ads}}\frac{d\theta^{-}}{dx} = 0 \tag{A.58}$$

At x=L

$$-aND^{eff}_{O_{ads}}\frac{d\theta^{-}}{dx} = \frac{i^{tpb}}{F} \tag{A.59}$$

At t=0

$$\theta^{-,eq}(t=0) = \frac{\sqrt{\frac{k^0_{ads}}{k^0_{des}}}\sqrt{pO_2^{bulk}}}{1+\sqrt{\frac{k^0_{ads}}{k^0_{des}}}\sqrt{pO_2^{bulk}}} \tag{A.60}$$

At the TPB interface, a Faradaic current is produced by the second charge transfer reaction. At the gas channel/cathode interface, a potential relative to a reference electrode of the same kind is applied so that the cathode potential is defined by setting the potential at the gas channel/cathode interface.

At x=0

$$\phi_{el} = \Delta\phi^{applied} \tag{A.61}$$

At x=L

$$\sigma^{eff}_{el}\frac{d\phi_{el}}{dx} = i^{tpb} \tag{A.62}$$

An important aspect of this model is the calculation of the current. Unlike the model for Surface Pathway 1, the total current cannot simply be calculated from the net reaction rate at the TPB interface since electronic charge is also consumed throughout the thickness of the electrode. To calculate the current density, the electronic charge flux must be calculated at the gas channel/cathode interface. This represents the total electronic charge entering the electrode. A similar calculation can also be done for Surface Pathway 1 however it is not required.

At x=0

$$i_{tot} = \sigma_{el}^{eff} \frac{d\phi_{el}}{dx} \tag{A.63}$$

References

[1] M. Kaviany. *Principles of Heat Transfer in Porous Media*. Springer, second edition, 1999.

[2] J. Fleig. On the current-voltage characteristics of charge transfer reactions at mixed conducting electrodes on solid electrolytes. *Physical Chemistry Chemical Physics*, 7:2027–2037, 2005.